Impact of drying rate on delayed strain behavior of cement-based materials - experimental and numerical study

Justin Kinda

▶ **To cite this version:**

Justin Kinda. Impact of drying rate on delayed strain behavior of cement-based materials - experimental and numerical study. Génie civil. Université Paris-Saclay, 2021. Français. NNT : 2021UPAST020 . tel-03505908

HAL Id: tel-03505908
https://theses.hal.science/tel-03505908

Submitted on 1 Jan 2022

HAL is a multi-disciplinary open access archive for the deposit and dissemination of scientific research documents, whether they are published or not. The documents may come from teaching and research institutions in France or abroad, or from public or private research centers.

L'archive ouverte pluridisciplinaire **HAL**, est destinée au dépôt et à la diffusion de documents scientifiques de niveau recherche, publiés ou non, émanant des établissements d'enseignement et de recherche français ou étrangers, des laboratoires publics ou privés.

Thèse de doctorat

NNT: 2021UPAST020

Impact of drying rate on delayed strain behavior of cement-based materials - experimental and numerical study

Thèse de doctorat de l'Université Paris-Saclay

École doctorale n° 579, sciences mécaniques et énergétiques, matériaux et géosciences
Spécialité de doctorat: solides, structures et matériaux
Unité de recherche: Université Paris-Saclay, ENS Paris-Saclay, CNRS, LMT- Laboratoire de Mécanique et Technologie 91190, Gif-sur-Yvette, France
Référent: ENS Paris-Saclay

Thèse présentée et soutenue à l'École normale supérieure Paris-Saclay, le 01 mars 2021, par

Justin Kinda

Composition du jury:

Jean-Michel Torrenti Professeur, Ecole des Ponts ParisTech	Président
Alain Sellier Professeur, Université Paul Sabatier - Toulouse III	Rapporteur
Matthieu Vandamme Chercheur HdR, Ecole des Ponts ParisTech	Rapporteur
Francois Hild Directeur de Recherche, CNRS	Examinateur
Catherine A. Davy Professeur, Ecole Centrale de Lille	Examinatrice
Bruno Huet Ingénieur Chercheur, LafargeHolcim	Invité
Farid Benboudjema Professeur, ENS Paris-Saclay	Directeur de thèse
Alexandra Bourdot Maître de Conférence, ENS Paris-Saclay	Coencadrante
Laurent Charpin Ingénieur Chercheur, EDF R&D	Coencadrant
Sylvie Michel-Ponnelle Ingénieur Chercheur, EDF R&D	Coencadrante

Contents

List of Figures

List of Tables

Remerciements

Je souhaiterais avant tout exprimer ma profonde gratitude à mon directeur de thèse Farid Benboudjema et à mes encadrants, Alexandra Bourdot, Laurent Charpin, Sylvie Michel-Ponnelle, de m'avoir accordé leur confiance pour mener ces travaux de thèse ; leurs conseils avisés lors de nos nombreux échanges ont contribué à l'aboutissement de ces travaux. J'ai grandi aussi bien professionnellement que personnellement à leurs côtés. Qu'ils sachent que leur curiosité scientifique et leur dynamisme d'esprit m'ont beaucoup guidés.

Qu'il me soit permis de remercier vivement Jean-Michel Torrenti de m'avoir fait l'honneur de présider le jury de cette thèse; merci vivement à Alain Sellier et Mathieu Vandamme de m'avoir fait l'honneur de rapporter ce travail de thèse; mes sincères remerciements vont également à Francois Hild, Catherine Davy et Bruno Huet pour avoir examiné avec beaucoup d'attention le manuscrit de thèse.

J'ai aussi eu la chance durant ces trois années de thèse de pouvoir évoluer dans trois équipes distinctes. Je remercie l'équipe Génie civil du groupe T25/MMC d'EDF de m'avoir accueilli pour ces trois années passées d'abord en tant que stagiaire puis ensuite doctorant. Je remercie le chef de groupe Youcef Sirsalane pour son implication au bon déroulement de la thèse ; Jean-Luc Adia pour sa disponibilité et son implication dans le stage et la thèse ; Julien Sanahuja qui a toujours bien voulu répondre à mes nombreuses sollicitations; Laurent Petit pour son humour et sa sagesse inspirante ; merci à la team Labo génie civil, Alexis Legrix, Romain Thion et Didier Leroy pour m'avoir accompagné chaleureusement dans la réalisation du programme expérimental. Merci également à Shun Huang , Khai Quynh Dinh, Herman Koala, pour nos nombreux échanges; je témoigne ma gratitude également à Jean-Philippe Mathieu , Nhu-Cuong Tran , Charles Toulemonde, Chaveli Bitsindou, François Soleilhet , Patrick Desgré , Patrick Semete.

Je remercie l'équipe technique du LMT, en particulier Remi Legroux qui n'a pas compté de ses heures pour permettre de réussir la campagne de la thèse. Je ne n'oublie pas que tu t'es rendu disponible des week-end pour permettre de lancer un essai dans les délais ! Je remercie également mes collègues doctorants et chercheurs du LMT. Je remercie Francois Hild, Stephane Roux et Amine Bouterf, pour avoir mis à ma disposition le code de corrélation d'images et pour les échanges sur les techniques d'imagerie. Je tiens à remercier mes compagnons de travail qui m'ont offert un cadre stimulant, je pense particulièrement à Nicolas Chan, Takwa Sayari, Pascale Saba, Xuyang Chang, Amelie Fau, Achraf Ouaddi, Rodriguez Itura Sebastian pour les moments de partage durant ces trois années.

Je suis profondément reconnaissant à l'équipe du Material Ageing Institute ; je remercie particulièrement Michel Mahe pour m'avoir communiqué son enthousiasme sur la microscopie, je me souviens de sa phrase célèbre, « il y a du monde !» en faisant référence aux hétérogénéités de la pâte de ciment vues au microscope. Merci également au chef de groupe T27/MMC d'EDF, Julien Stodolna, à toute la team Labo MAI Nicolas Brynaert, Dominique Loisnard.

Je remercie enfin ma famille, mes amis, leur soutien sans faille et leurs encouragements durant ces trois années de thèse.

Bonne lecture !

Résumé Long - Long abstract

Résumé long

Les enceintes du parc nucléaire français font l'objet d'un programme de maintenance coûteux en vue de maintenir une étanchéité suffisante en regard des critères réglementaires. L'ingénierie souhaite disposer de moyens pour optimiser ce programme de maintenance en vue de réduire les coûts. La perte de précontrainte est une cause majeure de cette perte d'étanchéité. Ainsi, tous les phénomènes à l'origine de cette perte de précontrainte doivent être maîtrisés, au premier plan le fluage et le retrait du béton, pilotés à long terme par son séchage. Pour prédire l'évolution de l'étanchéité à l'avenir, EDF a donc besoin de disposer de lois de comportement du béton des enceintes. Le développement de telles lois a déjà fait l'objet de nombreux travaux à EDF, qui se poursuivent au sein de cette thèse sur l'influence de la vitesse de séchage sur les déformations différées. En effet, les modèles de retrait et de fluage actuellement utilisés à EDF R&D supposent que la variation de retrait ou de fluage est liée à la variation d'humidité, indépendamment de la vitesse à laquelle se fait cette variation. Or, les éprouvettes de laboratoire étant de très petite taille par rapport à l'épaisseur des structures étudiées, le séchage est beaucoup plus rapide en laboratoire que sur les enceintes. Il est donc nécessaire de vérifier que l'indépendance à la vitesse de séchage est valable. Pour étudier cette thématique, il est nécessaire de pouvoir piloter le degré de saturation d'échantillons de béton. Or, le séchage du béton est très lent et induit des durées d'essai importantes. Ainsi, l'étude a été menée sur pâte de ciment, qui est la source des déformations différées et présente donc qualitativement le même comportement de retrait et de fluage que le béton. L'avantage de travailler avec la pâte de ciment, c'est qu'il est possible de réaliser des échantillons représentatifs beaucoup plus petits, qui s'équilibrent donc plus vite et permettent des durées d'essais raisonnables. Le présent travail vise donc à apporter une contribution à la compréhension des mécanismes de séchage, de retrait et de fluage à l'échelle de la pâte de ciment grâce à des essais expérimentaux novateurs, notamment vis à vis de la vitesse de séchage et de l'effet Pickett. Puis, à la lumière de ces résultats, l'objectif est de proposer un modèle prenant en compte ces effets hydriques sur le comportement différé du béton.

Dans le volet expérimental, le but de la campagne est d'étudier l'effet de la vitesse de séchage sur le fluage et le retrait. Une difficulté lors de la caractérisation du retrait et du fluage séchant est la fissuration des échantillons en raison des gradients de séchage au sein de l'échantillon. L'utilisation de petits échantillons de pâte de ciment qui s'équilibrent rapidement et donc présentent des gradients moins marqués, permet de limiter les effets de fissuration à l'échelle de la structure, et évite une microfissuration due aux contrastes de retrait et de fluage entre la pâte de ciment et les granulats. Ainsi il est possible d'isoler les effets purement matériaux à l'échelle de la pâte de ciment. Il a donc été décidé de réaliser des essais de retrait et de fluage sur des échantillons de pâte de ciment d'épaisseur 2 mm. Ces essais microscopiques ont été réalisés : (1) sous microscope électronique à

balayage environnemental (MEBE) à EDF R&D MMC et (2) dans la machine de traction-compression biaxiale Mini-Astrée du LMT à l'ENS Paris-Saclay, placée sous enceinte climatique avec une concentration en CO_2 contrôlée et suivis par une caméra ultrarapide. Les images obtenues lors de ces essais ont été analysées par corrélation d'images. Les résultats montrent que la vitesse de séchage n'a pas d'impact sur la déformation maximale de retrait de dessiccation. En parallèle, il a été entrepris une campagne macroscopique sur des échantillons séchants et prééquilibrés à différentes humidités relatives: 80 %HR, 58 %HR et 20 %HR. Ces essais mettent en évidence la diminution de la cinétique de fluage propre quand l'humidité relative diminue.

Pour ce qui est du volet numérique, l'objectif est de proposer des modèles de séchage, de retrait et de fluage qui intègrent au mieux l'impact de la vitesse de séchage, par l'étude numérique des essais réalisés. L'analyse du séchage a été menée en premier lieu. Un modèle de séchage prenant en compte la perméation de l'eau liquide et la diffusion de la vapeur d'eau a été adopté, avec comme variable principale le degré de saturation en eau liquide. Le modèle a été implémenté dans les outils de simulation d'EDF. Une attention particulière a été portée sur l'identification des paramètres et aux conditions aux limites de convection hydrique. Il est démontré que ce modèle de séchage permet de simuler des échantillons de différentes tailles (rayon de séchage de 1 mm, 36 mm) avec un jeu unique de paramètres. Une analyse de sensibilité au coefficient d'échange hydrique a été menée. La déformation de retrait de dessiccation est supposée être proportionnelle à la variation d'humidité relative. Le coefficient de proportionnalité est identifié à partir des mesures d'isotherme de retrait réalisées sur les échantillons d'épaisseur 200 µm, 500 µm et 2 mm. Le modèle s'est révélé particulièrement efficace pour reproduire le comportement en retrait de dessiccation d'échantillons de différentes tailles, séchant à différentes vitesses. En dernier lieu, le fluage a été étudié: deux modèles de la littérature ont été comparés. Le premier modèle est de type Burger avec une contribution du fluage propre irréversible modélisée selon la théorie de la consolidation. Par extension on appellera Burger l'ensemble du modèle de fluage propre et dessiccation utilisé à EDF. Le second est le modèle Micro-Prestress Solidification (MPS). Les deux modèles sont confrontés aux résultats expérimentaux, sous deux angles: (1) la dépendance du fluage propre à la teneur en eau (2), l'effet de taille et de vitesse de séchage sur le fluage de dessiccation. La comparaison montre que le modèle Burger est à même de prendre en compte l'effet de taille et de vitesse de séchage sur le fluage de dessiccation, ce qui n'est pas le cas pour le modèle MPS. Pour ce qui est de la dépendance à l'humidité du fluage propre à long terme, le modèle Burger prédit également mieux la cinétique que le modèle MPS. En effet, le modèle MPS surestime considérablement la cinétique du fluage propre: plus l'humidité relative est faible, plus le modèle surestime. Toutefois, la modélisation du taux de déformation du fluage propre en fonction du niveau d'humidité des deux modèles peut être améliorée.

Long abstract

The nuclear power plant containments buildings are subject to a costly maintenance program to maintain sufficient tightness regarding the regulatory criteria. Engineering wants to optimize this maintenance program to reduce costs. The loss of pre-stress is a significant cause of this loss of tightness. Thus, all the phenomena that cause the loss of prestressing must be controlled. First and foremost, the creep and shrinkage of the concrete are driven in the long term by its drying. To predict the evolution of the tightness in the future, EDF needs to have at disposal the containment's behavior laws. The development

of such laws has already been the subject of much work at EDF. This thesis is a continuation of this effort and focuses on the influence of the drying rate on delayed deformations. Indeed, the shrinkage and creep models currently used at EDF R&D assume that the variation of shrinkage or creep is related to moisture variation, independently of the rate at which this variation occurs. However, since the laboratory specimens are very small compared to the thickness of the structures studied, the drying process is much faster in the laboratory than in the test chambers. It is, therefore, necessary to verify that the independence of the drying rate is valid. An effective way to address this issue is to control the degree of saturation of concrete samples. However, the drying of concrete is very slow and induces significant test durations. Thus, the study was carried out on cement paste, which is the source of delayed deformations and thus presents qualitatively the same behavior of shrinkage and creep as concrete. The advantage of working with cement paste is that it is possible to make much smaller representative samples, equilibrating faster and allowing reasonable test durations. The present work aims to understand the drying, shrinkage, and creep mechanisms at the cement paste scale thanks to innovative experimental tests, particularly concerning the drying rate and the Pickett effect. Then, in the light of these results, the objective is to propose a model considering these hydric effects on the delayed behavior of concrete.

In the experimental part, the campaign aims to study the effect of the drying rate on creep and shrinkage. When characterizing drying shrinkage and creep, the difficulty is cracking of samples due to drying gradients. The use of small cement paste specimens that equilibrate quickly and therefore have less pronounced gradients allows to limit cracking due to drying gradients and avoids micro-cracking due to shrinkage and creep contrasts between cement paste and aggregates. Thus it is possible to isolate the purely material effects at the cement paste scale. Therefore, we decided to carry out shrinkage and creep tests on cement paste samples of 2 mm thickness. These microscopic tests were performed: (1) under an environmental scanning electron microscope (SEM) at EDF R&D MMC; and (2) in the Mini-Astrée biaxial tension-compression machine of the LMT at ENS Paris-Saclay, placed under a climatic chamber with a controlled CO_2 concentration and monitored by an ultrafast camera. We analyzed the images obtained during these tests by image correlation. The results show that the drying rate has no impact on the maximum drying shrinkage deformation. In parallel, we undertake a macroscopic campaign on drying and pre-equilibrated samples at different relative humidities: 80 %RH, 58 %RH, and 20 %RH. These tests show the decrease of the creep kinetics when the relative humidity decreases.

Regarding the numerical part, the objective is to propose drying, shrinkage, and creep models that best integrate the impact of the drying rate through the numerical study of the tests performed. We conducted the drying analysis first. A drying model taking into account the permeation of liquid water and the diffusion of water vapor was adopted, with the degree of liquid water saturation as the primary variable. The model has been implemented in the EDF simulation tools. Particular attention has been paid to identifying the parameters and the boundary conditions of water convection. The results demonstrate that this drying model can simulate samples of different sizes (drying radius 1 mm, 36 mm) with a single set of parameters. We conducted a sensitivity analysis of the water exchange coefficient. Second, the desiccation shrinkage strain is assumed to be proportional to the change in relative humidity. We identify the proportionality coefficient from the shrinkage isotherm measurements performed on the 200 µm, 500 µm, and 2 mm thick samples. The model is particularly effective in reproducing the desiccation shrinkage behavior of samples of different sizes, drying at different rates. Finally, we studied creep:

to do that, we compare two models from the literature. The first model is of Burger type with an irreversible creep contribution modeled according to the consolidation theory. By extension, we will call Burger the whole creep and desiccation model used at EDF. The second is the Micro-Prestress Solidification (MPS) model. The two models are compared with the experimental results from two angles: (1) the dependence of basic creep on water content; (2) the effect of size and drying rate on desiccation creep. The comparison shows that the Burger model can consider the effect of size and drying rate on the desiccation creep, which is not the case for the MPS model. Regarding the moisture dependence of the long-term creep, the Burger model also predicts the kinetics better than the MPS model. Indeed, the MPS model significantly overpredicts the kinetics of the basic creep: the lower the relative humidity, the more the model overestimates. Nevertheless, the relative humidity dependence of the basic creep of both models can be improved.

Background and outline of the thesis

Nuclear energy in France

The early 1970s marked a very important technological turning point in France's energy landscape. Since then, 59 PWR-type nuclear reactors had been built on 19 sites in France (the construction period spread over some 30 years). Today, the share of nuclear power in the production of electricity is about 75%. However, aging of nuclear power plants could eventually call into question the ability of these structures to meet increasingly stringent safety requirements for an extended period of time. This aging process is only really problematic if these components are non-replaceable; in a power plant, there are two of them:

1. the vessel containing the reactor core;

2. the containment, which is the subject of the present study.

Industrial and economic stakes

The current PWR nuclear fleet managed by EDF contains a set of 59 containment buildings which constitute the third and final containment barrier, an essential part of nuclear safety. It is therefore necessary to ensure sufficient air tightness throughout the life of the plant, the level of which is set by the safety authority. The stakes are therefore multiple: it is a question of keeping the assets in good working and safe conditions, extending their service life, while justifying or even adapting the installations at the right cost in the face of legislative and regulatory changes, regarding safety or environment. The issue of leak tightness of double-walled concrete containment buildings therefore remains a major challenge for the operational life of the 1300 MWe and 1450 MWe plants. Thus, the containments of the nuclear fleet are subject to a costly maintenance program in order to maintain a sufficient airtightness with regard to the regulatory criteria. As part of this effort, utilities need to have the means to optimize this maintenance program in order to reduce costs and guarantee the success of the ten-year ILRT (Integrated Leak Rate Tests) during which the leak tightness of the containment is assessed. Solutions are currently available for sealing complements (coatings) on the inner and outer faces of the wall of the containment. But these operations are long, expensive and complex at the same time. Consequently, the control of the state of health of each of the buildings of the fleet until the end of its operating life is necessary to optimize maintenance costs. The progress made in recent years thanks to the VERCORS mockup and the development of digital twins puts this objective of predicting leakage rates for double-walled containment structures within reach. Research efforts are continuing in R&D in this direction, based in particular on the analysis of aging phenomena, and this thesis is part of this effort.

Scientific issues

Scientific Background

The tightness of double-walled nuclear power plant buildings is based on the one hand on the tightness of the internal prestressed concrete wall, and on the other hand on the filtering of the air in the space between the walls. The prestressed concrete of the inner enclosure must therefore remain in a sufficient state of compression throughout the lifetime of the structure. The leakage rate of the containments is checked every ten years and compared to a strict criterion. The evolution of leakage through an enclosure is controlled by the drying and delayed deformation of concrete. The water state plays a direct role on the permeability of the concrete, but also an indirect role in that it influences the delayed deformations of the concrete. These delayed deformations induce part of the loss of prestress and consequently contribute to the risk of cracking or opening of existing cracks. It is necessary for EDF to have models to simulate the evolution of the delayed deformations of the concrete. These models must be calibrated on laboratory experiments when they are available, or failing that, on monitoring measurements carried out directly on civil engineering structures. Currently, EDF R&D has such a model, based on the postulate of the additivity of the main components of delayed deformations: basic creep, desiccation creep and desiccation shrinkage. The work carried out in recent years at EDF has focused on basic creep (without moisture change). However, in order to succeed in the transposition from the laboratory (where samples are small and therefore the drying is fast) to the structure (where drying is very slow), it is necessary to properly take into account the influence of humidity on the delayed deformations and more precisely that of the drying rate, an aspect of the model which has not been sufficiently studied, and little literature data exists on the subject. From this point of view, the VERCORS model constitutes an intermediate step between the laboratory and the real structure which is of great use in validating the proposed models.

Scientific challenges

Part of the difficulty in modeling delayed deformation of concrete lies in the complex impact of moisture on concrete, which is of at least three kinds:

1. Moisture variation causes a change in the stresses applied by the fluids occupying the porous space on the solid skeleton of concrete, resulting in macroscopic deformations called shrinkage.

2. At different humidities held constant, and under external loading, the magnitude of the basic creep deformations (corrected of shrinkage) is modified (they are less important at lower humidity). Little data support this effect, although there is a consensus in the models.

3. At variable humidity, an excess of deformation under load is observed with respect to the previous effects, due to:

    a. the initiation of cracking due to water gradients (which is well studied in the literature)

    b. the inception of cracking due to the gradients of shrinkage properties, with aggregates, anhydrous and some hydrates not being subjected to this (much less studied)

c. complex effects of water movement on hydrates that are debated in the literature.

An experimental characterization of these phenomena has been little studied for the moment because the technical difficulties are important. One can however cite some publications that the results of the present thesis seek to complete Gamble and Parott (1978); Day et al. (1984). Indeed, in the existing databases, in this case the RILEM and the Japanese Database, containing more than a thousand tests, we have not found any tests meeting our needs (weighing, shrinkage and creep tests on concrete samples drying at different rates, which is obtained by different sample sizes or ambient humidities). The results of this thesis will be used to fill this gap. A difficulty concerning the characterization of the influence of complex water effects on shrinkage and creep comes from the fact that on large sample sizes, water equilibration times are very long. This prevents a specimen from being subjected to variable but sufficiently homogeneous humidity to prevent shrinkage cracking. Consequently, if phenomena 1) and 2) can be investigated on macroscopic samples - as was done at EDF by Huang (2018) , and also by Aili (2017), phenomenon 3) requires very small sample sizes, which allow to free oneself from effects 3-a) and partially effect 3-b) to concentrate only on material aspect 3-c). To be able to work with thin samples with a representative volume, cement paste is more suitable than concrete, all the more so as the delayed behavior of the two materials are qualitatively the same. To sum up, the use of small paste samples, by avoiding the effects of cracking at the scale of the structure and by avoiding microcracking due to contrasts in shrinkage and paste-aggregate creep, could make it possible to isolate purely material effects at the level of the hydrates responsible for shrinkage and creep: the C-S-H.

The modeling of these phenomena by microscopic approaches is a major topic at EDF R&D MMC, the thesis of Huang (2018) addressing point ii) by micromechanical modeling and macroscopic testing (especially with respect to aging), and the thesis of Adia (2017) addressing points iii-a) and iii-c) by a numerical approach at the pore scale. While these models allow to better understand or predict certain phenomena, they do not directly allow simulations to be performed on the scale of a real structure, which is why it was decided in this thesis to improve the phenomenological models available elsewhere, thanks to the tests that will be carried out.

Objectives of the study and approach

The present study includes experimental and numerical parts. The experimental work aims at understanding drying, shrinkage and creep mechanisms at the cement paste scale through innovative experimental tests, in particular with respect to drying rate and Pickett effect. Then, in the light of these results, the objective is to propose a model taking into account these hydric effects on the delayed behavior of concrete.

Experimental part

Small and large size specimens will be used . The samples will be subjected to humidity histories in which a constant humidity value or a constant value of the humidity evolution rate will be set (humidity ramps). The experimental campaign includes:

1 The characterization at room temperature of shrinkage and creep in simple compression on specimens of 10×10×2 mm geometry under environmental scanning electron microscope (ESEM) at the Material Ageing Institute (MAI) of EDF R&D MMC, an instrument that combines the possibility of loading the sample, humidity control, and imaging one side of the sample. Although shrinkage tests in ESEM exist in the literature Neubauer and Jennings (2000), creep results with ESEM are not available. These tests required the development of a compression stage by adapting an existing tensile stage. These tests are analyzed by digital image correlation.

2 The characterization at room temperature of drying, shrinkage and creep in simple and biaxial compression with LMT's Mini-Astrée tensile-compression machine, on specimens of 10×10×2 mm geometry. The relative humidity is controlled by a climatic chamber. The imaging will then be carried out by photography. This test requires the design and manufacturing of jaws for the Mini-Astrée machine, which are adapted to the geometry of the specimens. An effort is also made to control the CO_2 content in the climatic chamber. These tests are analyzed by image correlation.

3 The characterization at room temperature of drying, shrinkage, and creep in simple compression on cylindrical specimens of dimensions 3.6×18 cm. These tests are carried out in the Civil Engineering laboratory of EDF R&D MMC, at three humidity levels of 11.10%, 58.15% and 81.2% RH controlled by saturated salt solutions. Plexiglas chambers are designed to maintain humidity during these tests.

Numerical part

The main objective is to test and improve when needed the models at the macroscopic scale, thanks to cement paste data for drying histories of the thesis. The modeling scale will be the macroscopic scale. The approach adopted is as follows:

1. Preliminary numerical study: this study carried out with data from the literature has helped to design the experimental and numerical program of this thesis. The first step in this study consisted in the implementation and validation of Bazant's Micro-Prestress Solidification law Jirásek and Havlásek (2014) according to the MFront formalism, interfaced with Code−Aster, the numerical simulation software of EDF R&D. In a second step, this MPS model as well as the creep model of EDF R&D are compared with the data of Day et al. (1984). This comparison could not be conclusive, due to the lack of certain data, which nevertheless allowed the identification of data gaps to be filled. This preliminary study was reported in Kinda et al. (2018).

2. Drying study: the first step consists in implementing in Code-Aster, a drying model according to the SECH-NAPPE formalism. In order to be able to work on a wide range of humidity (100%-20%), the drying model taking into account the permeation of liquid water and the diffusion of water vapour is adopted; and to integrate the desorption isotherm in the drying model, the principal variable of the model is the degree of saturation in liquid water.

3. Study of desiccation shrinkage: based on experimental observations the desiccation shrinkage strain is assumed to be proportional to the relative humidity variation. The coefficient of proportionality is identified from isothermal shrinkage measurements made on very thin samples. The predictive capacity of the adopted model, in particular on the size effect, has been investigated.

4. Creep study: finally, creep is studied; two models from the literature are compared. The first model is of Burger type with a contribution of irreversible inherent creep modelled according to the consolidation theory. The second is the Micro-Prestress Solidification (MPS) model. Special care is taken to identify the model parameters with ADAO (a module for Data Assimilation and Optimization, http://www.salome-platform.org/) developed at EDF R&D. The predictive capabilities of the two models will be compared with the experimental results, from two angles: (1) the dependence of the basic creep on the water content (2) the effect of size and drying rate on the drying creep.

Organization of Contents

This Ph.D dissertation is written as an article-based thesis. The manuscript is organized as follow:

- Chapter 1 provides an up-to-date account of the present state of knowledge on cement-based materials, especially about microstructure, drying, drying shrinkage and creep properties.
- Chapter 2 presents the application of Digital Image Correlation (DIC) technique to study the drying shrinkage of thin cement paste specimens. An emphasis was put on the validation of the technique.
- Chapter 3 presents the investigation, both experimentally and numerically of drying rate impact on moisture loss, exchange coefficient and drying shrinkage of cement paste.
- Chapter 4 presents the experimental study of creep of cement paste under variable humidity in ESEM, climatic chamber and sealed chambers of saturated salines solutions. The results of the experiments are reported; Pickett effect and size effects are highlighted.
- Chapter 5 concerns the numerical investigation of creep of cement paste based on experimental results presented in chapter 4. The delayed strains law used at EDF R&D (Burger) and the microprestress-solidification (MPS) law are compared, especially on their ability to predict size, drying rate effects and long term creep.

References

J-L. Adia. *Modélisation multi échelle des phénomènes de retrait et de fluage dans les matériaux cimentaires : approches numériques couplant les éléments finis et la méthode de Lattice-Boltzmann.* PhD thesis, 2017. 9

A. Aili. *Shrinkage and creep of cement-based materials under multiaxial load: poromechanical modeling for application in nuclear industry.* PhD thesis, Université Paris-Est, 2017. 9

R.L. Day, P. Cuffaro, and J.M. Illston. The effect of rate of drying on the drying creep of hardened cement paste. *Cement and Concrete Research*, 14(3):329–338, 1984. 9, 10

B.R. Gamble and L.J. Parott. Creep of concrete in compression during drying and wetting. *Magazine of concrete research*, 30(104):129–138, 1978. 9

S. Huang. *Ageing behaviour of concrete creep : application to the VeRCoRs concrete*. Thesis, 2018. 9

M. Jirásek and P. Havlásek. Microprestress–solidification theory of concrete creep: Reformulation and improvement. *Cement and Concrete Research*, 60:51–62, 2014. 10

J. Kinda, L. Charpin, J-L. Adia, F. Benboudjema, and S. Michel-Ponnelle. Impact of drying rate on delayed strains in cement-based materials. In *Interdisciplinary Approaches for Cement-based MAterials and Structural Concrete: Synergizing Expertise and Bridging Scales of Space and Time*, pages 719–723, 2018. 10

CM Neubauer and Hamlin M Jennings. The use of digital images to determine deformation throughout a microstructure part ii application to cement paste. *Journal of Materials Science*, 35(22):5751–5765, 2000. 10

Chapter 1

Literature review

1.1 Generality on cement-based materials

Hardened cement paste is the glue component of concrete. Through series of complex and parallel chemical reactions between cement powder and water, a complex microstructure is built up. This microstructure is made of various chemical components called hydrates, unhydrated phases, water, and multi-scale porosity. As hydration reactions proceed, the water-filled space is progressively replaced by solid hydration products, resulting in an increase of strength, decrease of internal relative humidity, and formation of multi-scale porosity.

Among all the hydrated products, Calcium Silicate Hydrate (C−S−H) gel is at the origin of cohesion of cement paste and has the greatest influence on the durability of the material. C−S−H is also the most affected phase during drying due to its nanoscale pore system and its high water content. Many models attempt to describe the nanostructure of C−S−H, but no consensus has been reached yet in the literature. The porosity that spans four orders of magnitude (1 nm-10000 nm) is a very complex multi-scale system. The pores at different scales are filled by more or less strongly bound water (free liquid water, chemically and physically bound water), vapor, and possibly air.

The role of water is complex because, in fresh states of concrete, its presence is desirable because it has a rather positive role on the fluidity of concrete. It allows in first place for transport, molding before setting. But in the solid-state, the higher the water content, the more porous concrete is, which is rather bad for all degradation and aging mechanisms (chloride penetration, carbonation, creep, shrinkage).

1.1.1 Hydration process

Schematic description of the hydration reaction Cement grains (fig.1.1.a) are highly charged at their surface, and once in contact with water, they dissolve (fig.1.1.b), to give an interstitial electrolytic solution, mainly made of calcium and hydroxide ions (Nonat and Mutin, 1992; Taylor, 1997). Schematically, hydration consists of reactions of cement grains with this electrolytic solution, which will mainly lead to the precipitation of calcium silicate hydrates (C−S−H) on the surface of grains (fig.1.1.c). Progressively, interactions between cement grains are replaced by interactions between (C−S−H) (fig.1.1.d).

Characterization of the hydration reaction As mentioned by Scrivener and Kirkpatrick (2008), innovative experimental techniques are available for studying the complex mixture of cementitious phases. Some notable examples are:

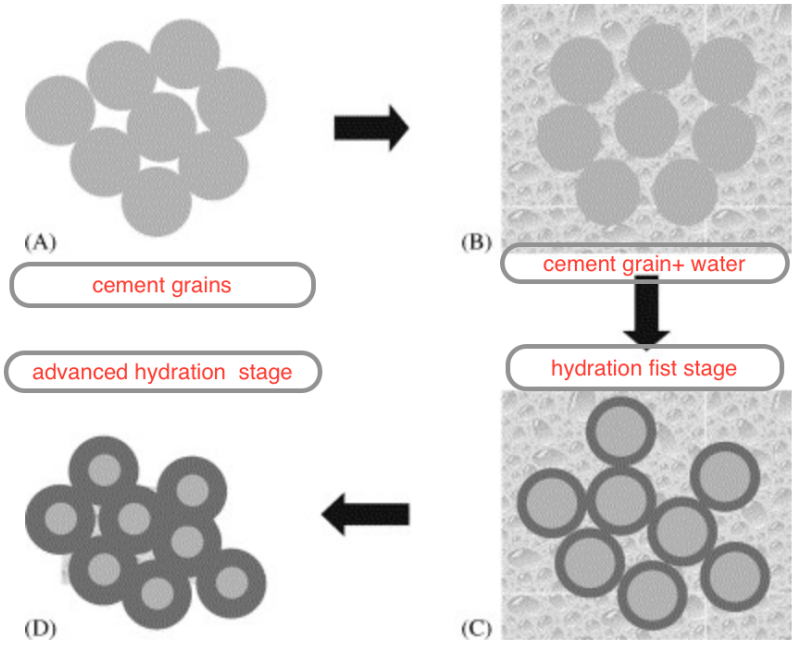

Figure 1.1: Schematic representation of hydration process: cement powder (A), contact with water and partially dissolution (B), C−S−H precipitates (C) onto surface of powder. In set solid (D), the contact area increase between grains is responsible for the mechanical strength increase, the acting force remaining the same (Lesko et al., 2001)

- Rietveld analysis of X-ray diffraction data enables quantification of complex phase mixtures (Scrivener et al., 2004).
- Scanning and transmission electron microscopies coupled with chemical micro-analysis, allows investigating micro-structural development and microchemistry of hydrated phases (Scrivener et al., 2004).
- Nuclear Magnetic Resonance (NMR) techniques, which provide information on C–S–H structure. (Scrivener et al., 2004; Plassais et al., 2005)
- Small-angle neutron and X-ray scattering to probe the "mesostructure" or "gel" porosity of C–S–H (Allen and Thomas, 2007).

The importance of hydration the microstructure of cement paste which is a pure product of the hydration process, is responsible for the durability performance of cementitious materials. First, the disjunction pressure, and its complementary part called micro-prestress, known as the two most influencing factors of drying shrinkage and creep, builds up during the hydration process in the hindered zones. Second, the hydration is responsible for the gradual deposition of new gel on the walls of the capillary pore, thus allowing the increase of the material stiffness, which is called solidification, one of the main mechanisms of short-term creep in the micro-prestress theory. Third, the capillary water and the free adsorbed water, both responsible for short-term creep, in micro-diffusion theory are pure products of the hydration process.

1.1.2 The nanostructure of C-S-H

As underlined by (Scrivener and Kirkpatrick, 2008), the performance of cementitious materials is driven by the physical and chemical processes taking place at the C−S−H scale.

A quantitative understanding of the structure of C−S−H from atomic to micrometer scale, and how its structure, at that scale interacts with drying, creep, and shrinkage of hydrated cement paste is a key point to build up predictive models for the assessment of long term behavior of concrete structures.

Nanostructure of C-S-H: description

In this section, we are going to discuss whether the C-S-H structure is colloidal or amorphous, depending on the scale of observation, the way it takes place, and its role in creep and shrinkage.

Pioneering works by (Powers and Brownyard, 1946; Feldman and Sereda, 1968) have addressed those questions for the first time by descriptive models for C−S−H. Later on, Jennings (2000), proposed a new model, a kind of combination of the two first models plus extra features; these models are described in section 1.1.2.
Since then, new experimental techniques have provided further justification for these pioneering works.

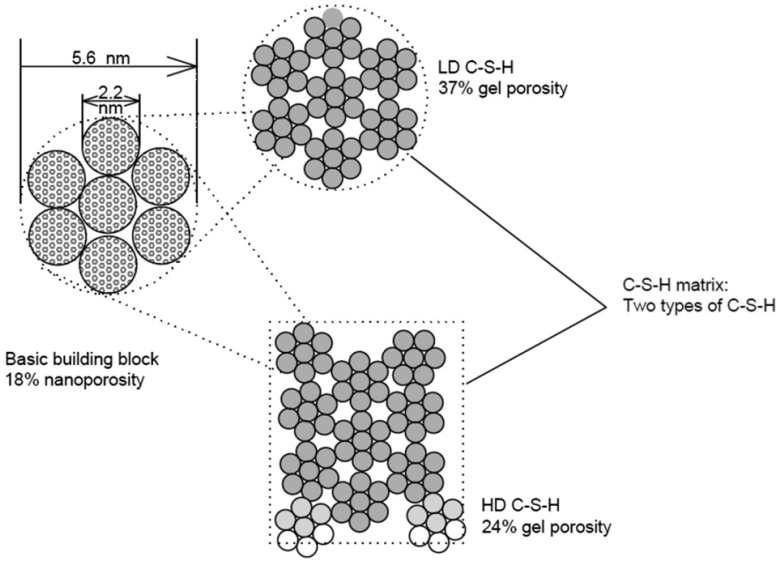

Figure 1.2: Microstructure of C−S−H: Low Density C−S−H and High density C−S−H (Maruyama et al., 2015)

It is commonly acknowledged today, that C−S−H could be decomposed in high density C−S−H gel, also called inner products, with high C/S ratio, a kind of granular structure (fig.1.2); and low density C−S−H gel having low C/S ratio, with lamellar shape type (Richardson, 2008) (fig.1.3). For OPC (Ordinary Portland Cement), the inner product C−S−H appears to be nearly equidimensional particles, with a characteristic length less than 10 nm with significant inter-particle porosity. In contrast, outer product C−S−H appear to have more directional, fibrillar morphology on the 100 nm scale with 3-dimensional capillary pore system between lamellar (Scrivener and Kirkpatrick, 2008). Each fibril consists of a few nm to tens of nm long and thickness less than 5 nm, with significant inter-particle porosity.

Nanostructure of C-S-H: Models

Papatzani et al. (2015) made a comprehensive review of C−S−H nanostructure models. The three of the most cited models in the literature are the following:

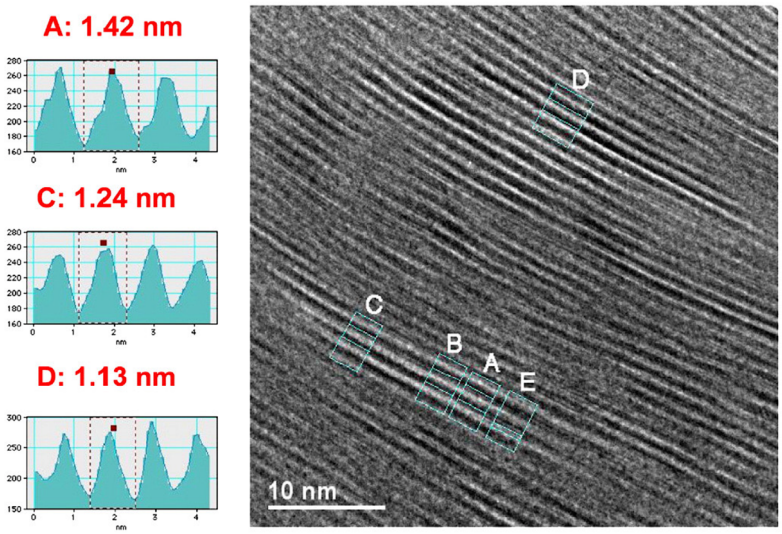

Figure 1.3: Deshydration of 1.4 nm tobermorite as captured using Transmission Electron Microscopy (TEM) (Richardson, 2008)

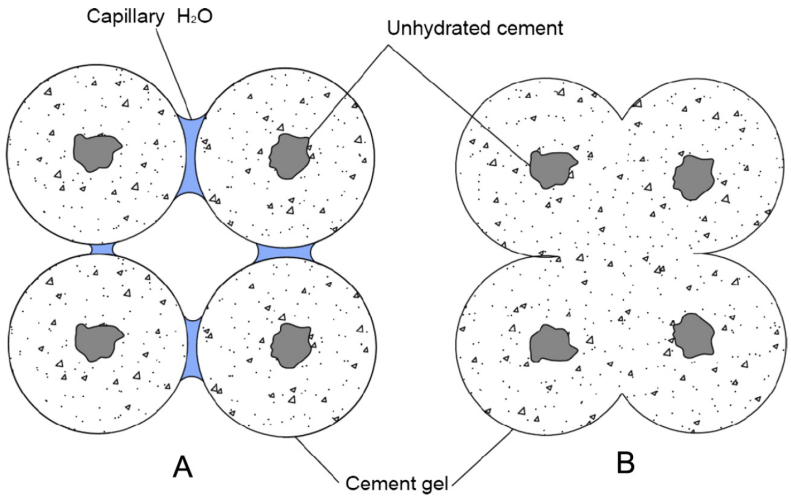

Figure 1.4: Main constituents of C−S−H in P-B model

- (Powers and Brownyard, 1946) model (P-B). This first model attempts to give a clear picture of the C−S−H structure. The purpose was to (i) understand basics mechanisms of shrinkage and swelling, (ii) approximate the surface area, (iii) determine the size of pores, and (iv) differentiate the different types of water within the hydrated cement paste. In the first version of P-B model, C−S−H structure can be viewed as spheres enclosing unreacted products with capillary water between spheres fig.1.4. The creep in this model originates from the breaking and restoration of bridges between C−S−H particles. The P-B model has shed light on the different types of water of C−S−H gel, but it shows two limitations: one of the limitations that persists today is that the exact particle size cannot be determined (Scrivener and Kirkpatrick, 2008; Papatzani et al., 2015); another limitation is the inability of the model to explain the irreversibility of sorption isotherm, which was resolved in 1966 by Feldman and Sereda (1968) who introduced a new model.

- Feldman and Sereda (1968) model (F-S). The authors postulate that C−S−H has a

tobermorite-crystal like structure, and therefore, C−S−H has a layered type structure as depicted in fig.1.5. This model provides quantitative informations on the relative contributions of interlayer water, adsorbed water, and capillary water to volume change. The main contribution of F-S model is that interlayer water is considered as a part of C−S−H structure and emphasizes the fundamental role of it in the evolution of mechanical and physical properties such as drying, creep, and shrinkage. The irreversibility of the sorption isotherm is related in this model to the fact that the energy barriers at desorption and sorption are different, which is associated with the ink-bottle effect.

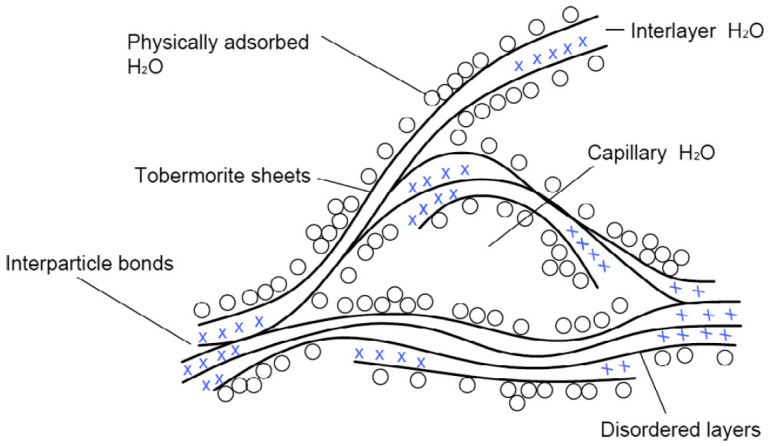

Figure 1.5: C−S−H layered structure (Feldman and Sereda, 1968)

- Jennings (2000) model. Jennings and co-workers proposed a colloidal model known as the Jennings model in an attempt to account for some physical properties of C−S−H in mature paste, including density, surface area, fractal character, pore size, and size of individual particles. The model is a combination of layered models similar to (F-S) and colloid type models similar to (P-B). The building unit of C−S−H in this model are particles, which assemble to form globules of 5-5.6 nm, see fig.1.6; and the globules, in turn, assemble to form packages of two types which differ by their packing density: Low Density (L−D) C−S−H and High Density (H−D) C−S−H. The proportions of those two types of C−S−H depend on the w/c ratio.

  The packing density plays a fundamental role in the creep process. Creep in the light of this model is viewed as a result of a compaction process. Hence the higher the packing density, the less concrete creeps, which may explain why high-performance concrete exhibits less creep. The part of C−S−H attributed to creep is Low-Density C−S−H. The surface area and pore size distributions obtained from SAXS (Small Angle X-ray Scattering), SANS (Small-Angle Neutron Scattering), NMR (Nuclear Magnetic Resonance Relaxation) studies are very consistent with this model.

1.1.3 Multi-scale porosity

The porosity is essential for the durability and mechanical performance of cement-based materials. The porosity is at the origin of defects of concrete. Hence the foremost way to increase concrete performance is to reduce its porosity. The most influencing factor of porosity is the w/c ratio (Scrivener and Kirkpatrick, 2008); the lower the w/c ratio, the

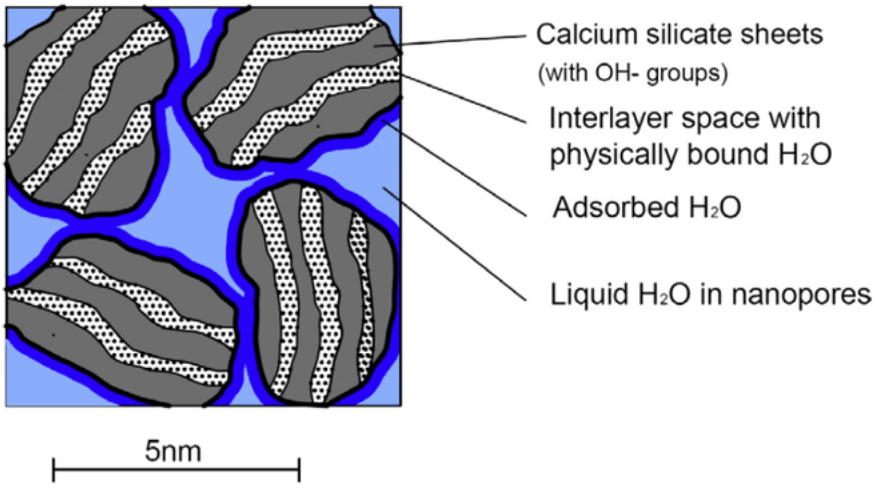

Figure 1.6: C-S-H globules, 5 nm characteristic length (Allen and Thomas, 2007)

Table 1.1: IUPAC pore size classification (Thommes et al., 2015)

Pore description	Radius (nm)
Micropores	< 2
Mesopores	2–50
Macropores	> 50

lower the porosity, and the better the mechanical performances. In the following section, the different types of porosity in cement paste and their main characteristics, along with the existing characterization techniques, are highlighted.

Different sizes of porosity

Different pores size exist in cement paste, and they are divided into three categories in the classification of Sing et al. (1985). The characteristics of pores in cement paste are summarized in tab.1.1.

Characterization technique: methods and limitations

The porosities of the material is defined as the volume of the porous networks, (V_p) in relation to the total volume (V_t)

$$p = \frac{V_p}{V_t} \tag{1.1}$$

The main methods currently used to characterize porosity are mercury intrusion porosimetry (MIP) and the water saturation method.

MIP technique has been used for the first time by Edelman et al. (1961), and since then, has been widely used. It consists of subjecting the dry material to a step-by-step increase of mercury pressure (typically between 0.01 and 400 MPa). The non-wetting nature of the mercury allows filling the voids of the material progressively. The intruded volume is converted into pore volume through Eq.1.2 (Washburn, 1921).

$$d = \frac{-4\gamma_{Hg} cos(\theta)}{P} \tag{1.2}$$

where θ [°] is the contact angle, usually taken equal to 140 (°); however recent study by (Muller and Scrivener, 2017) found a value of 120 ° , more convenient; γ_{Hg} the mercury surface tension; P the intrusion mercury pressure necessary to fill pores of diameter d. Although MIP is widely used, the technique and results interpretation are still controversial (Diamond, 2000). It is commonly accepted that MIP technique underestimates the macroscopic porosity (Zeng et al., 2012) and overestimates the microscopic porosity (Diamond, 2000). Moreover, the MIP technique is limited to pore sizes ranging between 375-0.003 µm. The microscopic porosity is overestimated because it requires the injection of mercury under high pressure, which causes the opening of communication channels to the macropores, which also fill up and usually does not communicate with the outside environment (Diamond, 2000).

Saturation method: this method investigates the porosity based on Eq.1.3. Experimentally, porosity is calculated according to the formula

$$\phi = \frac{M_{air} - M_{dry}}{M_{air} - M_{water}} \tag{1.3}$$

with ϕ the porosity accessible to water; M_{air} the saturated mass under water. The AFPC (1997) protocol recommends to saturate the sample with water; M_{dry} is the dry mass, and M_{water} the hydrostatic mass. The drying temperature recommended by AFPC (1997) method is 105°C. A further study by (Gallé, 2001) pointed out that this drying temperature is too high and may lead to overestimating the porosity accessible to water (dilation of porous space, microcracking). Tab.1.2, shows the variability of porosity values for different techniques for measuring dry mass (Gallé, 2001); the porosity variation between drying at 105°C and vacuum or 60°C is about 6%.

Table 1.2: Water porosity (ϕ_w), mercury porosity (ϕ_{Hg}), and threshold pore access diameter values for CEM I pure cement hardened paste, $\frac{w}{c} = 0.5$, (Gallé, 2001)

Dying method	ϕ_w(%)	ϕ_{Hg}(%)	Threshold pore access diameter (µm)
Oven-drying 60°C	37.3	27.8	0.12
Vacuum-drying	37.7	27.4	0.07
Nitrogen Freeze-drying-195°C	35.0	29.6	0.05

The values after drying at 60°C and vacuum drying are very close. Recent works (Soleilhet, 2017; Larbi, 2013) support these findings. Since porosity has a very important impact on the permeability of the material, a good knowledge of porosity will help to better predict drying, and therefore delayed strains (creep, shrinkage).

1.1.4 Water in cement paste

The purpose of this section is first to review the different types of water in cement paste, second to see how they relate to sorption isotherm, and last, to highlight the types of water concerned at different stages of the drying process.

classification of types of water in cement paste

Hardened cement paste is a porous and hydrophilic material. The pioneering work of Powers and Brownyard (1946), has shed light on the types of water in concrete. It was refined later by (Jennings, 2000). The classification of water derives straightforwardly from

the classification of pore space and how strong it is bounded to the solid skeleton (Regourd, 1982; Guenot-Delahaie, 1997):

- **capillary water** also called bulk water is defined as the water free of solid surface attractive forces (Mehta and Monteiro, 2006) and develops in pores wider than 10 nm. One may distinguish capillary water located in large pores with radius larger than 50 nm and water from mesopores with a radius between 10 and 50 nm range. The latter is responsible for capillary stress development during the drying process.

- **Adsorbed water** separated into free adsorbed water and hindered adsorbed water type:

  1. Free adsorbed water is formed in free adsorbed areas where the pore space is sufficient enough for a layer of 10 molecules wide (2.6 mm approximately) to develop (at 100% RH). This water is in contact with capillary water and vapor.
  2. Hindered adsorption water is trapped in pores smaller than 2.7 nm in size (2.7 nm is the size of 10 stacked water molecules). Hindered water can only communicate with the liquid and vapor in capillary pores by micro diffusion through nanopores.

- **Interlayer water** is the water contained in the interlayer space (less than 0.5 nm)

water and mechanical behavior

Jennings (2008) has shown that the ability of the structure to resist permanent microstructural rearrangement is increased as hydration proceeds. This is consistent with the recent findings by Maruyama et al. (2014), who observed an increase of both flexural and compressive strength of cement paste between 100 % and 95 % RH. In fact, at high relative humidities (typically above 95%), even after hydration has ceased, there is a continuous evaporation/condensation process of capillary water to maintain equilibrium followed by condensation of new hydrates; this process is accompanied by the formation of new C−S−H bounds (Maruyama et al., 2014). The phenomenon is called crystallization (Bazant and Prasannan, 1989); it is believed to increase the material stiffness, known as the aging phenomenon.

1.1.5 Water desorption isotherm

Measurement of desorption isotherm

Desorption isotherms are fundamental for quantifying and predicting the hygral behavior of the material subjected to drying. By definition, it is the water content vs. RH curve. For the last decades, a lot of effort has been made to characterize it, using different techniques with the intent to make it faster and more accurate. Different techniques exist, such as volumetric method (Maruyama et al., 2014), saturated salt solutions. (Baroghel-Bouny et al., 1999a; Baroghel-Bouny, 2007a; Semete et al., 2017), Dynamic Vapor Sorption method (Poyet et al., 2016).

A tool for investigating microstructure

Water sorption isotherms, which probe the pore structure of cement paste at all scales where evaporable water exists, is a very powerful tool for evaluating microstructures (Jennings et al., 2015; Brunauer et al., 1938; Hagymassy et al., 1969; Powers, 1958). Proper capture of sorption isotherms have been used to quantitatively explain changes in the pore structure that occur during drying (Jennings, 2008; Maruyama et al., 2014). For example, water that is either being removed or re-entering a sample at a particular RH can be linked to a specific class of pores (i.e., the interlayer, gel, or capillary spaces). The fundamental experimental work by Baroghel-Bouny et al. (1999b); Baroghel-Bouny (2007b) on cement paste has shown that, whatever the material mix, the desorption curves are identical below 40-50 %RH and scattered above these values. As interpreted by the authors, drying above 40-50 %RH on the one hand, involves the removal of water from porous capillary space (mesopores and large pores), which is very dependent on the paste mix such as w/c ratio, additives (silica-fume, ...); while on the other hand, drying below 40-50 %RH is intimately related to the removal of gel pore water. Recent studies (Maruyama et al., 2014, 2015) support these findings.

1.2 Drying

1.2.1 Mechanisms

When an unsealed system of cement-based material is exposed to lower relative humidity than its internal relative humidity, drying occurs. It consists of permeation of liquid water, plus possibly diffusion of vapor from inner to the outside of the system (fig.1.7).

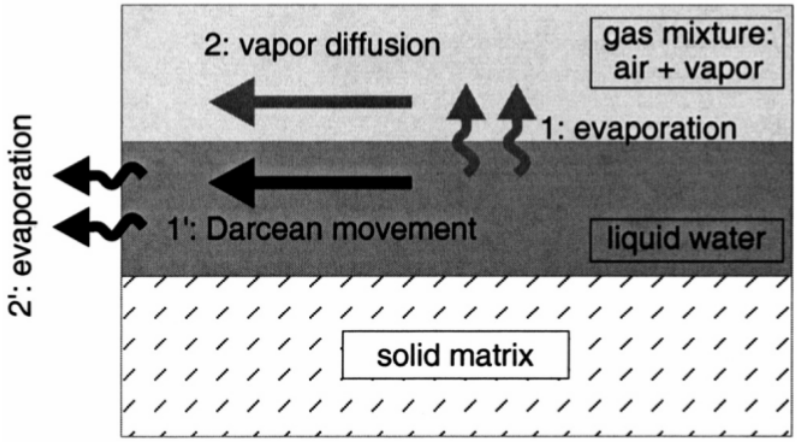

Figure 1.7: Drying process in cement based materials (Mainguy et al., 2001)

The rate of evaporation is dependent on the temperature properties of pore solution (Villani et al., 2014), the gradient of vapor pressure, the rate of airflow, and the diffusion coefficient (Mainguy et al., 2001). Evaporation from the drying surface induces a flow of liquid and diffusion of vapor within the material. As long as the liquid is continuous, the gradient of capillary pressure between the surface and the interior of the material drives the Darcy flow of pore solution (Mainguy et al., 2001). The rate of Darcy flow depends on the permeability, properties of the pore solution (viscosity, surface tension), and the

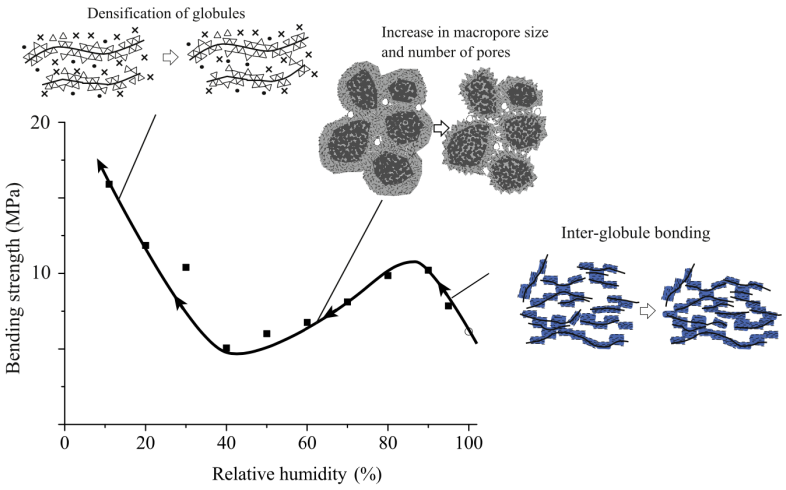

Figure 1.8: Schematic of relationship between the microstructural changes caused by drying at various RHs and strength (Maruyama et al., 2014)

degree of saturation (Van Genuchten, 1980; Scherer, 2015). As soon as the liquid phase becomes discontinuous, the vapor diffusion becomes dominant, with a smooth transition.

1.2.2 Interaction with microstructure evolution and mechanical behavior

The main objective of this part is to review the interaction in the porous structure of well-hydrated cement paste with water and the common techniques to characterize this interaction.

Maruyama et al. (2014) performed an extensive study on the effect of first desorption on the microstructure bulk change; they observed an increase in macropores volume and a decrease in mesopores volume during the first stage of drying from 95% to 40 %RH. The authors attribute it to the densification of C−S−H sheets due to the increase of surface free energy upon removal of adsorbed water. In latter drying stages, typically below 40 %RH, they find an increase of mesopores volume and decrease of interlayer basal space caused by the removal of interlayer water from globules. They associated it with compaction of C−S−H layers, which in turn induce the creation of internal mesopores. Fig.1.8 shows how these microstructural changes, evolution (increase or decrease) of packing density of building unit of C−S−H, manifests itself at the macroscopic scale with an impact (improvement or reduction respectively) on mechanical strength. These highlights are consistent with the earlier findings (Feldman and Sereda, 1968), which point out that a major rearrangement of the layers or sheets of tobermorite-like C−S−H occurs during first desorption.

1.2.3 Cracking

When exposed to drying, the specimen surface undergoes a contraction rapidly while the core of the specimen remains undeformed at this stage of drying, see fig.1.9. Gradients of water content appear between the surface and the core of the specimen, (Benboudjema et al., 2005; Hwang and Young, 1984). In the meantime, the surface of the specimen experiences tensile stresses while its core is under compression (Bazant and Wittmann, 1982;

De Sa et al., 2008; Samouh et al., 2019).

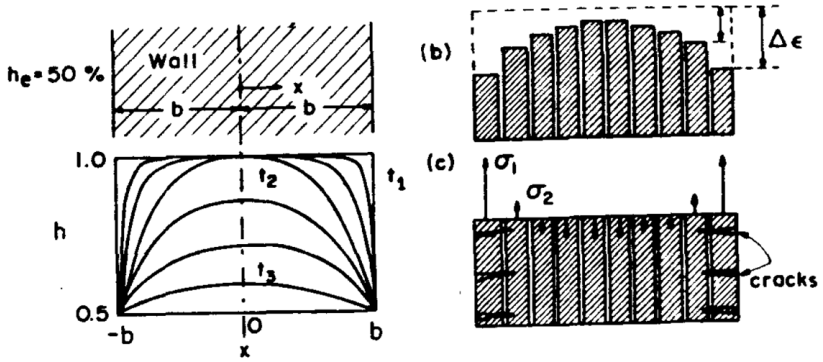

Figure 1.9: (a) Typical distributions of pore humidity at various times during drying; (b) free shrinkage and creep at various points of cross section; (c) internal stresses ((Bazant and Wittmann, 1982)

The larger the specimen, the larger the moisture gradient between the core and the surface of the specimen. Besides, the more likely the tensile stress may exceed the tensile strength of the material, and the most likely cracking might occur. When studying material behavior, cracking related to structural effects is problematic since measurements are the result of both material and structural behavior. Avoiding cracking is a crucial way to improve our understanding of material behavior. One way is to reduce as much as possible the size of the specimen (Bažant et al., 1976; Day et al., 1984; Neubauer and Jennings, 2000). On the one hand, this is useful for accelerating the drying process, as it is well known that drying of cement-based materials is a very slow process (Acker and Ulm, 2001). This idea of using cement paste specimens of small thickness for studying delayed strains has been proposed by Bažant et al. (1976), who used specimens of 0.72 mm thickness to investigate creep and shrinkage of cement paste at variable water content. Later, Day et al. (1984) followed up with 1.9 mm thick specimens. On the other hand, the thinner the specimen, the most likely natural carbonation will affect drying because, like desiccation, carbonation is a diffusion type process (Papadakis et al., 1989; Dweck et al., 2000; Thiery et al., 2007; Auroy et al., 2015). Thus limiting natural carbonation when testing samples of small thickness is crucial. It requires the use of an appropriate system to reduce the CO_2 content of the room environment (Day et al., 1984).

1.2.4 Carbonation

When concrete (or cement paste) is subjected to an environment containing CO_2, a transport of CO_2 initiates from the environment towards the interior of the sample, where it dissolves in the water of the cementitious matrix, producing HCO_3^- and CO_3^{2-} ions (Castellote et al., 2009; Galan et al., 2013; Leemann and Moro, 2017). These ions combine with Ca^{2+} ions, portlandite and C−S−H to produce calcite $CaCO_3$. During this process, C−S−H decalcifies, and this decalcification gives rise to C−S−H with a low Ca/Si ratio (Auroy et al., 2015), which impacts delayed shrinkage and creep behavior of the cement paste. The transformation of portlandite to calcite releases water into the microstructure (Auroy et al., 2015), reduces porosity because of the increase in the volume of the solid phase; the volume of calcite formed is 11-12% larger than that of CH (Borges et al., 2010). These modifications have significant consequences on drying. For example, the progression of the carbonation front affects the evolution of the drying profile, (Villain et al., 2007), which is especially true if the sample size is reduced. Reduction of porosity (especially capillary

pores) reduces the values of the desorption isotherm, (Auroy et al., 2015), which is fundamental in fact for drying modeling; carbonatation also induces mass uptake, which makes it difficult to measure mass loss induced by drying. The carbonation-drying coupling is not taken into account in our models, see chapter.5, since it is not a very important phenomenon in very large structures such as containment buildings. However, because we are interested in studying thin specimens, it is becoming more important. Hence there is a clear need to avoid or limit carbonation during shrinkage and creep testing on thin specimens (lesser or equal to 2 mm thick, for instance, in the scope of this study). Ideally, it would be good to be able to quantify carbonation at the end of these tests to check if it occurred or not, as it may bias the interpretation of the results.

1.3 Drying shrinkage

Drying shrinkage is defined as the volumetric change caused by drying. However, drying is an extremely slow process. In general, four primary theories for drying shrinkage can be found in literature:

- Capillary theory (Feldman and Sereda, 1968; Hansen, 1987): the liquid water changes the meniscus radius to maintain equilibrium with vapor.
- Disjoining pressure mechanism (Powers, 1968; Beltzung and Wittmann, 2005; Maruyama et al., 2015): due to the withdrawal of adsorbed water due to drying, the gel particles are pushed closer by Van Der Waals forces.
- Gibbs-Bangham shrinkage (Feldman and Sereda, 1968; Hansen, 1987; Maruyama et al., 2015): increase in solid surface tension due to removal adsorbed molecules
- Movement of interlayer water from C−S−H gel (Feldman and Sereda, 1968).

1.3.1 Review of mechanisms

Capillary pressure

From a thermodynamic point of view, the vapor-liquid equilibrium corresponds to a condition where the rate of evaporation is equal to that of condensation on a molecular level, which corresponds to a saturated state of 100% relative humidity. Under drying, the liquid water changes the meniscus radius to maintain equilibrium with vapor (Feldman and Sereda, 1968). The difference between the gas pressure above the meniscus and pressure inside the liquid is called capillary pressure and is expressed by Young-Laplace equation (Young, 1805)

$$P_c = P_g - P_l = \frac{2\gamma\cos\theta}{r_c - t} \tag{1.4}$$

In Eq.1.4, P_c is the capillary pressure [Pa], P_g the gas pressure [Pa], P_l is the liquid pressure [Pa], r_c the capillary radius of the meniscus [m], γ the surface tension between pore water and vapor [N/m], θ [°] the contact angle denoting the hydrophilicity of the material and t the thickness of adsorbed water [m], which is a function of relative humidity. The relationship between capillary pressure and relative humidity is further given by Kelvin's equation.

$$P_c = \rho_l R M^{-1} T \ln\left(\frac{RH}{x_w}\right) \tag{1.5}$$

In Eq.1.5, ρ_l [kg/m^3] is the density of liquid, M the molar mass of the liquid [kg/mol], R=8.314 [J/(mol.K)] the universal gas constant, T [K] the temperature and x_w accounts for the presence of ions in the pore solution. For an ideal solution (dilute) x_w can be simply considered as ionic concentrations (Baroghel-Bouny et al., 2011). But, for non-ideal solutions, a more complex description is required and various formulas have been proposed in the literature, (Nilsson, 1997; Cheng-long and Liang-sun, 2003).

Capillary pressure-driven shrinkage models are based on those two equations. Let us note this type of model is strongly related to the pore size distribution, and almost all existing capillary pressure-based models assume cylindric or circular pore shapes (Ye, 2015); which is a strong assumption but necessary for practical modeling. This mechanism is believed to dominate above 40-50 % relative humidity and takes place in large capillary pores (r > 50 nm) and mesopores (2 < r <50 nm), where liquid water and water vapor phases both exist, separated by a meniscus.

Disjoining pressure

Disjoining pressure, also called hydration pressure originates from the energy potential gap between the adsorbed water layers and the surface of hydration products such as C−S−H (Maruyama et al., 2014). Disjoining pressure is generated by confined water in the narrow pore space (pores radius < 2.6 nm wide, which corresponds to 10 water molecules wide) as hindered adsorbed layer and acts as a repulsive force toward the particles.

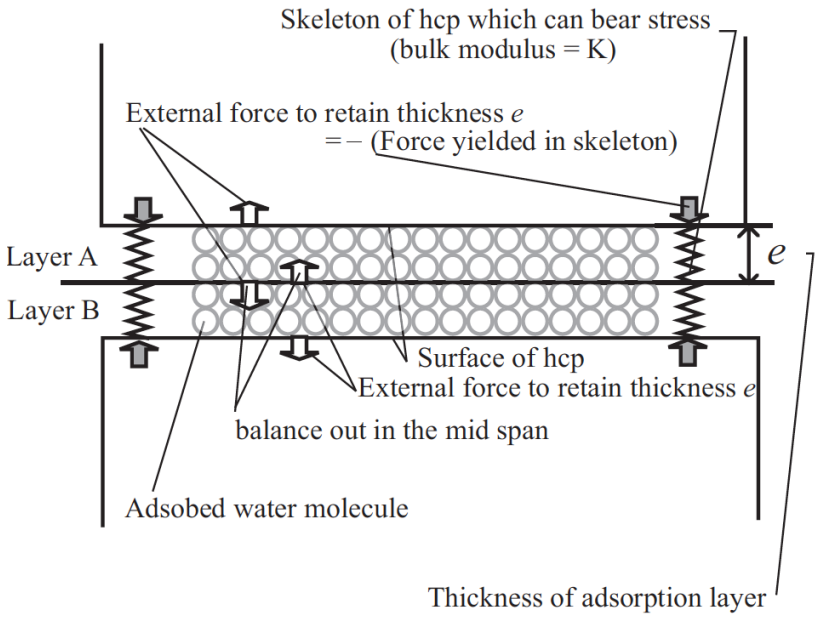

Figure 1.10: Schematic of mechanical equilibrium in hardened cement paste: the pore structure viewed as a two parallel planes, with the disjoining pressure keeping the thickness of adsorbed layer constant and balanced by the mechanical stress of the skeleton

The removal of adsorbed water in the hindered zone causes the relaxation of disjoining pressure, accompanied by reduction of the distance between adjacent surfaces of C−S−H layers (fig.1.10).

By assuming that (i) the disjoining pressure is fully controlled by the thickness of adsorption, and (ii) the thickness of adsorption is completely determined by the ambient

relative humidity and temperature, the disjoining pressure is very often modeled in literature by Eq.1.6

$$\Pi(e) = \rho_l \frac{RT}{M} ln\left(\frac{P}{P_0}\right) \tag{1.6}$$

where P is the vapor pressure at the existing state, P_0 the vapor pressure at the reference state of the system.

However, as noticed by (Maruyama, 2010), if assumption (ii) is valid, the desorption isotherm should be reversible, but in reality, the desorption isotherm shows hysteresis!

Surface tension

The surface tension is the state of stress of the solid phase due to interactions of adsorbed molecules with forces on surface (Feldman and Sereda, 1968).

The increase of surface tension due to desorption induces compressive stress causing the solid to shrink (fig.1.11). From a thermodynamic point of view, there are many ways to derive the increase of surface energy due to desorption (Powers, 1968). The starting point is from Gibbs-Duhem equation applied to surface phases at isothermal condition,

$$-Vdp + Ad\gamma + N_w d\mu_w = 0 \tag{1.7}$$

where $V = Al_a$ is volume [m^3], l_a the thickness of adsorbed liquid [m], and A the surface area [m^2]; N_w the mass of water of the surface phases [kg], μ_w [J/kg] the chemical potential per unit mass ; γ [N/m] the surface tension; p the pressure in surface phase which at equilibrium is equal to pressure in the vapor [Pa]. Rewritting Eq.1.7 as per unit area form,

$$-l_a dp + d\gamma + \Gamma_w d\mu_w = 0 \tag{1.8}$$

In Eq.1.8, $\Gamma_w = N_w/A$ is the surface concentration of molecules [kg/m^2]. Because the liquid phase and the vapor phase should be always in equilibrium, their chemical potential are equal,

$$d\mu_w = d\mu_v = RM^{-1}Td(lnRH) \tag{1.9}$$

In Eq.1.9, M is molar mass of liquid [kg/(mol)], R is the universal gas constant [J/(mol.K)] and T is Temperature [K]. Thus the isothermal change in surface tension can be expressed as:

$$d\gamma = -\Gamma_w RM^{-1}Td(ln(RH)) + l_a dp \tag{1.10}$$

From that point, most of the models neglect the term $l_a dp$ in eq.1.10. By assuming $l_a dp$ negligible, Eq.1.10 simplifies to Eq.1.11.

$$d\gamma = -\Gamma_w RM^{-1}Td(ln(RH)) \tag{1.11}$$

Thanks to the reversibility property of the process (Feldman and Sereda, 1968) at humidity range for which this force is active, the total differential of γ exists; the variation of it between two equilibrium points (denoted as RH_2 and RH_1 for instance) reads

$$\Delta\gamma = -RM^{-1}T\int_{RH_1}^{RH_2} \Gamma_w d(ln(RH)) \tag{1.12}$$

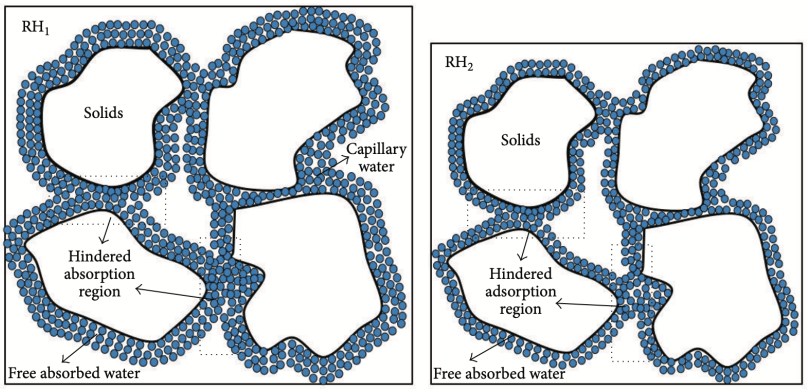

Figure 1.11: Schematic reprensentation of Gibbs-Banham shrinkage (Ye and Radlínska, 2016)

where $\Delta\gamma$ in fact measure change is states of the stress of the solid due to an interaction of the adsorbed water with forces on the solid surface, which put the solid in a state of compressive stress.

To relate to strain, the Bangham equation postulates a proportionality between strains and surface tension change, Eq.1.13 is used (Feldman and Sereda, 1968)

$$\varepsilon_{GB} = \Delta\gamma.\lambda \tag{1.13}$$

where ε_{GB} is named Gibbs-Bangham shrinkage and λ the coefficient of proportionality depending on material stiffness, specific mass, and pore wall surface [m/N].

1.3.2 Drying shrinkage and relative humidity

Successive experimental works on sorption isotherm and drying shrinkage (Baroghel-Bouny et al., 1999b; Baroghel-Bouny, 2007b; Jennings, 2008; Jennings et al., 2015; Maruyama et al., 2014, 2015) reveal a bimodal behavior of drying shrinkage regarding relative humidity. The corresponding value of the transition point is found to be 44%RH (Baroghel-Bouny et al., 1999b), 50%RH (Baroghel-Bouny, 2007b), 54%RH (Jennings, 2008), 45%RH by (Jennings et al., 2015) and 40 %RH (Maruyama et al., 2014). In all investigations, the driving mechanism of volumetric change was attributed (i) to capillary stress for relative humidity above the inflexion point and (ii) to surface tension for relative humidity below the inflexion point fig;1.3. Moreover, the combination of length change measurement along with the sorption measurements makes it possible to relate the water content with length change induced by drying (Baroghel-Bouny, 1994, 2007b; Bentz et al., 1995; Maruyama et al., 2014). Recently, (Maruyama et al., 2014) performed short-term length change isotherms and water vapor sorption isotherm of ordinary cement pastes of 1 year age, pre-equilibrated at different humidities. It was found that the water behavior in hardened cement paste had two different domains, above and below 40 %RH. Their results also showed a good correlation between (i) water vapor BET surface area and the incremental strain of hardened cement paste for relative humidity between 5 %RH and 40 %RH, and (ii) the incremental statistical thickness of water adsorption and incremental strain for relative humidity ranging from 40 %RH to 98 %RH. It was concluded then that drying shrinkage above 40 % RH was driven by disjoining or hydration pressure and below 40%RH by a change in surface energy. These conclusions are consistent with the fundamental works (Feldman and Sereda, 1968).

1.3.3 Concluding remarks on drying shrinkage mechanisms

Powers (1968) was the first author to provide a physical description of mechanisms of drying shrinkage and to propose a model in the viewpoint of thermodynamics. Subsequently, the mechanisms of drying shrinkage have been intensively investigated.

Some basic questions remain: how is drying shrinkage correlated to microstructure change? Where does the irreversibility of drying shrinkage come from? Despite great efforts, no agreement has been achieved so far about the dominant mechanism. It has been argued that different mechanisms may govern at different relative humidity ranges and pore sizes (tab.1.3).

Table 1.3: Mechanisms of drying shrinkage from Soroka quoted by (Benboudjema, 2002) and updated

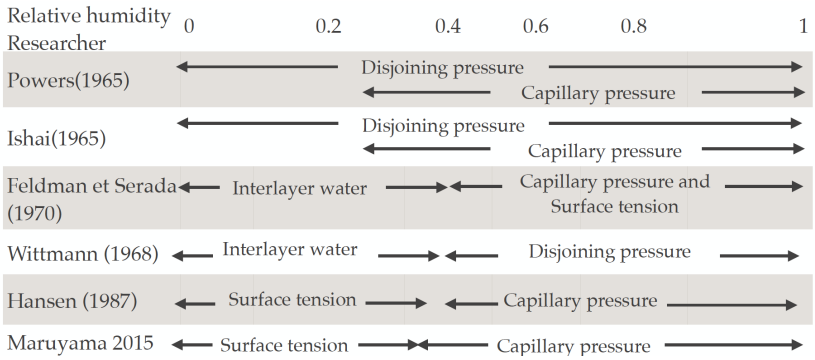

Let us point out that disjoining pressure change is inevitably related to surface tension change because the removal of adsorbed water, which is the driving factor of disjoining pressure, also draws particles closer, which is the primary cause for the increase in surface tension. Moreover, the capillary meniscus, if present adjacent to nanopores, would also affect the disjoining pressure. Hence, drying shrinkage on the entire relative humidity range is controlled by capillary pressure and surface tension as pointed out earlier (Hansen, 1987). Therefore, if one accepts that surface tension and capillary pressure are reversible processes (Feldman and Sereda, 1968), it means indirectly that drying shrinkage as a thermodynamically reversible process is independent of the drying rate. In other words, whatever the path of drying, the value of drying shrinkage at equilibrium for a given relative humidity step should be the same. To investigate the impact of drying rate on drying shrinkage is one of the major goals of this thesis.

1.4 Basic creep

1.4.1 Mechanism of basic creep

The cement paste is a two-phase composite material consisting of elastic inclusions embedded in a viscoelastic matrix, fig.1.12.

The elastic inclusions are portlandite (CH), ettringite (AF_t) calcium, monosulfate (AF_m) and possibly unreacted clinker phase. At a smaller scale, the C−S−H matrix is composed of C−S−H gel and capillary pores. The C−S−H gel itself is made of C−S−H layers or particles with interlayer water between an inner gel porosity. The creep mechanisms are taking place at the C−S−H scale. Several theories have been proposed in the literature to explain the basic creep of cement paste, but none of them have yet been universally accepted. However, it is commonly accepted that water plays a fundamental role in the

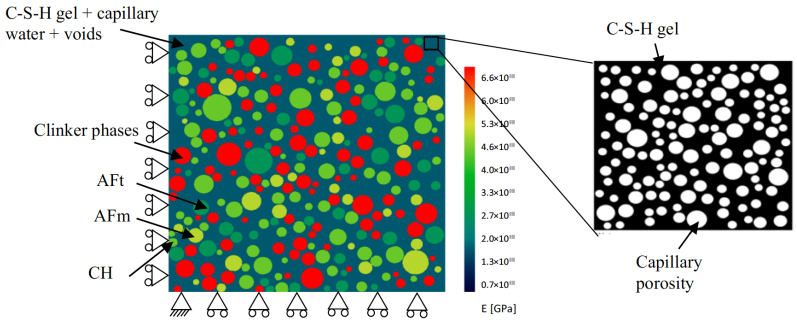

Figure 1.12: Schematic microstructure of cement paste, with color indicating the stiffness of each phase (Hu et al., 2019)

creep of concrete (Tamtsia and Beaudoin, 2000). Several authors (Bažant and Moschovidis, 1973; Philajavaara, 1974) have reported the decrease in the amplitude of the basic creep for previously dried samples. Besides, it was observed that specimens pre-dried at relative humidities close to zero showed almost no creep (Glucklich and Ishai, 1962). However the underlying phenomenon of creep is still poorly understood today and is a matter of intensive on-going research ((Tamtsia and Beaudoin, 2000; Bažant et al., 1997; Acker and Ulm, 2001; Vandamme and Ulm, 2009; Jennings, 2008; Zhang et al., 2014; Rossi et al., 2012; Torrenti and Le Roy, 2018). The analysis of the kinetics of basic creep tests on cement paste and concrete highlight two distinct kinetics regimes regardless of the mix composition (Ruetz, 1968; Ulm et al., 1999): short term creep with rapid kinetics from loading up to few days after loading and long term creep, which has slow kinetics.

1.4.2 Short term basic creep

Short-term creep is strongly affected by the movement of water content and redistribution in capillary porous space (Ruetz, 1968; Wittmann, 1973; Wyrzykowski and Lura, 2014). In fact, the applied external load triggers the free adsorbed water movement into capillary porous space (Bazant and Wittmann, 1982; Torrenti et al., 2013). At the microscopic level, the stress is transmitted through the hydration products that surround capillary pores. At the C−S−H scale, this mechanism is typically represented with a linear dashpot (Giorla and Dunant, 2018). At the macroscopic scale, the mechanism is modeled by a Kelvin chain. The added spring allows representing the elastic phases of the cement matrix.

1. In model B3 and its derivatives (Bažant et al., 1997, 2004; Jirásek and Havlásek, 2014; Rahimi-Aghdam et al., 2019), this creep is modeled by several Kelvin chains, not because of some arrangement of any physical object in the microstructure, but to describe the creep compliance by Dirichlet series whose terms correspond to the Kelvin chain factors. This is of great help to speed up numerical computation.

2. In the model by Benboudjema and derivatives (Benboudjema, 2002; Benboudjema et al., 2005; Foucault et al., 2012; Hilaire, 2014; Charpin et al., 2017; Giorla and Dunant, 2018), only one Kelvin chain is used. (Bazzoni, 2014) reported that the C−S−H particles form as needles of single size characteristic of the binder; Muller (2014) reported that the intrinsic gel porosity has a single characteristic size. Irfan-ul Hassan et al. (2016) shows that this short-term creep is completely reversible by analyzing 3-minutes creep tests. Therefore, we think that using one Kelvin chain is more representative of the physical process during short-term creep.

1.4.3 Long term basic creep

It is commonly accepted in the literature that the long-term behavior is logarithmic and completely irreversible and is taking place in the inter-layer basal space of C−S−H (Bažant et al., 1997; Benboudjema, 2002; Sellier et al., 2016). Moreover it has been identified by classical testing methods at the macroscopic scale (Acker and Ulm, 2001) and by nano-indentation at the C−S−H scale (Vandamme and Ulm, 2009). Almost all the existing models today agree on the following points: (i) the long term basic creep is completely irreversible, (ii) and comes from viscous phenomena occurring in C−S−H interlayers, (iii) and this viscous process involves a reorganization of nanostructure of C−S−H, and (iv) the interlayer water lubricates the C−S−H layer surface, which reduces the creep modulus (Suwanmaneechot et al., 2020). But how this reorganization occurs is still a subject of debate (Ye, 2015). Is it sliding (Bažant et al., 1997), or compaction (Vandamme and Ulm, 2009), breaking and remaking of C−S−H bounds (Sellier et al., 2016), microcracking (Rossi et al., 2012)? Two mains theories are widely adopted for modeling the long term creep:

1. In the Micro-prestress theory (Bažant et al., 1997), it is modeled by a non-linear Maxwell dashpot where the viscosity depends on the micro-prestress. The micro-prestress characterizes self-equilibrated stresses at the nanoscale level. It is initially produced by incompatible volume changes in the microstructure during hydration. These stresses stretch and break the interatomic bonds of C−S−H layers, allowing slip of parallel C−S−H sheets or adjacent C−S−H globules, which is believed to be the main cause of creep in concrete in the long term.

2. In the consolidation theory, the long-term creep originates from compaction or consolidation of the C−S−H nanostructure under load, (Vandamme and Ulm, 2009). From the modeling viewpoint, Sellier and Buffo-Lacarriere (2009); Sellier et al. (2016) modeled long-term creep by a non-linear Maxwell module, where the viscosity depends on the creep strains. Following the same idea, Hilaire (2014) proposed a model where the viscosity is made dependent on time.

1.5 Drying creep

1.5.1 Experimental observations

For a specimen subjected to both drying and mechanical load, the part of the deformation not explained by basic creep and drying shrinkage is called desiccation creep.

$$\boldsymbol{\varepsilon}_{dc} = \boldsymbol{\varepsilon}_{tot} - \boldsymbol{\varepsilon}_{bc} - \boldsymbol{\varepsilon}_{sh} - \boldsymbol{\varepsilon}_{el} \tag{1.14}$$

where: $\boldsymbol{\varepsilon}_{tot}$ is the total strain tensor, $\boldsymbol{\varepsilon}_{el}$ the elastic strain, $\boldsymbol{\varepsilon}_{sh}$ drying shrinkage strain tensor, $\boldsymbol{\varepsilon}_{bc}$ the basic creep strain tensor and $\boldsymbol{\varepsilon}_{dc}$ the drying creep strain tensor.

Drying creep corresponds to the additional deformation when concrete is stressed together with internal moisture change. This behavior, called Pickett effect, is quite paradoxical. A pre-dried specimen creeps less than a saturated one, but when drying, the lower the relative humidity at which the concrete is exposed, the more it will creep (Acker and Ulm, 2001).

1.5.2 Mechanisms of drying creep

Two mechanisms had been proposed in the literature to explain this phenomenon.

Structural origin of drying creep

To explain the transient creep effect caused by humidity change, the most apparent mechanism may be skin microcracking (Wittmann and Roelfstra, 1980). When an unloaded specimen is subjected to drying, tensile stresses due to hydric gradients may exceed the tensile strength of the material and lead to surface microcracking. The larger the structure, the larger the gradient will be, and the more likely cracking. Therefore this mechanism is intimately related to the structure and could be drastically reduced by testing very thin specimens, (Day et al., 1984; Bažant and Yunping, 1994). But when a specimen is subjected to compression and drying, the microcracking is less prominent than that of the non-loaded specimen. Therefore, the measured strain is greater than the sum of basic creep and drying shrinkage measured separately.

Intrinsic mechanism

However, many researchers found that the transient creep effects, under humidity change, could not be only attributed to the microcracking or damage (Bažant et al., 1997; Benboudjema et al., 2005; Havlásek and Jirásek, 2016). Experimental studies (Day et al., 1984; Bažant and Yunping, 1994) have demonstrated that even thin specimens show significant drying creep; although the very small thickness of specimens allows reducing the hygric gradient, source of surface microcracking. Therefore, other mechanisms were proposed to explain this complex coupled hydro-mechanical behavior. It mainly includes the seepage theory (Ruetz, 1968), the stress-induced shrinkage theory (Bažant and Chern, 1985; Benboudjema et al., 2005), the poromechanics theory (Sellier et al., 2016), micro-prestress relaxation theory (Bažant et al., 1997; Jirásek and Havlásek, 2014; Rahimi-Aghdam et al., 2019), stress concentration theory (Brooks, 2001).

1.5.3 Modeling drying creep

Above all the mentioned theories, the most widely used is drying induced shrinkage (Bažant and Chern, 1985). According to this theory, simultaneous loading and drying causes microdiffusion of water between micropores and macropores. This enhances bound breakage of C−S−H gel , which in turn causes intrinsic drying creep

$$\dot{\boldsymbol{\epsilon}} = \mu|\dot{h}|\boldsymbol{\sigma} \tag{1.15}$$

Later on, Bažant et al. (1997) proposed that intrinsic drying creep that is not only due to water flow between micropores and macropores, but any phenomenon likely to affect the thermodynamic balance of C−S−H, described by the notion of relaxation of microprestress.

Recently, Benboudjema et al. (2005) studied the interaction between drying, shrinkage, creep, and cracking in concrete. The authors suggested that the drying process and intrinsic drying creep mechanisms occurred with different kinetics. They modeled the drying creep effect by adding Kelvin–Voigt unit to the rheological model of basic creep

$$\eta\dot{\boldsymbol{\epsilon}} + \theta|\dot{h}|\kappa\boldsymbol{\epsilon} = \theta|\dot{h}|\boldsymbol{\sigma} \tag{1.16}$$

where η is the viscosity of the micro-diffusing water; κ the stiffness of the load-bearing absorbed water layers; $\theta = 1s$ a unit conversion factor. This model assumes that the material skeleton bounds the micro diffusion process in the adsorbed water layer.

Sellier and Buffo-Lacarriere (2009) proposed a coupled hygro-thermo-mechanical model based on the framework of poromechanics. In their model, the effect of temperature and humidity on creep is established by introducing several Biot coefficient terms to directly correct creep amplitude.

References

P. Acker and F-J. Ulm. Creep and shrinkage of concrete: physical origins and practical measurements. *Nuclear Engineering and Design*, 203(2):143–158, 2001. 23, 29, 30

AFPC. Compte-rendu des journées techniques AFPC-AFREM durabilité des bétons. *Méthodes recommandées pour la mesure des grandeurs associées à la durabilité*, 65:121–125, 1997. 19

A.J. Allen and J.J. Thomas. Analysis of c–s–h gel and cement paste by small-angle neutron scattering. *Cement and Concrete Research*, 37(3):319–324, 2007. v, 14, 18

M. Auroy, S. Poyet, P. Le Bescop, J-M. Torrenti, T. Charpentier, M. Moskura, and X. Bourbon. Impact of carbonation on unsaturated water transport properties of cement-based materials. *Cement and concrete research*, 74:44–58, 2015. 23, 24

V. Baroghel-Bouny. *Caractérisation microstructurale et hydrique des pâtes de ciment et des bétons ordinaires et à très hautes performances.* PhD thesis, Ecole Nationale des Ponts et Chaussées, 1994. 27

V. Baroghel-Bouny. Water vapour sorption experiments on hardened cementitious materials. Part I: Essential tool for analysis of hygral behaviour and its relation to pore structure. *Cement and Concrete Research*, 2007a. ISSN 00088846. doi: 10.1016/j.cemconres.2006.11.019. 20

V. Baroghel-Bouny. Water vapour sorption experiments on hardened cementitious materials: Part i: Essential tool for analysis of hygral behaviour and its relation to pore structure. *Cement and Concrete Research*, 37(3):414–437, 2007b. 21, 27

V. Baroghel-Bouny, M. Mainguy, T. Lassabatere, and O. Coussy. Characterization and identification of equilibrium and transfer moisture properties for ordinary and high-performance cementitious materials. *Cement and Concrete Research*, 1999a. ISSN 00088846. doi: 10.1016/S0008-8846(99)00102-7. 20

V. Baroghel-Bouny, M Mainguy, T Lassabatere, and Olivier Coussy. Characterization and identification of equilibrium and transfer moisture properties for ordinary and high-performance cementitious materials. *Cement and concrete research*, 29(8):1225–1238, 1999b. 21, 27

V. Baroghel-Bouny, M. Thiéry, and X. Wang. Modelling of isothermal coupled moisture–ion transport in cementitious materials. *Cement and Concrete Research*, 41(8):828–841, 2011. 25

Z. P. Bažant and Z. Moschovidis. Surface-diffusion theory for drying creep effect in portland cement paste and concrete. *Journal of the American Ceramic Society*, 56(5):235–241, 1973. 29

Z.P. Bazant and S. Prasannan. Solidification theory for concrete creep. i: Formulation. *Journal of engineering mechanics*, 115(8):1691–1703, 1989. 20

Z.P. Bazant and F.H. Wittmann. Creep and shrinkage in concrete structures. 1982. v, 22, 23, 29

Z.P. Bažant, A.B. Hauggaard, S. Baweja, and F-J. Ulm. Microprestress-solidification theory for concrete creep. I: Aging and drying effects. *Journal of Engineering Mechanics*, 123 (11):1188–1194, 1997. 29, 30, 31

Z.P. Bažant, G. Cusatis, and L. Cedolin. Temperature effect on concrete creep modeled by microprestress-solidification theory. *Journal of engineering mechanics*, 130(6):691–699, 2004. 29

A. Bazzoni. Study of early hydration mechanisms of cement by means of electron microscopy. Technical report, EPFL, 2014. 29

Z. P. Bažant and J. C. Chern. Concrete creep at variable humidity: constitutive law and mechanism. *Materials and Structures*, 18(1), 1985. ISSN 1871-6873. 31

Z. P. Bažant, A. A. Asghari, and J. Schmidt. Experimental study of creep of hardened portland cement paste at variable water content. *Matériaux et Constructions*, 9(4):279–290, 1976. ISSN 0025-5432, 1871-6873. 23

Z.P. Bažant and X. Yunping. Drying creep of concrete: constitutive model and new experiments separating its mechanisms. *Materials and Structures*, 27(1):3–14, 1994. 31

F. Beltzung and F. H Wittmann. Role of disjoining pressure in cement based materials. *Cement and Concrete Research*, 35(12):2364–2370, 2005. 24

F. Benboudjema. *Modélisation des déformations differées du béton sous sollicitation biaxiales. Application aux enceintes de confinement de bâtiments réacteurs des centrales nucléaires.* PhD thesis, Université de Marne la Vallée, 2002. xi, 28, 29, 30

F. Benboudjema, F. Meftah, and J.M. Torrenti. Interaction between drying, shrinkage, creep and cracking phenomena in concrete. *Engineering Structures*, 27(2):239–250, 2005. 22, 29, 31

D. P. Bentz, D. A. Quenard, V. Baroghel-Bouny, E. J. Garboczi, and H. M. Jennings. Modelling drying shrinkage of cement paste and mortar part 1. structural models from nanometres to millimetres. *Materials and Structures*, 28(8):450–458, 1995. 27

P.HR Borges, J.O. Costa, N.B. Milestone, C.J. Lynsdale, and R.E. Streatfield. Carbonation of CH and c–s–h in composite cement pastes containing high amounts of BFS. *Cement and Concrete Research*, 40(2):284–292, 2010. 23

JJ Brooks. The influence of pore stress on creep of hardened cement paste. *Creep, Shrinkage and Durability Mechanics of concrete and other Quasi-Brittle Materials*, 2001. 31

S. Brunauer, P. H. Emmett, and E. Teller. Adsorption of gases in multimolecular layers. *Journal of the American chemical society*, 60(2):309–319, 1938. 21

M. Castellote, L. Fernandez, C. Andrade, and C. Alonso. Chemical changes and phase analysis of OPC pastes carbonated at different CO 2 concentrations. *Materials and Structures*, 42(4):515–525, 2009. Publisher: Springer. 23

L. Charpin, T.O. Sow, X.D. De Pradel, F. Hamon, and J.-P. Mathieu. Numerical Simulation of 12 Years Long Biaxial Creep Tests: Efficiency of Assuming a Constant Poisson's Ratio. In *Poromechanics 2017 - Proceedings of the 6th Biot Conference on Poromechanics*, pages 997–1004. Elsevier, 2017. 29

L. Cheng-long and L. Liang-sun. A two-ionic-parameter approach for ion activity coefficients of aqueous electrolyte solutions. *Fluid phase equilibria*, 205(1):69–88, 2003. 25

R.L. Day, P Cuffaro, and JM Illston. The effect of rate of drying on the drying creep of hardened cement paste. *Cement and Concrete Research*, 14(3):329–338, 1984. 23, 31

C. De Sa, F. Benboudjema, M. Thiery, and J. Sicard. Analysis of microcracking induced by differential drying shrinkage. *Cement and Concrete Composites*, 30(10):947–956, 2008. 23

S. Diamond. Mercury porosimetry: an inappropriate method for the measurement of pore size distributions in cement-based materials. *Cement and concrete research*, 30 (10):1517–1525, 2000. 19

J. Dweck, P. M. Buchler, A.C.V. Coelho, and F.K Cartledge. Hydration of a portland cement blended with calcium carbonate. *Thermochimica Acta*, 346(1):105–113, 2000. 23

L. Edelman, D.S. Sominskii, and Kopchiko. N.V. Pore size distribution in cement rock. *Kolloidnyi Zhurnal*, 23(2), 1961. 18

R. F. Feldman and P. J. Sereda. A model for hydrated portland cement paste as deduced from sorption-length change and mechanical properties. *Matériaux et Construction*, 1: 509–520, 1968. v, 15, 16, 17, 22, 24, 26, 27, 28

A. Foucault, S. Michel-Ponnelle, and E. Galenne. A new creep model for npp containment behaviour prediction. In *International conference on Numerical modeling Strategies for sustainable concrete structures*, 2012. 29

I. Galan, C. Andrade, and M. Castellote. Natural and accelerated CO2 binding kinetics in cement paste at different relative humidities. *Cement and Concrete Research*, 49:21–28, 2013. Publisher: Elsevier. 23

C. Gallé. Effect of drying on cement-based materials pore structure as identified by mercury intrusion porosimetry: a comparative study between oven-, vacuum-, and freeze-drying. *Cement and Concrete Research*, 31(10):1467–1477, 2001. xi, 19

A.B. Giorla and C.F. Dunant. Microstructural effects in the simulation of creep of concrete. *Cement and Concrete Research*, 105:44–53, 2018. 29

J. Glucklich and O. Ishai. Creep mechanism in cement mortar. In *Journal Proceedings*, volume 59, pages 923–948, 1962. 29

I. Guenot-Delahaie. Contibution to physical analysis and modelling of concrete basic creep. 1997. 20

J. J. Hagymassy, S. Brunauer, and R. S. Mikhail. Pore structure analysis by water vapor adsorption: I. t-curves for water vapor. *Journal of Colloid and Interface Science*, 29: 485–491, 1969. 21

W. Hansen. Drying shrinkage mechanisms in portland cement paste. *Journal of the American Ceramic society*, 70(5):323–328, 1987. 24, 28

P. Havlásek and M. Jirásek. Multiscale modeling of drying shrinkage and creep of concrete. *Cement and Concrete Research*, 85:55–74, 2016. 31

A. Hilaire. *Etude des déformations différées des bétons en compression et en traction, du jeune au long terme : application aux enceintes de confinement*. PhD thesis, École normale supérieure de Cachan - ENS, 2014. 29, 30

Z. Hu, A. Hilaire, J. Ston, M. Wyrzykowski, P. Lura, and K. Scrivener. Intrinsic viscoelasticity of c-s-h assessed from basic creep of cement pastes. *Cement and Concrete Research*, 121:11–20, 2019. v, 29

C-L. Hwang and J.F. Young. Drying shrinkage of portland cement pastes i. microcracking during drying. *Cement and Concrete Research*, 14(4):585–594, 1984. 22

M. Irfan-ul Hassan, B. Pichler, R. Reihsner, and C. Hellmich. Elastic and creep properties of young cement paste, as determined from hourly repeated minute-long quasi-static tests. *Cement and Concrete Research*, 82:36–49, 2016. 29

H.M. Jennings. A model for the microstructure of calcium silicate hydrate in cement paste. *Cement and concrete research*, 30:101–116, 2000. 15, 17, 19

H.M. Jennings. Refinements to colloid model of c-s-h in cement: CM-II. *Cement and Concrete Research*, 38(3):275–289, 2008. 20, 21, 27, 29

H.M. Jennings, A. Kumar, and G. Sant. Quantitative discrimination of the nano-pore-structure of cement paste during drying: New insights from water sorption isotherms. *Cement and Concrete Research*, 76:27–36, 2015. 21, 27

M. Jirásek and P. Havlásek. Microprestress–solidification theory of concrete creep: Reformulation and improvement. *Cement and Concrete Research*, 60:51–62, 2014. 29, 31

B. Larbi. *Caractérisation du transport diffusif dans les matériaux cimentaires: influence de la microstructure dans les mortiers*. PhD thesis, Université Paris-Est, 2013. 19

A. Leemann and F. Moro. Carbonation of concrete: the role of CO2 concentration, relative humidity and CO2 buffer capacity. *Materials and Structures*, 50(1):30, 2017. Publisher: Springer. 23

S. Lesko, E. Lesniewska, A. Nonat, J-C. Mutin, and J-P. Goudonnet. Investigation by atomic force microscopy of forces at the origin of cement cohesion. *Ultramicroscopy*, 86:11–21, 2001. v, 14

M. Mainguy, O. Coussy, and V. Baroghel-Bouny. Role of air pressure in drying of weakly permeable materials. *Journal of engineering mechanics*, 127(6):582–592, 2001. v, 21

I. Maruyama. Origin of drying shrinkage of hardened cement paste: hydration pressure. *Journal of advanced Concrete Technology*, 8(2):187–200, 2010. 26

I. Maruyama, Y. Nishioka, G. Igarashi, and K. Matsui. Microstructural and bulk property changes in hardened cement paste during the first drying process. *Cement and Concrete Research*, 58:20–34, 2014. v, 20, 21, 22, 25, 27

I. Maruyama, G. Igarashi, and Y. Nishioka. Bimodal behavior of csh interpreted from short-term length change and water vapor sorption isotherms of hardened cement paste. *Cement and Concrete Research*, 73:158–168, 2015. v, 15, 21, 24, 27

P.K. Mehta and P.J. Monteiro. Microstructure and properties of hardened concrete. *Concrete: Microstructure, properties and materials*, pages 41–80, 2006. 20

A.C.A. Muller. Characterization of porosity & csh in cement pastes by ^{1}h nmr. Technical report, EPFL, 2014. 29

A.C.A. Muller and K.L. Scrivener. A reassessment of mercury intrusion porosimetry by comparison with 1h nmr relaxometry. *Cement and Concrete Research*, 100:350–360, 2017. 19

C.M. Neubauer and H.M. Jennings. The use of digital images to determine deformation throughout a microstructure part ii application to cement paste. *Journal of Materials Science*, 35(22):5751–5765, 2000. 23

L.O. Nilsson. A model for convection of chloride. In *"A System for Estimation of Chloride Ingress into Concrete. Theoretical Background", HETEK Rep. No 83, Chap. 7*, pages 47–68. The Danish Road Directorate Copenhagen, 1997. 25

A Nonat and JC Mutin. From hydration to setting. In *Rilem proceedings*, pages 171–171. Chapman & Hall, 1992. 13

V.G. Papadakis, C.G. Vayenas, and M.N. Fardis. A reaction engineering approach to the problem of concrete carbonation. *AIChE Journal*, 35(10):1639–1650, 1989. 23

S. Papatzani, K. Paine, and J. Calabria-Holley. A comprehensive review of the models on the nanostructure of calcium silicate hydrates. *Construction and building materials*, 74:219–234, 2015. 15, 16

S.E. Philajavaara. A review of some of the main results of a research on the aging phenomena of concrete: effect of moisture conditions on strength, shrinkage and creep of mature concrete. *Cement and Concrete Research*, 4(5):761–771, 1974. 29

A. Plassais, M.-P. Pomiès, N. Lequeux, J.-P. Korb, D. Petit, F. Barberon, and B. Bresson. Microstructure evolution of hydrated cement pastes. *Physical Review*, 72, 2005. 14

T. C. Powers. The thermodynamics of volume change and creep. *Matériaux et Construction*, pages 487–507, 1968. 24, 26, 28

T.C. Powers. Structure and physical properties of hardened portland cement paste. *Journal of the American Ceramic Society*, 41(1):1–6, 1958. 21

T.C. Powers and T.L. Brownyard. Studies of the physical properties of hardened portland cement paste. In *Journal Proceedings*, volume 43, pages 101–132, 1946. 15, 16, 19

S. Poyet, K. Trentin, and E. Amblard. The use of sorption balance for the characterization of the water retention curve of cement-based materials. *Journal of Advanced Concrete Technology*, 14(7):354–367, 2016. 20

S. Rahimi-Aghdam, Z. P. Bazant, and G. Cusatis. Extended microprestress-solidification theory (XMPS) for long-term creep and diffusion size effect in concrete at variable environment. *Journal of Engineering Mechanics*, 145(2), 2019. 29, 31

M. Regourd. Microstructures et propriétés des ciments, mortiers et bétons. *Ciments, bétons, plâtres et chaux*, 1982. 20

I. G. Richardson. The calcium silicate hydrates. *Cement and Concrete Research*, 38:137–158, 2008. v, 15, 16

P. Rossi, J-L. Tailhan, F. Le Maou, L. Gaillet, and E. Martin. Basic creep behavior of concretes investigation of the physical mechanisms by using acoustic emission. *Cement and concrete research*, 42(1):61–73, 2012. 29, 30

W. Ruetz. A hypothesis for the creep of hardened cement paste and the influence of simultaneous shrinkage. *Proceedings of the Structure of Concrete and its Behavior under Load*, pages 365–387, 1968. 29, 31

H. Samouh, E. Rozière, and A. Loukili. Experimental and numerical study of the relative humidity effect on drying shrinkage and cracking of self-consolidating concrete. *Cement and Concrete Research*, 115:519–529, 2019. 23

G.W. Scherer. Drying, shrinkage, and cracking of cementitious materials. *Transport in Porous Media*, 110(2):311–331, 2015. 22

K. L. Scrivener and R. J. Kirkpatrick. Innovation in use and research on cementitious material. *Cement and Concrete Research*, 38:128–136, 2008. ISSN 0008-8846. doi: 10.1016/j.cemconres.2007.09.025. 13, 14, 15, 16, 17

K. L. Scrivener, T. Füllmann, E. Gallucci, G. Walenta, and E. Bermejo. Quantitative study of portland cement hydration by diffraction/rietveld analysis and independent methods. *Cement and Concrete Research*, 34:1541–1547, 2004. 14

A. Sellier and L. Buffo-Lacarriere. Towards a simple and unified modelling of basic creep, shrinckage and drying creep of concrete. *European Journal of Environmental and Civil Engineering*, 13(10):1161–1182, 2009. 30, 32

A. Sellier, S. Multon, L. Buffo-Lacarrière, T. Vidal, X. Bourbon, and G. Camps. Concrete creep modelling for structural applications: non-linearity, multi-axiality, hydration, temperature and drying effects. *Cement and Concrete Research*, 79:301–315, 2016. 30, 31

P. Semete, B. Fevrier, Y. Le Pape, J. Delorme, J. Sanahuja, and A. Legrix. Concrete desorption isotherms and permeability determination: effect of the sample geometry. *European Journal of Environmental and Civil Engineering*, 21:42–62, 2017. 20

K.S.W. Sing, D.H. Everett, R.A.W. Haul, L. Moscou, J. Pierotti, R.A .and Rouquerol, and T. Siemieniewska. International union of pure and applied chemistry: reporting physisorption data for gas/solid systems with special reference to the determination of surface area and porosity. *Pure Appl. Chem*, 57(603):e619, 1985. 18

F. Soleilhet. *Etudes expérimentales et numériques des matériaux cimentaires sous sollicitations hydro-mécaniques*. PhD thesis, Université Paris-Saclay, 2017. 19

P. Suwanmaneechot, A. Aili, and I. Maruyama. Creep behavior of csh under different drying relative humidities: Interpretation of microindentation tests and sorption measurements by multi-scale analysis. *Cement and Concrete Research*, 132:106036, 2020. 30

B.T. Tamtsia and J.J. Beaudoin. Basic creep of hardened cement paste a re-examination of the role of water. *Cement and concrete research*, 30(9):1465–1475, 2000. 29

H.F.W. Taylor. *Cement chemistry*, volume 2. Thomas Telford London, 1997. 13

M. Thiery, G. Villain, P. Dangla, and G. Platret. Investigation of the carbonation front shape on cementitious materials: effects of the chemical kinetics. *Cement and Concrete Research*, 37(7):1047–1058, 2007. Publisher: Elsevier. 23

M. Thommes, K. Kaneko, A.V. Neimark, J. P. Olivier, F. Rodriguez-Reinoso, J. Rouquerol, and K. S.W. Sing. Physisorption of gases, with special reference to the evaluation of surface area and pore size distribution (iupac technical report). *Pure and applied chemistry*, 87(9-10):1051–1069, 2015. xi, 18

J-M. Torrenti and R. Le Roy. Analysis of some basic creep tests on concrete and their implications for modeling. *Structural Concrete*, 19(2):483–488, 2018. 29

J-M. Torrenti, G. Pijaudier-Cabot, and J-M. Reynouard. *Mechanical behavior of concrete*. John Wiley & Sons, 2013. 29

F-J. Ulm, F. Le Maou, and C. Boulay. Creep and shrinkage coupling: new review of some evidence. *Revue française de génie civil*, 3(3-4):21–37, 1999. 29

M. Van Genuchten. A closed-form equation for predicting the hydraulic conductivity of unsaturated soils. *Soil science society of America journal*, 44(5):892–898, 1980. 22

M. Vandamme and F.-J. Ulm. Nanogranular origin of concrete creep. *Proceedings of the National Academy of Sciences*, 106(26):10552–10557, 2009. 29, 30

G. Villain, M. Thiery, and G. Platret. Measurement methods of carbonation profiles in concrete: Thermogravimetry, chemical analysis and gammadensimetry. *Cement and Concrete Research*, 37(8):1182–1192, 2007. Publisher: Elsevier. 23

C. Villani, R. Spragg, M. Pour-Ghaz, and Jason W.W. The influence of pore solutions properties on drying in cementitious materials. *Journal of the American Ceramic Society*, 97 (2):386–393, 2014. 21

E. W. Washburn. Note on a method of determining the distribution of pore sizes in a porous material. *Proceedings of the National academy of Sciences of the United States of America*, 7(4):115, 1921. 18

F.H. Wittmann. Interaction of hardened cement paste and water. *Journal of the American ceramic society*, 56(8):409–415, 1973. 29

F.H. Wittmann and P.E. Roelfstra. Total deformation of loaded drying concrete. *Cement and Concrete Research*, 10(5):601–610, 1980. 31

M. Wyrzykowski and P. Lura. The effect of external load on internal relative humidity in concrete. *Cement and concrete research*, 65:58–63, 2014. 29

H. Ye. Creep mechanisms of calcium–silicate–hydrate: An overview of recent advances and challenges. *International Journal of Concrete Structures and Materials*, 9(4):453–462, 2015. 25, 30

H. Ye and A. Radlínska. A review and comparative study of existing shrinkage prediction models for portland and non-portland cementitious materials. *Advances in Materials Science and Engineering*, 2016. v, 27

T. Young. An essay on the cohesion of fluids. *Philosophical transactions of the royal society of London*, (95):65–87, 1805. 24

Q. Zeng, K.i Li, T. Fen-Chong, and P. Dangla. Pore structure characterization of cement pastes blended with high-volume fly-ash. *Cement and Concrete Research*, 42(1):194–204, 2012. 19

Q. Zhang, R. Le Roy, M. Vandamme, and B. Zuber. Long-term creep properties of cementitious materials: Comparing microindentation testing with macroscopic uniaxial compressive testing. *Cement and Concrete Research*, 58:89–98, 2014. 29

Chapter 2

Investigation of drying shrinkage of cement-based materials assisted by Digital Image Correlation

2.1 Motivation

When exposed to drying, a gradient of water content appears between the surface and the core of the specimen (Benboudjema et al., 2007; Hwang and Young, 1984). Due to differential shrinkage, the surface of the specimen experiences tensile stresses while its core is under compression (Benboudjema, 2002; De Sa et al., 2008; Samouh et al., 2019). The larger the specimen, the larger the moisture gradient between the core and the surface of the specimen. In addition, the tensile stress may exceed the tensile strength of the material, and cracking might occur (Mauroux et al., 2012). When studying material behavior, cracking related to structural effects is problematic since measurements are the result of both material and structural behavior. The study presented in this chapter aims at improving the understanding of the effect of drying rate on the delayed strain of cement-based materials. For that purpose, experimental tests, where crack could be avoided or limited as much as possible, have been designed. Avoiding cracking is a crucial way to improve the understanding of material behavior. One way is to reduce as much as possible the size of the specimens (Bažant et al., 1976; Day et al., 1984; Neubauer et al., 2000; Neubauer and Jennings, 2000). On the one hand, this is useful for accelerating the drying process as it is known that drying of cement-based materials is a very slow process (Acker and Ulm, 2001). This idea of using cement paste members of small thickness for studying delayed strain has been proposed by Bažant et al. (1976), who used 0.72 mm thick specimens to investigate creep and shrinkage of cement paste at variable water content. Later on Day et al. (1984) followed up with 1.9 mm thick specimens. However, in both studies, some information is missing (weight loss evolution, desorption isotherm, and cracking characterization). On the other hand, the thinner the specimen, the most likely natural carbonation will affect drying because, like desiccation, carbonation is a diffusion type process (Papadakis et al., 1989; Thiery et al., 2007; Morandeau et al., 2014). Thus limiting natural carbonation when testing samples of small thickness is crucial. It requires the use of an appropriate system to reduce the CO_2 content of the ambient environment (Day et al., 1984).
In this study, two techniques are used to study the drying shrinkage on very thin cement paste specimens:

1. The first method consists of using Environmental Scanning Electron Microscope

(ESEM) assisted by Digital Image Correlation (DIC). ESEM enables to control pressure, temperature, and then indirectly relative humidity, at the same time when imaging the sample surface at a chosen time frequency (Neubauer et al., 2000; Jankovic, 2008). Sub-micrometer spatial resolution images could be achieved using Secondary Electron (SE) or Back-Scattered Electron (BSE) mode. SE imaging is mostly sensitive to topography. BSE imaging is more sensitive to chemical contrast. Let us keep in mind that, ESEM images may be affected by a considerable amount of imaging artefacts (Maraghechi et al., 2019; Sutton et al., 2007b; Guery et al., 2013) which may impede DIC accuracy for displacement and strain assessment.

2. The second method is to use a climatic chamber system assisted by DIC. The CO_2 of the ambient air in the chamber is reduced as much as possible using the appropriate technique, described in this chapter. The monitoring is performed by using an optical camera to image the whole sample surface, unlike ESEM imaging, where only a small region of the surface is followed.

There are three important challenges to overcome with both experimental techniques.

1. Challenge number one is to avoid cracking because if it occurs, true drying shrinkage, which is characteristic of the material, cannot be assessed. To address this issue, samples of very small thicknesses are studied, and the relative humidity is decreased slowly. Particular attention has also been paid during sample preparation to achieve the highest possible homogeneity as much as possible between samples.

2. Challenge number two is to acquire images in ESEM or Climatic Chamber, at different relative humidity conditions and at constant room temperature suitable for DIC. It was decided not to use speckle deposit since it can impede the drying process, even if this would have been of great help to improve the accuracy of DIC, especially when images are taken at variable relative humidity.

3. The last challenge is finally to develop an ok analysis to assess strains induced by drying shrinkage with the lowest possible uncertainty.

This chapter presents the study undertaken to tackle those objectives and is organized as follows. In the first section, the experimental program is presented. In the second section, digital image correlation method is introduced, followed by the analysis of the uncertainties likely to occur in the experiments and how to limit their impact. In the third section, the investigation of the DIC technique is carried out to validate the experiments. The last section presents the investigation of drying length change isotherm results, a comparison between different experimental results is proposed, and the impact of the drying rate on drying-induced deformations is investigated.

2.2 Experimental programm

2.2.1 Samples preparation

The studied material is a cement paste of water to cement ratio (w/c) of 0.52. A cement of type CEM I 52.5 N CE HES BENOR from Gaurin, with a density of 3.19 g/cm^3 is used, referring to VERCORS concrete (Charpin et al., 2018; Mathieu et al., 2018). The main characteristics of cement are presented in Tab.2.1.

Table 2.1: Chemical composition (in % wt)

SIO_2	Al_2O_3	Fe_2O_3	TIO_2	MnO	CaO	MgO	SO_3	Na_2O	K_2O	Cl^-
20.8	4.5	2.3	0.3	0.1	63.2	2.1	3.3	0.16	0.73	0.05

Unlike in VERCORS concrete formulation (Thion et al., 2019), no admixture was added since the water-cement ratio was high enough to facilitate the casting process. All specimens came from different batches following the same fabrication process. For each batch, the paste (2 L) was mixed with a thick stainless mixing blade of 5 L capacity for 1.5 min; then tap water was added (1 min). Finally, for another 1.5 min, the mixer was turned on after the paste was scrapped in the mixer. Specimens were cast in cylindrical molds of sizes ⌀36×180 mm or ⌀30×40 mm. The specimens were demolded 24 h later and were placed in hermetic containers at constant room temperature ($T = 20 \pm 1°C$) with a bottle of water inside to prevent desiccation (fig.2.1.a) for at least 90 days before testing. Small plates of different thicknesses were obtained by cutting the cylinders with a diamond saw (fig.2.1.b). The cylinders were kept flooded with water during cutting to avoid temperature rise. The thin slabs were then covered with plastic and aluminum foil to prevent exchange with the environment.

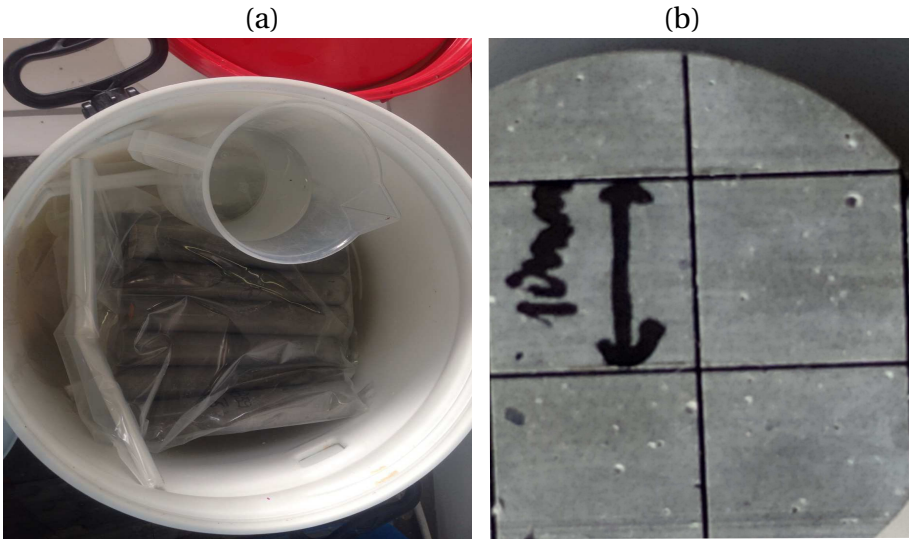

Figure 2.1: Sample preparation process. (a) Curing conditions and (b) sawing of cylinder to obtain prism of size 10×10×2 mm.

Porosity (accessible to water) measurement was carried out to verify according to the AFREM standard with two specificities:

- Samples were saturated with water at approximately pH 12.
- The samples were directly immersed in water before vacuuming, whereas in the AFREM recommendations, a first vacuum of 25 mbar is to be performed, and then water is gradually introduced for about 15 min during a second vacuuming phase.

It allows to verify that vertical casting does not lead to excessive porosity gradient (tab.2.2). The maximum difference between all six tested samples is 0.6%. Therefore the homogeneity of the samples was considered to be very satisfactory.

Table 2.2: Porosity (%) values of two cylinders and at three locations

Porosity(%)	Bottom	Middle	Top	Average
Sample 1	46.5	46.48	46.47	46.48
Sample 2	46.59	46.43	45.99	46.33
Average	46.54	46.45	46.23	46.4

Two geometries are involved in investigating the effect of size and shape on the ultimate drying shrinkage. For macroscopic tests, cylinders ⌀36×180 mm are used; in case of microscopic tests, specimens were 10×10×(2, 0.5 and 0.2) mm slabs (fig.2.2). Let us note that the variability in the thickness of thin slabs is ±30 µm (which corresponds to the thickness of the diamond saw wire). The feature of each test is specimen geometry and drying thickness, plus the relative humidity control system and the rate of drying. The acronyms used to describe the experiments are listed in tab.5.1. For example, DS-P2mm-ESEM-LCIs will read: **D**rying **S**hrinkage test on **P**rismatic specimen of **2 mm** thickness in **ESEM**, **L**ength **C**hange **Is**otherm testing. The experimental program is summarized on tab.2.4.

2.2.2 ESEM experiments

A new experimental protocol in ESEM for the assessment of drying shrinkage behavior is proposed hereafter. The objective of these tests is to speed-up the drying rate so that the long-term drying length change is assessed within a very short period of time. The description of the technique is given hereafter. Experiments DS-P2mm-ESEM-FD and DS-P2mm-ESEM-LCIs of tab.2.4 are concerned:

- **specific preparation**: specimens of size 10×10×2 mm were sawed from cylinders with an impregnated diamond blade, while they were kept flooded during cutting to avoid temperature rise and carbonation with room air. The specimens were first wrapped with a plastic sheet and then with aluminum to keep them in endogenous conditions and to prevent carbonation. 24 h hours before testing, the specimens were kept under 5°C to prevent drying and hence cracking during the pumping cycles of the ESEM. There was no speckle deposit on the specimen surface to enhance

Table 2.3: Acronyms used to describe specimen geometry and experimental condition

DS	Drying Shrinkage
P2mm	Prism of 2 mm thickness
P500 µm	Prism of 500µm thickness
C36mm	Cylinder of 36 mm diameter
CC	climatic chamber
SS	Salt Solution[1]
FD	Fast Drying
LCIs	Length Change Isotherm
RH20	20% Relative humidity

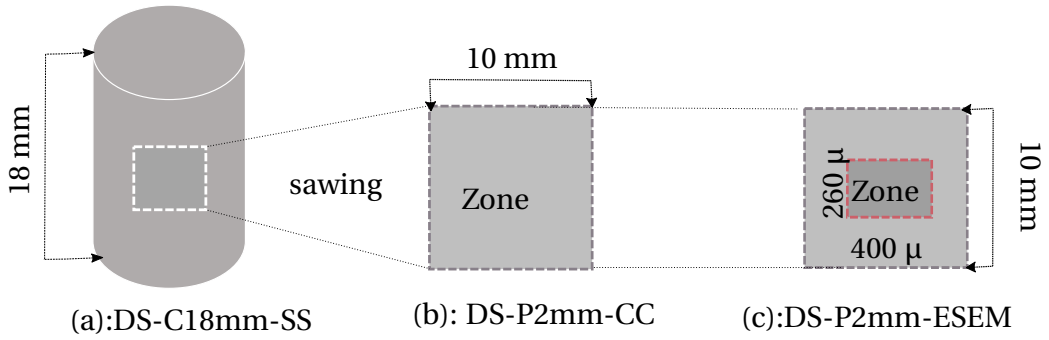

Figure 2.2: Specimens for multiscale investigation of drying shrinkage using saturated saline solution (a) Climatic chamber (b) and ESEM (c) techniques

Table 2.4: Summary of experimental campaign undertaken on cement paste. TDS = Transitional Drying Shrinkage

Test	Geometry (mm)	TDS	LCIs	System
DS-P2mm-ESEM-FD	10×10×2		✓	ESEM
DS-P2mm-ESEM-LCIs	10×10×2		✓	ESEM
DS-P500µm-CC-LCIs	10×10×0.5		✓	CC
DS-P200µm-CC-LCIs	10×10×0.2		✓	CC
DS-P2mm-CC-FD	10×10×2	✓		CC
DS-C18mm-SS-RH80	⌀36×180	✓		SS
DS-C18mm-SS-RH58	⌀36×180	✓		SS
DS-C18mm-SS-RH20	⌀36×180	✓		SS

contrast since it may prevent natural drying; for that reason, the natural contrast is used.

- **Environment**: An ESEM of type Quanta-650 was used. The relative humidity was controlled by varying the pressure inside the chamber while keeping the temperature at a constant value of 24°C; the temperature was regulated through an air conditioning system and monitored using a PT100 temperature sensor provided with the microscope. We have taken advantage of BSE imaging mode (fig.2.3) in order to benefit from both chemical and topography contrast. This imaging mode also allows to probe up to 30 nm depth. Since the energy of backscattered electrons carries the signature of the atoms it has been interacting with, it gives a clue on these atoms, being on surface or in bulk.

- **Strain measurement**: Images are post-processed by DIC. The BSE detector has been used with an acceleration voltage of 30 kV and a working distance of 9.5 mm, adjusted by trial and error strategy (fig.2.3). The scanned area was 266×400

µm with a definition of 1048×1524 pixels, and the pixel size is then 260 nm.

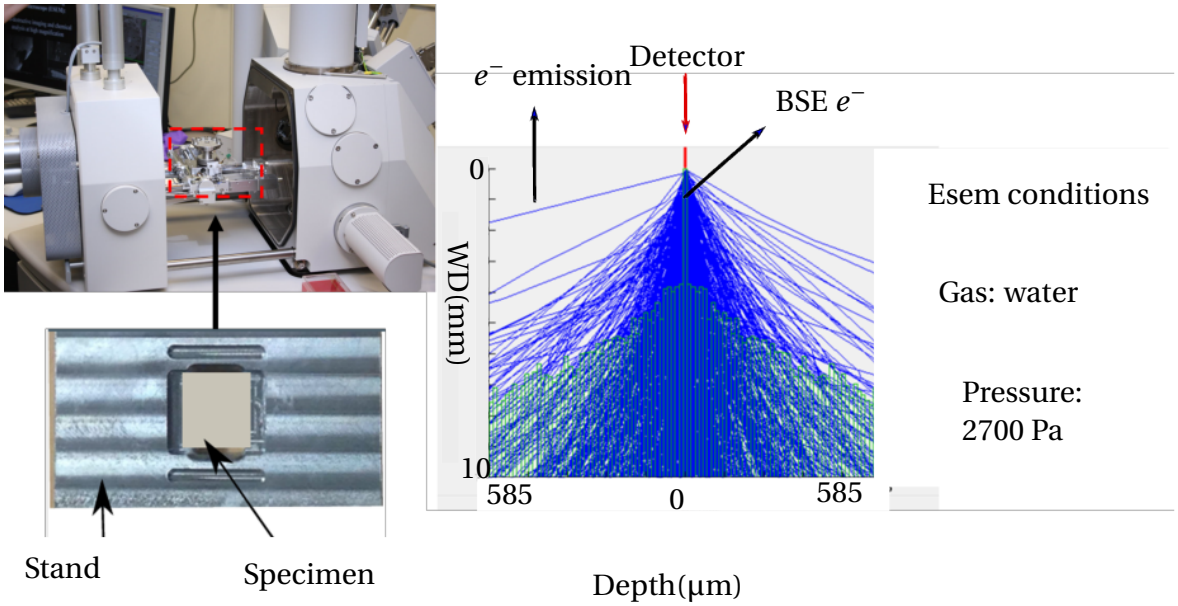

Figure 2.3: Experimental set-up for drying shrinkage measurement in ESEM using BSE mode to image the sample on stand

- **Testing procedure**: A specific stand was designed (fig.2.3) to allow the specimen to dry from all faces. This stand was clipped in ESEM, and then the sample was put on. A first global image was pictured using a Navcam Camera to track any desired position on the sample surface when the chamber is closed. The ESEM chamber was then closed, and the air inside the chamber was pumped to reach an equilibrium of 2700 Pa or slightly less, depending on the current temperature.

2.2.3 Climatic chamber experiments

A new protocol was developed for measuring the short drying length change on a thin slab in a climatic chamber. The purpose was (i) to provide data for validation of ESEM experiment and (ii) to evaluate the effect of drying rate on the ultimate drying shrinkage. The procedure of these experiments, referred to in tab.2.4 as DS-P500µm-CC-LCIs, DS-P200µm-CC-LCIs and DS-P2mm-CC-FD, is described hereafter.

- **Specific preparation**: the same sample preparation as in cases of ESEM testing was used, except the fact that the step of cooling the sample to 5°C was not necessary.

- **Environment**: The relative humidity and temperature were controlled using a climatic chamber. They were monitored using PT100 sensors for temperature and for relative humidity. To deal with carbonation, a specific box was designed, allowing air to pass through and be filled with lime powder compacted to reduce the space between grains. The box was placed in the air inlet of the climatic chamber, fig.2.5, so when the air comes in, CO_2 was captured before reaching the chamber space, where the specimen lies. It proved to reduce the CO_2 content of room air to less than 100 ppm (between 20 and 90 ppm).

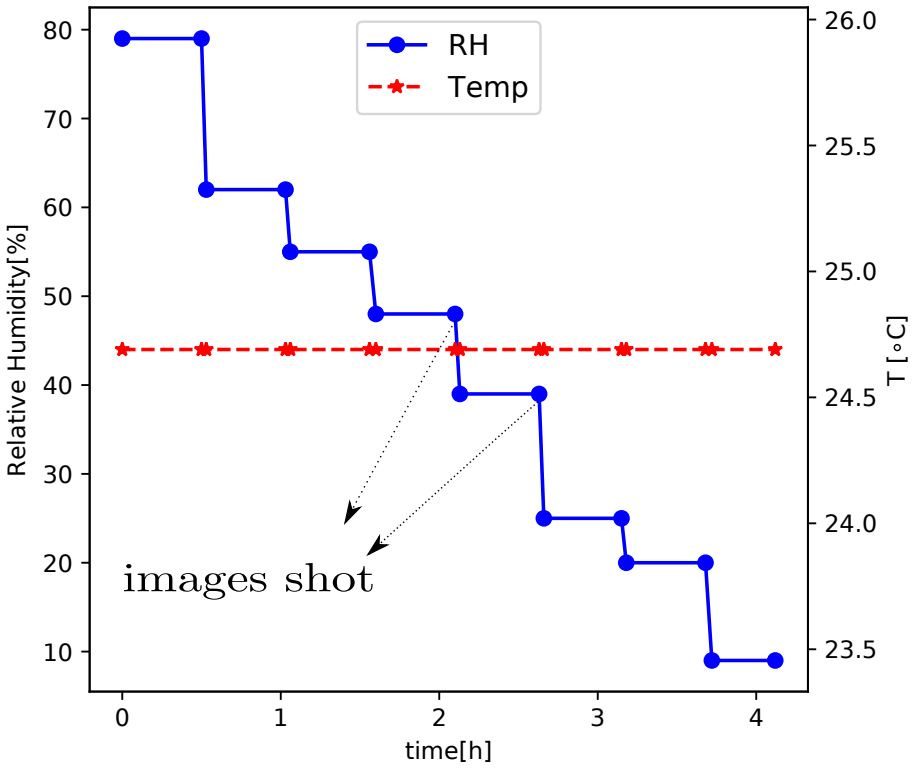

Figure 2.4: Illustration of target humidity, controled in ESEM, test DS-P2mm-ESEM-LCIs.

- **Strain measurement**: Images were acquired and analyzed by DIC using mesh sizes of 50×50 pixels. As in the ESEM case, only natural contrast of cement paste was used. The experimental set-up is shown in fig.2.5. An optical camera of type Edmund optic, equipped with 0.125× telecentric lens (in order to limit effects of out of plane movement), was used. The surface of the specimen was constantly illuminated using LED light. It was checked that lighting did not induce temperature rise. All the surface of the specimen was imaged with a definition of 1000×1000 pixels, which correspond to a physical pixel size of 10µm.

2.2.4 Experiments with saturated salt solutions humidity control system

These tests were designed in order to provide with ultimate drying shrinkage data of slow and long drying experiments to be compared with results of short-term measurements (ESEM, climatic chamber). In the following, the procedure for these long drying length change tests (DS-C18mm-SS-RH80, DS-C18mm-SS-RH58, DS-C18mm-SS-RH20 of tab.2.4) is given.

- **Specific preparation**: Tested samples are ⌀36×180 mm cylinders. The specimens were ground and stored under endogenous conditions until the start of the test.
- **Environment**: It was decided to design sealed humidity chambers (fig.2.6) capable of maintaining some humidity generated by a given saturated salt solution (tab.2.5), minimizing water exchanges with the atmosphere, set at 50 % RH. Temperature and humidity were monitored with a PT100 temperature sensor and a Rotronics capacitive probe. The probes were placed on the wall of the chamber as close as possible

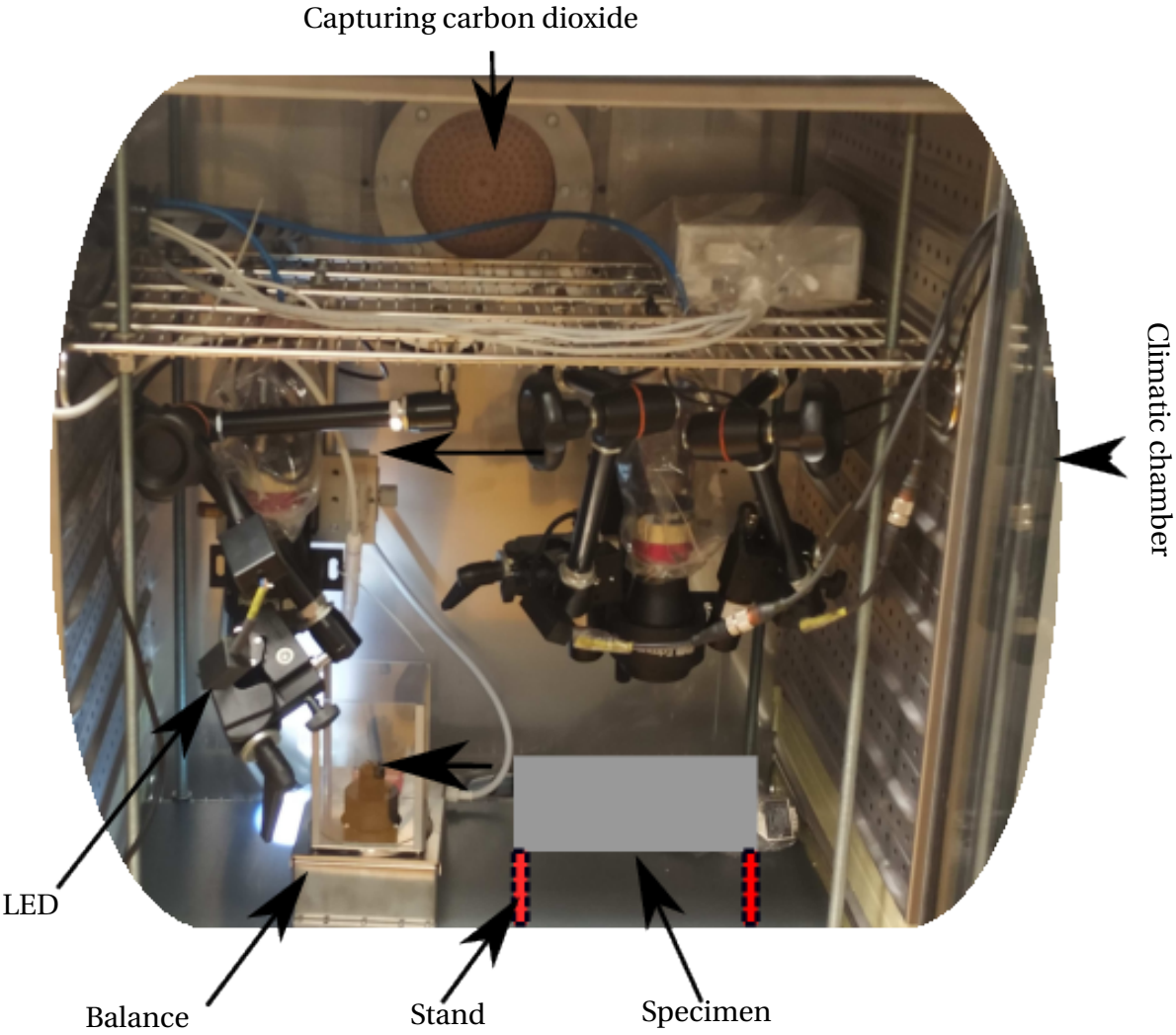

Figure 2.5: Experimental set-up for drying shrinkage measurement in climatic chamber conditioning system.

to the specimen. Because the air in the chamber did not circulate (in order to avoid cracking), the relative humidity decreased slowly.

Table 2.5: Saturated solution for generating relative humidities in macroscopic tests

RH(%)	11	58	81.2
Saturated solution	$LiCl_2$	NaBr	KCl

- **Strain measurement**: For each specimen, the axial strain was monitored using three LVDT (Linear Variable Differential Transformer) displacement sensors, installed at 120° (allowing correction of possible unexpected sample bending); the measurement was made on a 10.8 cm basis.

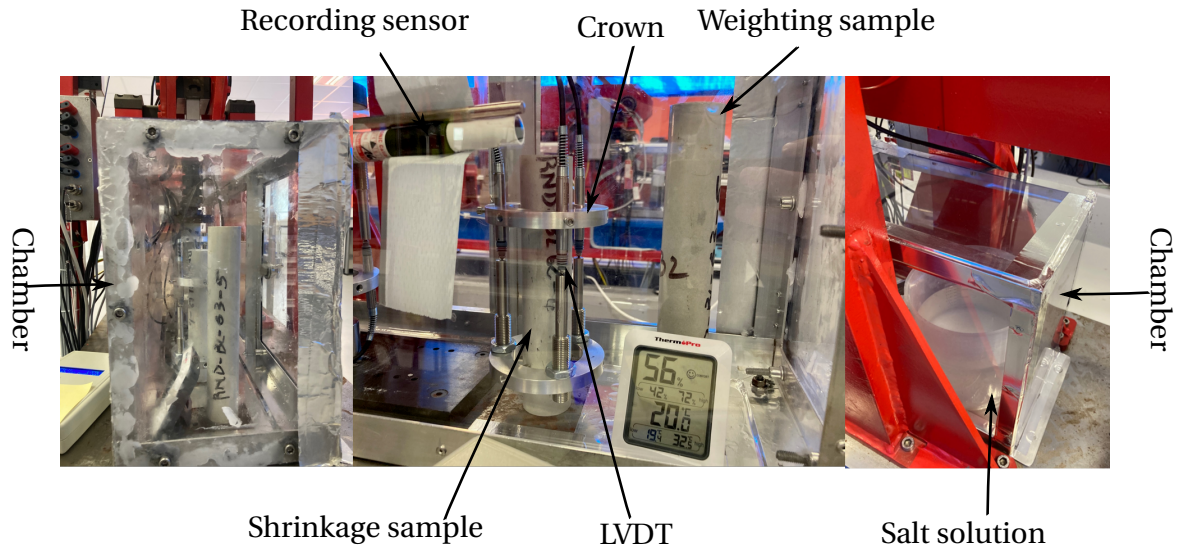

Figure 2.6: Experimental set-up for drying shrinkage measurement in relative humidity chamber controlled by saturated salt solution.

2.3 Brief description of Digital image correlation

2.3.1 Principle of DIC

The inputs of DIC are two gray level pictures, denoted as $f(\mathbf{x})$ (reference image) and $g(\mathbf{x})$ (deformed image) (Hild and Roux, 2008). DIC searches for displacement field $\mathbf{u(x)}$ that relate f and g based on gray level conservation:

$$f(\mathbf{x}) = g(\mathbf{x}+\mathbf{u}(\mathbf{x})) \tag{2.1}$$

The outputs are displacement fields between the 2 input images plus possibly extra corrections e.g. gray level and the difference between $f(\mathbf{x})$ and $g(\mathbf{u(x)}+\mathbf{x})$, also called residual. Mainly, two types of correlation techniques exist: local and global correlation techniques. For local DIC, the displacement $\mathbf{u}$ is sought for each center of each Zone of Interest (ZOI). The minimization is performed independently for each ZOI.

For global DIC, displacement $\mathbf{u}$ is sought such that it satisfies continuity requirement. The displacement is written as in Eq. 2.2:

$$\mathbf{u}(\mathbf{x}, t) = \sum_i v_i(t)\mathbf{\Psi}_i(\mathbf{x}) \tag{2.2}$$

where v_i denotes the discretization of displacement $\mathbf{u}$ according to chosen basis functions $\mathbf{\Psi}_i$ in the sense of finite element framework. Two main outputs are sought, the residual of calculation and the displacement. The former represents the quality of the correlation between the two input images. The latter allows computing the strain whenever possible. In the present study, DIC is carried out using *Correli-RT3*, software developed at LMT Laboratory (Tomičević et al., 2013). It offers the advantage of performing global DIC analysis using finite element mesh with triangular elements. It also introduces mechanical regularization (Tomičević et al., 2013), which makes it possible to track subpixel displacements, which reveals to be powerful when it comes to analyzing natural textures such as cement paste without speckle deposit on its surface. In fact, the regularization acts as a mechanical filter on the displacement field to erase high-frequency fluctuations

likely to occur due to image acquisition noise. The cut-off frequency of this filter is characterized through a single parameter, called here regularization length. When the regularization length is less than the mesh size, it means that the regularization has no effect; that is why it is always taken greater or equal to the element size.

2.3.2 Uncertainty sources in DIC measurement

The accuracy of strain evolution is of central importance, especially when small deformations are sought (Grediac and Hild, 2011). Uncertainty in the type of experiments performed in this study, being in ESEM (Maraghechi et al., 2019) or in a climatic chamber may originate from various sources. First of all, due to relative humidity variations, the images can suffer from contrast and brightness variations. This may impede the DIC method because the information registered on the material point is not the same. In the case of ESEM testing, this type of error can be minimized or even canceled out by superimposing several images of scanning as recommended in (Sutton et al., 2009). Regarding experiments in climatic chambers, two images acquired under the same operating conditions may have gray levels that vary by a random quantity whose difference can reach a few tenths of the dynamic range. Second, we have thermal errors coming from thermal heating. In ESEM, scanning causes local heating of the material. This kind of error can be minimized by turning on the electron beam for few minutes before acquisition of the reference image so that the thermal balance could be reached before imaging (Sutton et al., 2007a). For climatic chamber, the lighting source may cause thermal heat of the sample surface. Third, out-of-plane movements may occur during tests leading to artificial strain. This artifact is handled in the ESEM study by setting the working distance to a constant value throughout the test. For climatic chamber testing cases, the telecentric lens allows minimizing this kind of artifact.

2.4 DIC technique investigation

In this section, we focus on the DS-P2mm-ESEM-LCIs test tab.2.4, first to assess DIC performance, and second to validate this measurement technique by comparison of results of tests carried out in ESEM and in climatic chamber. The Region of Interest (ROI) and the different mesh sizes to use in this study are presented in fig.2.7.

The images used for evaluation of the DIC technique are displayed in fig.2.8; they exhibit enough contrast for DIC to be applied.

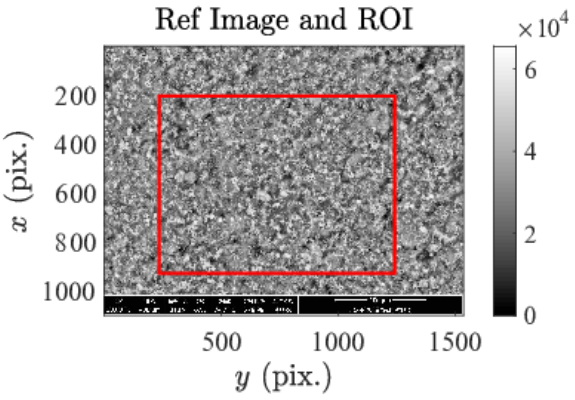

(a) Zone of analysis

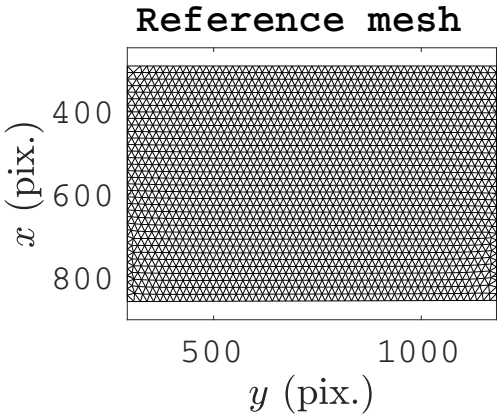

(b) Mesh: 16 ×16 pixels

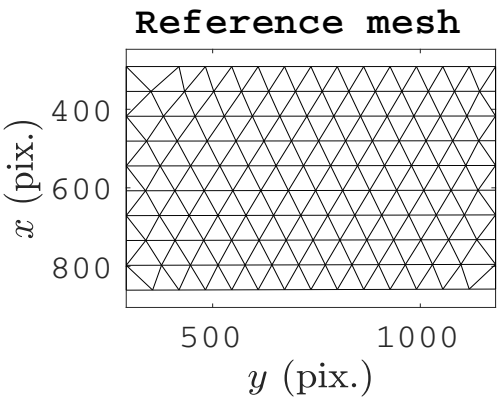

(c) Mesh: 64 ×64 pixels

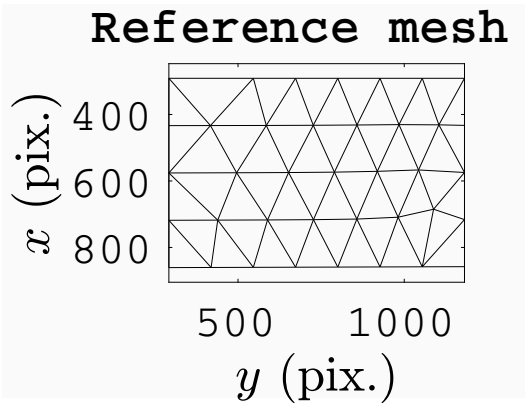

(d) Mesh: 128 ×128 pixels

Figure 2.7: Region of Interest (a) and (b, c, d) different mesh sizes tested in uncertainty analysis.

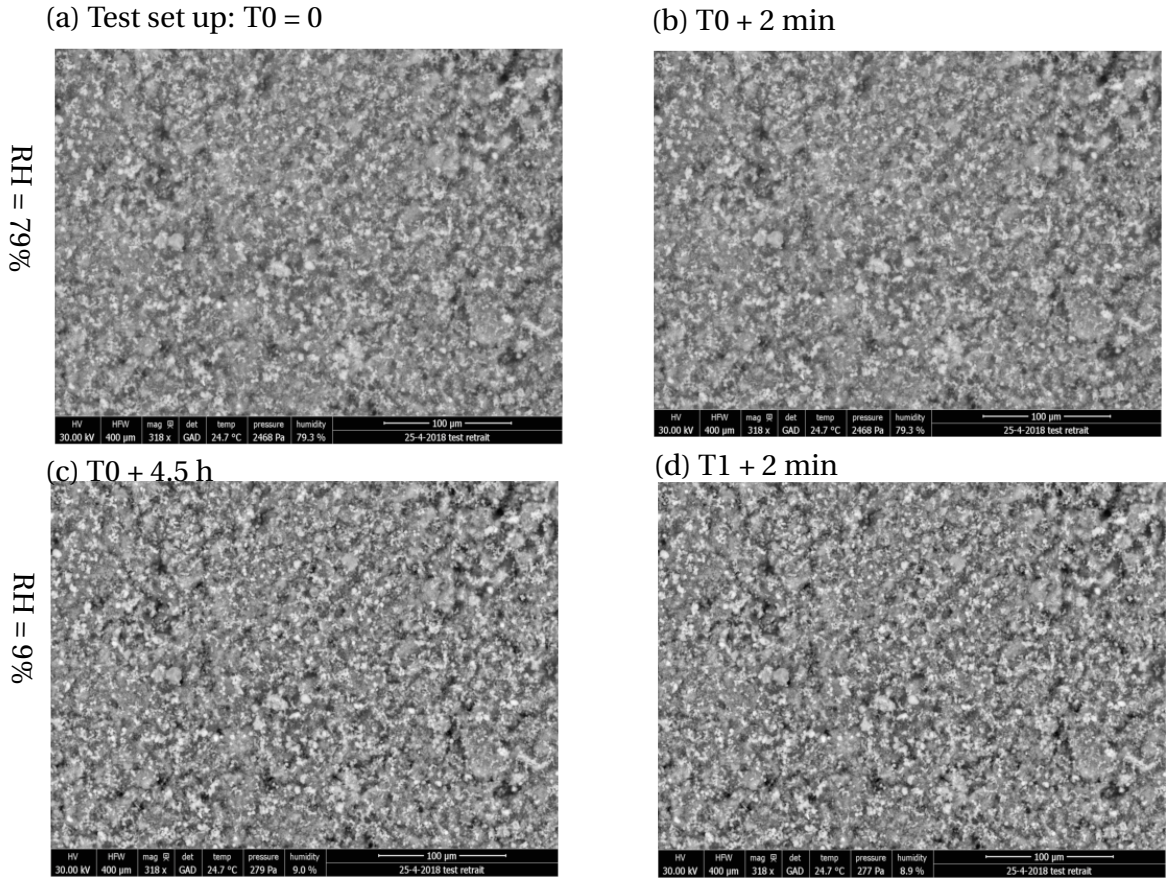

Figure 2.8: Images taken at T_0 (test start) and T_1 (test end) for uncertainty analysis, (schematic drying path is given in fig.2.4)

2.4.1 Displacement and residual strain maps study

In this section, for a demonstration purpose, DIC was run between an image at a relative humidity of 79 % and pressure of 2468 Pa (fig.2.8.b) and an image pictured at a relative humidity of 9 % and pressure of 277 Pa (fig.2.8.c). The comparison has been made using two mesh sizes: a coarse mesh of 33 µm (fig.2.11) and a fine mesh of 4.2 µm (fig.2.10): in both cases, the regularization length is 133 µm. The output residual along with the deformed mesh is presented for both mesh sizes in fig.2.9. The residual map shows that it is quite homogeneous over the study zone (fig.2.7), and its value remains below 5% (Eq.2.3).

$$R = \frac{\sigma(f-g)}{max(f)-min(f)} \tag{2.3}$$

where R is the residual, σ denotes the root mean square value of the picture difference, f and g respectively the reference and the deformed images, $max(f)-min(f)$ is dynamic range of reference image f. Hence the residual is the ratio of uncorrelated pixels over the total number of pixels of the reference reference image (1048×1524 pixels for instance in ESEM images).

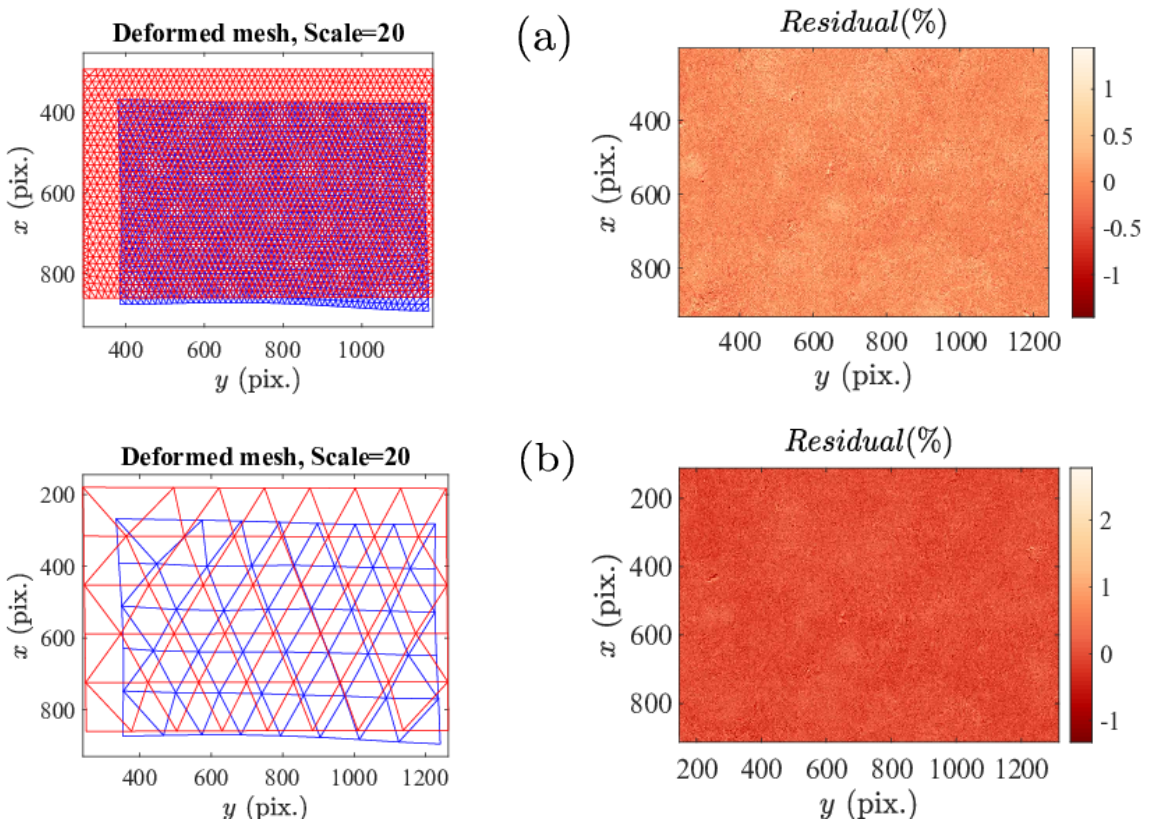

Figure 2.9: Deformed mesh along with associated residual map: element size= 4.2 µm; regularization length = 133 µm (a), element size=33 µm, regularization length = 133 µm (b)

The measured displacement fields associated with these residuals are shown for both meshes sizes in fig.2.10 and fig.2.11. The analysis of this displacement in the central zone shows a quasi-linear variation over the ROI.

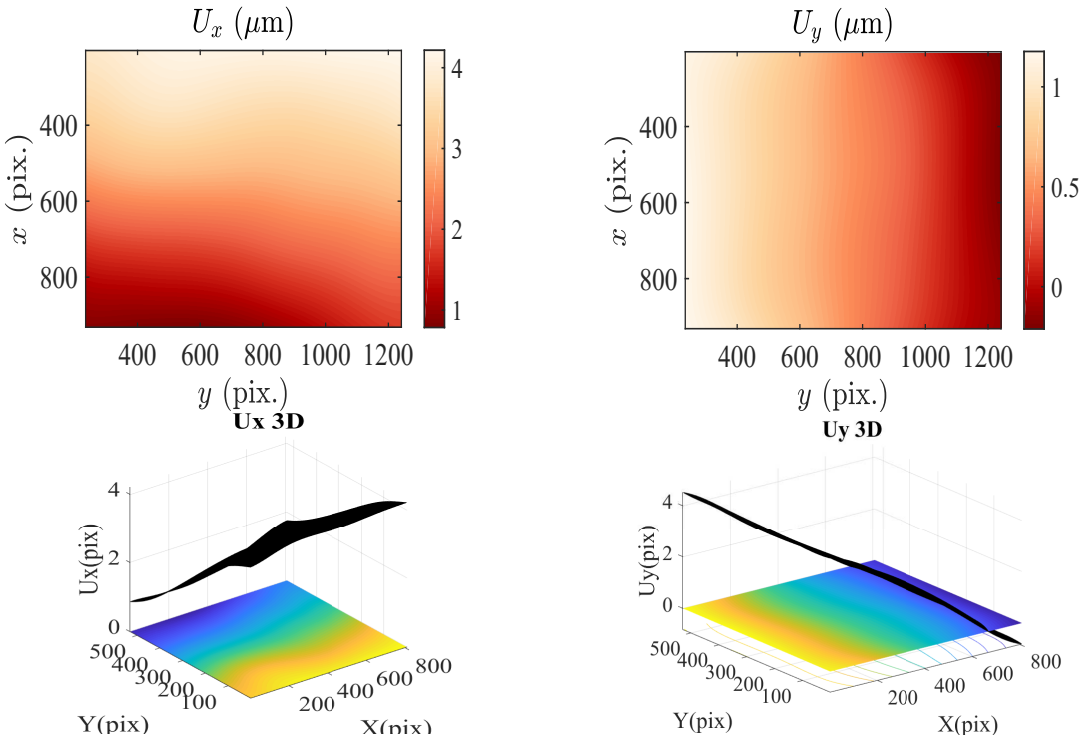

Figure 2.10: Displacement result of DIC calculation for element size 4.2 µm and regularization length of 133 µm

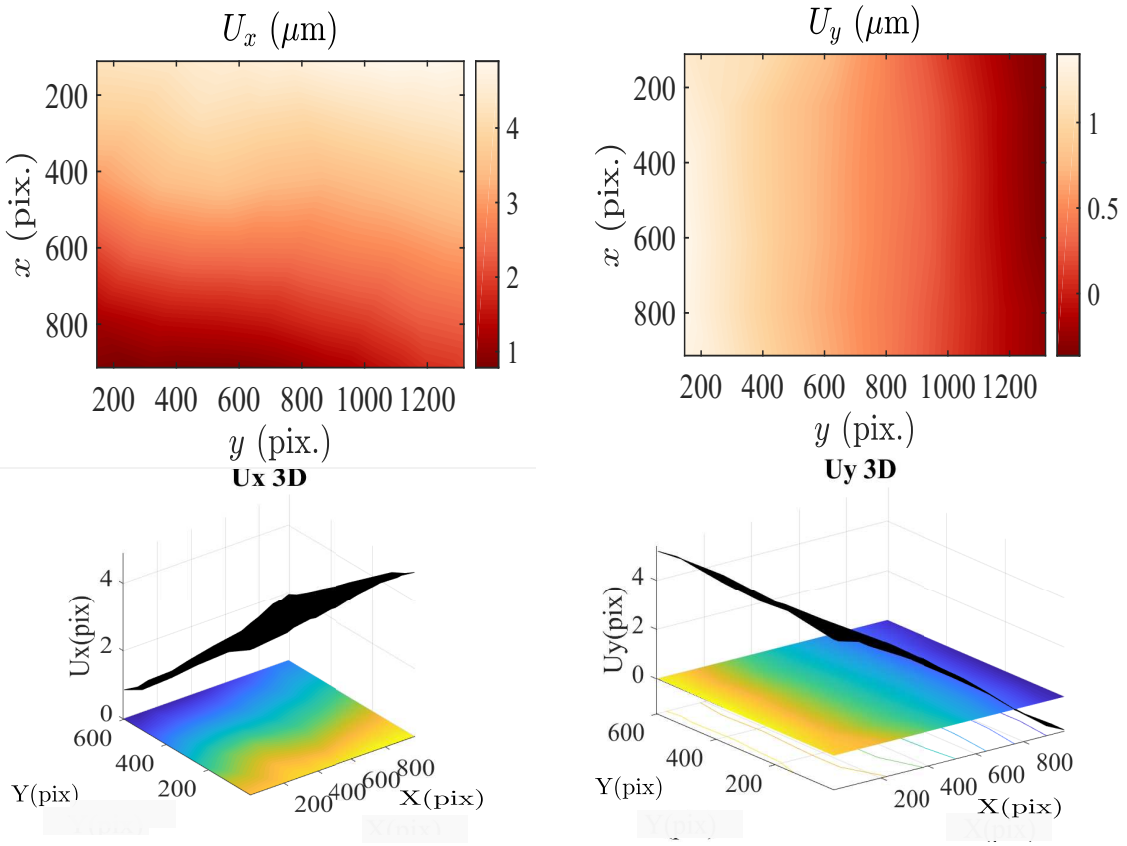

Figure 2.11: Displacement result of DIC calculation for element size 33 µm and regularization length of 133 µm (between T_0 and T_1)

The linearity of displacement over the ROI demonstrates that the hypothesis of uniform strain is satisfied.

2.4.2 Strain sensitivity study

DIC was run on every pair of images acquired at the very end of each relative humidity step represented in fig.2.4 and for different element sizes.

The benefit of regularization to reduce the uncertainty of measurement is also tested. The results of analyze for a relative humidity of 79 %, 39 %, and for 9% RH are presented in figs.2.12, 2.13 and 2.14 respectively. In each figure, the uncertainty on strain ϵ_{xx}, ϵ_{yy}, ϵ_{xy}, ϵ_{dev} are presented, they are evaluated as the standard deviation of the strains maps.

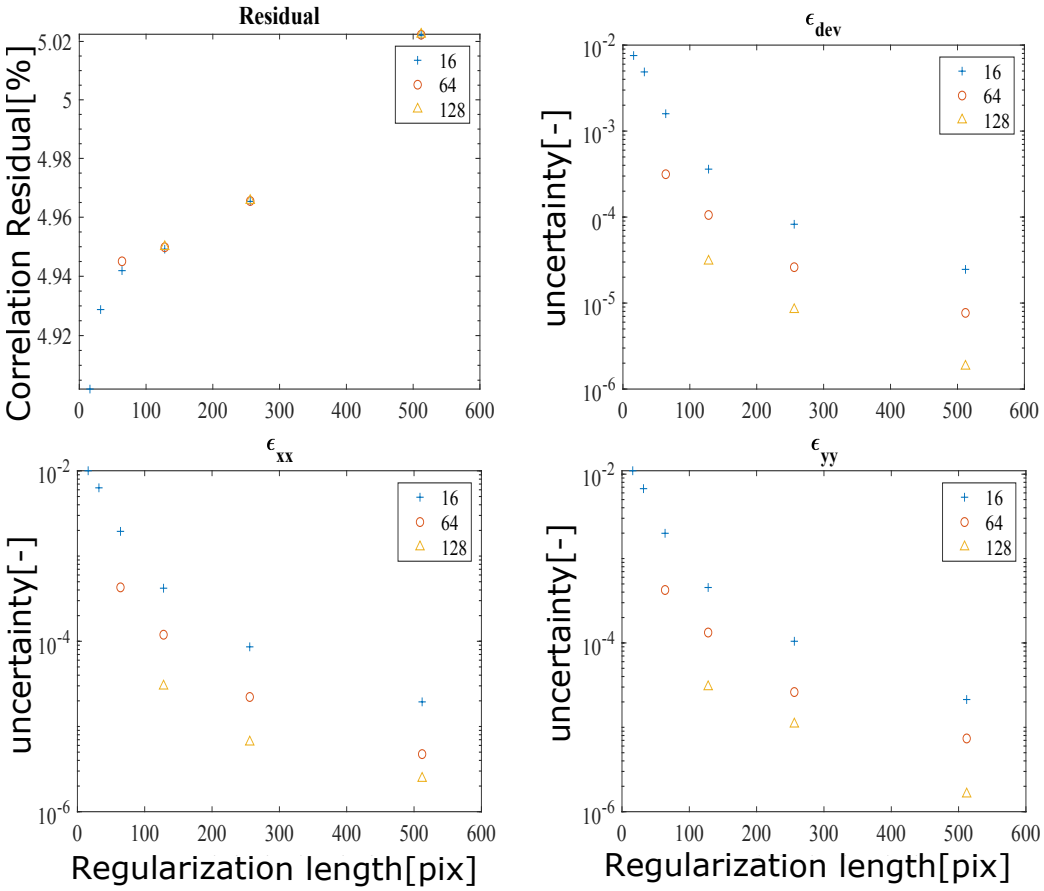

Figure 2.12: Result of DIC applied on images acquiredapproximately 2 minutes one after another at relative humidity step of 79 %, 0.5 h after the start of the test. Correlation residual and standard uncertainty for ϵ_{dev}, ϵ_{xx} and ϵ_{yy} as a function the length of regularization for different mesh sizes (16, 64, 128 pix).

The greater the regularization length, the smaller the uncertainty on the strain is. These results clearly show the advantage of regularization, which allows decreasing the error on strain down to 10^{-4}. The measurement error on strain is significantly minimized by increasing element size and a stronger regularization. As it can be noticed, the uncertainty on mean strain could be reduced to less than 10^{-4} thanks to proper regularization. This is interesting because we are expecting strain levels of the order of 10^{-3}-10^{-2} for this type of material in the range of investigated relative humidity.

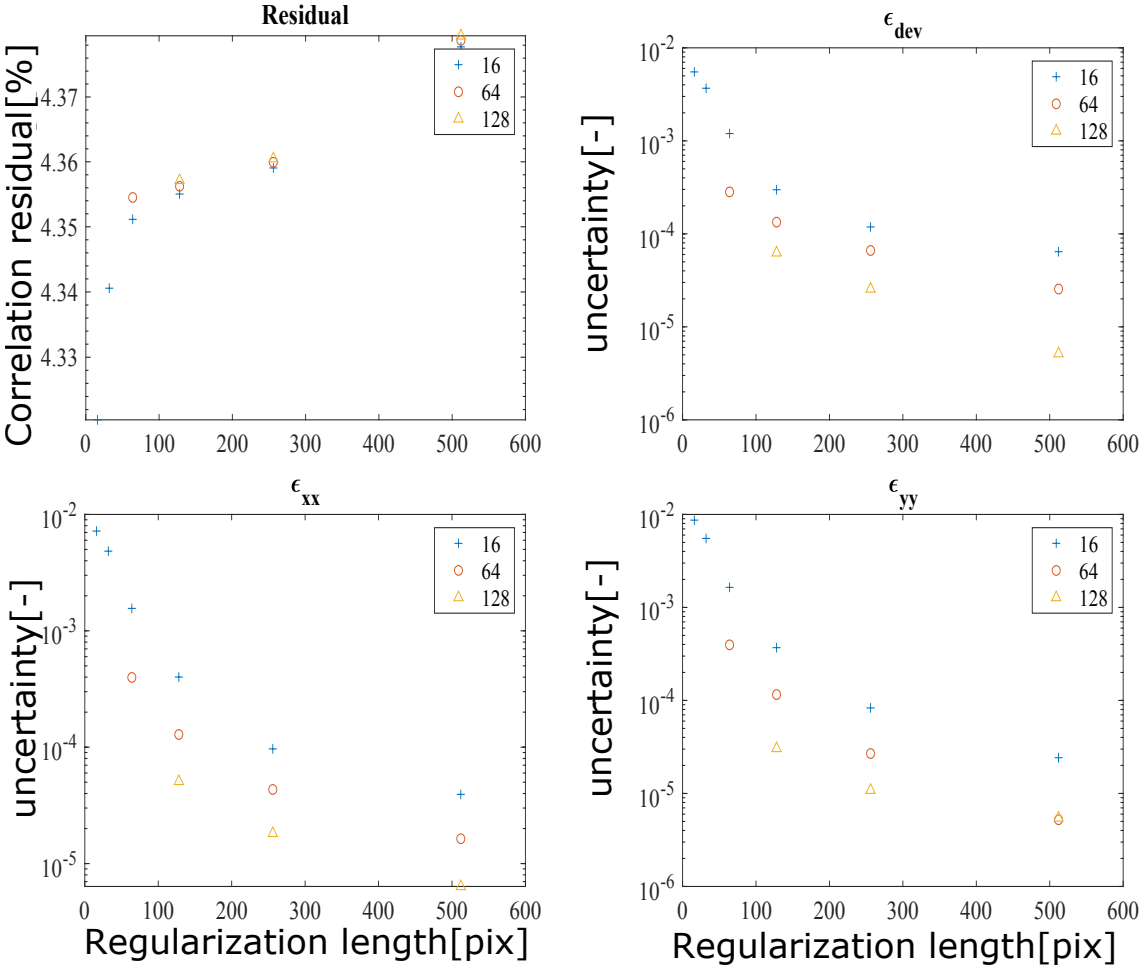

Figure 2.13: Result of DIC applied on images acquired approximately 2 minutes one after another at relative humidity step 39% RH, 1.7 h after the start of the test. Correlation residual and standard uncertainty values for ϵ_{dev}, ϵ_{xx}, and ϵ_{yy} as a function the length of regularization for different mesh sizes (16, 64, 128 pix)

2.4.3 Discussion on uncertainty results

The imaging technique developed in this study allows to image surfaces without any speckle deposit. As described above, the principle of DIC consists of comparing two gray level images, and three main outputs are displayed: the first one is the grey level residual, which represents the quality of the correlation between the two registered images. The level of residual is always below 5 %. It is checked that the residual map is homogeneous over the ROI, and its value remains acceptable. The uncertainty analysis performed using different regularization lengths shows that the strain uncertainty can be reduced to less than 10^{-4} -10^{-5}. There is a compromise to be made between the spatial resolution and the measurement uncertainty. If average strains are sought, then one must use a very large regularization and coarse mesh. Yet if local behavior is sought, then the mesh size and the regularization length must be as small as possible in respect to the local contrast of the surface. Regarding the uncertainty results and because we are more interested in mean strains, we decided to use a mesh size of 133 µm with a regularization length of 133 µm.

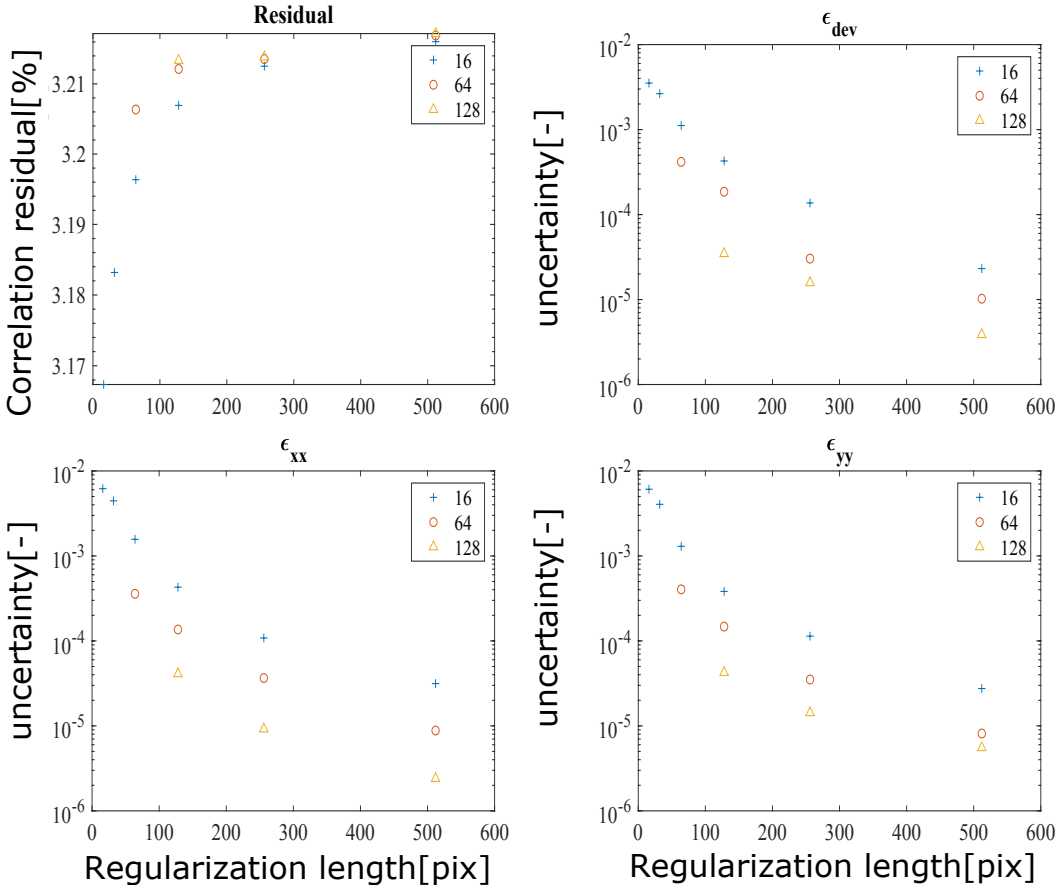

Figure 2.14: Result of DIC applied on image acquired approximately 2 minutes one after another at relative humidity step **9**% RH, 4 h after the start of the test. Correlation residual and standard uncertainty for ϵ_{dev}, ϵ_{xx}, and ϵ_{yy} as a function the length of regularization for different mesh sizes (16, 64, 128 pix).

2.4.4 Comparison of techniques

In this section, a confrontation is made between DS-P2mm-ESEM-FD in ESEM and DS-P2mm-CC-FD in Climatic Chamber. One should question if the measured strain in the ESEM test holds any meaning because we calculate the strain from an image size of 266×400 [µm x µm] that represents a tiny window from the total heterogeneous surface of 10×10 mm. Moreover, the sample surface might be affected by carbonation, cracking, not visible to the naked eye, and possibly outside the observation zone. To address this issue, the comparison between the climatic chamber and ESEM results is presented in fig.2.15.

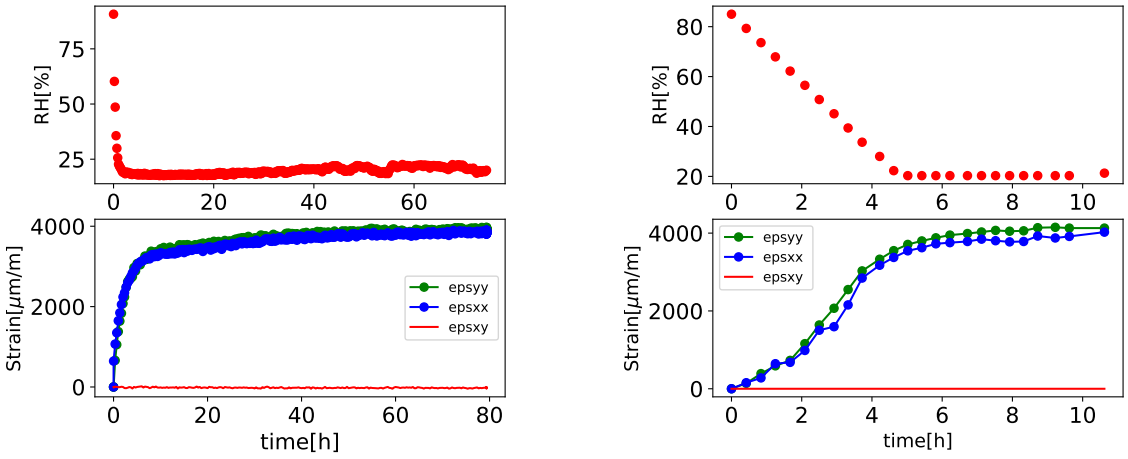

(a) DS-P2mm-CC-FD (b) DS-P2mm-ESEM-FD

Figure 2.15: Comparison of drying shrinkage measurement. (a) Climatic chamber and (b) ESEM

The amplitude of drying shrinkage reached when drying from 80% to 20% relative humidity is found to be 3940 µm/m for climatic chamber test (fig.2.15.a) and 4077 µm/m for ESEM test (fig.2.15.b); the difference between is only 147 µm/m. The comparison is very satisfactory and allows us to validate the experimental techniques.

2.5 Investigation of drying shrinkage

2.5.1 Effect of drying rate on drying shrinkage

Since the pioneering works of Pickett (1942), experimental investigations have shown that the kinetics of drying shrinkage depends on the drying rate, (Hansen, 1966; Hwang and Young, 1984). In fact, the specimen size or shape will influence the rate at which water moves toward the environment, and therefore will impact the rate of shrinkage. Yet, the open question is whether the final drying shrinkage level depends on the drying rate or equivalently on the size and shape of the structure.

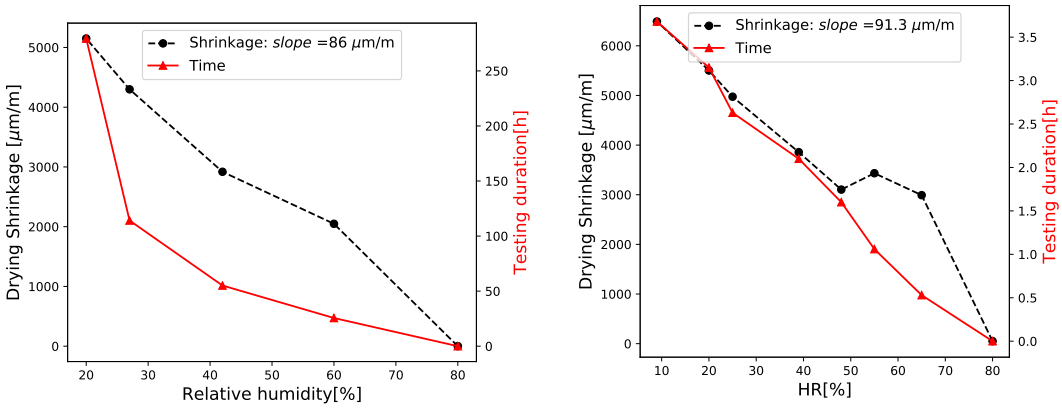

(a): DS-P500µm-CC-LCIs (b): DS-P2mm-ESEM-LCIs

Figure 2.16: Drying shrinkage coefficient assessment: effect of drying rate

In fig.2.16, the test duration is displayed with the change of drying shrinkage versus humidity. Despite the large difference in the rate of drying of fig.2.16. (a) (-15% relative humidity/hour) and fig.2.16.(b) (-0.24% relative humidity/hour), drying shrinkage seems to reach almost the same value at each relative humidity step. In this study, the drying shrinkage coefficient k_{sh} [-] (Eq.2.4) is assessed through different experiments conducted on specimen thickness 200 µm, 500 µm and 2000 µm (fig.2.17).

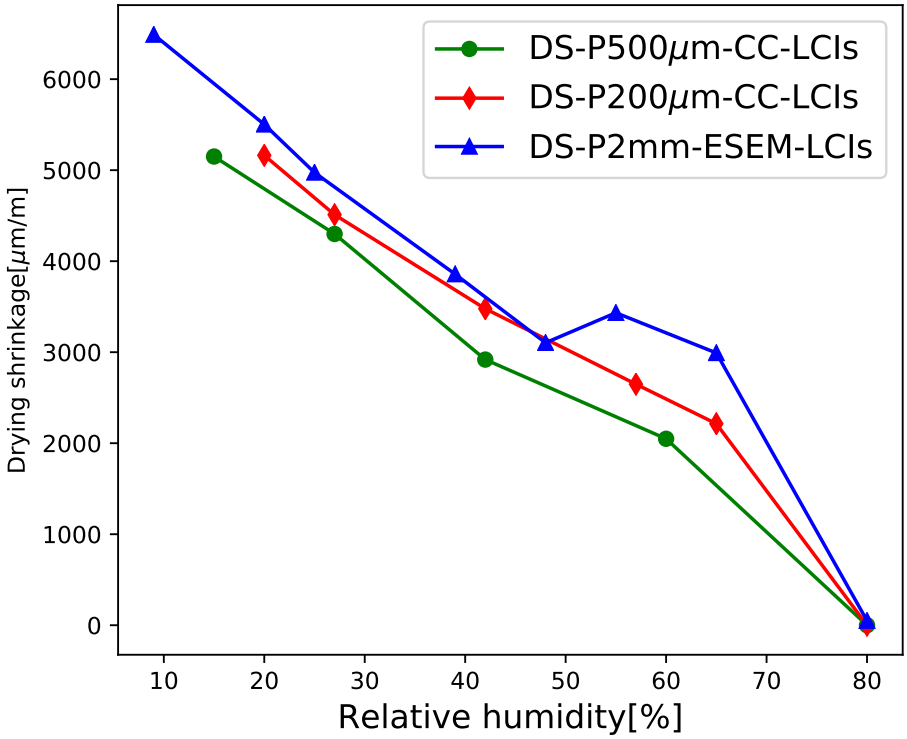

Figure 2.17: Drying length change assessed by DIC using two different systems: DS-P500µm-CC-LCIs specimen , k_{sh} = 8.5 10^{-5}; DS-P200µm-CC-LCIs, k_{sh} = 8.6 10^{-5}; DS-P2mm-ESEM-LCIs: ESEM, k_{sh} = 9.1 10^{-5}. More details on the tests are given in tab.2.4

$$\dot{\epsilon} = k_{sh}\dot{h} \tag{2.4}$$

where $\dot{\epsilon}$ [s^{-1}] is the rate of variation of drying shrinkage related to change of relative humidity $\dot{h}$ [s^{-1}].

These results show that drying shrinkage can be assumed to be proportional to relative humidity even for a large range of humidity (typically from 80%-20% RH). Let us assume that the drying shrinkage rate is proportional to the variation of humidity. The results on fig.2.17 shows that the drying shrinkage coefficient is almost the same regardless, of the specimen size, with a mean value of k_{sh} = 8.74 10^{-5}[-] where $\dot{\epsilon} = k_{sh}\dot{h}$.

The so-called drying shrinkage coefficient does not depend on the specimen size, at least from a material point of view.

In fig.2.17, the drying shrinkage curve of DS-P2mm-ESEM-LCIs exhibits a non-expected behavior between 50-60 % RH range. Such behavior has already been observed on Vycor 7930 Corning glass (Amberg and McIntosh, 1952) and reported in (Vlahinić et al., 2009). This behavior has been attributed to the morphology of the material. In this case, this behavior may be induced by the heterogeneity at the microscale level of cement paste. More investigation, both experimentally and numerically, would be needed to clarify this point.

RH [%]	Shape	Geomtry [mm]	Initial RH [%]	Drying thickness [mm]	Experiment	Drying shrinkage [$\mu m.m^{-1}$]
20	Cylinder	36×180	88%	18	DS-C18-SHC-RH20	5280
20	Prism	10×10×2	80%	2	DS-P2mm-ESEM-LCIs	5502
20	Prism	10×10× 0.5	80%	0.5	DS-P500µm-CC-LCIs	5150
20	Prism	10×10×0.2	80%	0.2	DS-P500µm-CC-LCIs	5160

Table 2.6: Comparison of the final drying shrinkage at equilibrium for experiments in tab.2.4 at 20 % RH

The undertaken study makes it also possible to compare drying shrinkage reached at 20% RH for different sizes and shapes of specimen and in different drying conditions. This comparison is displayed on tab.2.6.

From those results, fig.2.15, 2.17 and tab.2.6, our point of view is that for a given material, for a given relative humidity, at room temperature, the final drying shrinkage is independent of the rate of drying, at least on the cement paste level. This result is supported by other findings (Day et al., 1984; Hwang and Young, 1984; Bissonnette et al., 1999). It would be interesting to verify if the same conclusion stands at mortar and concrete levels since aggregates could induce cracking at the mesoscopic level in these materials compared to the cement paste. The answer to that question is of first importance for the prediction of structure delayed strain by modeling. At the concrete level, Campbell-Allen and Rogers (1975) found by analyzing the existing literature data that the assumption stating that the final drying shrinkage strongly depends on the specimen size is not well supported; but the only impacting factor is the skin cracking, which is likely to occur in massive structures. However, the depth of skin-cracks is negligible compared to the overall thickness of the structure. Moreover, most of the cracks would close upon the pres-stressing (in pre-stressed structures). So, for pre-stressed structures, the drying rate will not affect that much the final drying shrinkage. However, it would be useful to investigate further the skin cracking effect on drying shrinkage, especially on a laboratory scale (millimeter and centimeter-scale), since skin cracking would significantly affect the measurements.

2.5.2 Comparison with literature results

To the best knowledge of the authors, it is the first time that DIC has been used to investigate the drying shrinkage coefficient dependence on humidity range and rate of drying. Therefore, it is interesting to compare the present results to studies made in the past on similar materials with different measurement methods. The main characteristics of those tests compared to the ones performed in this chapter are summarized in tab.2.7.

Table 2.7: Experimental method of different experiment literature in comparison to the ones performed in this chapter

Parameters	Neubauer and Jennings	Baroghel-Bouny et al.	Maruyama et al.	DS-P2mm-ESEM-LCIs	DS-P200µm-CC-LCIs
$\frac{w}{c}$	0.5	0.34	0.55	0.525	0.525
Curing	Lime water	endogenous curing	Lime water	endogenous	endogenous
Curing Temp.	20	23	20	20	20
Drying thickness	1	1.5	0.5	1	0.1
Test Temp.	10	23	20	20	20
Age (d)	28	365	180	365	180
RH control	ESEM	Salt solution	TMA	ESEM	CC
Initial RH	80	90	90	80	80
Monitor system	DIC	dial gauges	LVDT	DIC	DIC

A brief description of each test is given below.

Experiment of Baroghel-Bouny et al. (1999) : performed drying shrinkage isotherm study on cement paste with w/c =0.34 through measuring the diameter length change for 1-year-old slice specimens by dial gauges with an accuracy of 1 µm.

Experiment of Maruyama et al. (2015) : performed short drying length variation test on ordinary cement paste with w/c =0.55. The relative humidity was controlled by a thermomechanical analyzer (TMA) associated with an RH generator (AXS TMA4000SA and HC9700, Bruker). The tested specimens were six months old, and the length change was monitored by LVDT (accuracy of 0.5 µm).

Experiment of Neubauer and Jennings (1997) : first test to investigate drying shrinkage of cement paste combining ESEM and Image matching technique. The authors used a small specimen of 10×10×2 mm geometry made of ordinary cement paste, similar to the tested sample for the ESEM test in the present chapter. Images of a field of view of 100 µm with a resolution of 512×512 pixels were taken. The test started at 80 % RH, and the specimen was kept at that RH for about 10 min before the first image was taken. Sequence images at 80%-60%-40%-20%-5% RH are taken with ten minutes between each. The testing temperature was 10°C.

Comparison

The desorption length changes result presented in fig.2.18 point out two ranges of RH, above and below 45% RH in agreement with the literature. In (Baroghel-Bouny et al., 1999), the authors found a change at 44% RH, and in (Maruyama et al., 2015), the change occurred at 40% RH. In the former range (45% <RH<80%), which corresponds to pore sizes between 20 and 50 Å, the driven mechanism is attributed to capillary pressure (Coussy et al., 2004). But for RH < 45 %, the capillary pores (larger than 20 Å are empty, the water phase is disconnected, and the C-S-H surface layers are covered by adsorbed water (Baroghel-Bouny et al., 1999). Therefore a drying shrinkage model accounting only for capillary effects will not be suitable for this humidity range. The model should also account for surface tension (Coussy et al., 2004; Maruyama et al., 2015). The key idea is that such a model should take into account at least two driving mechanisms (El Tabbal et al., 2020).

2.5.3 Potential application of the method

The behavior of large structures, such as large bridges or nuclear containment buildings, is mainly dependent on the evolution of drying shrinkage, especially in the long term. Common engineering practice is to use empirical formulas to extrapolate the final drying shrinkage based on short-term measurements, which may lead to large errors, especially when the test duration is far less than the time necessary to reach equilibrium (Dohnalová and Havlásek, 2020; Samouh et al., 2017). Yet, even on the laboratory scale, drying shrinkage assessment is difficult. It is very time-consuming because the drying of cement-based materials is a very slow process. Furthermore, the deformation phenomena are very dependent on factors such as material mix, geometry, size, and possible cracking due to hydric gradient for large specimen sizes. Therefore using specimens of small size in environmental controlled humidity seems to be an interesting idea. The experimental technique

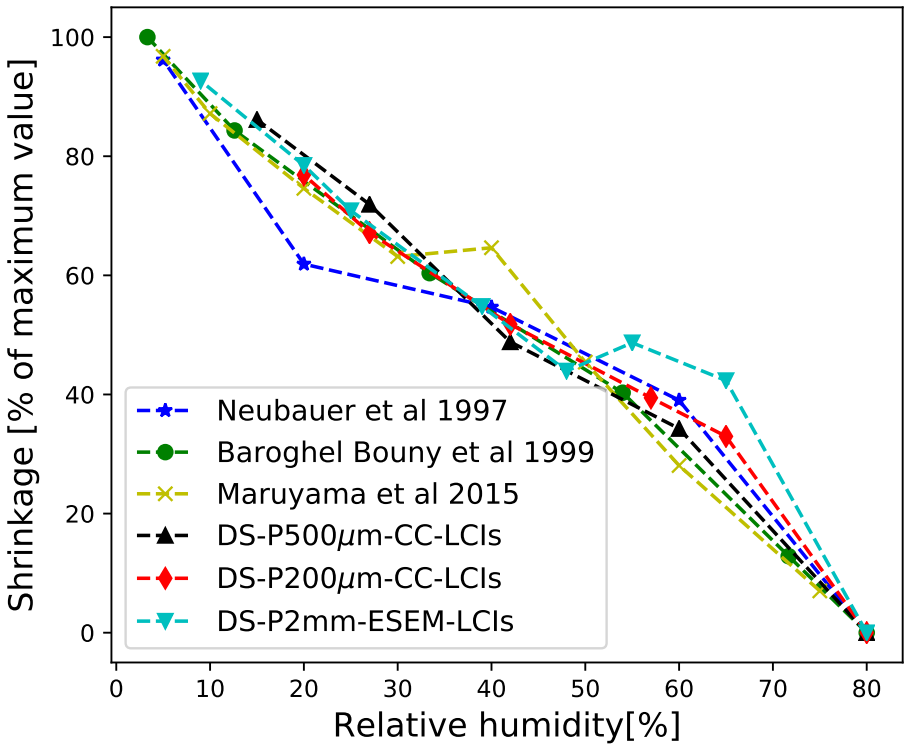

Figure 2.18: Drying Shrinkage [relative to maximum value] vs. relative humidity: data from experiments P500µm-CC-LCIs, DS-P200µm-CC-LCIs, and DS-P2mm-ESEM-LCIs; and from Neubauer and Jennings (1997), Baroghel-Bouny et al. (1999), Maruyama et al. (2015).

we developed combines the use of very thin specimens and DIC by taking advantage of different relative humidity control systems at our disposal. Using thin specimens to assess drying deformations has several advantages. First, it is possible to reach equilibrium for a given RH within a reasonable amount of time. Second, the thinner the specimen, the lower is the hydric gradient, and less cracking may occur.
This technique is intended to be applied in parallel with classical shrinkage tests described in (Maruyama et al., 2015; Baroghel-Bouny et al., 1999) so as to infer potential synergies of these different methodologies, particularly in view of the DIC technique filling gaps of information at size range in which classical shrinkage tests are not possible.

2.6 Conclusion

An alternative method for investigating drying shrinkage behavior based on DIC is proposed in this chapter:

1. we started by performing a sensitivity study to show the accuracy of DIC. The technique allowed us to reach an uncertainty level below 100 µm/m for relative humidities ranging from 80 % to 9% RH. The use of DIC also allowed for checking that the strains were uniform at the observation scale, which validated that a representative element volume had been obtained and crack was not present or diffuse.

2. The confrontation between the ESEM method and climatic chamber showed that the final value of drying shrinkage was the same regardless of the drying rate. The ESEM method presents the advantage of accelerating the drying process without inducing cracking.

3. By comparing the final drying shrinkage reached at 20 % RH, for two shapes (cylinder and prism) and various drying thicknesses (18, 1, 0.25, 0.1 mm), it was found that neither the specimen shape nor the rate of drying affected the final drying shrinkage. Furthermore, the results showed that drying shrinkage at equilibrium was linearly dependent on relative humidity. These findings are of first importance since they suggest that it is possible to build simple drying shrinkage models for concrete.

4. The length change isotherm of the studied cement paste was investigated, using ESEM and climatic chamber, both assisted by DIC. The results were compared to literature data, using more well-established drying shrinkage assessment methods. The comparison gives satisfactory results demonstrating that the developed technique was trustworthy. Last, the potential of the experimental technique developed was highlighted.

From these results, two perspectives are listed below:

- First, the results presented may help to testing or building delayed strain models for concrete structures, which are able to take into account the effect of rate of drying. This is a critical point when such models are used at the structure level because the experiments used in the lab to calibrate models exhibit much faster drying than that of structures. One possible way to tackle that goal is to predict drying shrinkage tests of specimen of large size with length change isotherm coefficient obtained by the method presented in this study. Moreover, via homogenization, drying shrinkage values at equilibrium for a given relative humidity can be upscaled from the cement paste to concrete (Xi and Jennings, 1997).

- Second, as it is carried herein for drying shrinkage, the effect of rate of drying on creep could also be investigated with the same approach. This will require the development of a mechanical compression system in a climatic chamber or ESEM. But the outcome will be very important from both fundamental and practical viewpoints. In fact, this will be an opportunity to investigate for a large range of relative humidity and for different drying rates the relationship between shrinkage and drying creep. Since the method made possible the assessment of drying shrinkage, free of skin cracking, the part of Pickett effect (Pickett, 1942) attributed to cracking will be avoided, and the study will focus on the intrinsic cause of drying creep. Should drying creep be predicted from drying shrinkage measurements as stated by (Day et al., 1984)? This study is currently undertaken.

References

P. Acker and F-J. Ulm. Creep and shrinkage of concrete: physical origins and practical measurements. *Nuclear Engineering and Design*, 203(2):143–158, 2001. 41

C. Amberg and R. McIntosh. A Study of Adsorption Hysteresis by Means of length changes of a rod of porous glass. *Canadian Journa of Chemistry*, 30:1012–1032, 1952. 59

V. Baroghel-Bouny, M. Mainguy, T. Lassabatere, and O. Coussy. Characterization and identification of equilibrium and transfer moisture properties for ordinary and high-performance cementitious materials. *Cement and Concrete Research*, 29:1225–1238, 1999. vi, 60, 61, 62

Z. P. Bažant, A. A. Asghari, and J. Schmidt. Experimental Study of creep of hardened concrete portland cement paste at variable water content. *Materials and Structures*, 1976. 41

F. Benboudjema. *Modélisation des déformations différées du béton sous sollicitations biaxiales.Application aux confinements des réacteurs des centrales nucléaires.* PhD thesis, Université de Marne la Vallée, 2002. 41

F Benboudjema, Fekri Meftah, and J-M Torrenti. A viscoelastic approach for the assessment of the drying shrinkage behaviour of cementitious materials. *Materials and Structures*, 40(2), 2007. 41

B. Bissonnette, P. Pierre, and M. Pigeon. Influence of key parameters on drying shrinkage of cementitious materials. *Cement and Concrete Research*, 1999. ISSN 00088846. doi: 10.1016/S0008-8846(99)00156-8. 60

D. Campbell-Allen and D.F. Rogers. Shrinkage of concrete as affected by size. *Matériaux et Construction*, 8(2):193–202, 1975. 60

L. Charpin, A. Courtois, F. Taillade, B Martin, B. Masson, and J. Haelewyn. Calibration of Mensi/Granger constitutive law: evidences of ill-posedness and practical application to VeRCoRs concrete. In *SMSS*, 2018. 42

O. Coussy, P. Dangla, T. Lassabatere, M. Mainguy, and V. Baroghel-Bouny. The equivalent pore pressure and the swelling and shrinkage of cement-based materials . *Cement and Concrete Research*, 2004. ISSN 00088846. doi: 10.1016/S0008-8846(99)00102-7. 61

R.L. Day, P. Cuffaro, and J.M. Illston. The effect of rate of drying on the drying creep of hardened cement paste. *Cement and Concrete Research*, 14(3):329–338, 1984. 41, 60, 63

C. De Sa, F Benboudjema, M. Thiery, and J. Sicard. Cement & Concrete Composites Analysis of microcracking induced by differential drying shrinkage. *Cement and Concrete Composites*, 30(10):947–956, 2008. ISSN 0958-9465. doi: 10.1016/j.cemconcomp.2008.06.015. 41

L. Dohnalová and P. Havlásek. Size effect on the ultimate drying shrinkage of concrete-Experimental evidence and engineering practice. In *Acta Polytechnica CTU Proceedings*, volume 26, pages 13–18, 2020. 61

G. El Tabbal, P. Dangla, M. Vandamme, M. Bottoni, and S. Granet. Modelling the drying shrinkage of porous materials by considering both capillary and adsorption effects. *Journal of the Mechanics and Physics of Solids*, page 104016, 2020. ISSN 0022-5096. doi: https://doi.org/10.1016/j.jmps.2020.104016. 61

M. Grediac and F. Hild. *Mesures de champs et identification en mécanique des solides*. Lavoisier, 2011. 50

A. Guery, F. Latourte, F. Hild, and S. Roux. Characterization of sem speckle pattern marking and imaging distortion by digital image correlation. *Measurement Science and Technology*, 25(1):015401, 2013. 42

W. Hansen. Influence of size and shape of memeber on the shrinkage and creep of concrete. *Journal of the American Concrete Institute*, 63(10):267–290, 1966. 58

F. Hild and S. Roux. CORRELI Q4 : A Software for "Finite-element" Displacement Field Measurements by Digital Image Correlation Internal report no. 269. Technical report, Laboratoire de Mécanique et de Technologie (LMT), Cachan, 2008. 49

C-L. Hwang and J.F. Young. Drying shrinkage of portland cement pastes i. microcracking during drying. *Cement and Concrete Research*, 14(4):585–594, 1984. 41, 58, 60

D. Jankovic. Nondestructive determination of drying deformations in cement paste by means of esem and digital image analysis, optical micro-and nanometrology in microsystems technology ii. *Proceedings of SPIE Europe photonics Europe*, pages 7–10, 2008. 42

S. Maraghechi, J. P. M. Hoefnagels, R. H. J. Peerlings, O. Rokoš, and M. G. D. Geers. Correction of Scanning Electron Microscope Imaging Artifacts in a Novel Digital Image Correlation Framework. *Experimental Mechanics*, 2019. ISSN 17412765. doi: 10.1007/s11340-018-00469-w. 42, 50

I. Maruyama, G. Igarashi, and Y. Nishioka. Bimodal behavior of C-S-H interpreted from short-term length change and water vapor sorption isotherms of hardened cement paste. *Cement and Concrete Research*, 73:158 – 168, 2015. vi, 60, 61, 62

J.P Mathieu, L. Charpin, P. Sémété, C. Toulemonde, G.H.J. Boulant, and F. Taillade. Temperature and humidity-driven ageing of the VeRCoRs mock-up. In *Computational Modelling of Concrete and Concrete Structures*, 2018. 42

T. Mauroux, F. Benboudjema, P. Turcry, A. Aït-Mokhtar, and O. Deves. Study of cracking due to drying in coating mortars by digital image correlation. *Cement and Concrete Research*, 2012. ISSN 00088846. doi: 10.1016/j.cemconres.2012.04.002. 41

A. Morandeau, M. Thiery, and P. Dangla. Investigation of the carbonation mechanism of CH and C-S-H in terms of kinetics, microstructure changes and moisture properties. *Cement and Concrete Research*, 2014. ISSN 00088846. doi: 10.1016/j.cemconres.2013.11.015. 41

C. M. Neubauer and H. M. Jennings. Drying shrinkage of cement paste as measured in an environmental scanning electron microscope and comparison with microstructural models. *Journal of Materials Science*, 32:6415–6427, 1997. vi, 60, 61, 62

C. M. Neubauer and H. M. Jennings. Use of digital images to determine deformation throughout a microstructure part ii: Application to cement paste. *Journal of Materials Science*, 35(22):5751–5765, 2000. 41

C. M. Neubauer, E. J. Garboczi, and H. M. Jennings. Use of digital images to determine deformation throughout a microstructure Part I. Deformation mapping technique. *Journal of Materials Science*, 2000. ISSN 00222461. doi: 10.1023/A:1004874911909. 41, 42

V. G. Papadakis, C. G. Vayenas, and M. N. Fardis. A reaction engineering approach to the problem of concrete carbonation. *AIChE Journal*, 1989. ISSN 15475905. doi: 10.1002/aic.690351008. 41

G. Pickett. The effect of change in moisture-content on the crepe of concrete under a sustained load. In *Journal Proceedings*, volume 38, pages 333–356, 1942. 58, 63

H. Samouh, E. Rozière, and A. Loukili. Influence of specimen size and measurements duration on the long-term extrapolation of drying shrinkage. *Construction and Building Materials*, 150:276–286, 2017. 61

H. Samouh, E. Rozière, and A. Loukili. Experimental and numerical study of the relative humidity effect on drying shrinkage and cracking of self-consolidating concrete. *Cement and Concrete Research*, 2019. ISSN 00088846. 41

M. A. Sutton, N. Li, D. Garcia, N. Cornille, J. J. Orteu, S. R. McNeill, H. W. Schreier, X. Li, and A. P. Reynolds. Scanning electron microscopy for quantitative small and large deformation measurements Part II: Experimental validation for magnifications from 200 to 10,000. *Experimental Mechanics*, 47(6):789–804, 12 2007a. 50

M. A. Sutton, J. J. Orteu, and H. Schreier. *Image correlation for shape, motion and deformation measurements: basic concepts, theory and applications*. Springer Science & Business Media, 2009. 50

M.A. Sutton, N. Li, D.C. Joy, A.P. Reynolds, and X. Li. Scanning electron microscopy for quantitative small and large deformation measurements part i: Sem imaging at magnifications from 200 to 10,000. *Experimental mechanics*, 47(6):775–787, 2007b. 42

M. Thiery, G. Villain, P. Dangla, and G. Platret. Investigation of the carbonation front shape on cementitious materials: Effects of the chemical kinetics. *Cement and Concrete Research*, 2007. ISSN 00088846. doi: 10.1016/j.cemconres.2007.04.002. 41

R. Thion, S. Huang, L. Charpin, and J. Sanahuja. 6125-2104-2018-01576-FR-Procédure de fabrication de matériaux cimentaires VeRCoRs au labo GC. Tech. rep., R&D MMC. Technical report, EDF R&D, 2019. 43

Z. Tomičević, F. Hild, and S. Roux. Mechanics-aided digital image correlation. *The Journal of Strain Analysis for Engineering Design*, 48(5):330–343, 2013. 49

I. Vlahinić, H. M. Jennings, and J.J Thomas. A constitutive model for drying of a partially saturated porous material. *Mechanics of Materials*, 41(3):319–328, 2009. 59

Y. Xi and H.M. Jennings. Shrinkage of cement paste and concrete modelled by a multiscale effective homogeneous theory. *Materials and Structures*, 30:329–339, 1997. 63

Chapter 3

Experimental and numerical investigation of drying. Surface exchange effects, impact on drying shrinkage

3.1 Motivation for the study

The durability of major pre-stressed structures such as nuclear power plants or large bridges has been a critical topic for many years (Acker and Ulm, 2001; Bendboudjema, 2002; Charpin et al., 2018; Bažant and Jirásek, 2018). Since the durability of such structures strongly depends on the level of pre-stress, every phenomenon causing changes of the pre-stress level should be studied. The first of these phenomena is drying (Bažant et al., 1976; Bazant and Chern, 1985; Hansen, 1987; Baroghel-Bouny et al., 1999; Baroghel-Bouny, 2007; Cagnon et al., 2015; El Tabbal et al., 2020) since it is the primary source of drying shrinkage and drying creep that are essential phenomena occurring in such large structures (Granger, 1995; Bendboudjema, 2002; Foucault et al., 2012; Jirásek and Havlásek, 2014; Sellier et al., 2016; Ishida and Tiao, 2018; Rahimi-Aghdam et al., 2019). The modeling viewpoint adopted in this study is a staggered thermo-hydro-mechanical model (Bendboudjema, 2002; Hilaire, 2014; Soleilhet, 2017; Sleiman et al., 2020), which makes it possible to study the thermal behavior in a first step. In a second step, drying is computed using thermal results as input. In the final step, both fields feed in the mechanical calculation. In this chapter, the temperature is assumed to be constant and equal to room temperature. Thus, the prediction accuracy of mechanical calculations will strongly depend on the drying properties (Benboudjema and Torrenti, 2012; Di Bella et al., 2017). We focus here on the intrinsic behavior without cracking due to drying shrinkage gradients. Therefore, a progressive decrease of relative humidity is applied. Moreover, since drying shrinkage occurs only in the cement paste (except in the case where lightweight aggregates are used), experimental studies focus on the cement paste.

The first part of this chapter focuses on the investigation of drying both from experimental and numerical viewpoints. The water desorption isotherm of the studied material is measured and used as input for the drying model. The parameters of the drying model are identified and used for the prediction of mass loss of specimens of various sizes under different drying conditions. In the case of specimens with small thickness, the surface moisture transfer coefficient is carefully examined to ensure it could be calibrated independently of drying model bulk parameters. The unknown that has been chosen to study the drying process is the saturation degree. Herein, the Richards-Fick drying model was chosen to model the drying process (Sleiman et al., 2020). In the second part of the chap-

ter, drying shrinkage is studied after the calibration of the drying model. Drying shrinkage is considered to be proportional to the variation of pore relative humidity (Wittmann and Roelfstra, 1980; Benboudjema and Torrenti, 2012; Bažant and Jirásek, 2018; Menu et al., 2018).

3.2 Experimental method

3.2.1 Material

Details on the studied material were reported in Section.2.2.1.

3.2.2 Measurements of mass loss

Four distinct mass-loss experiments were performed:

- Cylinder ⌀36 mm diameter exposed to 50% RH in a large room, where humidity was controlled by a Circulated Air Conditioning (CAC) system.
- Cylinders ⌀36 mm in diameter exposed to drying, at 20-58-80 % relative humidity, imposed by saturated saline solutions in small hermetic chambers (humidity was not constant but slowly decreased from an initial value close to the sample initial internal RH, to the target value imposed by the Saturated Saline Solution (SSS). This protocol reduces the risk of cracking by drying shrinkage gradient. Mass loss of these cylinders was recorded using a balance of type of KERN with 6200 g capacity and with a precision of 0.1 g.
- Prism of 1×10×10 mm geometry, drying at different humidities step using Dynamic Vapor System (DVS). A digital microbalance with 1 g total capacity and 0.1 µg of precision is used.
- Prism of 0.5×10×10 mm size, drying at different humidity steps controlled by a Climatic Chamber (CC). A Mettler Toledo balance type with 220 g of total capacity and 0.01 mg of precision is used.

3.2.3 Measurement of desorption isotherm

Desorption isotherms are fundamental for the quantification and prediction of the behavior of the material subjected to drying. By definition, it is the water content vs. RH curve. For the last decades, a lot of efforts had been made to characterize it using different techniques with the intent to make it faster and more accurate. Different techniques exist, such as saturated salt solutions (Baroghel-Bouny et al., 1999; Baroghel-Bouny, 2007), volumetric method (Maruyama et al., 2014), Dynamic Vapor Sorption method (Poyet et al., 2016).

In this study, the desorption isotherm measurement was performed on cement paste using (i) powder obtained by hand grinding and (ii) on Prism of 1×10×10 mm, both from cylinder specimens of 6 months age cured under endogenous conditions. The dynamic Vapor Sorption (DVS) method was used, and the tests were carried out at a temperature of 25°C. This method is quick and has shown to provide compatible results with classical methods such as saturated water solutions of desiccators or climatic chambers (Garbalinska et al., 2017; Simon et al., 2017). Moreover, the results obtained from powder and from the slab of 1 mm in thickness are similar (fig.3.1)

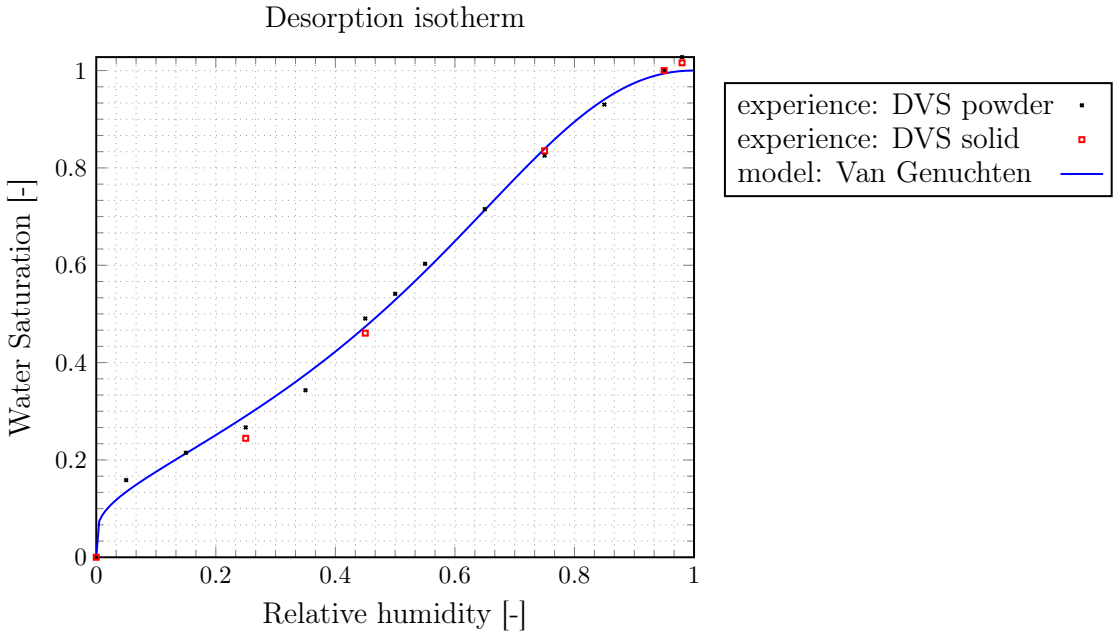

Figure 3.1: Experimental desorption isotherm of the studied cement paste ($w/c = 0.52$) and numerical fit using Van Genuchten's model ($a = 6.131\ 10^7$ Pa , $b = 0.512$)

3.2.4 Measurement of drying shrinkage

The drying shrinkage measurements were performed by Digital Image Correlation or by LVDT probes:

- Shrinkage tests in salt solutions (C18-SS-RH20, C18-SS-RH58, C18-SS-RH80): axial strain was monitored using three LVDT (Linear Variable Differential Transformer) sensors installed at 120°. The measurement was made on a 10.8 cm basis (Huang, 2018; Kinda et al., 2021).

- Shrinkage tests in ESEM and climatic chamber (P2mm-ESEM-FD, P500µm-CC-LCIs, P2mm-CC-SD): Image are acquired all along with the test duration and analyzed by DIC. For ESEM tests, a backscattered electron (BSE) imaging mode was used, while for the latter, a classical optical camera was used. The images are then post-processed by DIC (Hild and Roux, 2008) to assess strains (Mauroux et al., 2012; Kinda et al., 2021).

3.2.5 Summary of experimental campaigns and global strategy for numerical study

The abbreviations used to describe the experiment throughout this chapter are listed in tab.3.1.

The experimental campaign is summarized on tab.3.2.

Table 3.1: Acronyms used to describe specimen geometry and experimental condition

DS	Drying Shrinkage
P2mm	Prism of 2 mm thickness
P500 µm	Prism of 500µm thickness
C36mm	Cylinder of 36 mm diameter
CC	climatic chamber
SS	Salt Solution[1]
SD	Slow Drying
FD	Fast Drying
LCIs	Length Change Isotherm
RH20	20% Relative humidity

Table 3.2: Summary of experimental campaign undertaken on cement paste. DS = Transient Drying Shrinkage; LCI = Length Change Isotherm. SS = Saturated Solution. DVS =Dynamic Vapor Sorption. CAC= Circulating Air Conditioning

Test	Geometry (mm)	mass	DS	LCI	system
P2mm-ESEM-FD	10×10×2	-	✓	-	ESEM
P1mm-DVS	10×5×1	-	✓	-	DVS
P500µm-CC-LCIs	10×10×0.5	-	✓	✓	CC
P2mm-CC-SD	10×10×2	✓	✓	-	CC
C18-SS-RH80 %	36×180	✓	✓	-	SS
C18-SS-RH58 %	36×180	✓	✓	-	SS
C18-SS-RH20 %	36×180	✓	✓	-	SS
C18-CAC-RH50 %	36×180	✓	✓	-	CAC

3.3 Model for drying of cementitious materials

Drying of cementitious materials is a very complex phenomenon, involving permeation, diffusion, adsorption-desorption, and condensation-evaporation (Mainguy, 1999; Mainguy et al., 2001; Thiery et al., 2007). The model used herein is the Richard-Fick proposal accounting for permeation of liquid and diffusion of water vapor in the porous network of the material (Hilaire, 2014; Soleilhet, 2017), using the saturation degree as a primary variable (Sleiman et al., 2020). The main mass balance equation reads Eq.3.1

$$\frac{\partial S_l}{\partial t} = \nabla(D(S_l)\nabla S_l) \tag{3.1}$$

where D is the global diffusion coefficient depending non-linearly on liquid water saturation degree (S_l) named saturation hereafter. Under the assumption of constant gaz pressure, the global diffusion coefficient is given by :

$$D(S_l) = \frac{1}{\left(1-\frac{\rho_v}{\rho_l}\right)}\frac{\partial P_c}{\partial S_l}\left[\frac{K^{eff}(S_l)}{\phi\mu_l} + D^{eff}(S_l)\left(\frac{M_v}{\rho_l RT}\right)^2 P_{vsat}\exp\left(P_c\frac{Mv}{\rho_l RT}\right)\right] \tag{3.2}$$

with $\varnothing$ the porosity of the material, K^{eff} the effective permeability of the liquid, D^{eff} the effective gas diffusion coefficient, P_c the capillary pressure. ρ_l, ρ_v, μ_l are respectively the density of the liquid and gas, the dynamic viscosity of the liquid. T is the temperature, and R the perfect gas constant. P_{vsat} and M_v are respectively the saturating vapor pressure and the water molar mass.

The first term in Eq.3.2 represents the liquid permeation mechanism and the second term accounts for vapor diffusion. The former is dominant when saturation is high, while

the latter becomes predominant at lower saturation (Mainguy et al., 2001; Thiery et al., 2007). This observation will be helpful in building the strategy for model identification. In fact, whenever possible, the parameter related to liquid permeation will be identified on mass loss of specimen exposed to high humidity, typically above 50% RH; and the ones dealing with vapor diffusion should be identified on experiments performed at lower humidity, typically below 30% RH. Studies in the literature (Baroghel-Bouny et al., 1999; Maruyama et al., 2015) provide the clear fact that a transition zone exists between the two mechanisms, but the relative humidity at which one mechanism becomes more dominant than another makes no consensus in the literature. This point will be discussed later in this chapter based on simulation results.

The effective permeability K^{eff} decreases when saturation diminishes. It can be split into the product of two functions $K^{eff}(S) = K_0 k_{rl}(S)$ (Hilaire, 2014): a constant parameter, denoted K_0, which is the intrinsic permeability of the material at full saturation, to be identified by inverse analysis on mass loss experiment; and the relative permeability k_{rl} , given by the Van Genuchten relation (Mualem, 1976),

$$k_{rl} = S_l^{n_k}\left(1-(1-S_l^b)^{1/b}\right)^2 \tag{3.3}$$

where n_k is an empirical parameter accounting for the morphology of the material pore network to be identified by inverse analysis on mass loss. The second parameter b is the same as used in Van Genuchten's model for the desorption isotherm.

$$P_c(S_l) = a[S_l^{-b}-1]^{1-1/b} \tag{3.4}$$

The gas diffusion D_{eff} dependence on the saturation coefficient is given by Millington's empirical relationship, (Thiery et al., 2007), and and reads Eq.3.5.

$$D^{eff}(S_l) = D_0.\phi^{amq}(1-S_l)^{bmq} \tag{3.5}$$

where a_{mq} is interpreted as a reduced porosity to enhance the fact that air movement within the material encounters more resistance than in case of free diffusion in the open air for a given temperature. a_{mq} is to be identified by inverse analysis of mass loss of specimen drying preferably below 20% RH while b_{mq} and D_0 are set respectively to 4.2 and 10^{-5} m^2/s (Thiery et al., 2007).

To solve the differential equation of drying, the boundary condition of Neumann Eq.3.6 or of Dirichlet, Eq.3.7 is imposed depending on the drying conditions (more details will be given hereafter).

$$j_{x^-} = C_s(S_s - S_e) \tag{3.6}$$

$$S_s = S_e \tag{3.7}$$

Where j_{x^-} $[kg/m^2/s]$ is the moisture flux toward the environment; S_s and S_e are respectively the vapor saturation of the specimen surface and that of surrounding air; C_s $[kg/m^2/s]$ the surface exchange coefficient.

3.4 Numerical simulation of drying: model identification, prediction and size effect

3.4.1 Mesh and Boundary conditions

The meshes used for the simulations are presented in fig.5.2.

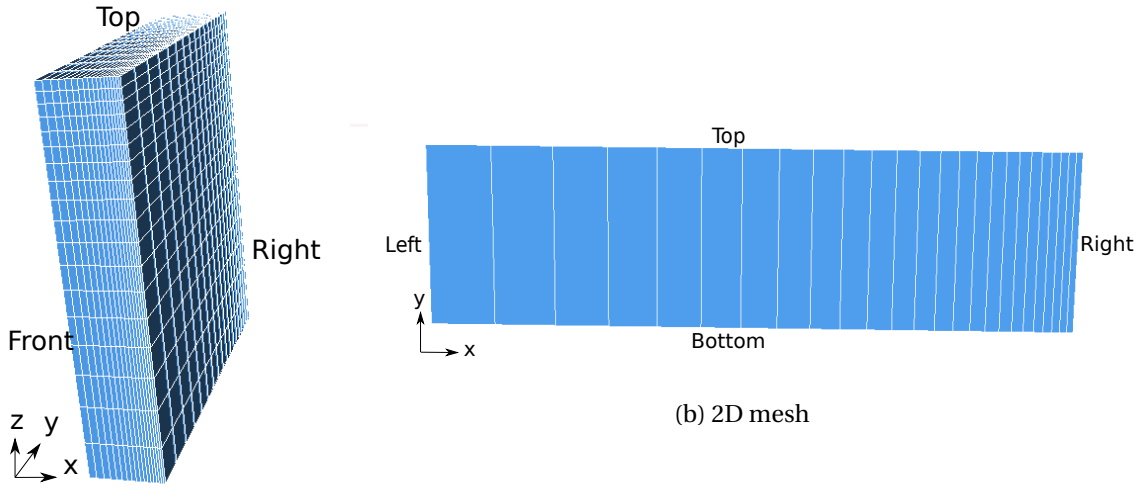

(a) 3D mesh

(b) 2D mesh

Figure 3.2: Mesh for drying and drying shrinkage simulations

An axisymmetric configuration for cylinders and 1/8 for prismatic samples was used. The discretization and the boundary conditions are presented in fig.5.2 and tab.5.3. Note that a fine mesh was considered at each drying face of the samples.

Table 3.3: Boundary conditions. DSF = Drying Surface, ND = Non Drying Surface.

Face	3D	2D
Top	ND	ND
Bottom	ND	ND
Left	ND	ND
Right	DSF	DSF
Front	ND	
Back	DSF	

3.4.2 Simulation strategy

The way these experiments are used in our simulations in order to fulfill the objectives of the study is as follow:

- C18-CAC-RH50: identification of liquid permeation parameters n_k (Eq.3.3) and K_0 of Richard model
- C18-SS-RH20: identification of vapor diffusion parameter a_{mq} (Eq.3.5) of Fick model and the exchange coefficient C_s (Eq.3.6).
- C18-SS-RH80, DS-C18-SS-RH58, P1mm-DVS: validation of drying model identification by predicting mass loss
- P500µm-CC-LCIs: determination of drying shrinkage coefficient of the studied material
- P2mm-ESEM-FD, DS-P2mm-CC-SD, DS-C18-SS-RH80, DS-C18-SS-RH58: validation of drying and shrinkage model parameters by predicting drying shrinkage for different sizes and rates of drying.

3.4.3 Identification of desorption isotherm

Isotherm: from experimental measurement to data for simulations

For finite element simulation purposes, one needs to move from experimentally measured water content to an equivalent humidity or saturation, depending on the primary variable needed in drying calculations. Given the drying model, which will be described hereafter, the water content in desorption experiments was converted to saturation. It was achieved by dividing the water content at equilibrium for a given relative humidity by the one at the maximum humidity (max RH) (not necessarily the saturated state). This point is a critical step because the desorption isotherm, in the end, will strongly depend on the chosen max RH. This max RH should be close to 1 as much as possible, with the highest possible confidence on the corresponding water content, which in turn depends on the measurement technique. We have decided to use 95% as max RH, which corresponds to the starting humidity step in our experiment in the DVS apparatus. Measurements performed on powders and solids give very similar results, fig.3.1.

Fit of desorption curve

First, parameters a and b of capillary pressure (Eq.3.4) were identified successfully and the results are displayed in fig. 3.1. These parameters are used as input to feed the drying simulation. Let us note that, given the fact that the humidity at full saturation is set to 95%, the saturation corresponding to a relative humidity of 100% is slightly greater than 1 due to the use of max RH (the saturation is a relative parameter).

3.4.4 Identification of drying parameters

The fixed parameters in drying simulations are reported on tab.3.4 while the identified parameters are presented in tab.3.5.

Table 3.4: Fixed parameters of drying model

ϕ[−]	ρ_{paste} [kg/m^3]	S_{init} [-]	bmq [-]	P_{vsat} [Pa]	μ_l [Pa.s]	ρ_l [kg/m^3]	ρ_v [kg/m^3]	T [K]	D_0 [$m^2.s^{-1}$]
0.465	1870	0.99	4.2	3062	0.001	1000	0.018	293	10^{-5}

Table 3.5: Identified parameters of drying model

K [m^2]	n_k[−]	a_{mq} [-]	C_s [$kg.m^{-2}.s^{-1}$]
1.02 10^{-21}	2.52	5	3.6 10^{-9}

Liquid permeation parameters

Second, parameters n_k and K_0 of the liquid permeation term in Eq.3.2 are identified using test DS-C18-CAC-RH50 of tab.3.2; and Dirichlet boundary coefficient. In fact, the air velocity around the sample in this experiment was high enough to allow for instantaneous evaporation of vapor at the sample surface; therefore, imposing a constant saturation condition at the surface or adopting a very large exchange coefficient is more adapted in this situation. The comparison between experiment and simulation is presented in fig.3.3, showing that the result is trustworthy.

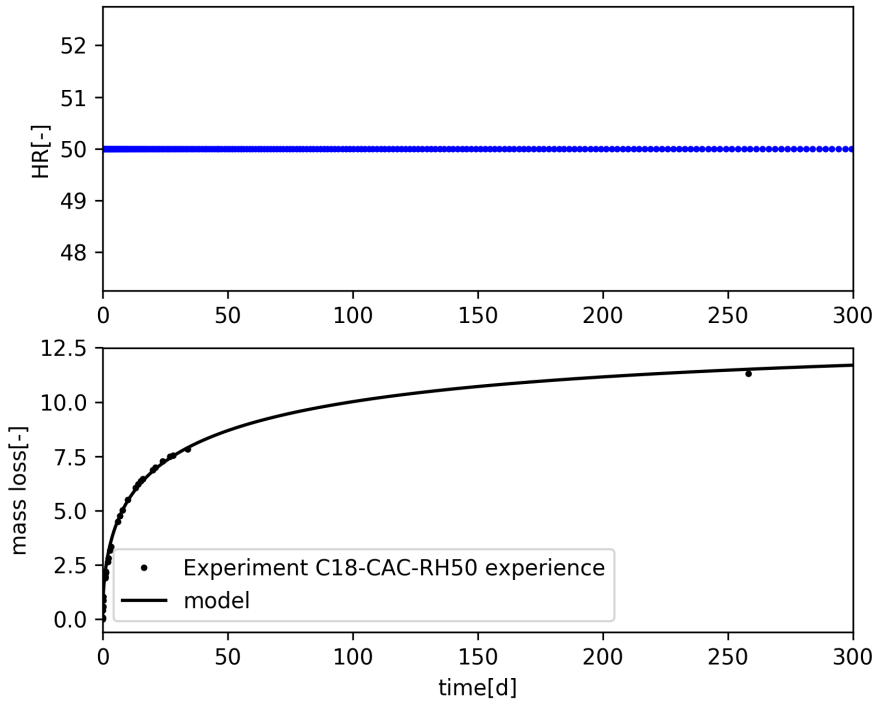

Figure 3.3: Identification of intrinsic water permeability $K_0 = 1.02 \times 10^{-21}$ m^2 and the tortuosity parameter of Van Genuchten's relationship $n_k = 2.52$ on experiment DS-C18-CAC-RH50 (tab.3.2) performed at 20° C and 50% of humidity in free air.

Vapor diffusion parameters

Last the parameter a_{mq} of the vapor diffusion term of Eq.3.2 is identified thanks to experiment DS-C18-SS-RH20 presented on tab.3.2. A type of Neumann boundary conditions was used for this experiment, which means to identify a supplementary term, called C_s. Results displayed in fig.3.4 demonstrate that the identification is trustworthy.

3.4.5 Scaling potential

Since models are usually calibrated on laboratory tests and then used to predict the behavior at the structural level, the scaling potential of the drying model is tested. The same parameters identified in the previous section are used to predict drying moisture loss for different specimen sizes and different drying conditions.

First, the prediction accuracy for different humidity levels is studied through the simulation of experiments C18-SS-RH80 and C18-SS-RH58 of tab.3.2. The numerical results are compared to experimental observations in fig.3.5, and the agreement is very satisfactory.

The rate of mass loss of test C18-SS-RH20 is also well captured (calibration was on 140 days while validation is performed over 200 days). Using the identified exchange coefficient for Neumann boundary conditions along with the Richards model (water permeation) shows us that the kinetics of mass loss is underestimated even if the "final mass loss" is well captured as expected (fig.3.6). Therefore, the exchange coefficient is only a reflection of the indoor drying conditions, not the specimen size nor the model.

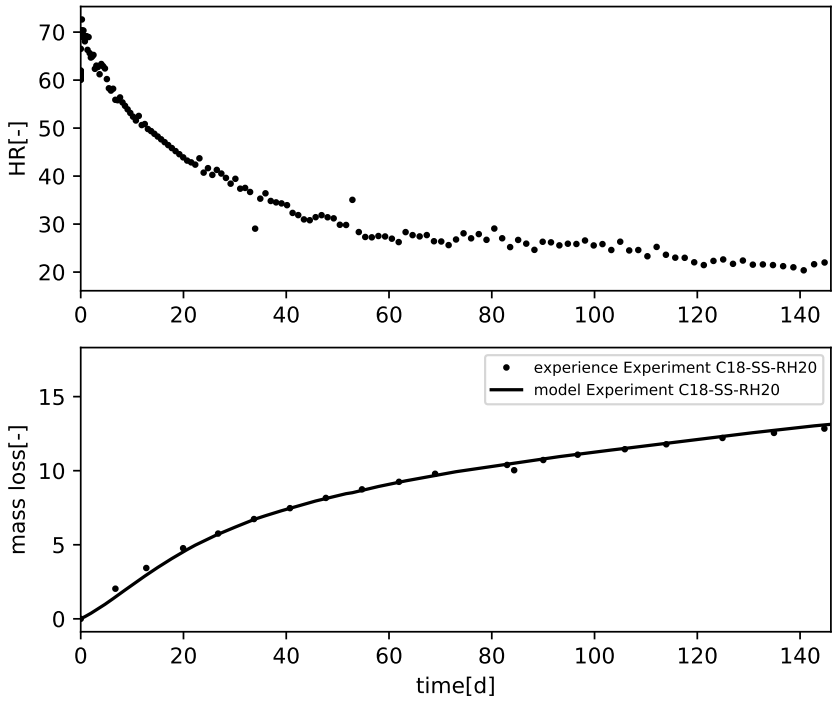

Figure 3.4: Experimental result of test DS-C18-SS-RH20 of tab.3.2 and numerical comparison. Impact of using identified surface exchange coefficient $C_s = 3.6 \times 10^{-9} [kg/m^2/s]$ and vapor diffusion parameter $a_{mq} = 5[-]$.

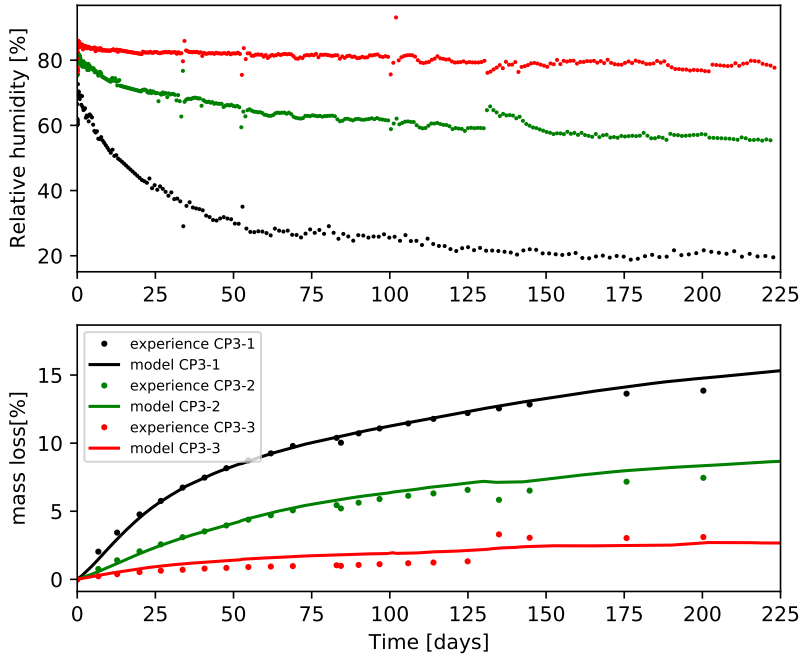

Figure 3.5: Prediction of mass loss of 36 × 180 mm cylinders, drying at different relative humidity levels (experiments C18-SS-RH80, C18-SS-RH58 and C18-SS-RH20). Only the first 140 days data from C18-SS-RH20 was used in model identification.

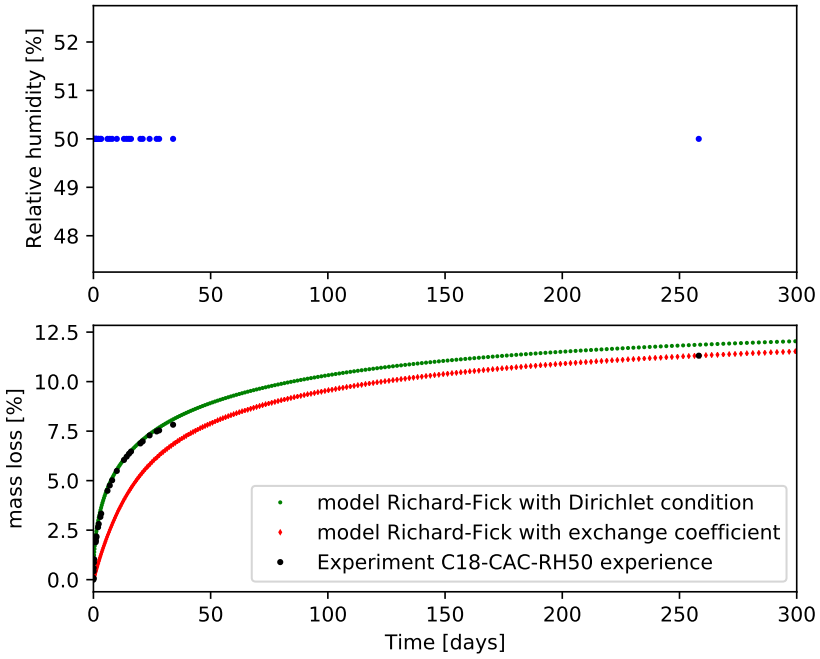

Figure 3.6: Simulation of the experiment DS-C18-CAC-RH50 using the complete Richards-Fick model with the two types of boundary conditions: Dirichlet (without exchange coefficient) and Neumann (with the identified exchange coefficient)

Second, the accuracy of the model to predict size effects is tested. For that purpose, experiment P1mm-DVS performed on a slab of 1. mm in thickness (see more description on tab.3.2) is simulated successfully. The result in fig.3.7 shows a good agreement with the experiment.

An attempt to predict the moisture loss response of prismatic of 0.5 mm thick sample drying in a climatic chamber, referred to as test P500µm-CC-LCIs on tab.3.2 was conducted, and the overall trend of mass loss is well captured (fig.3.8).

3.4.6 Prediction of drying saturation profile - effect of surface exchange

The prediction of the saturation profiles of the tests on ⌀36 × 180 mm cylinders is shown in fig.3.9. It is seen that if surface humidity is imposed slowly enough (fig.3.5), the saturation profiles are almost flat, as in the case of fig.3.9-(a-b). On the contrary, when the relative humidity is imposed rapidly on the surface (fig.3.3), the hydric gradients between the core and the surface of the sample are very strong, especially in the first moments of exposure as shown in fig.3.9-(d). For an intermediate drying rate level, the gradients are less pronounced fig.3.9-(c).

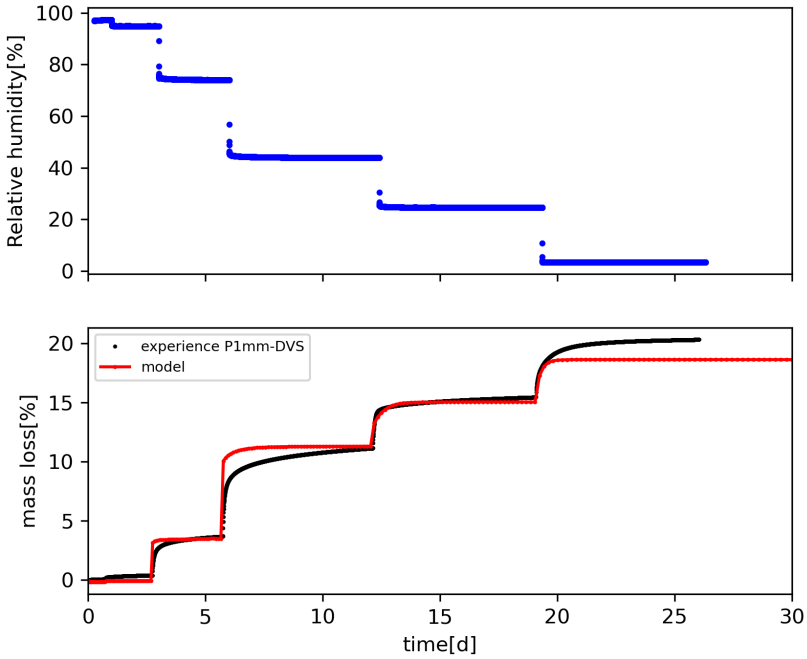

Figure 3.7: Prediction of mass loss of small prism (P1mm-DVS experimentm) of 1 mm drying thickness using the identified models.

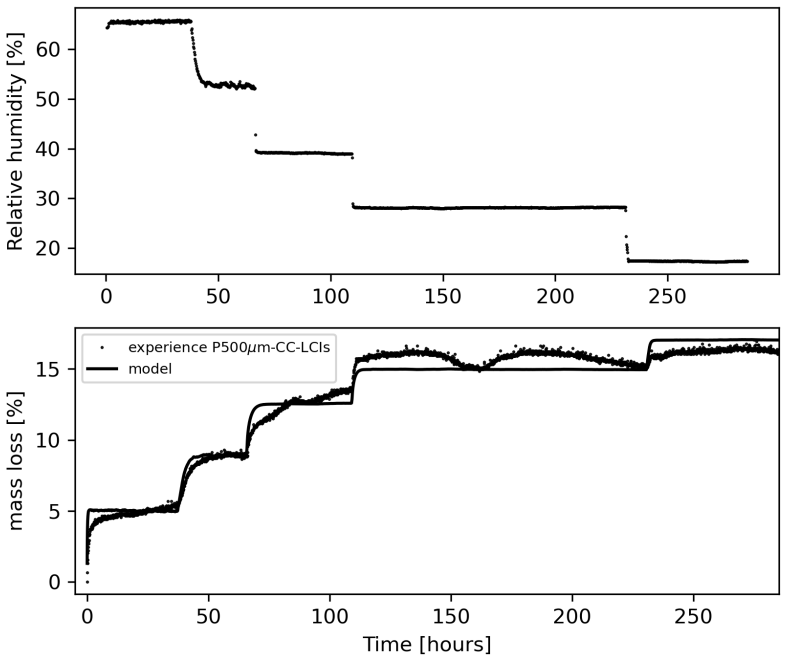

Figure 3.8: Prediction of mass loss of small prism ($10 \times 10 \times 0.5$ mm) with 0.25 mm drying thickness using the parameters identified above

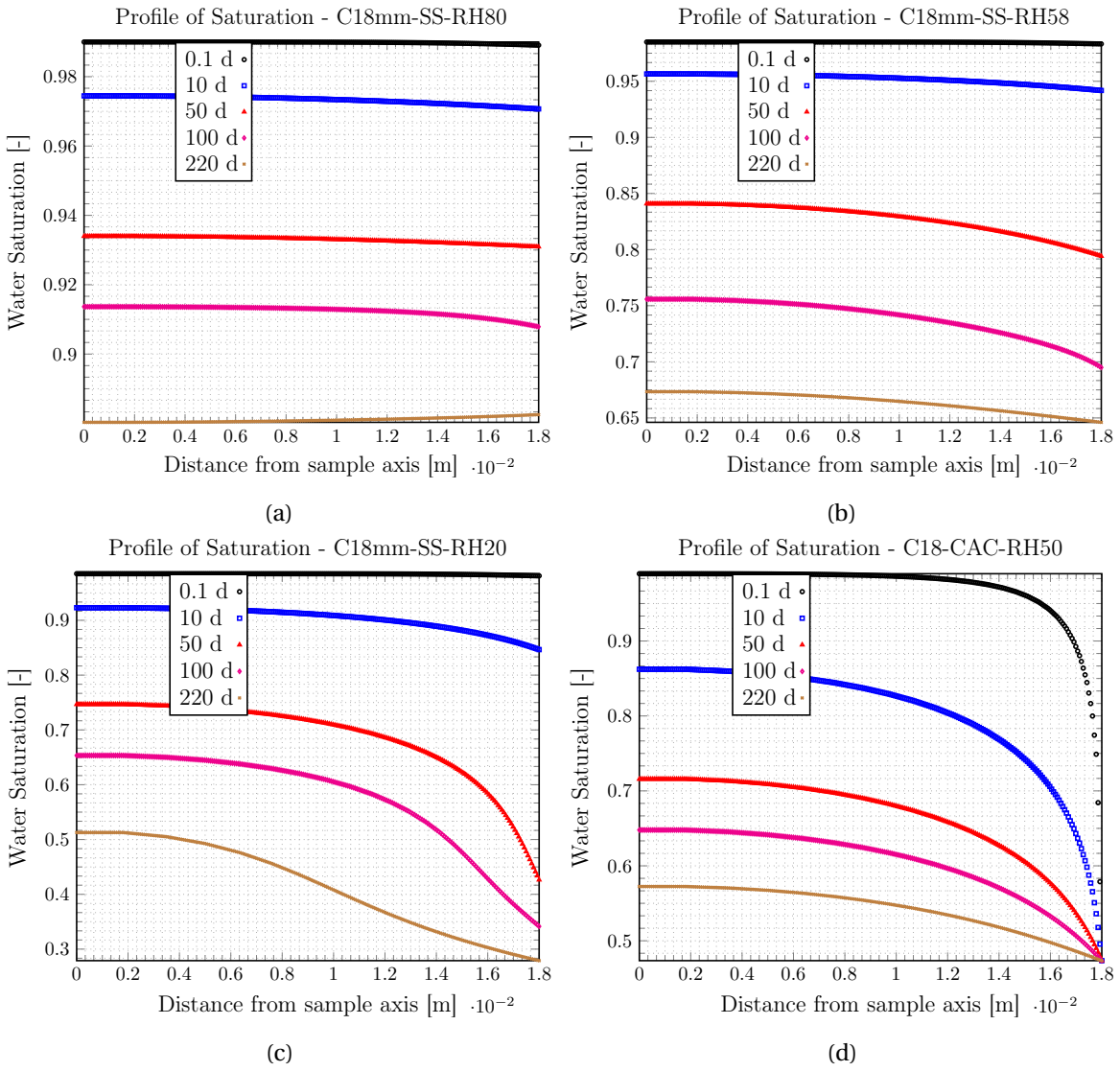

Figure 3.9: Evolution of water saturation profiles of cylindrical, ⌀36 × 180 mm specimen (tests C18mm-SS-RH80, C18mm-SS-RH60, C18mm-SS-RH20 and C18-CAC-RH50)

3.4.7 Discussion on model identification

The drying process was modeled using the Richards-Fick model to account for liquid permeation and vapor diffusion (Mainguy et al., 2001; Thiery et al., 2007; Hilaire, 2014; Soleilhet, 2017; Sleiman et al., 2020). Three parameters of the model and additionally surface factor were successfully identified using two experiments (DS-C18-CAC-RH50 and DS-C18-SS-RH20). The identification strategy consists of identifying the parameters of liquid permeation on experimental mass loss of DS-C18-CAC-RH50 test, and the one related to vapor diffusion thanks to DS-C18-SS-RH20 results. The model was used to predict the mass loss of specimen 1. mm in thickness (P1mm-DVS), presented in fig.3.7; and the one with 0.5 mm thickness in a climatic chamber (fig.3.8). For simulation of P1mm-DVS, Dirichlet type boundary conditions were used, while in P500µm-CC-LCIs test conducted in a climatic chamber, the identified surface factor C_s was necessary. Simulations of mass loss of cylinders 36 mm in diameter submitted to drying at different humidity levels were successful, as shown in fig.3.5. Those results suggest that the drying model used herein correctly accounts for the size on a large range of humidity. The simulations also emphasize that the boundary conditions to be used in simulations should not be only directed by the specimen size but also depend on surrounding environmental factors. The air velocity around the sample seems to be the major environmental factor. In fact, even though the specimen of experiments C18-SS-RH20, C18-SS-RH58, C18-SS-RH80 are relatively large compared to test P1mm-DVS, the air change rate on the specimen surface, on the contrary, was relatively low because of the use of a hermetic chamber without any ventilation. Since the air change rate was very low, a moisture transfer coefficient was then introduced to prescribe a realistic boundary condition. A constant surface exchange coefficient $C_s = 3.6\ 10^{-9}\ [kg/m^2/s]$ identified on test C18-SS-RH20 was used in this study. The exchange coefficient has the beneficial effect of limiting hydric gradients between the surface and the core of samples, as shown in fig.3.9. Therefore, it allows reducing the risk of hydric gradient cracking during drying. A further study on the surface exchange coefficient is undertaken in the following section.

3.5 Investigation on surface moisture transport coefficient

3.5.1 Drying process and surface evaporation

Water leaves material through evaporation on its surface. A complete review of the drying process has been made by Crank (2002); Hall and Hoff (2002); Wang and Pereira (1986), and the attempt here is to recall the main findings. First, when exposed to drying, the material surface heats up or cools down to balance with the surrounding atmosphere temperature. Second, it goes up under a constant drying rate period, during which liquid flow through the porous medium is fast enough to maintain a wet surface. The evaporation on the surface proceeds the same way as in the case of flat water surface evaporation as if the solid phase was absent. Otherwise, this stage is not observed for materials where the initial water content is low (Hall and Hoff, 2002). Last, in the final stage, the drying rate decreases. In fact, the film of liquid water becomes discontinuous, the liquid flow slows down, and the material surface may no longer be fed with water, so it starts to dry (the film water is shrinking) due to evaporation. As a consequence, the evaporation rate drops.

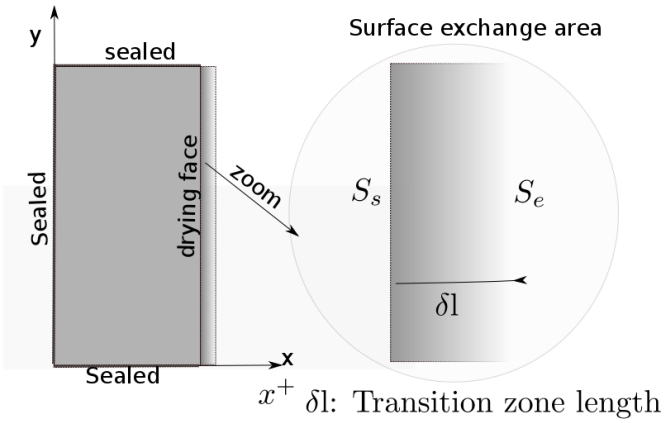

Figure 3.10: Sketching the boundary condition with surface effect

3.5.2 Boundary conditions with surface factor

Let us note $x = 0$ the surface of the material (fig.3.10) in contact with the surrounding atmosphere. For the sake of simplicity, we consider herein, a unidirectional drying hypothesis at a surface defined by its normal x^+. The moisture flux on the material surface (fig.3.10) denoted j_{x^+} is obtained by projecting Eq.3.1 onto the normal direction x^+ and reads Eq.3.8:

$$j_{x^+} = \mathrm{D}(\mathrm{S}_l)\frac{\partial \mathrm{S}_l}{\partial x} \tag{3.8}$$

When the flux of water j_{x^+} from the bulk, driven by diffusion within the porous medium, is fast enough (thin specimen or highly porous materials) to exceed the evaporation rate at the surface, controlled by the surrounding environmental factors such as air velocity, temperature, humidity (Hall and Hoff, 2002; Hall and Allison, 2010), a humidity gradient is created between the surface of porous medium and region of air outside its influence. A moisture flux, j_{x^-} of vapor, is then established. j_{x^-} is driven by vapor diffusion in air and is modeled by using Fick's law (Hall and Hoff, 2002; Hall and Allison, 2010) expressed in Eq.3.9:

$$j_{x^-} = \mathrm{D}_{vs}\frac{\partial \mathrm{C}_v}{\partial x} \tag{3.9}$$

where D_{vs} is the diffusivity of vapor of the surface, and C_v is vapor concentration of air.

By defining the water saturation in the air in analogy with material saturation S_l as $\mathrm{C}_v = \rho_v \mathrm{S}$, Eq.3.9 rewrites in form of Eq.3.10:

$$j_{x^-} = \rho_v \mathrm{D}_v \frac{\partial \mathrm{S}}{\partial x} \tag{3.10}$$

where ρ_v is the density of vapor water. Note that ρ_v, and D_{vs} depend on environment factors such as air temperature and humidity, air velocity (Hall and Hoff, 2002).

The term $\frac{\partial \mathrm{S}}{\partial x}$ of Eq.3.10 is the most difficult to deal with in evaporation problems (Hall and Hoff, 2002). A first approximation is to assume a linear variation of it in the transition zone (Huang et al., 2015), which is expressed as:

$$\frac{\partial \mathrm{S}}{\partial x} = \frac{\mathrm{S}_{mat} - \mathrm{S}_{env}}{\delta} \tag{3.11}$$

where S_{mat} is the vapor saturation of the surface of porous medium, S_{env} the vapor saturation of air out of zone of influence of the solid surface, and δ the length of the transition zone.

Introducing Eq.3.11 in Eq.3.10 yields:

$$j_{x^-} = C_s(S_{mat} - S_{env}) \tag{3.12}$$

where C_s is the so-called surface factor or surface mass loss coefficient [kg.$m^{-2}s^{-1}$], explicitly defined by

$$C_s = \frac{\rho_v D_{vs}}{\delta} \tag{3.13}$$

C_s may be identified by inverse analysis (Huang et al., 2015) on mass loss (a method used in this chapter) or by analytical calculation (Hisatake et al., 1995); the thickness of the boundary layer is of the order of $\delta = 1mm$ (Bakhshi et al., 2012; Huang et al., 2015). Hisatake et al. (1995) proposed

$$\delta = \sqrt{\frac{\nu l}{U}} \tag{3.14}$$

where U $[m/s]$ is the flow velocity outside the boundary layer; ν $[m^2/s]$ the kinetic viscosity, and l [m] is the drying thickness, which is considered as the characteristic length of drying. For instance, for $U = 1m/s$, $\nu = 1.510^{-5}m^2/s$, $l = 0.01m$, the thickness of the boundary layer $\delta = 1.2mm$.

3.5.3 Numerical study of the moisture transfer coefficient

Thanks to the calibrated model of the previous section, simulations were performed on specimens 1, 2, and 5 mm in thickness. Two types of boundary conditions were tested for each simulation. In the case of Robin type boundary conditions, the mass loss transfer coefficient C_s was varied from 10^{-5} $kg.m^{-2}.s^{-1}$ (very high value, close to Dirichlet type boundary conditions) to 10^{-10} $kg.m^{-2}.s^{-1}$ (very low value, far from Dirichlet boundary conditions) to cover a wide range of environmental drying conditions (air change rate, temperature, humidity).

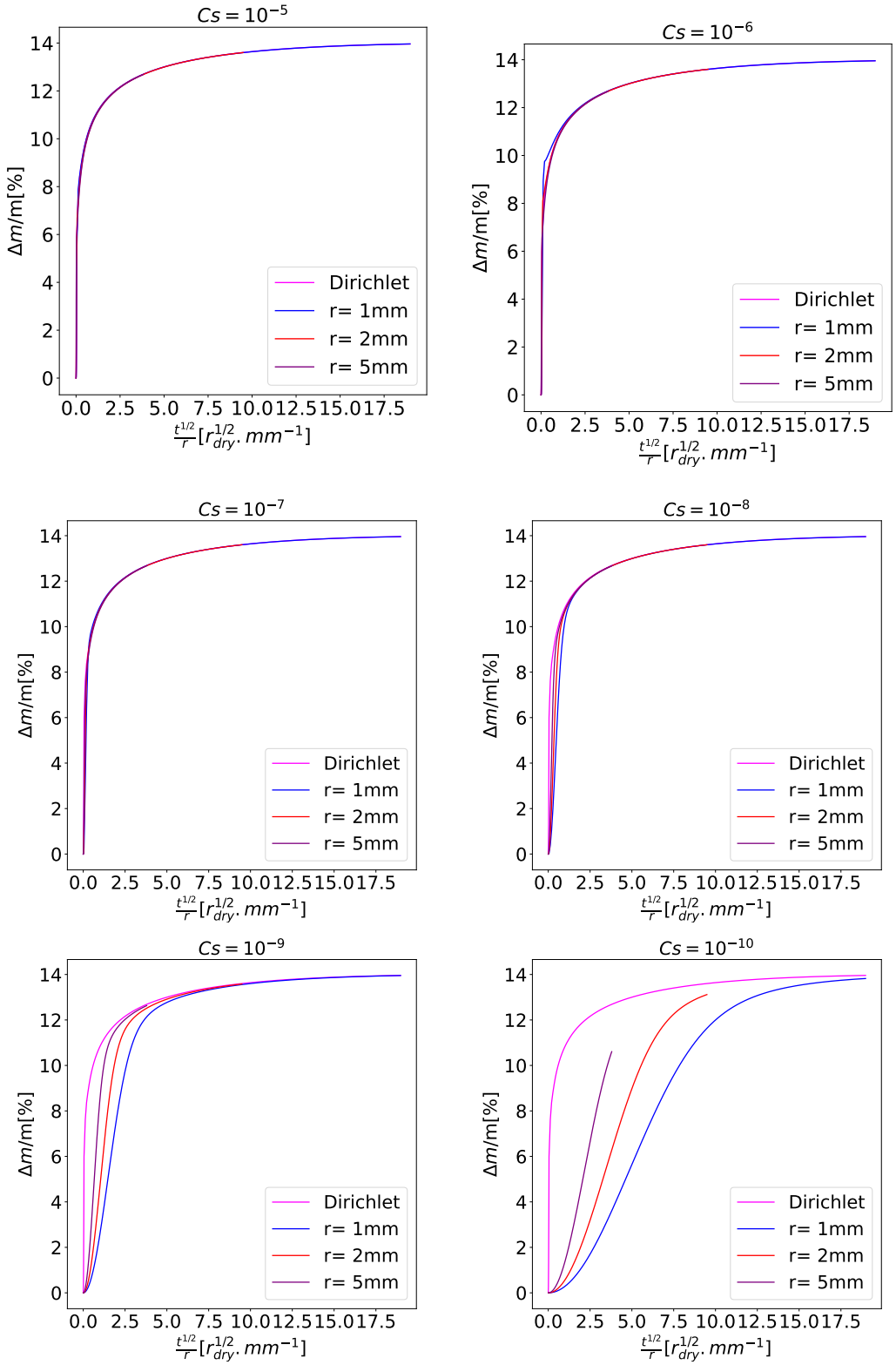

Figure 3.11: Evolution of mass loss, when using Dirichlet and Robin boundary conditions and different values of exchange coefficient C_s for specimens of different drying thickness r; $\frac{t^{1/2}}{r}$ is the drying equivalent time.

According to the results of the sensitivity analysis shown in fig.3.11 for mass loss, an exchange coefficient greater herein or equal to 10^{-7} gives identical results as Dirichlet condition, regardless of the specimen size. Those results demonstrate that a threshold

value of exchange coefficient exists above which, whenever applying Dirichlet or Neumann type boundary condition gives the same mass loss results independently of the specimen size. In the numerical simulations undertaken, this value is found to be 10^{-7} $kg.m^{-2}.s^{-1}$.

3.5.4 Surface bulk constant number

The sensitivity of the kinetics of mass loss is studied. The results displayed in fig.3.12 demonstrate that a threshold value exists above which the kinetic of mass loss is the same regardless of the drying thickness or the material intrinsic permeability. The threshold of exchange coefficient, which separates convection to diffusion action on material surface is estimated to be 10^{-7} $kg.m^{-2}.s^{-1}$.

These results suggest that it is possible to derive a practical number, which will tell us whenever we are in or out of the zone of influence of the exchange coefficient (fig.3.10) for a given material (diffusivity D, dry material density ρ_d) of a given size (drying thickness l) exposed to certain drying condition (exchange coefficient C_s). Considering a volume of water per unit area flowing along a drying thickness l and crossing surface A, the rate of evaporation noted R, is given by

$$R = -\frac{1}{A}\frac{dm}{dt} \tag{3.15}$$

Let us introduce the following dimensionless variables:

- $\vartheta = \frac{D_s}{l^2} \times t$ the dimensionless time; where t [s] is the time, D_s $[m^2.s^{-1}]$ the average diffusivity of the material in a steady state; $l = \frac{V}{A}$, where $V[m^3]$ is the volume of the drying specimen and A its surface exposed to drying.
- $w = \frac{m}{m_f}$ the unit mass per dry material (mass at given time during drying normalized by the mass of completely dried material); $m = \rho_d \times A \times l \times w$, $m_f = \rho_d \times A \times l$. m_f is the mass of dry material and ρ_d the dry mass per unit volume.

Using these variables, Eq.3.15 becomes:

$$R = -\frac{\rho_d D_s}{l}\frac{dw}{d\vartheta} \tag{3.16}$$

The continuity of moisture transfer rate on the surface requires that $R = j_{x^-}$

$$R = -\frac{\rho_d D_s}{l}\frac{dw}{d\vartheta} = C_s(S_s - S_e) \tag{3.17}$$

The left board side of Eq.3.17 is controlled by the diffusion process in bulk, while the right board side is a signature of the surface evaporation process. Therefore, we introduce the dimensionless Surface Bulk Constant SBC number.

$$SBC = \frac{C_s l}{\rho_d \times D_s} \tag{3.18}$$

where l is the drying thickness, which is considered as the characteristic length of drying; C_s the surface exchange coefficient given by Eq.3.13, is completely determined by the drying condition; and D_s the water diffusivity in bulk at a steady state in concrete. By analogy to the Biot number (Smith, 2011; Omini et al., 1990), which expresses the ratio of the heat transfer resistance inside of a body to the heat transfer resistance of its surface, the SBC number defined in this chapter defines the ratio of moisture transfer resistance

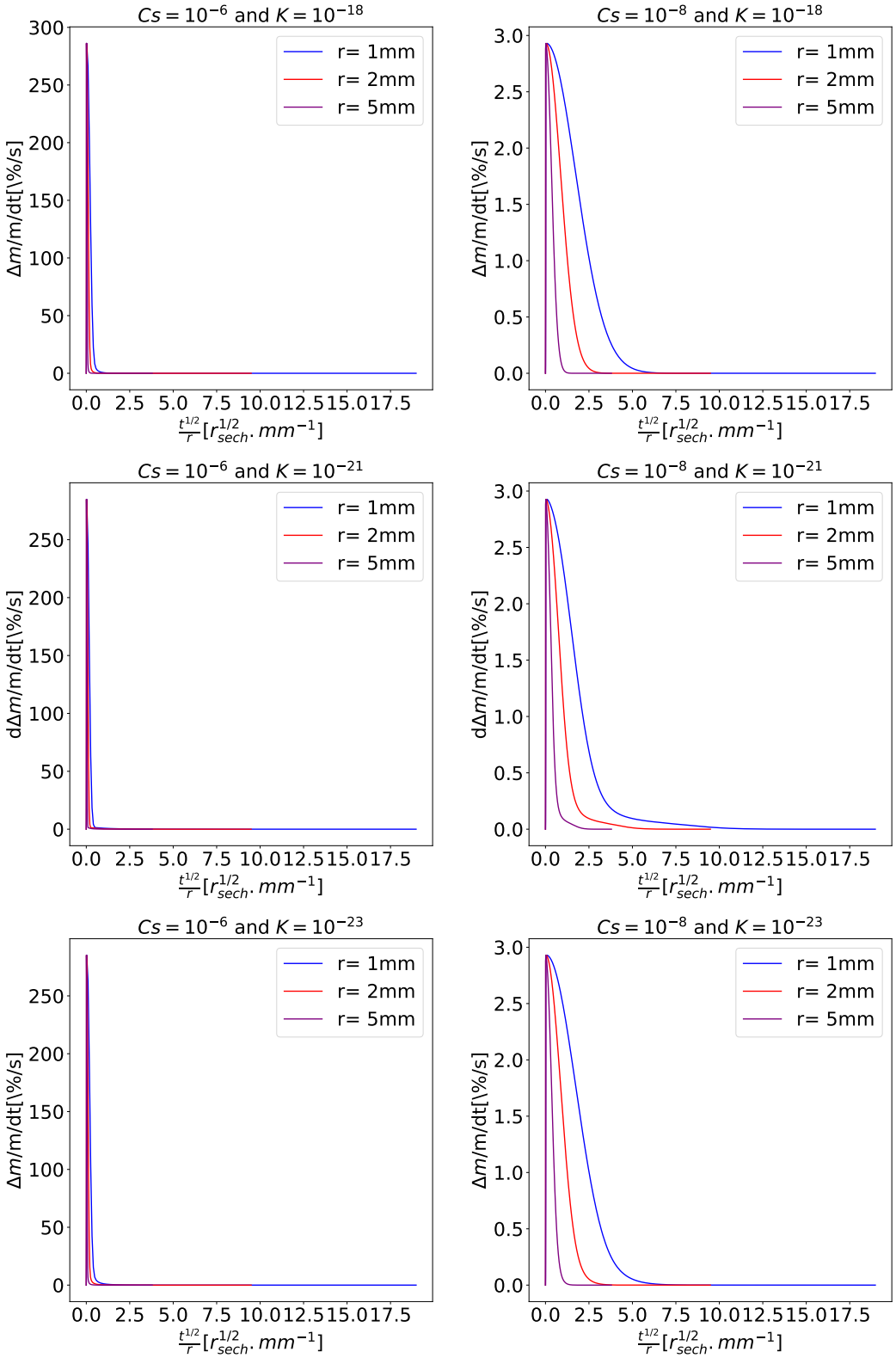

Figure 3.12: Kinetic of mass loss evolution for material intrinsic permeability of K = 10^{-18}, 10^{-21} and 10^{-23} m^2, each for exchange coefficient C_s = 10^{-6}, 10^{-7}, 10^{-8} $kg.m^{-2}.s^{-1}$ and drying thicknesses $r = 1, 2, 5$ mm

inside a structure to the moisture transfer resistance on its surface. It is noteworthy that by increasing drying thickness l, or surface evaporation C_s (air rate change, temperature increase) or decreasing diffusivity D_s, the SBC number increases also, and the diffusion

in the bulk concrete dominates. Conversely, the smaller the specimen, the smaller SBC, meaning that the surface effects become more and more dominant.

3.6 Experimental study and numerical modeling of drying shrinkage

3.6.1 Mechanisms

Shrinkage of cement-based materials occurs over a broad range of scales from nanometer to the meter level. Four mechanisms are proposed to explain drying shrinkage in the literature, and they all act at the nanometer level. The mechanisms are well-documented thanks to intensive research since the pioneering work of Feldman and Sereda (1964), and Powers (1968), and we recall the definition of each mechanism briefly:

- Capillary pressure: the capillary pressure acts on the water−air menisci in the partially empty pores, which induces anisotropic compressive stress causing the rigid solid skeleton to shrink (Coussy et al., 2004; Rougelot et al., 2009).
- Movement of interlayer water: the microstructure of C-S-H is a layered-bricks structure with water molecules in between. Therefore, the removal of water due to drying will cause C-S-H sheets to shrink, which results in macroscopic contractions (Jennings, 2008).
- Surface tension: a molecule of water within the material is submitted to attractive and repulsive forces in all directions from neighboring molecules. But in the case of molecules lying on the surface, due to lack of symmetry, there is a non-zero resultant force perpendicular to the surface, causing its contraction like a stretched elastic skin (El Tabbal et al., 2020).
- Disjoining pressure: it is visualized as the force pushing apart adjacent solid particles on water penetration in regions where free adsorption related to Van der Walls forces cannot fully develop when relative humidity is increased. As a direct consequence of drying, the removal of this interlayer water will cause the disjoining pressure to decrease and the particles to shrink (Maruyama, 2010).

On the one hand, physics-based models focus on those mechanisms, but due to lack of experimental data at intermediate scales, jumps over six orders of magnitude are performed to predict data at the millimeter scale and then compared against macroscopic test results (Coussy et al., 2004; El Tabbal et al., 2020). On the other hand, another class of models known as phenomenological are derived from macroscopic observations at centimeter scales but lack physical base, (Bažant and Jirásek, 2018; Granger, 1995). Therefore it is interesting to know the latter models type are still valuable on smaller scales. The purpose of this section is to dig into that question. The drying shrinkage model adopted in this chapter supposed that drying shrinkage strains were proportional to the variation of relative humidity (Eq.3.19). In the following, the model parameter is calibrated from experimental measurements, and the ability of the model to predict drying shrinkage from micrometer scale to centimeter-scale is tested. The drying strain is analyzed, assuming that endogenous shrinkage can be neglected since all the specimens involved in this study were well hydrated. They are at least three months old, and the water to cement ratio was sufficiently large.

3.6.2 Adopted drying shrinkage model

The rate of drying shrinkage is considered to be proportional to the rate of humidity change (Bažant et al., 2004; Bažant and Jirásek, 2018) and formulated

$$\dot{\epsilon}_{sh} = k_{sh}\dot{h} \tag{3.19}$$

where k_{sh} [-] is the shrinkage coefficient, which relates an increment of shrinkage strain to an increment of the local humidity within the material.

3.6.3 Experimental determination of drying shrinkage coefficient

In a first attempt, the drying shrinkage coefficient is assessed experimentally thanks to experiment P500µm-CC-LCIs. The coefficient of shrinkage is considered to be the ratio between the shrinkage over the relative humidity difference. The value of this coefficient is found to be $k_{sh} = 8.6 \times 10^{-5}$ for the experimental result displayed in fig.3.13. The duration for equilibrium at different relative humidity steps is reported on tab.3.6.

Table 3.6: Duration for equilibrium at different relative humidity steps

Relative humidity (%)	80	60	42	27	20
Duration (h)	24	24	30	60	165

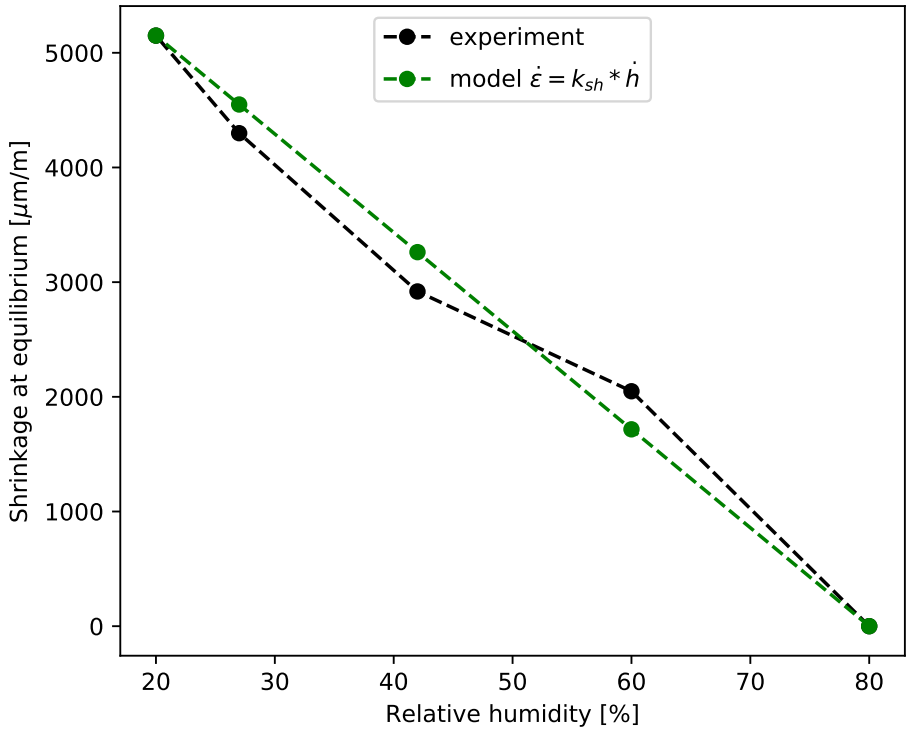

Figure 3.13: Determination of drying shrinkage coefficient $k_{sh} = 8.6 \times 10^{-5}$ by sorption length change measurements on a small prism (experiment P500µm-CC-LCIs), performed in climatic chamber.

3.6.4 Prediction of drying shrinkage

Specimen of various sizes are used for different drying kinetics, and strains are measured at different scales. Using the identified drying shrinkage coefficient $k_{sh} = 8.6 \times 10^{-5}$ [-] to perform finite element simulations, the experimental results of drying shrinkage from centimeter to micrometer scales are well reproduced. centimeter scale is shown on fig.3.14, millimeter scale on fig.3.15 and micrometer scale on fig.3.16 and fig.3.17.

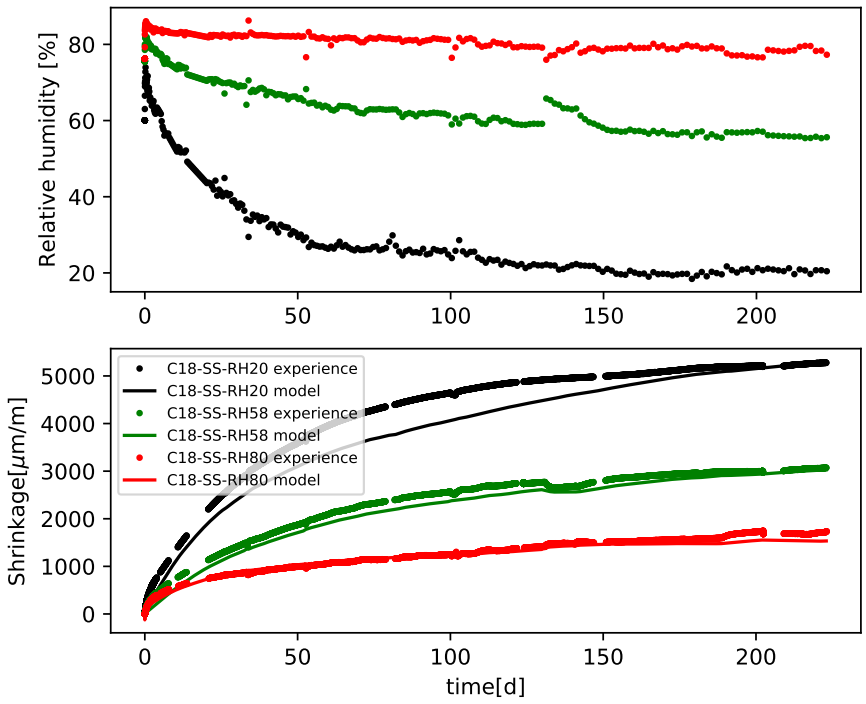

Figure 3.14: Prediction of drying shrinkage at centimeter level using $k_{sh}\dot{h}$ model, with the parameters identified above for experiments C18-SS-RH80, C18-SS-RH58 and C18-SS-RH20

For each case, a drying simulation was performed first using the drying model identified in the previous section (the parameters were kept the same), and the result was used to feed the mechanical calculations. This suggests that the drying model identification is trustworthy. The agreement with experimental results also tells us that, for the cement paste, if the water desorption isotherm of material is measured, and if drying of the material can be simulated, the drying shrinkage can be predicted in a straightforward manner. A single experiment of a few days duration helps to identify the drying shrinkage coefficient. Considering the pore relative humidity as a primary variable for shrinkage and saturation for drying is a good combination for the prediction of drying shrinkage. Yet, the simulations were performed only on cement paste specimens in this study, and a similar work should be performed on concrete, with the combination of homogenization calculations.

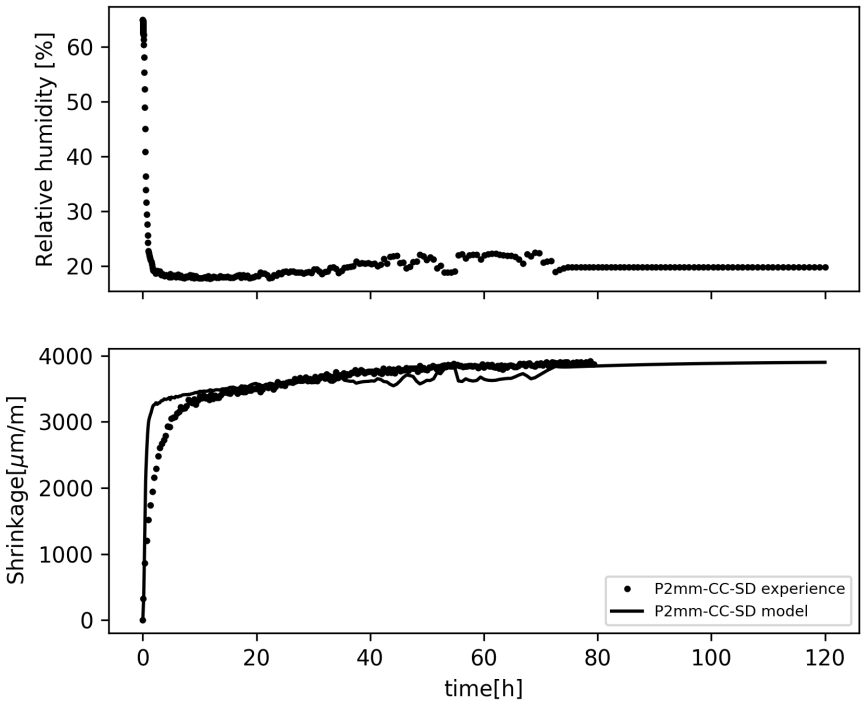

Figure 3.15: Prediction of drying shrinkage of small prism P2mm-CC-SD with 1 mm drying thickness using the parameters identified above.

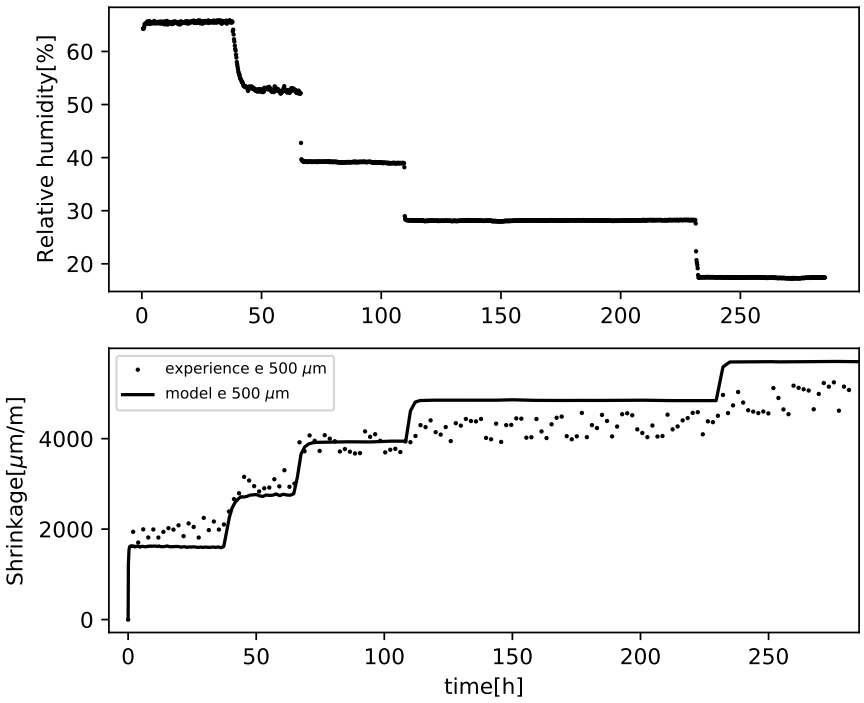

Figure 3.16: Prediction of drying shrinkage of small prism P500µm-CC-LCIs with 0.25 mm drying thickness using the parameters identified above.

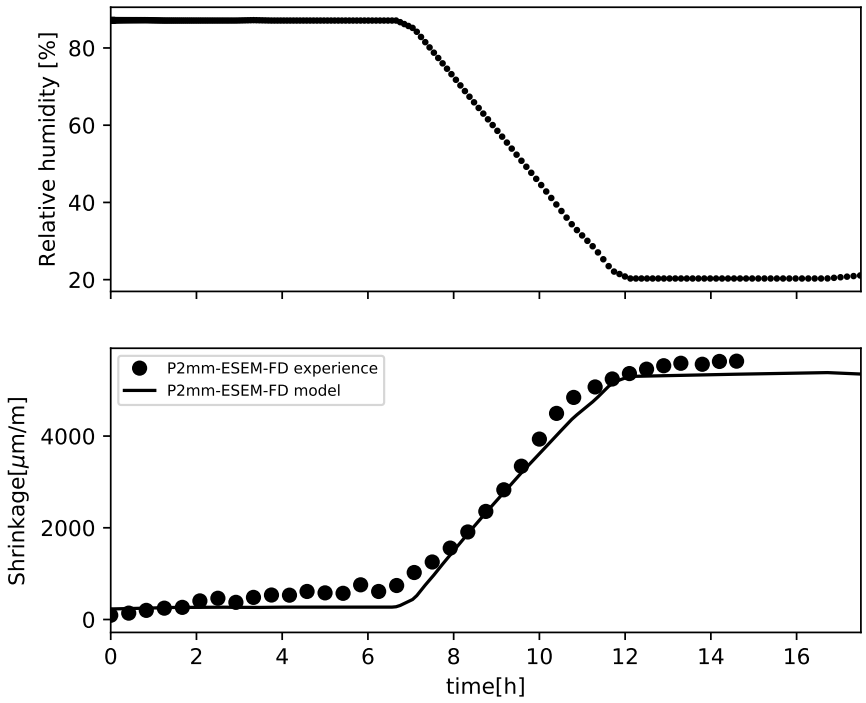

Figure 3.17: Prediction of drying shrinkage of small prism P2mm-ESEM-FD with 1 mm drying thickness using the parameters identified above.

3.7 Conclusion

Tests were performed on hardened cement paste specimens. The cement paste was tested with different geometries: cylinder ⌀36 mm in diameter and thin slabs 0.5, 1, 2 mm thick. The specimens were dried at various rates and with different steps of humidity, using different conditioning systems: environmental scanning electronic microscope (ESEM), climatic chamber (CC), Dynamic Vapor Sorption (DVS), and saturated salt solution (SSS). Drying modeling was performed via a Richards-Fick model, which accounts for water permeation and vapor diffusion. The parameters of the model plus a unique moisture transfer coefficient were identified. The prediction of mass loss showed that the model was trustworthy to account for the drying rate, size, and humidity influence on the moisture loss. This point is important since it tells us that for a given structure, the parameters of the model could be determined from laboratory tests. At the structure scale, boundary conditions of the Dirichlet type were suitable, but for laboratory tests, the choice of boundary condition is not straightforward. In fact, for some experiments presented in this study, it was necessary to identify Robin-type boundary conditions essentially due to the low air change rate, not only on the specimen size as one may think. However, the strategy of identification adopted in this study reveals that it is possible to identify the material parameters and the surface factor independently. It is quite appealing to draw a more precise criterion about the impact of the surface factor. In the second section of this chapter, a sensitivity study on the surface factor is conducted, and a practical number named surface bulk constant (SBC) was derived to predict the influence of such factor on moisture loss rate for any material of a given size drying at given specific conditions. In the last section, the drying shrinkage model $\dot{\varepsilon} = k_h \dot{h}$ was tested. Let us stress that k_h was identified directly on experiment results of only 250-hour duration, on prismatic specimen 0.5 mm in thickness; these results demonstrate that this kind of model is able to account for the drying rate effect on drying shrinkage. Particularly the model is found to be trustworthy for a broad range of humidities ranging from 95% to 20 %. Since this model is only based on the pore humidity variation rate, the quality of results is mainly due to the quality of drying results, which is strongly dependent on the water desorption isotherm.

As a perspective, we could think of predicting drying shrinkage at the concrete scale and further on the structural scale with this model type based on single length change measurement. The linearity of drying shrinkage with relative humidity makes it possible to fully calibrate the model for large ranges of relative humidity based on one single drying shrinkage experiment. It will be time effective to carry out experiments on cement paste and retrieve the corresponding coefficient for concrete through homogenization.

References

P. Acker and F-J. Ulm. Creep and shrinkage of concrete: physical origins and practical measurements. *Nuclear Engineering and Design*, 203(2):143–158, 2001. 67

M Bakhshi, Barzin Mobasher, and C Soranakom. Moisture loss characteristics of cement-based materials under early-age drying and shrinkage conditions. *Construction and Building Materials*, 30:413–425, 2012. 81

V. Baroghel-Bouny. Water vapour sorption experiments on hardened cementitious materials. Part I: Essential tool for analysis of hygral behaviour and its relation to pore structure. *Cement and Concrete Research*, 2007. 67, 68

V. Baroghel-Bouny, M Mainguy, T Lassabatere, and Olivier Coussy. Characterization and identification of equilibrium and transfer moisture properties for ordinary and high-performance cementitious materials. *Cement and concrete research*, 29(8):1225–1238, 1999. 67, 68, 71

Z.P. Bazant and J C Chern. Concrete creep at variable humidity: constitutive law and mechanism. *Materials and structures*, 18(1):1, 1985. 67

Z.P. Bažant and M Jirásek. *Creep and hygrothermal effects in Concrete Structures*. Springer New York LLC, 2018. 67, 68, 85, 86

Z.P. Bažant, A A Asghari, and J Schmidt. Experimental study of creep of hardened Portland cement paste at variable water content. *Materials and Structures*, 9(4):279–290, 1976. 67

Z.P. Bažant, G Cusatis, and L Cedolin. Temperature effect on concrete creep modeled by microprestress-solidification theory. *Journal of engineering mechanics*, 130(6):691–699, 2004. 86

F. Benboudjema and J-M Torrenti. Prediction of mechanical consequences of drying: From laboratory to concrete structures. *Cement and concrete research*, 42(7):1014–1023, 2012. 67, 68

F. Bendboudjema. *Modélisation des déformations différées du béton sous sollicitations bi-axiales.Application aux confinements des réacteurs des centrales nucléaires*. PhD thesis, Université de Marne la Vallée, 2002. 67

H. Cagnon, T. Vidal, A. Sellier, X. Bourbon, and G. Camps. Cement and Concrete Research Drying creep in cyclic humidity conditions. *Cement and Concrete Research*, 76:91–97, 2015. ISSN 0008-8846. doi: 10.1016/j.cemconres.2015.05.015. 67

L. Charpin, Y. Le Pape, E. Coustabeau, E. Toppani, G. Heinfling, C. Le Bellego, B. Masson, J. Montalvo, A. Courtois, J. Sanahuja, and N. Reviron. A 12 Year EDF Study of Concrete Creep under Uniaxial and Biaxial Loading. *Cement and Concrete Research*, 103:140–1,59, 2018. doi: 10.1016/j.cemconres.2017.10.009. 67

O. Coussy, P. Dangla, T. Lassabatere, and V. Baroghel-Bouny. The equivalent pore pressure and the swelling and shrinkage of cement-based materials. *Materials and structures*, 37:15–20, 2004. 85

J. Crank. *The Mathematics of Diffusion*. OXFORD UNIVERSITY PRESS, 2002. ISBN 0 19 853344 6. 79

C. Di Bella, M. Wyrzykowski, and P. Lura. Evaluation of the ultimate drying shrinkage of cement-based mortars with poroelastic models. *Materials and Structures*, 2017. ISSN 1871-6873. doi: 10.1617/s11527-016-0870-0. 67

G. El Tabbal, P. Dangla, M. Vandamme, M. Bottoni, and S. Granet. Modelling the drying shrinkage of porous materials by considering both capillary and adsorption effects. *Journal of the Mechanics and Physics of Solids*, page 104016, 2020. ISSN 0022-5096. doi: https://doi.org/10.1016/j.jmps.2020.104016. 67, 85

R. F. Feldman and P. J. Sereda. Sorption of water on compacts of bottle-hydrated cement. i. the sorption and length-change isotherms. *Journal of Applied Chemistry*, 1964. 85

A. Foucault, S. Michel-Ponnelle, and E. Galenne. A new creep model for NPP containment behavior prediction. In *Proceedings of the 1st SSCS (Strategies for Sustainable Concrete Strategies)*, 2012. 67

H. Garbalinska, M. Bochenek, W. Malorny, and J. Von Werder. Comparative analysis of the dynaamic vapor sorption (dvs) technique and traditional method for sorption isotherms determination-exemplified at autoclaved aerated concrete samples of four density classes. *Cement and Concrete Research*, 91:97–105, 2017. 68

L Granger. *Comportement différé du béton dans les enceintes de centrales nucléaires: analyse et modélisation*. PhD thesis, Ecole Nationale des ponts et Chaussées, 1995. 67, 85

C. Hall and W.D. Hoff. *Water transport in brick, stone and concrete*. CRC Press, 2002. 79, 80

M.R. Hall and D. Allison. Evaporative drying in stabilised compressed earth materials using unsaturated flow theory. *Building and Environment*, 45:509–518, 2010. 80

W. Hansen. Drying Shrinkage Mechanisms in Portland Cement Paste. *Journal of the American Ceramics Societey*, 70(5):323–328, 1987. ISSN 1551-2916. doi: 10.1111/j.1151-2916.1987.tb05002.x. 67

A. Hilaire. *Etude des déformations différées des bétons en compression et en traction, du jeune au long terme: application aux enceintes de confinement*. PhD thesis, Ecole normale supérieure Cachan, 2014. 67, 70, 71, 79

F. Hild and S. Roux. CORRELI Q4 : A Software for "Finite-element" Displacement Field Measurements by Digital Image Correlation Internal report no. 269. Technical report, LMT, France, 2008. 69

K. Hisatake, M. Fukuda, J. Kimura, M. Maeda, and Y. Fukuda. Experimental and theoretical study of evaporation of water in a vessel. *Journal of applied physics*, 77(12):6664–6674, 1995. 81

Q. Huang, Z. Jiang, X. Gu, W. Zhang, and B. Guo. Numerical simulation of moisture transport in concrete based on a pore size distribution model. *Journal of engineering mechanics*, 67:31–43, 2015. 80, 81

S. Huang. *Ageing behaviour of concrete creep : application to the VeRCoRs concrete*. PhD thesis, Université Paris-Est, 2018. 69

T. Ishida and W. Tiao. Future of multiscale modelling of concrete-Toward a full integration of cement chemistry and concrete structural engineering. *Rilem Technical Letters*, 2018. doi: 10.21809/rilemtechlett.2018.60. 67

H.M. Jennings. Refinements to colloid model of C-S-H in cement: CM-II. *Cement and Concrete Research*, pages 275–289, 2008. 85

M. Jirásek and P. Havlásek. Microprestress–solidification theory of concrete creep: Reformulation and improvement. *Cement and Concrete Research*, 60:51–62, 2014. 67

J. Kinda, A. Bourdot, L. Charpin, S. Michel-Ponnelle, and F. Benboudjema. Investigation of drying shrinkage of cement based materials assisted by digital image correlation. *Journal of Materials in Civil Engineering*, 2021. 69

M. Mainguy. *Modèles de diffusion non linéaire en milieux poreux. Applications a la dissolution et au séchage des matériaux cimentaires*. PhD thesis, ENPC - École des Ponts ParisTech, 1999. 70

M. Mainguy, O. Coussy, and V. Baroghel-Bouny. Role of air pressure in drying of weakly permeable materials. *Journal of engineering mechanics*, 127:582–592, 2001. 70, 71, 79

I. Maruyama. Origin of Drying Shrinkage of Hardened Cement Paste: Hydration Pressure. *Journal of Advanced Concrete Technology*, 2010. ISSN 1346-8014. doi: 10.3151/jact.8.187. 85

I. Maruyama, Y. Nishioka, G. Igarashi, and K. Matsui. Microstructural and bulk property changes in hardened cement paste during the first drying process. *Cement and Concrete Research*, 2014. ISSN 00088846. doi: 10.1016/j.cemconres.2014.01.007. 68

I. Maruyama, G. Igarashi, and Y. Nishioka. Bimodal behavior of C-S-H interpreted from short-term length change and water vapor sorption isotherms of hardened cement paste. *Cement and Concrete Research*, 73:158–168, 2015. 71

T. Mauroux, F. Benboudjema, P. Turcry, A. Aït-Mokhtar, and O. Deves. Study of cracking due to drying in coating mortars by digital image correlation. *Cement and Concrete Research*, 2012. ISSN 00088846. doi: 10.1016/j.cemconres.2012.04.002. 69

B. Menu, M. Jolin, B Bissonnette, and L. Molez. Evaluation de la sensibilité à la fissuration des bétons projétés au jeune âge. In *Proceedings of the Conférence Internationale Francophone NoMaD 2018*, 2018. 68

Y. Mualem. A new model for predicting the hydraulic conductivity of unsaturated porous media. *Water resources research*, 12(3):513–522, 1976. 71

O. Omini, A. Sparavigna, and A. Strigazzi. Thermal diffusivity and biot number: A new experimental method. *Applied Physics*, 50:35–37, 1990. doi: 10.1007/BF00323951. 83

T.C. Powers. The thermodynamics ofvolume change and creep. *Matériaux et Constructon*, 6, 1968. 85

S. Poyet, K. Trentin, and Amblard E. The use of sorption balance for the characterization of the water retention curve of cement-based materials. *Journal of Advanced Concrete Technology*, 14:354–367, 2016. 68

S. Rahimi-Aghdam, Z.P. Bažant, and G. Cusatis. Extended Microprestress-Solidification Theory for Long-Term Creep with Diffusion Size Effect in Concrete at Variable Environment. *Journal of engineering mechanics*, 2019. doi: 10.1061/(ASCE)EM.1943-7889.0001559. 67

T. Rougelot, F. Skoczylas, and N. Burlion. Water desorption and shrinkage in mortars and cement pastes: Experimental study and poromechanical model. *Cement and Concrete Research*, 2009. ISSN 00088846. doi: 10.1016/j.cemconres.2008.10.005. 85

A. Sellier, S. Multon, L. Buffo-Lacarrière, T. Vidal, Bourbon X., and G. Camps. Concrete creep modelling for structural applications: non-linearity, multi-axiality, hydration, temperature and drying effects. *Cement and concrete research*, 2016. doi: 10.1016/j.cemconres.2015.10.001. 67

C. Simon, F. G. Fernandez, L. G Esteban, P. Palacios, R. Hosseinpourpia, and C. Mai. Comparison of the saturated salt and dynamic vapor sorption method in obtaining the sorption properties of pinus pinea l. *European journal of Wood and Wood Products*, 75(6): 919–926, 2017. 68

H.C. Sleiman, M. Briffaut, Dal Pont S., A. Tengattini, and B. Huet. Influence of common simplifications on the drying of cement-based materials up to moderate temperatures. *International Journal of Heat and Mass Transfer*, 150, 2020. 67, 70, 79

P. G. Smith. *Thermal processing of food*. Springer, 2011. ISBN 978-1-4419-7661-1. doi: 10.1007/978-1-4419-7662-8. 83

F. Soleilhet. *Etudes expérimentales et numériques des matériaux cimentaires sous sollicitations hydro-mécaniques*. PhD thesis, Cachan, Ecole normale supérieure, 2017. 67, 70, 79

M. Thiery, V. Baroghel-Bouny, N. Bourneton, G. vilain, and C. Stéfani. Modélisation du séchage des bétons. Analyse des différents modes de transfert hydrique. *Revue européenne de génie civil*, 11(5):541–578, 6 2007. 70, 71, 79

K.W. Wang and N.C. Pereira. Handbook of Environmental Engineering. In *Water ressources in natural processes*, volume 4, 1986. 79

F.H. Wittmann and P.E. Roelfstra. Total deformation of loaded drying concrete. *Cement and Concrete Research*, 10:601–610, 1980. 68

Chapter 4

Creep of cement paste at variable humidity: Pickett effect and size effect - Experimental study

4.1 Motivation

The motivation of the present study is the investigation of the influence of relative humidity, drying rate and size effects on creep. In fact, the question of modeling the long-term behavior of large structures such as containment of nuclear power plants (Benboudjema, 2002; Reviron, 2009; Foucault et al., 2012; Charpin et al., 2017) addresses a safety problem of first importance. However, predicting this behavior is delicate (Benboudjema and Torrenti, 2001) because the material exhibits a paradoxical behavior known as Pickett effect (Pickett, 1942), which is still a matter of intensive research today (Hilaire, 2014; Mathieu et al., 2018; Ishida and Wang, 2018; Samouh et al., 2019; Rahimi-Aghdam et al., 2019). The Pickett effect corresponds to the additional deformation when concrete is stressed together with internal moisture change (Acker and Ulm, 2001; Benboudjema et al., 2005). Pre-dried specimens creep less than saturated ones, but when drying, the lower the relative humidity at which the sample is exposed, the more it will creep (Acker and Ulm, 2001). According to the current state of the art, drying creep is coming from two sources (Wittmann and Roelfstra, 1980; Bazant and Chern, 1985; Granger, 1995): intrinsic creep and microcracking. The first mechanism is a material characteristic, while the latter is a structural effect. From an experimental point of view, the characterization of the Pickett effect, which is a crucial point for creep modeling, is difficult (Bažant and Yunping, 1994). The difficulty comes from the fact that on large specimens, equilibrium times are very long, (Baroghel-Bouny et al., 1999; Cagnon et al., 2015). This phenomenon prevents a specimen from being subjected to variable but sufficiently homogeneous humidity to prevent shrinkage cracking (Hwang and Young, 1984; De Sa et al., 2008). The use of small cement paste samples (Bažant et al., 1976; Day et al., 1984; Neubauer and Jennings, 2000) by avoiding the effect of shrinkage cracking due to contrast in paste-aggregate and drying cracking due to stress gradients could make it possible to isolate purely material effects at the level of hydrates responsible for creep and shrinkage in C-S-H.

The following experimental study aims to contribute to bridging that gap by performing experiments at various drying rates using three conditioning systems:

1. Environmental Scanning Electron Microscopy (ESEM): axial creep and shrinkage measurements on samples 10×10×2 mm in size for different drying rates.

2. Climatic Chamber (CC): axial and biaxial creep, shrinkage, and mass loss measurements on specimens 10×10×2 mm in size, for different drying rates.

3. Saturated Salt Solution (SSS): axial creep (drying and pre-dried) with recovery, shrinkage, mass loss measurements for three relative humidities, 20%, 60% and 80% on specimens ⌀36 × 180 mm in size.

The experimental results are made available so that researchers can challenge their models, especially regarding the influence of humidity, size effect, and drying rate on creep.

4.2 Sample preparation

Details on the studied material were reported in Section.2.2.1.

4.3 Study of drying creep and shrinkage in ESEM

4.3.1 Overall description

A new experimental protocol in ESEM for the assessment of drying shrinkage and drying creep is proposed. The equipment for this study is introduced on fig.4.1. Creep and

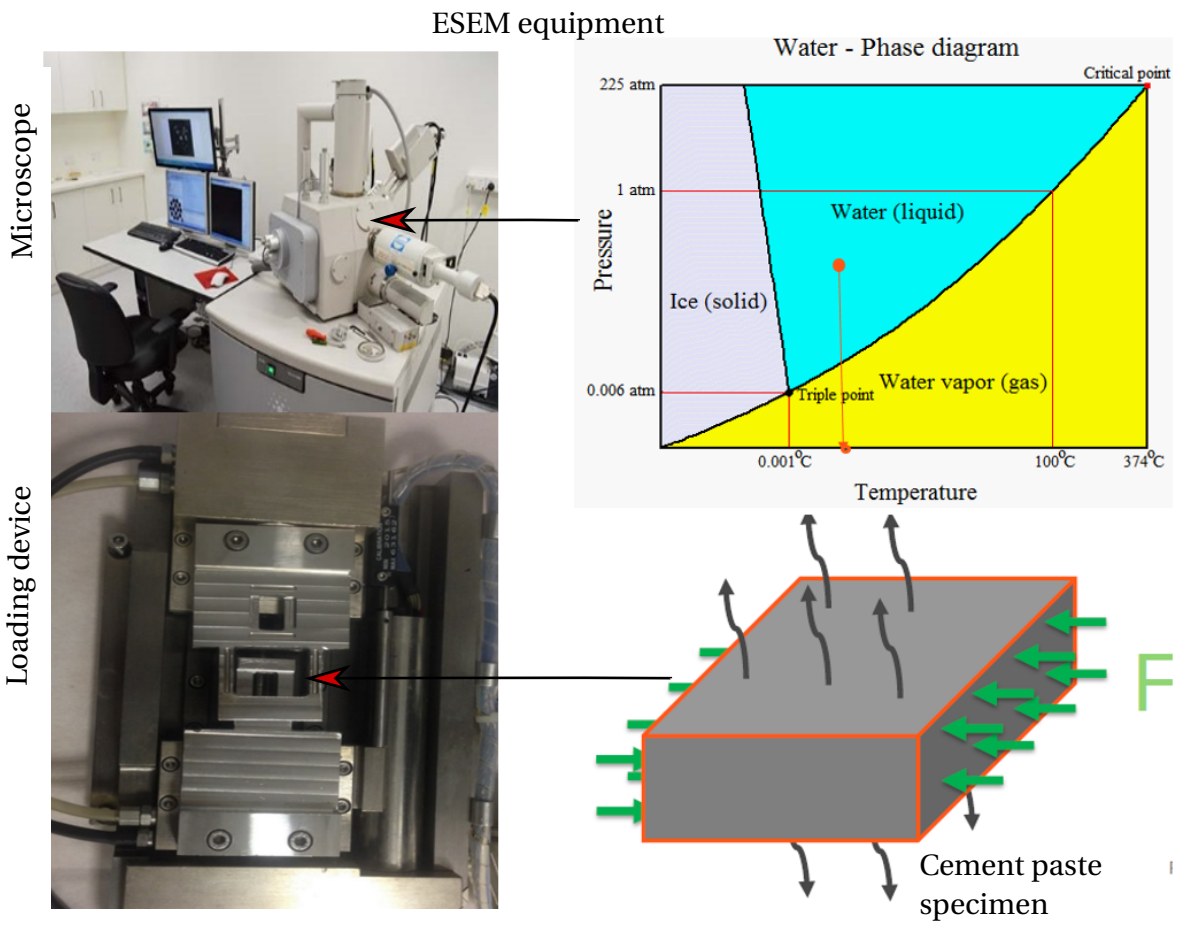

Figure 4.1: Overview of experimental set up

shrinkage tests were performed on cement paste specimens of size 10×10×2 mm, under

ESEM, and strain measurements were performed by Digital Image Correlation (DIC) (Tomičević et al., 2013). One of the central goals of the experimental campaign presented in this study was to avoid surface microcracking. In fact, to reach the initial relative humidity, the air was pumped out, and the very low pressure of less than 2.7 % of atmospheric pressure was reached. However, the gas inside the material was initially at atmospheric pressure. This means that if the surface of the specimen is exposed to severe drying, very high relative humidity gradients occur, and this gradient may induce surface cracking. Therefore, there is a need to prevent the specimens from drying at this stage. Two strategies were adopted: (1) the sample was stored for at least 24 hours under 5°C relative humidity before the test starts; (2) a bottle containing 2 ml water was introduced in the ESEM chamber, and droplets were deposited around the sample. This water was previously externally heated to approximately 40° C and decarbonized with an external vacuum pump. Heating aimed at allowing the water to evaporate quickly during the pumping stage and prevent the specimen surface from drying due to its low-temperature level. The pumping was intended to withdraw the entrapped air, likely to contain carbon dioxide that may cause carbonation. For each test, a 4 × 4 matrix of images centered on the observation area of the sample surface was acquired to verify that there was no apparent microcracking at the scale of observation (fig.4.2). An additional visual scan of the entire surface confirmed that there was no cracking present at the surface visible with naked eye or carbonation at the preparation stage.

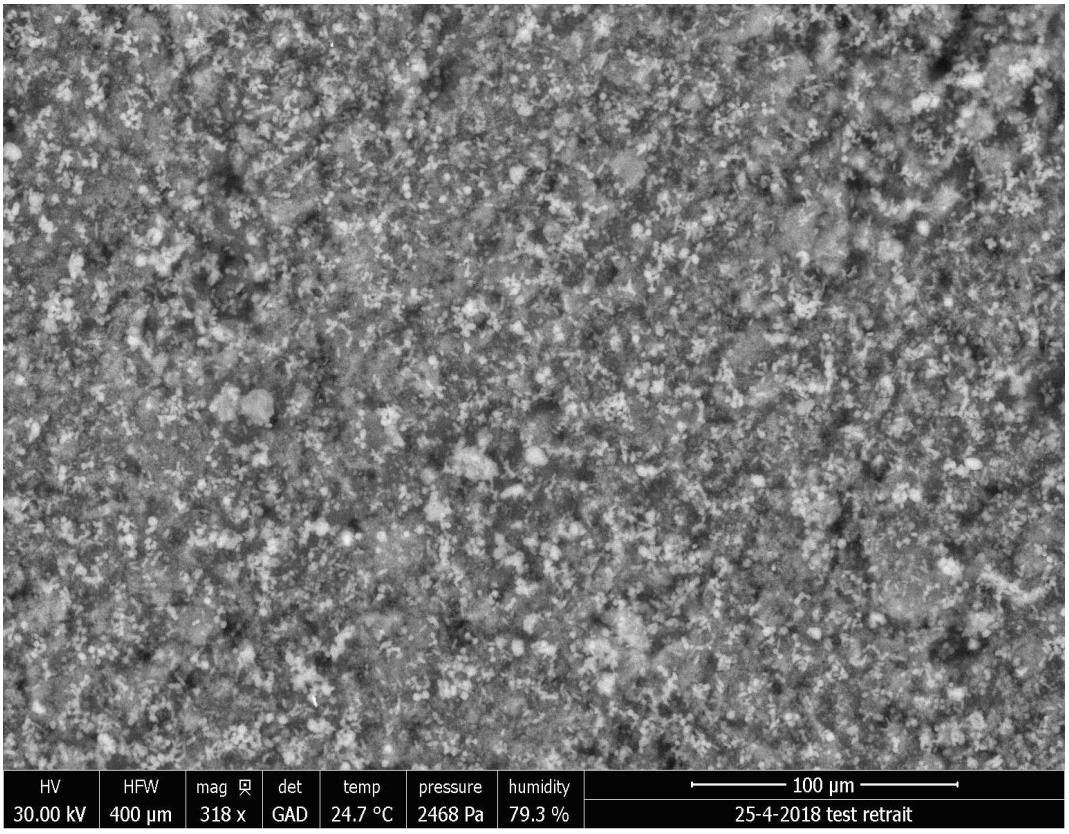

Figure 4.2: ESEM image with natural contrast of cement paste

4.3.2 Environment

An ESEM Quanta-650 was used. The relative humidity was controlled by varying the pressure inside the ESEM chamber while keeping the temperature at a constant value of 24°C. The temperature was regulated through an air conditioning system and monitored using a PT100 temperature sensor provided with the microscope. The relative humidity is indirectly determined by Rankine relation,

$$HR = \frac{P_v}{exp(13.7 - \frac{5120}{T})} \tag{4.1}$$

where P_v (Pa) is the vapor pressure in ESEM chamber, HR (%) the relative humidity; T(K) the temperature in the chamber, and the denominator corresponds to the Rankine formula.

A preliminary test was performed by introducing a relative humidity sensor in the ESEM chamber. The comparison of the two techniques of measurement gave very close results, as shown in fig.4.3. Unfortunately, the chamber temperature was controlled entirely by room temperature, and a tiny modification affects the relative humidity. The load level was 7 MPa, which corresponds to 1/4 of the compressive strength at 90 days.

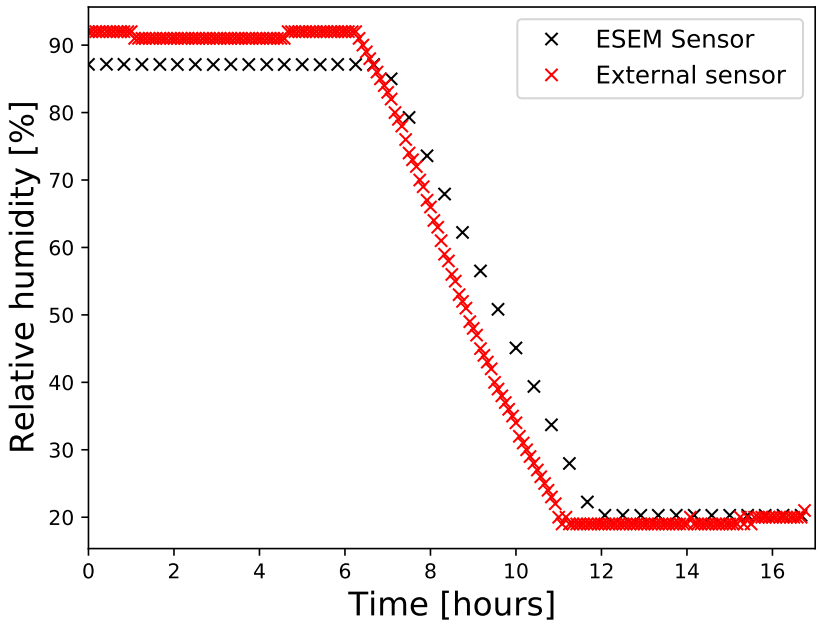

Figure 4.3: Relative humidity measurement in ESEM using the internal sensor (ESEM sensor) and external capacitive hygrometer (External sensor)

4.3.3 Loading in ESEM

The last challenge to overcome in order to perform creep tests in ESEM is to be able to perform in-situ loading. The loading system is presented in fig.4.4. It is a uniaxial compression machine made of a mobile jaw and a fixed jaw mounted on a Deben-type machine for uniaxial compressive tests. A Teflon sheet was placed at the contact between each jaw and the specimen in order to limit friction.

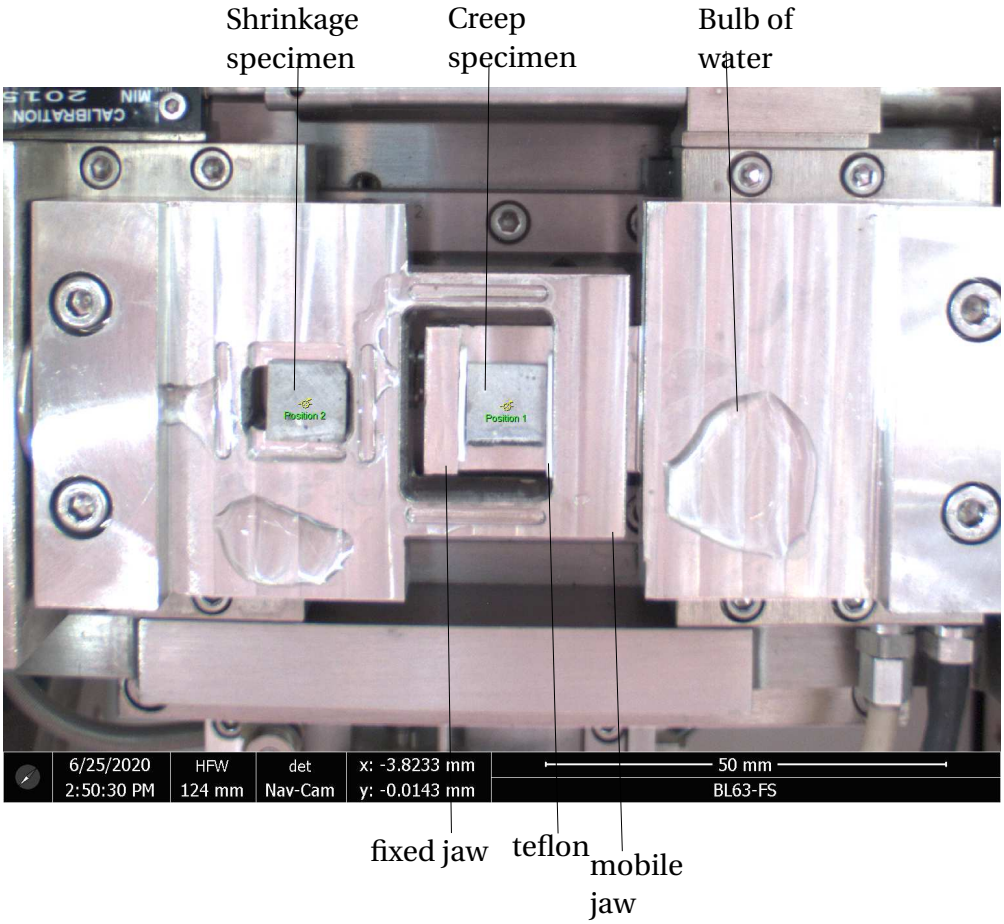

Figure 4.4: Experimental set up for in situ creep and shrinkage tests in ESEM

In order to check the loading quality, we have compared the results of in-situ compression tests with those obtained with a conventional testing machine (fig.4.5), and many conclusions can be drawn. First, the loading rates were similar between both compressive tests; (2) second, the compressive strength obtained by the two loading systems were quite the same, which means that centering of the specimen in the ESEM in-situ test is correct. Last, the loading rates in creep tests were the same as those of compressive tests, and the forces remained constant, which indicates that the force regulation went well. An important issue is to verify if the specimen was not bending during the in-situ creep test, see Section.4.3.4.

4.3.4 Imaging for strain evaluation

We have taken advantage of the Back Scattered Electron (BSE) imaging mode in order to benefit from both chemical and topography contrast. This imaging mode also allows to probe up to 30 nm depth. Since the energy of the backscattered electron carries the signature of the atoms, it gives a clue on the atoms on the surface or in bulk. An acceleration voltage of 30 kV with a working distance (WD) of 9.5 mm was used. Those parameters were adjusted by trial and error. The scanned area was 266×400 µm with a spatial resolution of 1048×1524 pixels; the pixel size was then 260 nm. Special attention was paid to avoid out-of-plane displacements, as shown in fig.4.6. The WD is the distance between the BSE detector and the surface of the sample; therefore, if the specimen bends, the WD will decrease. Hence the WD was recorded for each image pictured during the tests. Fig.4.7 shows that it remained constant for all images, then it was concluded that there was no out-of-plane displacement induced by loading, and consequently, there was

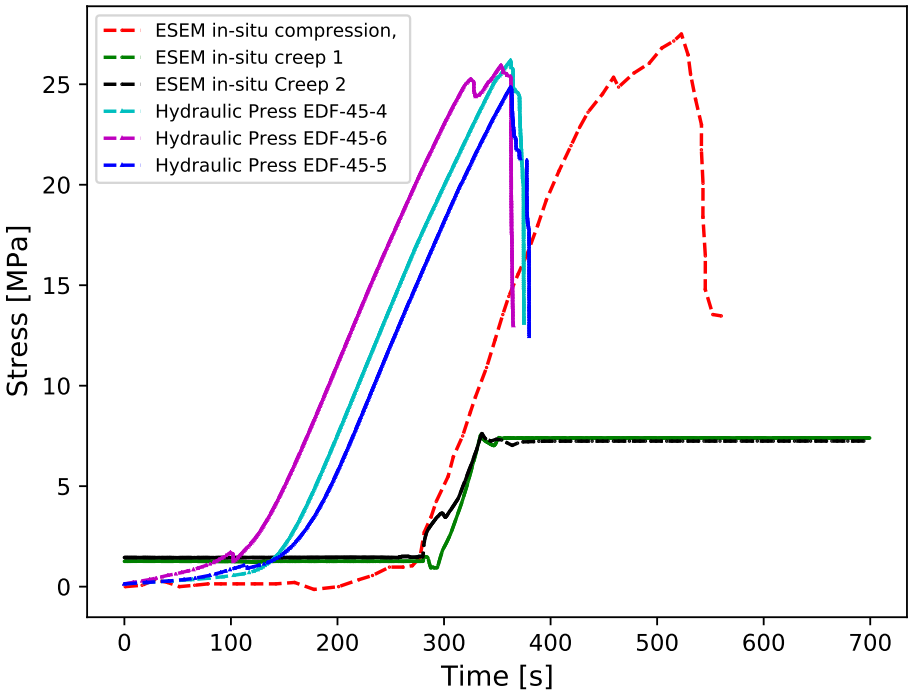

Figure 4.5: Compressive test on cement paste : 10×10×2 mm slabs tested in ESEM and ⌀36×180 mm cylinders tested with a classical testing machine

a spurious strain. The acquired images were post-processed by 2D-DIC Tomičević et al. (2013).

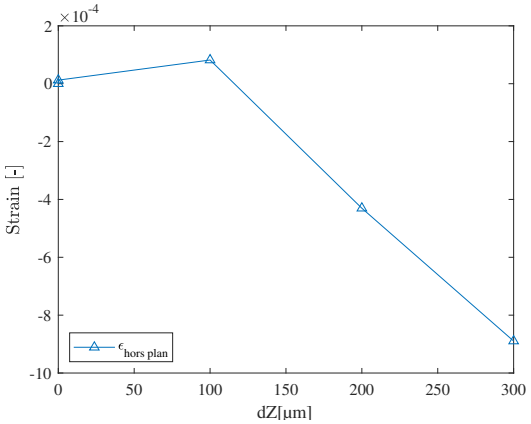

Figure 4.6: Out-of plane strain with manual change of working distance dZ in ESEM

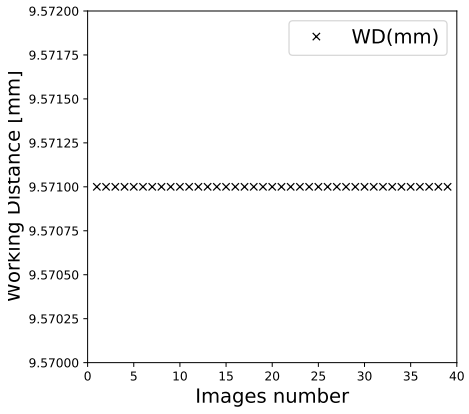

Figure 4.7: Working distance of images acquired in ESEM, P2mm-ESEM-SD test

4.3.5 Protocol for ESEM campaign

The procedure for the tests under ESEM is the following:

1. Configure the pressure regulation program
2. Set up two samples on the loading stage. A Teflon sheet was placed between the loading plate and the sample loaded surfaces.

3. Pre-load the sample at -20 N compressive force.
4. Close the chamber, take a global image with Navcam of the ESEM. It will help navigate on the sample surface during the test.
5. Reopen the chamber, introduce a beaker with 2 ml of deaerated water at about 40°C and few water droplets around each sample. This is intended to prevent cracking during the load stage.
6. Close the ESEM chamber, choose the ESEM mode according to the starting relative humidity of the test and given the current temperature, choose the appropriate pressure, then start the pumping process, and wait until the desired pressure is achieved.
7. Move the loading stage to reach the working distance of 9.5 mm (specific to GAD detector type),
8. Turn on the beam, choose the position on sample surface for imaging, make adjustments of brightness and contrast, to reach the best possible image quality.
9. Take an initial image of the two samples.
10. Load to an intermediate load level and acquire images again.
11. Load from this intermediate level to the load level for the creep test, and image samples again.
12. Launch automatic image acquisition and start the pressure regulation program.

4.3.6 ESEM tests results

Drying shrinkage, total strain, relative humidity, temperature, and loading force were monitored simultaneously in each test. The temperature was kept constant at 24 °C. Unfortunately, the mass loss could not have been monitored in this campaign. The main characteristics of the tests are summarized in tab.4.1.

Table 4.1: Main characteristics of tests performed under ESEM

Test	curing humidity	Geometry (mm)	Creep	Shrinkage	Mass
P2mm-ESEM-FD	80%	10×10×2	✓	✓	-
P2mm-ESEM-SD	Endogenous	10×10×2	✓	✓	-

Two drying rates (at which the relative humidity was decreased) were tested, a Slow Drying test labeled as P2mm-ESEM-SD and a fast one called P2mm-ESEM-FD (tab.4.1). First, the relative humidity was reasonably well controlled for both drying rates as presented in fig.4.8.a. Then the drying shrinkage evolution, which was obtained by Digital Image Correlation, as shown in fig.4.8.b.

Third, the evolution of loading forces of creep tests is presented in fig.4.9.a. Last, total strains of simultaneously drying and loaded samples, for both drying rates are displayed in fig.4.9.b.

As expected, the lower the drying humidity, the larger drying shrinkage (fig.4.8), and the total strain in these tests (fig.4.9). Most of the strains occur during the humidity transition period and evolve with very slow kinetics when the relative humidity remained constant. The load level was 144 N, which corresponds to a compressive stress of 7 MPa.

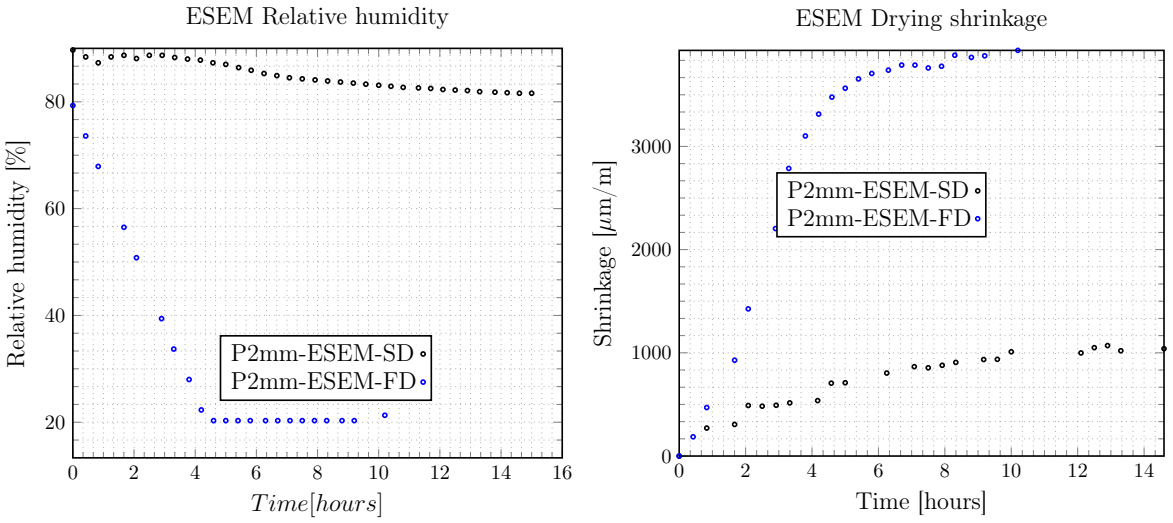

(a) Relative humidity

(b) Drying shrinkage

Figure 4.8: Evolution of relative humidity (a) and (b) corresponding drying shrinkage for the tests in ESEM

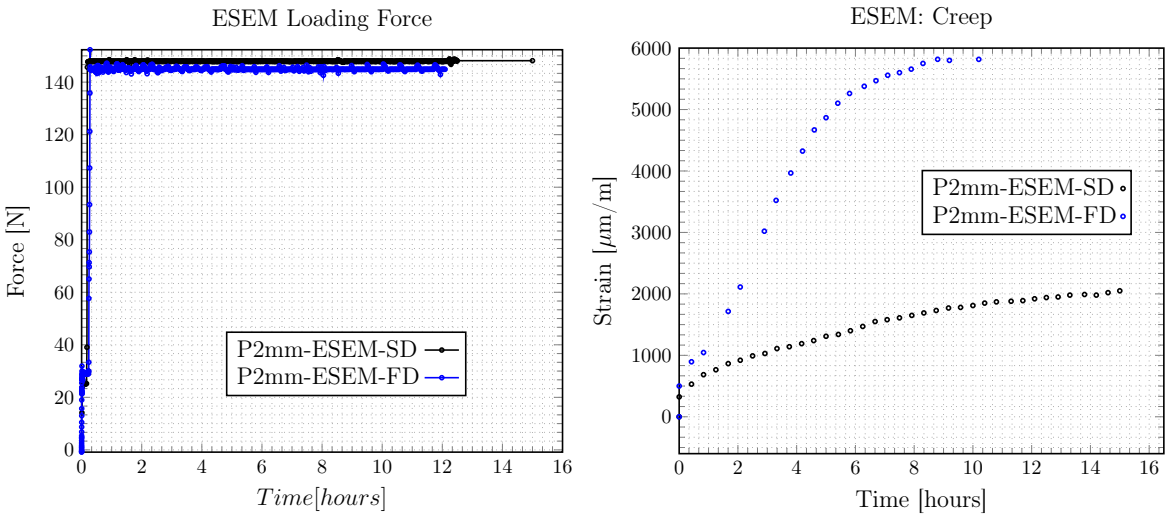

(a) Applied forces

(b) Total strain

Figure 4.9: (a) Evolution of loading force and (b) corresponding creep strains for the tests under ESEM

It explains why the magnitude of the total strain is not much higher than that of drying shrinkage.

4.4 Study of drying shrinkage and creep in climatic chamber

4.4.1 Overall description

A new protocol was developed for studying creep and shrinkage along with mass loss measurements of thin cement paste slabs in a climatic chamber (fig.4.10). The purpose was (i) to provide data for validation of the ESEM experiment, and (ii) to evaluate the ef-

fect of drying rate on both drying shrinkage and drying creep of very thin cement paste slabs 2 mm in thickness, in uniaxial and biaxial compressive tests. Total creep and drying shrinkage tests were carried out simultaneously on separate specimens for each. The mass loss of drying shrinkage specimen was also monitored every 10 minutes during the test with Metler Toledo balance with 0.01 mg of precision. As in ESEM cases, only natural contrast of the cement paste was used here. The experimental set-up is shown in fig.4.10.

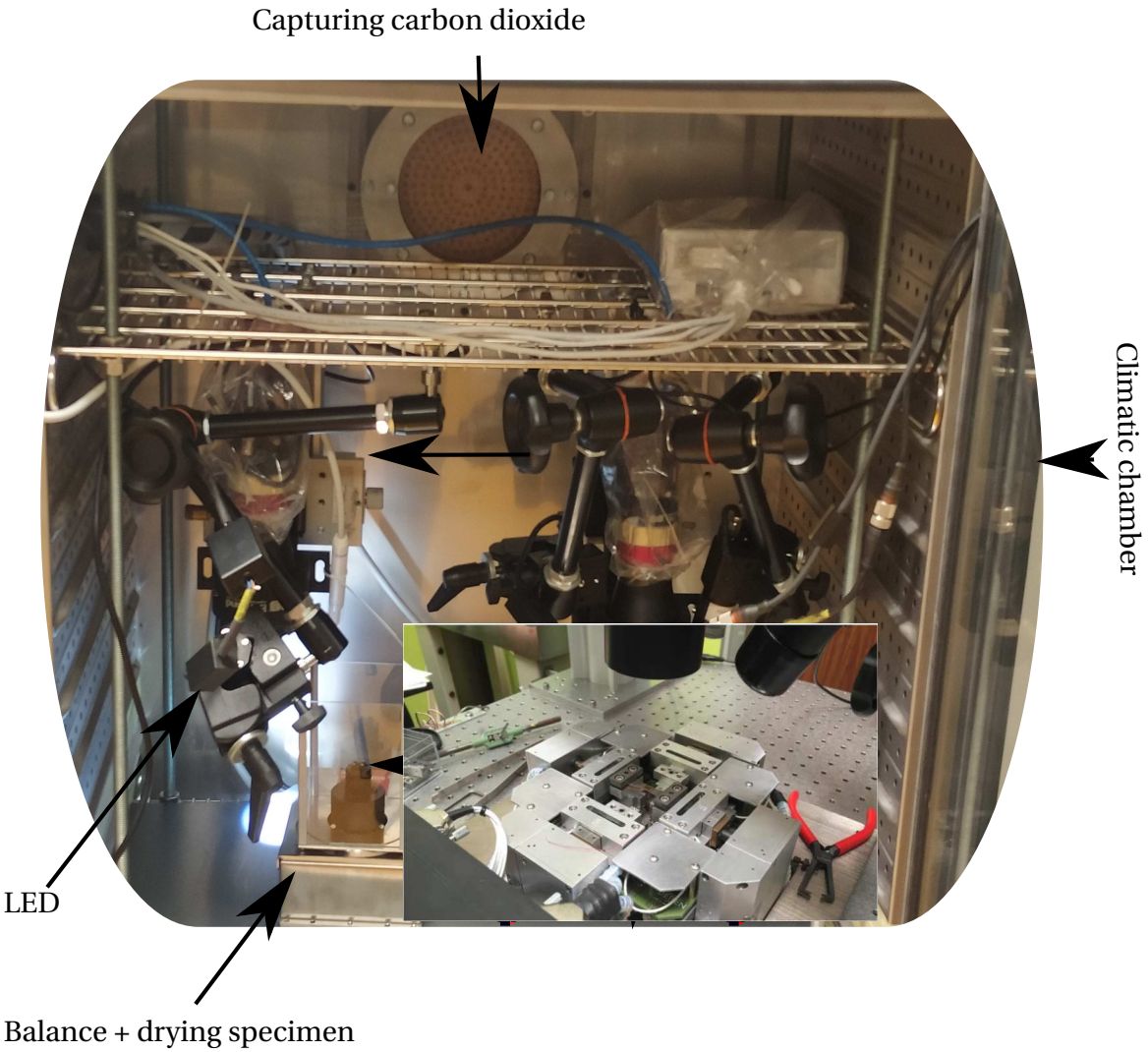

Figure 4.10: Overview of climatic chamber conditioning system.

4.4.2 Environmental control: relative humidity, temperature and carbon dioxide

The relative humidity and temperature were controlled using a climatic chamber. For each specimen, one sensor was used to monitor temperature, carbon dioxide, and relative humidity. To deal with carbonation, a specific box was designed, allowing air to pass through and be filled with lime powder compacted to reduce the space between grains. The box (fig.4.11) was placed in the air inlet of the climatic chamber, fig.4.10, so when the air came in, CO_2 was captured before reaching the chamber space where the specimens were placed. It was proven to reduce CO_2 content of the room air to less than 100 ppm (between 20 and 90 ppm), see fig.4.12.

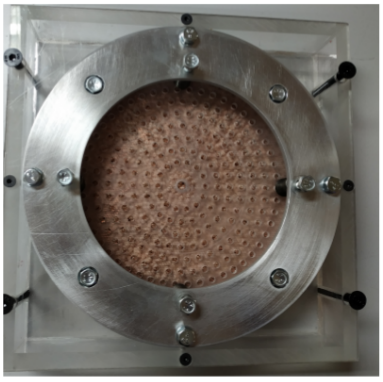

Figure 4.11: System for capturing CO_2 of air in the chamber space

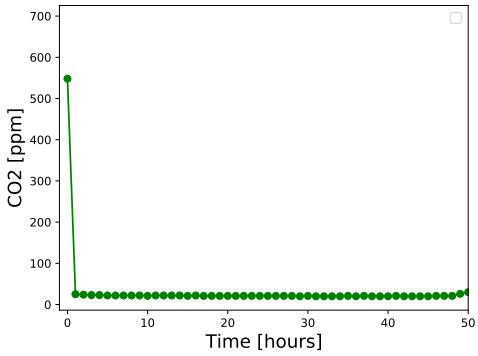

Figure 4.12: Evolution of CO_2 air content in climatic chamber

4.4.3 Loading and centering

The loading was performed with an electromechanical testing machine, mini-ASTREE (Bertin, 2016) (fig.4.13). The machine is able to prescribe arbitrary forces in two orthogonal directions, with opposite actuators that can be controlled in a symmetric fashion so that the specimen center is motionless. F_1 will denote the load amplitude applied by the two coupled actuators along one direction and F_2 for the other two coupled actuators in the orthogonal direction. Uniaxial/Biaxial compressive and tensile tests can be run with a load range $F_{1,2}$ in $\pm$ 2000 N. The maximum sample thickness was 8 mm, and the maximum stroke of each actuator was 5 mm. An anti-wrinkling device is designed for positioning the specimen.

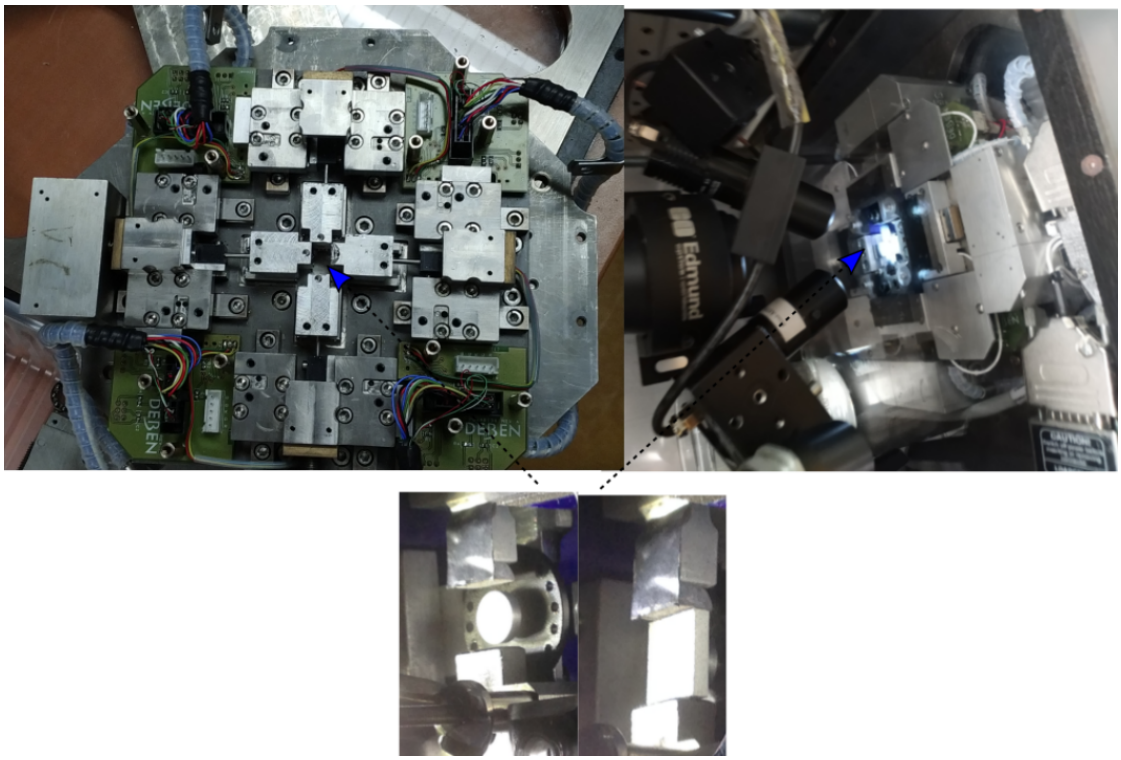

Figure 4.13: Mini-ASTREE machine and loading system for in-situ mechanical test in the climatic chamber

For the creep test, the loading sequence is as follows: in the first part, the load is in-

creased at a constant rate from 20 N (preload level) to 200 N in a time window of 36 s. During that stage, images are acquired for both specimens every 1 s. In the second step, the load is kept at the constant level (200 N), and images were acquired every 10 min for both specimens. The applied load level is one-third of the compressive strength at 90 days.

4.4.4 Imaging and strain measurement

One camera with 0.125× telecentric lens (in order to limit effects of out of plane movement) is used. The optical camera is linked to commercial software StreamPix to allow for automatic acquisition. The surface of the specimen was illuminated all time using LED lighting. It has been checked that lighting does not induce a temperature rise. The images of 700×688 pixel definition were taken on an area of 9.7×9.7 mm, which corresponds to physical size of 75 pix/mm. These images are analyzed by DIC using an element size of 50×50 pixels and a regularization length of 128 pix. The ROI was chosen at the center of the image.

4.4.5 Protocol for climatic chamber campaign

The procedure of the campaign in the climatic chamber is as follow:

1. Set up the carbon dioxide capturing device, the sensors for carbon dioxide, temperature, humidity, and mass balance in the climatic chamber.
2. Wait for climatic chamber humidity to stabilize at 80 %RH.
3. Set up the two samples: (weighing + shrinkage) sample on balance, creep specimen on the loading machine.
4. Pre-load at -20 N the specimen for creep
5. Set up the program for relative humidity control
6. Adjust image contrast and brightness on the camera
7. Launch loading, simultaneous image acquisition
8. Launch climatic chamber control

4.4.6 Climatic chamber test results

The two tests performed in the climatic chamber are presented in tab.4.2.

Table 4.2: Main characteristics of tests performed in CC

Test	curing humidity	Geometry (mm)	Creep	Shrinkage	Mass
P2mm-CC-1-SD	80%	10×10×2	✓	✓	✓
P2mm-CC-2-FD	80%	10×10×2	✓	✓	✓

The evolution of carbon dioxide and relative humidity are presented in fig.4.14 for the Slow Drying (P2mm-CC-1-SD) and Fast Drying (P2mm-CC-2-FD) rates in climatic chamber, fig.4.2. It is seen that the CO_2 level is increasing when a constant humidity of 20% is

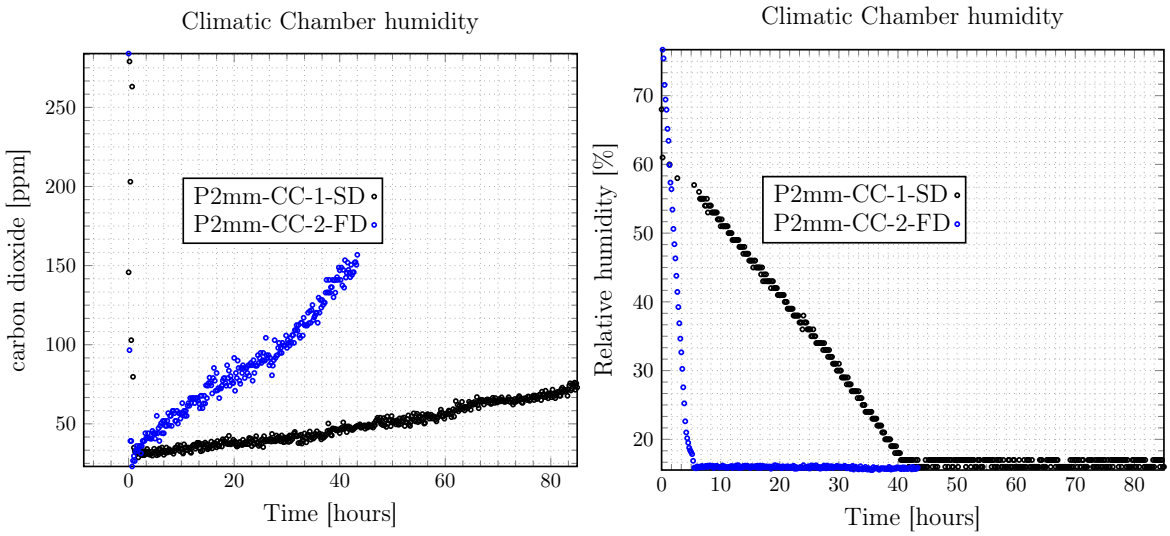

Figure 4.14: Environmental conditions during climatic chamber tests, carbon dioxide (CO_2) and relative humidity

reached. Fortunately, at that humidity level, the low saturation of the specimen stops the carbonation process (Turcry et al., 2017).

The results of mass loss and drying shrinkage for the two drying rates are displayed in fig.4.15.a-b. As expected, the mass loss at the end of drying does not depend on the rate at which the specimen was dried. Moreover, drying shrinkage at the end of testing does not depend on the rate of drying either.

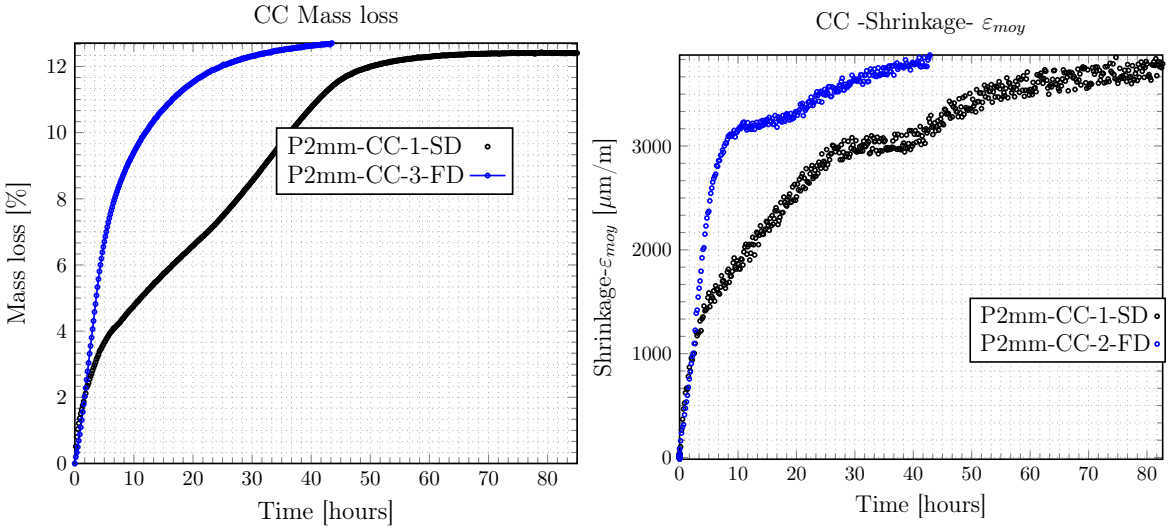

(a) Mass loss

(b) Drying shrinkage

Figure 4.15: Mass loss and drying shrinkage evolution in both tests in climatic chamber

The biaxial and uniaxial creep results are displayed together with the corresponding loading forces in fig.4.16 for axial strains and in fig.4.17 for lateral strains. Unfortunately, the relative humidity history in the biaxial and axial tests are different, which makes direct comparisons difficult. Yet, the comparison could be carried out indirectly by numerical simulation. It allows for benchmarking models.

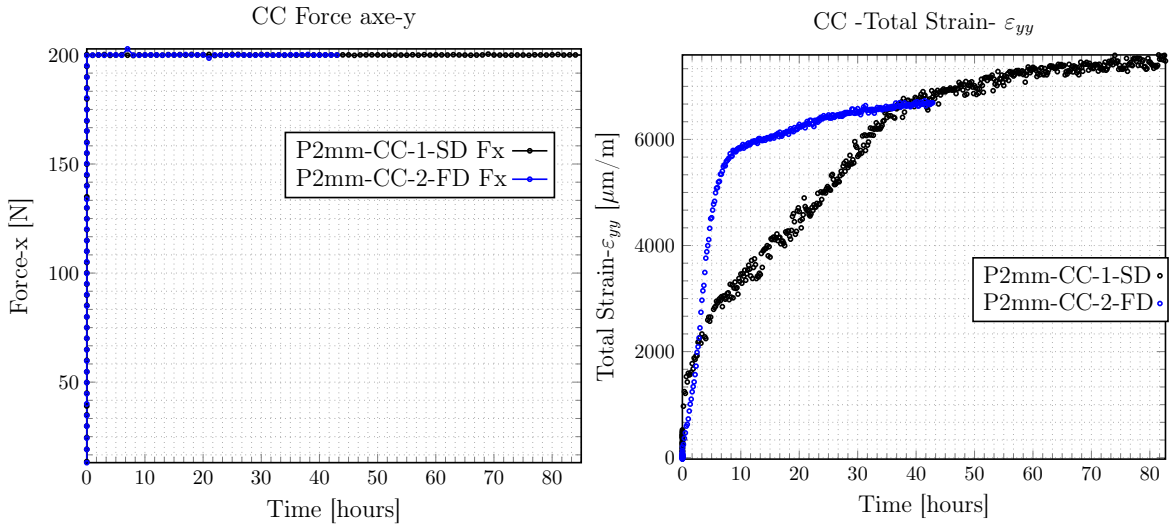

(a) Axial loading force

(b) Axial strain

Figure 4.16: Evolution of axial strain (for tests in climatic chamber) with the corresponding applied forces

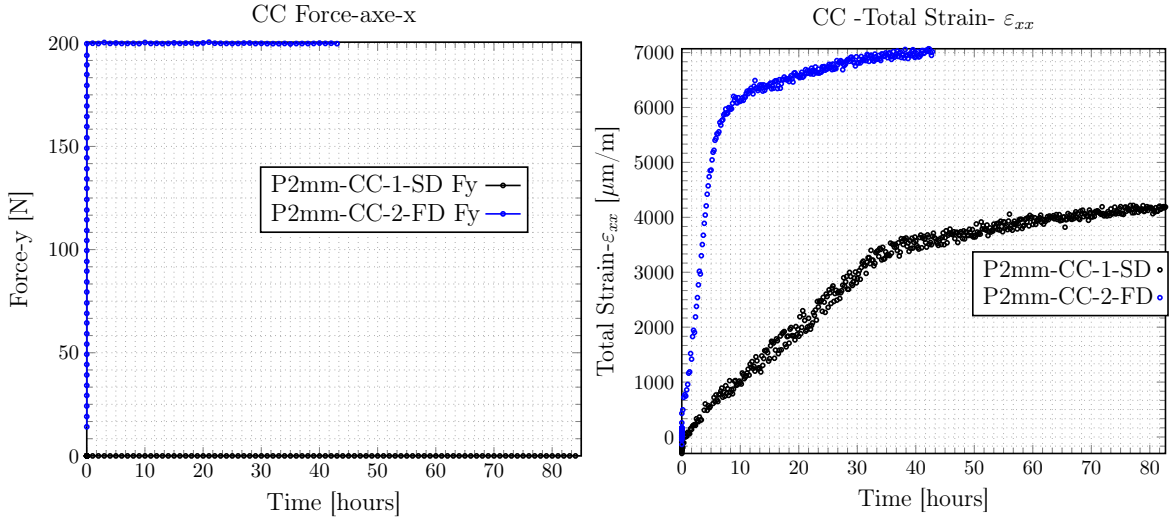

(a) Lateral loading force

(b) Lateral strain

Figure 4.17: Evolution of lateral strains for creep tests in climatic chamber

4.5 Macroscopic creep and shrinkage tests at three relative humidities

4.5.1 Overall description of experiments

The purpose of the experiments described in this section is the characterization of drying shrinkage and total creep under uniaxial loading at 20 °C. These experiments were carried out on one geometry (⌀36×180 mm), one material, and for different levels of relative humidity. The relative humidity was controlled using Saturated Salt Solutions (SSS). Because the air in the chamber is not circulated (in order to avoid cracking), the relative humidity decreased slowly. The experiments are summarized in Tab.4.3, with their acronyms to be used hereafter.

Table 4.3: Summary of experimental campaign undertaken on cement paste

Acronym	Relative humidity (%)	Testing
D-C18mm-SS-RH80	81	Drying
DSC-C18mm-SS-RH80	81	Drying shrinkage followed by creep
TCR-C18mm-SS-RH80	81	Creep followed by Recovery
D-C18mm-SS-RH58	58	Drying
DSC-C18mm-SS-RH58	58	Drying shrinkage followed by Creep
TCR-C18mm-SS-RH58	58	Creep followed by Recovery
D-C18mm-SS-RH20	20	Drying
DSC-C18mm-SS-RH20	20	Drying shrinkage followed by Creep
TCR-C18mm-SS-RH20	20	Creep followed by Recovery

4.5.2 Environment

It was decided to design sealed humidity chambers (fig.4.18), capable of maintaining some humidity generated by a given saturated salt solution (tab.4.4), and minimizing water exchanges with the atmosphere, set at 50 %RH.

Table 4.4: Saturated solution for generating relative humidities in macroscopic tests chambers

RH (%)	11	58	81.2
Saturated solution	$LiCl_2$	NaBr	KCl

Temperature and humidity were monitored with PT100 temperature sensors and a Rotronics capacitive probe. The probes were placed on the wall of the chamber as close as possible to the specimens, fig.4.18.

4.5.3 Loading and centering

The specimens' surfaces were grounded (fig.4.19), and the specimens were stored under endogenous conditions until the start of the test. Grinding aimed to provide specimens with a planar surface suitable for mechanical loading. For creep specimens, a centering operation was performed to ensure that the load is applied correctly so that the stress state would be homogeneous throughout the sample. Centering was necessary to compensate for the geometrical defects of the sample. To do that, the sample was loaded at 500 daN (6 MPa), and the sample was rotated until the relative deviation between each of the 3 LVDT, compared to the average, was less than 20%.

4.5.4 Strain measurement

For each specimen, the axial strain was monitored using three LVDT (Linear Variable Differential Transformer) displacement sensors, installed at 120° in order to be able to compute the longitudinal strain correctly; the measurement was made on a 10.8 cm gauge length, fig.4.19.

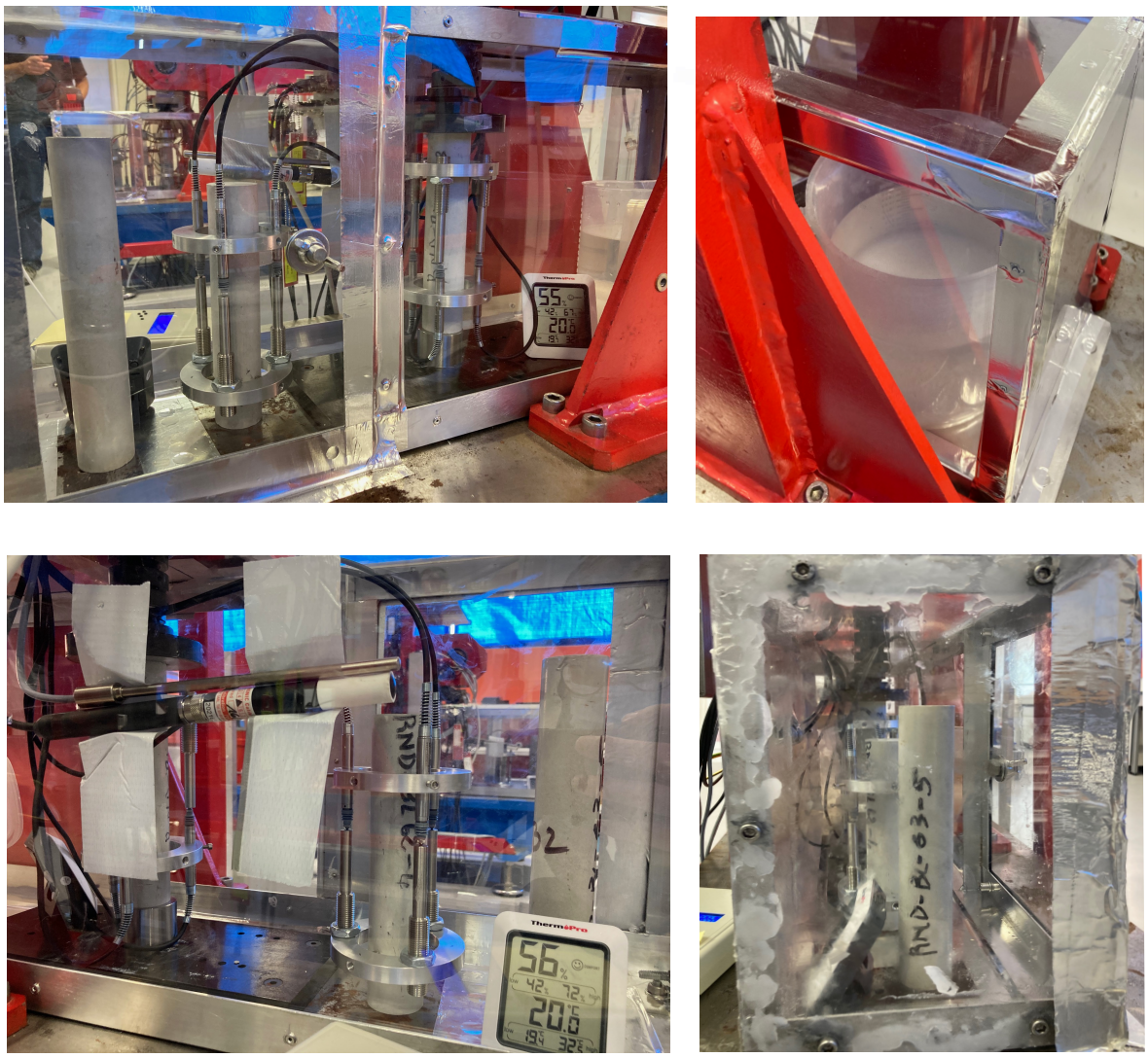

Figure 4.18: Overview of the experimental set up for creep, drying shrinkage and mass loss tests in sealed chambers with relative humidity controlled by saturated salt solution

4.5.5 Results of macroscopic creep and shrinkage tests

Environmental conditions

The temperature and relative humidity histories during the macroscopic campaign are presented in fig.4.20. Although the relative humidity for each testing cell was equilibrated before the beginning of the campaign, it increased quickly when the specimen was introduced in the chamber due to the release of water vapor by the specimen. Then it decreased in a second period until it is stabilized.

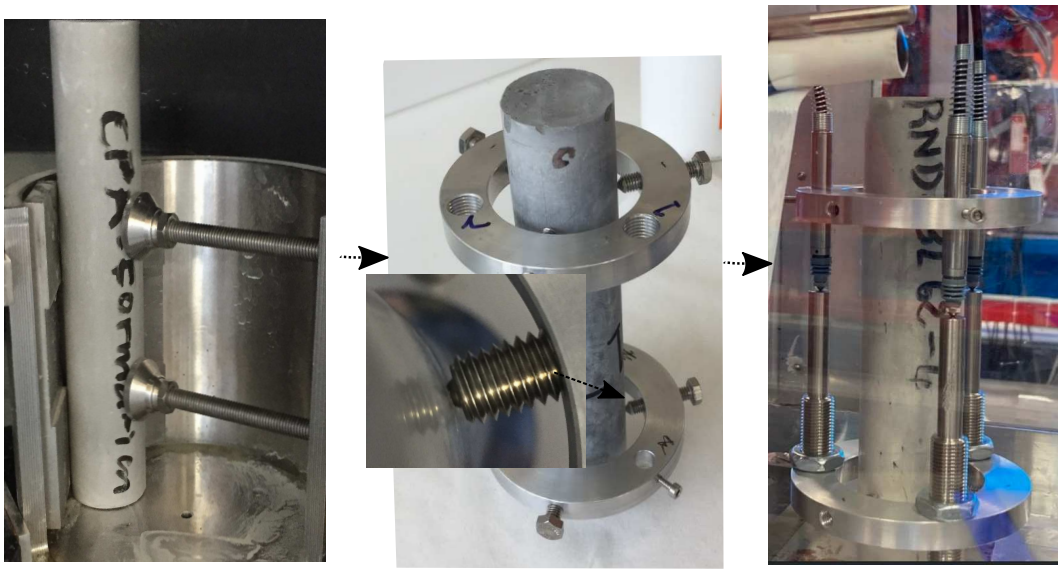

Figure 4.19: Surface preparation for mechanical loading and LVDT installation for strain monitoring

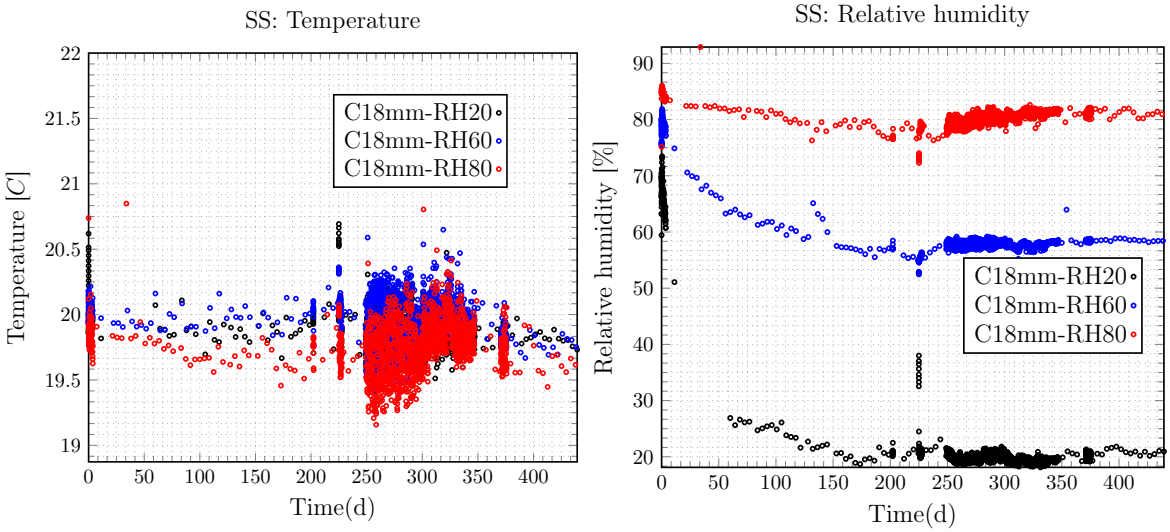

(a) Ambient Temperature

(b) Relative humidity

Figure 4.20: Evolution of temperature and relative humidity in macroscopic tests.

Mass loss

The mass loss results are presented in fig.4.21. It was periodically monitored on a companion specimen for each humidity cell. The mass of all specimens was recorded at the beginning and the end of the tests. The total mass loss is presented in tab.4.5.

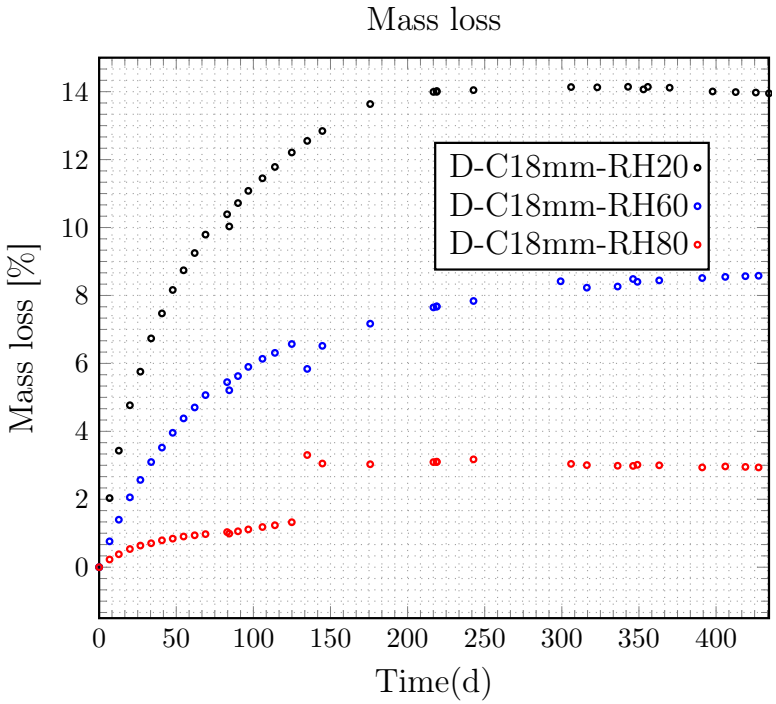

Figure 4.21: Mass loss evolution in macroscopic tests

Table 4.5: Total mass loss of all specimens tested in macroscopic campaign at 80%, 58% and 20 % relative humidities

Specimen	Test	Final mass loss (%)
D-C18mm-SS-RH80	Drying	2.24
DSC-C18mm-SS-RH80	Drying Shrinkage	2.34
TCR-C18mm-SS-RH80	Total Strain	3.31
D-C18mm-SS-RH58	Drying	9.70
DSC-C18mm-SS-RH58	Drying Shrinkage	9.61
TCR-C18mm-SS-RH58	Total Strain	9.41
D-C18mm-SS-RH20	Drying	15.92
DSC-C18mm-SS-RH20	Drying shrinkage	15.76
TCR-C18mm-SS-RH20	Total Strain	16.05

For specimen D-C18-SS-RH80 (mass loss at 80% RH), the mass loss showed (fig.4.21) a significant jump from 1.35% (124.9 days of testing) to 3.30% (135 days of testing). It doubled in 10 days and remained almost constant until the end of the test. One of the possible reasons is that the specimen for mass measurement was regularly exposed to relative humidity between 40-50 % during mass monitoring; this repeated exposure to a gradient of about 30-40%RH, for an extended period, seems to create a cumulated effect, which in turn, caused the discontinuity on the mass loss curve, observed in fig.4.21.

Loading forces and strain results

The mechanical results of the campaign performed on ⌀36×180 mm cylinder, and at 80%, 58% and 20% relative humidity (tab.4.3) are presented in this section. For the sake of clarity, two main groups of results are distinguished: the group labeled as DSC (Drying Shrinkage then Creep) and TCR (Total Creep then Recovery). The following observations

Table 4.6: Some informations on the macroscopic strains

Test	ϵ^{el} Load (µm/m)	ϵ^{el} Unload (µ/m)	Amplitude (µ/m)	Reversible strain (%)
DSC-C18mm-SS-RH20	1150	1150	7360	19
DSC-C18mm-SS-RH58	1000	900	5330	22
DSC-C18mm-SS-RH80	800	950	4600	28
TCR-C18mm-SS-RH20	950	890	-	-
TCR-C18mm-SS-RH58	900	870	9330	18.
TCR-C18mm-SS-RH80	870	1000	5600	26

are drawn:

1. In fig.4.23.a, just a few weeks before unloading, the displacement hit its limits, and the force was not regulated anymore. As a consequence, the specimen started to relax, as seen in fig.4.23.a but the effect on the strain was not significant.

2. In fig.4.22.a, the force in DSC-C18mm-SS-RH80 test increased significantly in the end due to a temporary defect of the loading system.

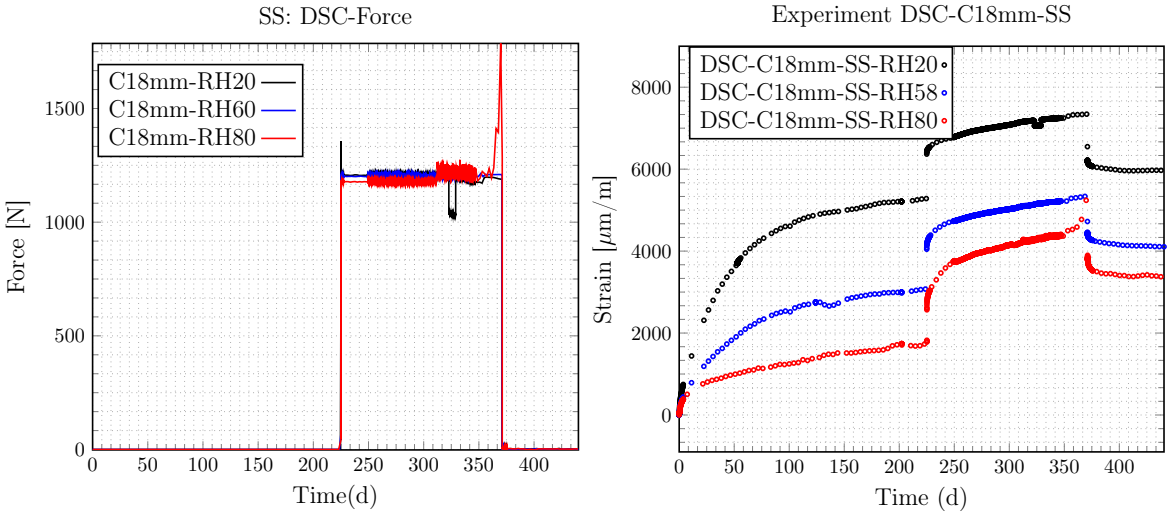

(a) Force

(b) Strain

Figure 4.22: Evolution of total strains for three relative humidity history, with the corresponding loading history during macroscopic tests

3. Instantaneous strains computed from fig.4.23.b and 4.22.b and displayed in tab.4.6, suggest that elastic strain is quite the same at loading and unloading, regardless of the drying and loading history. Moreover, figs.4.23.b-4.22.b show that the rate of deformation after unloading appears to be very slow. The reversible part of the total strain, calculated for all drying and loading history, is found to range between 18 to 28 % of the total strain.

4. In fig.4.23.b, the test TCR-C18mm-SS-RH20 strain result comprises two phases with a one month gap without data. The LVDT sensors had saturated in that period due to excessive strain. The first LVDT was saturated in the testing period of t = 21-58 days, the second between t = 26-58 days and the last between t = 36-58 days; the LVDT were then reset to zero at t = 58 days (note the specimen is kept loaded), for the measurement to continue; then, it was decided to post-process separately, the two periods of measurement. In order to simulate this experiment, the simulation

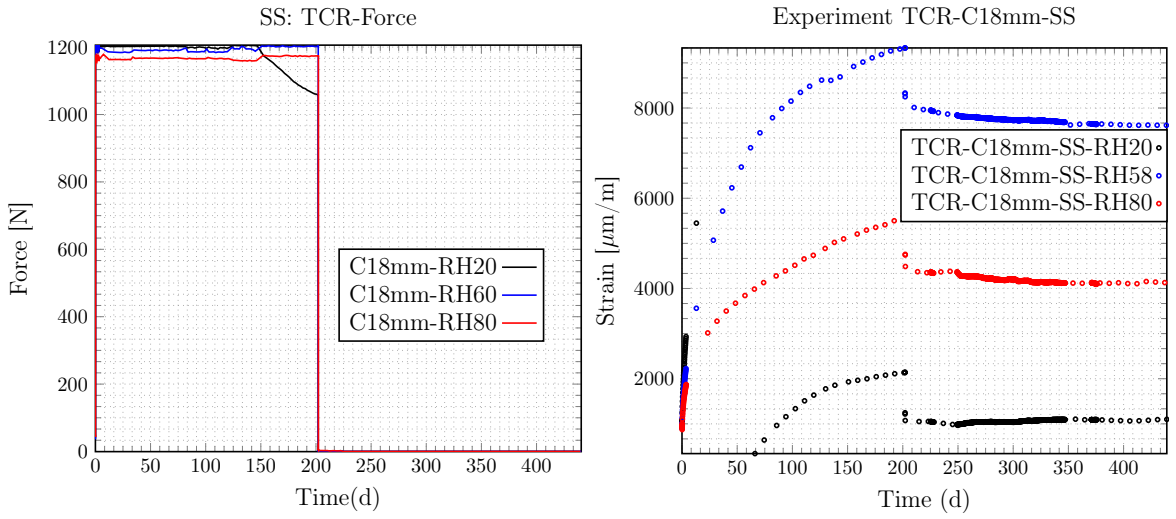

(a) Force

(b) Strain

Figure 4.23: Loading history (a) and the evolution of delayed strains for three relative humidity history (b).

data must be post-processed in such a way that it is also reset to 0 from 58 d. In practice, this means subtracting from the part of the data for $t >= 58$ d, the deformation at $t = 58$ d.

5. The results of total strain displayed in fig.4.23.b show that total creep is accelerated by drying. The lower the relative humidity, the higher the total strain, tab.4.6. The same trend is observed in fig.4.22.b, during the free-load period. The total strain increased with decreasing relative humidity, as expected.

4.6 Analysis and Discussion

4.6.1 Dependence of basic creep on relative humidity

Experimental observations (Bažant et al., 1976; Wittmann, 1970; Abiar, 1986) showed that cement paste and concrete creep less at reduced water content, which is consistent with the present experimental study (fig.4.24). To the best knowledge of the authors, the only experimental data showing this feature of basic creep on cement paste are those of (Wittmann, 1970).

The present contribution allows bridging that gap partly. It is noteworthy that recent advancements in nano-indentation and micro-indentation techniques allows better characterization of the dependence of creep modulus on relative humidity at the micro-scale (Vandamme and Ulm, 2013; Zhang et al., 2014; Frech-Baronet et al., 2017; Chen et al., 2020; Suwanmaneechot et al., 2020), but macroscopic data are still essential for building, testing and improving macroscopic models (Giorla and Dunant, 2018).

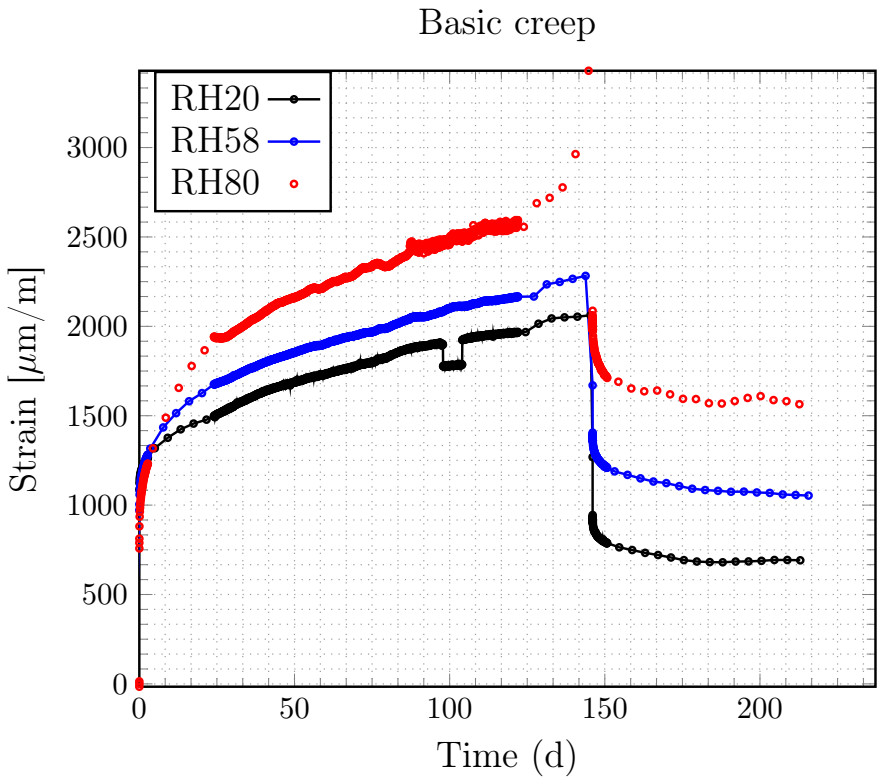

Figure 4.24: Evolution of basic creep strains for different relative humidity levels. The strains correspond to the loading period when moisture equilibrium of samples was reached (tests DSC-C18mm-SS-RH20, DSC-C18mm-SS-RH58 and DSC-C18mm-SS-RH80)

4.6.2 Separation of mechanisms of drying creep and basic creep

One of the difficulties of modeling the creep behavior comes from the difficulty of characterizing the drying and basic creep behavior separately. Even for specimens simultaneously submitted to drying and loading, the mechanisms of basic creep are still activated, and the longer the test duration, the more likely basic creep deformation will develop. Therefore, (short term) accelerated drying tests allow to increase the drying creep component rapidly while limiting the development of basic creep. The ratio of drying creep over basic creep strain is computed, by Eq.5.9, and will be referred to as creep rate factor,

$$C^F = \frac{J^{TC} - J^{BC}}{J^{BC}} \tag{4.2}$$

where C^F [-] is the creep rate factor inspired but different from the one defined by (Vlahinić et al., 2012). J^{TC} [μm/m/MPa] the total creep compliance, J^{BC} [μm/m/MPa] the basic creep compliance.

The basic creep data used for calculation is obtained from a uniaxial compressive creep test under endogenous conditions carried out on similar material tested at 90 days age (Huang, 2018). The creep rate factor evaluates the drying strain contribution to the total strain of various materials subjected to drying. Fig.4.25 compares the evolution of creep rate factors with time for microscopic and macroscopic testing, and it tells us that the basic creep component is low in accelerated drying tests.

These findings are of first importance since accelerated drying tests like the one performed in this study make it easier to identify the drying part of the models such in (Benboudjema et al., 2001; Bažant et al., 2004; Hilaire, 2014; Jirásek and Havlásek, 2014; Sellier

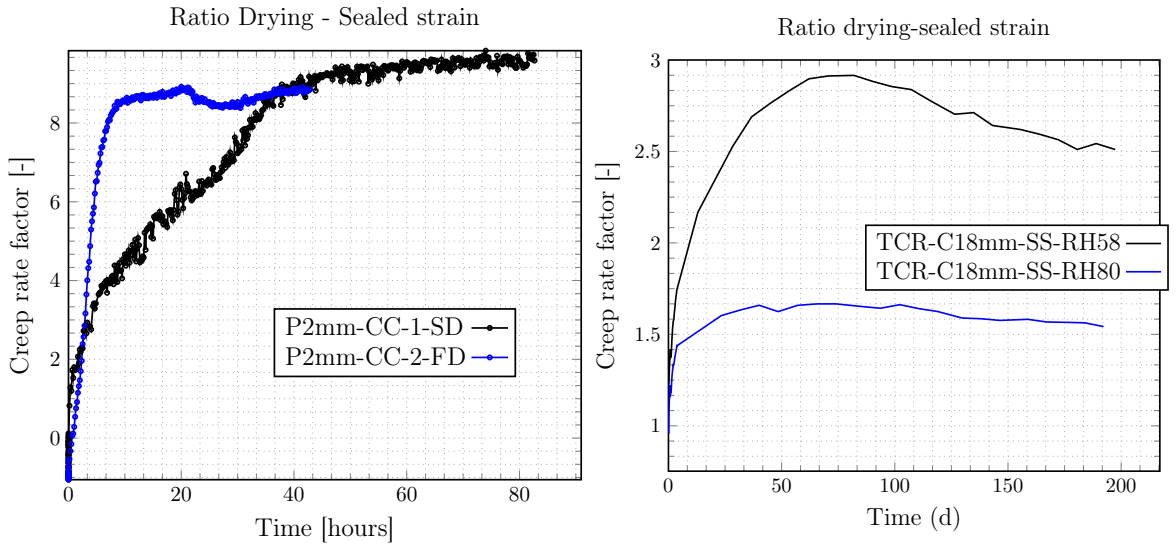

(a) Microscopic

(b) Macroscopic

Figure 4.25: Evolution of creep rate factor vs. time (inspired from (Vlahinić et al., 2012)) for microscopic tests (P2mm-CC-1-SD, P2mm-CC-2-FD) in climatic chamber and macroscopic tests (TCR-SS-RH80 and TCR-SS-RH60) using saturated salt solutions technique.

et al., 2016; Rahimi-Aghdam et al., 2019).

4.6.3 Shrinkage vs. mass loss

The evolution of drying shrinkage with mass loss is studied, for microscopic tests (10×10×2 mm geometry) and macroscopic tests (⌀36×180 mm geometry) and displayed shown in fig.4.26.a,b.

The following remarks can be drawn:

- Microscopic tests: the relationship between drying shrinkage and mass loss displayed in fig.4.26.a does not depend on the drying rate. Three regimes are observed: (1) in the first stage (80 to 50%), drying shrinkage evolves linearly with mass loss; (2) in the second stage (50 to 20%), mass loss continues to increase without subsequent drying shrinkage, when the relative humidity reaches the constant value of 20%; and (3) in the last stage drying shrinkage increases linearly again with mass loss. Firstly, it is interesting to note that the linear relationship of drying shrinkage with mass loss suggests that drying has not caused cracking. Hence the drying shrinkage corresponds to the intrinsic behavior of the material. It is also interesting to analyze the source of the plateau observed around a shrinkage of about 3000 µm/m. It corresponds to a relative humidity of 40-50 % as seen on the drying length change isotherm, fig.4.26.c. Successive experimental works on sorption isotherm and drying shrinkage (Baroghel-Bouny et al., 1999; Baroghel-Bouny, 2007; Jennings, 2008; Jennings et al., 2015; Maruyama et al., 2014, 2015) reveal a bimodal behavior of drying shrinkage with relative humidity. The corresponding value of the inflexion point is found to be 44% (Baroghel-Bouny et al., 1999), 50% (Baroghel-Bouny, 2007), 54% (Jennings, 2008), 45% (Jennings et al., 2015) and 40 % (Maruyama et al., 2014). In all those investigations, the driving mechanism of volumetric change was attributed (i) to capillary stress for relative humidity above the inflexion point and (ii) to surface tension for RH below the inflexion point. Similarly, we think that in fig.4.26.a,b,

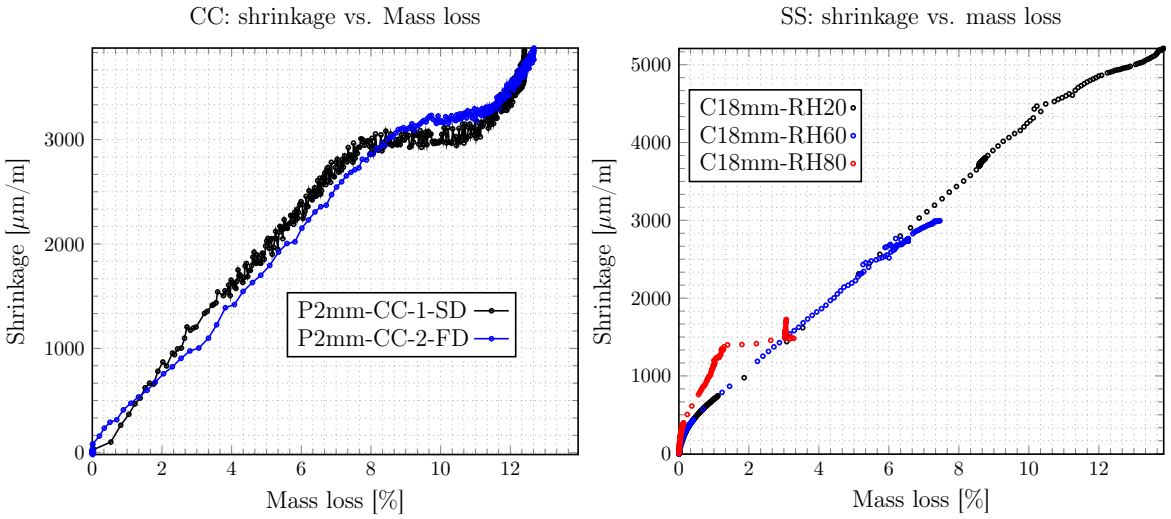

(a) Microscopic testing

(b) Macroscopic testing

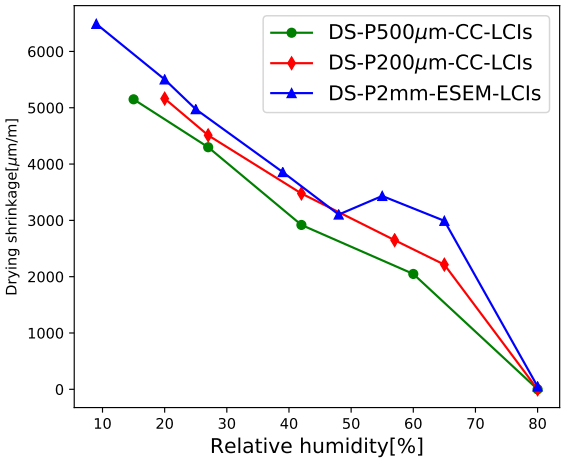

(c) Relationship between drying shrinkage at equilibrium with relative humidity (Kinda et al., 2021)

Figure 4.26: Evolution of Drying shrinkage vs. mass loss at different scales: microscopic testing (a), macroscopic testing (b); and relationship between drying shrinkage at equilibrium with relative humidity (c).

the capillary pressure and the disjoining pressure are at stake during stages 1 and 3 respectively.

- Macroscopic tests: in fig.4.26.b, three stages of evolution are distinguished, for all tested specimens. For specimens exposed to 60% and 20 %RH, a rapid increase of shrinkage with mass loss is observed at the beginning, followed by a linear evolution with slope 335 µm/m/(1.% mass loss), and in last stage, the rate is decreasing progressively. Regarding the relationship of specimens submitted to drying at 80%RH, the evolution is fast and non-linear at the beginning, then linear with slope 850 µm/m/(1%) for mass loss at middle range and at the end, mass loss does not cause any shrinkage.

4.6.4 Relation between creep and shrinkage in microscopic tests

The evolution of uniaxial drying creep compliance with drying shrinkage is plotted in fig.4.27.a for P2mm-CC-1-SD (slow drying rate in the climatic chamber) and P2mm-ESEM-

FD (fast drying rate in ESEM). In these uniaxial loading tests, regardless of the drying rate, a bilinear relationship is observed with the inflection point around 3000 µm/m, which is the same value of drying shrinkage observed in shrinkage vs. mass loss (previous section). However, for the biaxial creep test (fig.4.27.b), the drying creep strain evolves linearly with drying shrinkage for drying shrinkage range 0-3000 µm, which corresponds to a relative humidity range from 100 to 50 % (fig.4.26.c). This linearity of drying creep vs. drying shrinkage was previously observed by Day et al. (1984) for cement paste and by Gamble and L.J. (1978) for concrete.

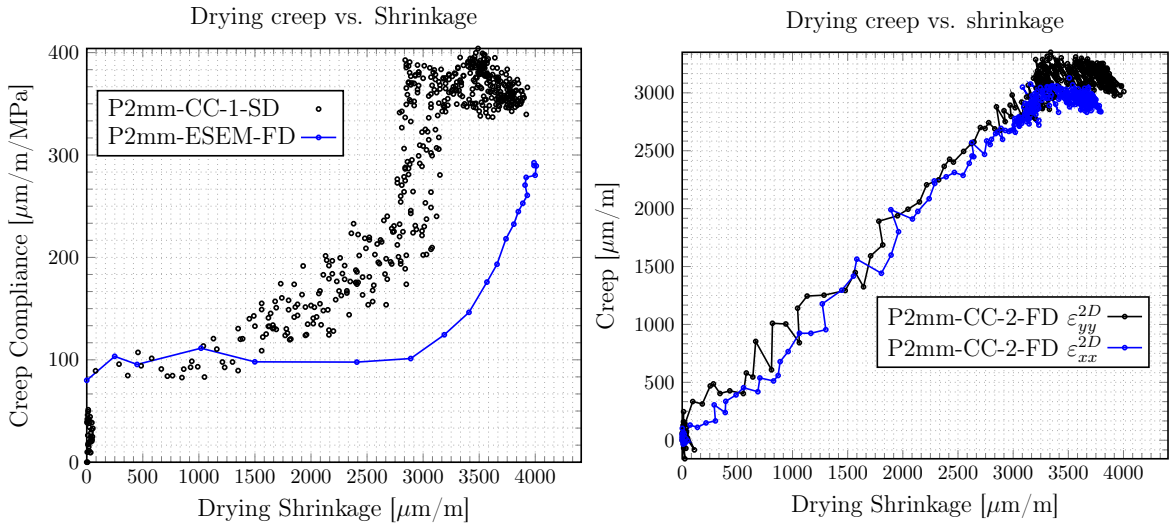

(a) Axial creep

(b) Biaxial creep

Figure 4.27: Drying creep vs. Drying shrinkage

4.6.5 Investigation on the kinetics of drying creep

The drying creep relation with mass loss in the case of slow drying (P2mm-CC-1-SD), and fast drying (P2mm-CC-2-FD) is linear, and the coefficient does not depend that much on the drying rate (fig.4.29).

The linearity tells us that the drying creep response is driven by the loss of water, and the structural effect on drying creep is avoided or limited in the way that its impact is not significant. In other words, the intrinsic drying creep and drying have the same kinetics. This is very interesting since it suggests that a model where the rate of drying creep rate is linearly proportional to the rate of variation of saturation or humidity at material points will be suitable for retrieving the intrinsic drying creep behavior of cement paste. Such a model was proposed in the past by (Bažant and Chern, 1985), and as a starting point, it will be interesting to test this model against the current experimental data.

Moreover, earlier investigation of drying shrinkage by means DIC method, both in ESEM and climatic chamber, have shown that using specimens of 10×10×2 mm geometry allows assessing experimentally the intrinsic drying shrinkage. Therefore, skin-micro-cracking contribution to drying shrinkage and creep of small size in the present study could be neglected. The two results analyzed together demonstrate that the characterization of drying shrinkage and drying creep behavior of cement paste at the material scale is possible with the new techniques of characterization presented in this study.

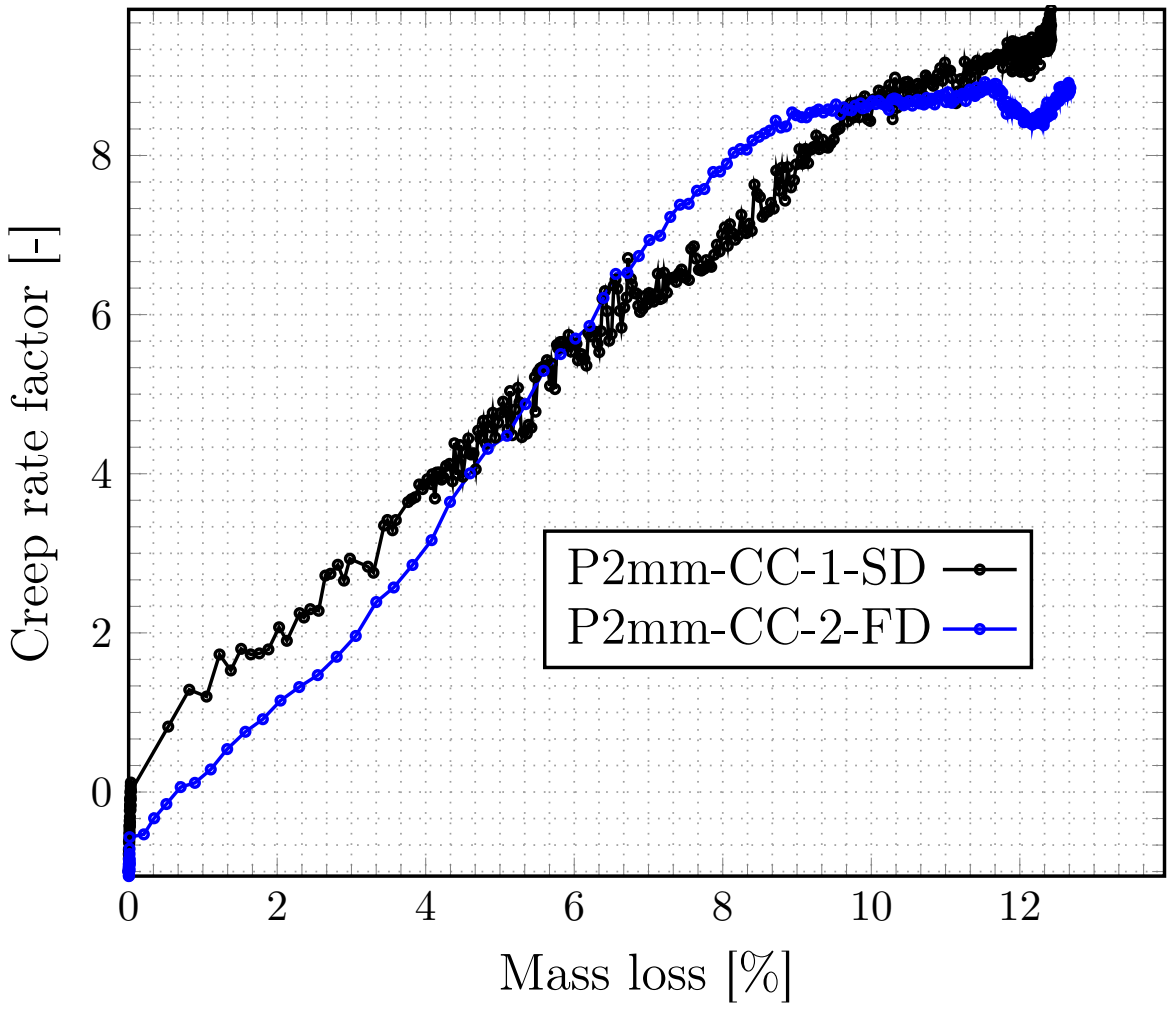

Figure 4.28: Microscopic

Figure 4.29: Evolution of creep rate factor vs. mass loss for microscopic tests (P2mm-CC-1-SD, P2mm-CC-2-FD) rate in climatic chamber

4.7 Conclusion

The objective of this experimental campaign was to gain knowledge about the influence of relative humidity, drying rate, and size effects on creep. The tests were performed on paste samples (w/c = 0.52). The innovative part of the study was the development of creep tests in ESEM and climatic chamber under axial and biaxial mechanical loading. The techniques provide the opportunity to investigate the relationship between drying, free drying shrinkage, and intrinsic drying creep, within a short amount of time, for a large range of relative humidity and drying rates. The method made possible the assessment of drying shrinkage, free of skin cracking (Kinda et al., 2021), avoiding the part of Pickett effect (Pickett, 1942) attributed to cracking and allowing to investigate the intrinsic mechanism of drying creep.

The relationship between mass loss, shrinkage, drying creep, and basic creep was examined for both classical macroscopic creep tests (⌀36×180 mm cylinder) and original microscopic creep tests (10×10×2 mm prism) and the main results are summarized as follows:

1. The long-term kinetics of basic creep is lower at reduced humidity.

2. Drying creep tests on small slabs allow to investigate the purely drying creep behavior of the material since interaction with basic creep and cracking are low.

3. Drying shrinkage as well as drying creep evolves almost linearly with mass loss.

4. Drying and drying creep have the same kinetics.

The results are regarded as important with respect to the prediction of creep strains when the environmental humidity changes. From these results, two perspectives are listed below:

- The results presented in this chapter could assist in testing or building creep models for concrete structures, which are able to take into account the effect of drying rate, size, and relative humidity on the creep modulus. This is a critical point when such models are used at the structure level because the experiments used in the lab to calibrate the model exhibit much faster drying than the drying of structures.

- The innovative creep test techniques developed in this study, in ESEM, and in a climatic chamber, are down-scalable. Even though we have focused the attention on mean strain measurements, DIC, which has been used for the strain assessment, also allows for full-field measurements at all scales, which means that the present techniques are also valuable for studying the interaction between drying creep and the micro-structure at smaller scales. It all depends on the possibility of acquiring images of sufficient quality for DIC processing.

References

G. Abiar. *cinétique de dessiccation et déformations différées du béton (analyse et modélisation)*. PhD thesis, 1986. 113

P. Acker and F-J. Ulm. Creep and shrinkage of concrete: physical origins and practical measurements. *Nuclear Engineering and Design*, 203(2):143–158, 2001. 95

V. Baroghel-Bouny. Water vapour sorption experiments on hardened cementitious materials: Part i: Essential tool for analysis of hygral behaviour and its relation to pore structure. *Cement and Concrete Research*, 37(3):414–437, 2007. 115

V. Baroghel-Bouny, M. Mainguy, T. Lassabatere, and O. Coussy. Characterization and identification of equilibrium and transfer moisture properties for ordinary and high-performance cementitious materials. *Cement and concrete research*, 29(8):1225–1238, 1999. 95, 115

Z. P. Bazant and J. C. Chern. Concrete creep at variable humidity: constitutive law and mechanism. *Materials and Structures*, 18(1), 1985. ISSN 1871-6873. 95

Z. P. Bažant, A. A. Asghari, and J. Schmidt. Experimental Study of creep of hardened concrete portland cement paste at variable water content. *Materials and Structures*, 1976. 95

Z. P. Bažant, A. A. Asghari, and J. Schmidt. Experimental study of creep of hardened portland cement paste at variable water content. *Matériaux et Constructions*, 9(4):279–290, 1976. ISSN 0025-5432, 1871-6873. 113

Z.P. Bažant and J.C. Chern. Concrete creep at variable humidity: constitutive law and mechanism. *Materials and structures*, 18(1):1, 1985. 117

Z.P. Bažant and X. Yunping. Drying creep of concrete: constitutive model and new experiments separating its mechanisms. *Materials and Structures*, 27(1):3–14, 1994. 95

Z.P Bažant, G. Cusatis, and L. Cedolin. Temperature effect on concrete creep modeled by microprestress-solidification theory. *Journal of engineering mechanics*, 130(6):691–699, 2004. 114

F. Benboudjema. *Modélisation des déformations differées du béton sous sollicitation biaxiales. Application aux enceintes de confinement de bâtiments réacteurs des centrales nucléaires*. PhD thesis, Université de Marne la Vallée, 2002. 95

F. Benboudjema and J-M Torrenti. Modelling desiccation shrinkage of large structures. In *EPJ Web of conferences*, volume 6, 2001. 95

F. Benboudjema, F. Meftah, A. Sellier, G. Heinfling, and JM. Torrenti. A basic creep model for concrete subjected to multiaxial loads. In *Fourth International Conference on Fracture Mechanics of Concrete and Concrete Structures*, pages 162–168, 2001. 114

F. Benboudjema, F. Meftah, and J.M. Torrenti. Interaction between drying, shrinkage, creep and cracking phenomena in concrete. *Engineering Structures*, 27(2):239–250, 2005. 95

M. Bertin. *Mechanical and fatigue properties of bellows determined with Integrated DIC and IR Thermography*. PhD thesis, Université Paris-Saclay, 2016. 104

H. Cagnon, T. Vidal, A. Sellier, X. Bourbon, and G. Camps. Cement and Concrete Research Drying creep in cyclic humidity conditions. *Cement and Concrete Research*, 76:91–97, 2015. ISSN 0008-8846. 95

L. Charpin, TO. Sow, X. De Pradel, F. Hamon, and J-P Mathieu. Numerical simulation of 12 years long biaxial creep tests: Efficiency of assuming a constant poisson's ratio. pages 997–1004, 2017. 95

Z. Chen, J. Frech-Baronet, and L. Sorelli. Microindentation two-fold creep model for characterizing short- and long-term creep behavior of cement pastes. *Mechanics of Materials*, 2020. ISSN 0167-6636. 113

R.L. Day, P. Cuffaro, and J.M. Illston. The effect of rate of drying on the drying creep of hardened cement paste. *Cement and Concrete Research*, 14(3):329–338, 1984. 95, 117

C. De Sa, F. Benboudjema, M. Thiery, and J. Sicard. Analysis of microcracking induced by differential drying shrinkage. *Cement and Concrete Composites*, 30(10):947–956, 2008. 95

A. Foucault, S. Michel-Ponnelle, and E. Galenne. A new creep model for npp containment behaviour prediction. In *International conference on Numerical modeling Strategies for sustainable concrete structures*, 2012. 95

J. Frech-Baronet, L. Sorelli, and J. P. Charron. New evidences on the effect of the internal relative humidity on the creep and relaxation behaviour of a cement paste by micro-indentation techniques. *Cement and Concrete Research*, 91:39–51, 2017. 113

B.R. Gamble and Parott L.J. Creep of concrete in compression during drying and wetting. *Magazine of concrete research*, 30(104):129–138, 1978. 117

A. B. Giorla and C. F. Dunant. Microstructural effects in the simulation of creep of concrete. *Cement and Concrete Research*, 105:44–53, 2018. 113

L. Granger. *Comportement différé du béton dans les enceintes de centrales nucléaires: analyse et modélisation*. PhD thesis, Ecole Nationale des ponts et Chaussées, 1995. 95

A. Hilaire. *Etude des déformations différées des bétons en compression et en traction, du jeune au long terme : application aux enceintes de confinement*. Theses, École normale supérieure de Cachan - ENS Cachan, 2014. 95, 114

S. Huang. *Ageing behaviour of concrete creep : application to the VeRCoRs concrete*. Thesis, 2018. 114

C-L. Hwang and J.F. Young. Drying shrinkage of portland cement pastes i. microcracking during drying. *Cement and Concrete Research*, 14(4):585–594, 1984. 95

T. Ishida and T. Wang. Future of multiscale modelling of concrete-toward a full integration of cement chemistry and structural engineering. *Rilem Technical Letters*, pages 17–24, 2018. 95

H.M. Jennings. Refinements to colloid model of c-s-h in cement: CM-II. *Cement and Concrete Research*, 38(3):275–289, 2008. 115

H.M. Jennings, A. Kumar, and G. Sant. Quantitative discrimination of the nano-pore-structure of cement paste during drying: New insights from water sorption isotherms. *Cement and Concrete Research*, 76:27–36, 2015. 115

M. Jirásek and P. Havlásek. Microprestress–solidification theory of concrete creep: Reformulation and improvement. *Cement and Concrete Research*, 60:51–62, 2014. 114

J. Kinda, L. Charpin, F. Benboudjema, A. Bourdot, S. Michel-Ponnelle, and A. Bourtef. Investigation of drying shrinkage of cement based materials assisted by digital image correlation. 2021. 116, 118

I. Maruyama, Y. Nishioka, G. Igarashi, and K. Matsui. Microstructural and bulk property changes in hardened cement paste during the first drying process. *Cement and Concrete Research*, 58:20–34, 2014. 115

I. Maruyama, G. Igarashi, and Y. Nishioka. Bimodal behavior of csh interpreted from short-term length change and water vapor sorption isotherms of hardened cement paste. *Cement and Concrete Research*, 73:158–168, 2015. 115

J.P. Mathieu, L. Charpin, P. Sémété, C. Toulemonde, G.H.J. Boulant, and F. Taillade. Temperature and humidity-driven ageing of the VeRCoRs mock-up. In *Computational Modelling of Concrete and Concrete Structures*, 2018. 95

C.M. Neubauer and H.M. Jennings. The use of digital images to determine deformation throughout a microstructure part ii application to cement paste. *Journal of Materials Science*, 35(22):5751–5765, 2000. 95

G. Pickett. The effect of change in moisture-content on the crepe of concrete under a sustained load. In *Journal Proceedings*, volume 38, pages 333–356, 1942. 95, 118

S. Rahimi-Aghdam, Z. P. Bažant, and G. Cusatis. Extended microprestress-solidification theory (XMPS) for long-term creep and diffusion size effect in concrete at variable environment. *Journal of Engineering Mechanics*, 145(2), 2019. 95, 115

N. Reviron. *Etude du fluage des bétons en traction. Application aux enceintes de confinement des centrales nucléaires à eau sous pression.* PhD thesis, Ecole Normale Supérieure de Cachan, 2009. 95

H. Samouh, E. Rozière, and A. Loukili. Experimental and numerical study of the relative humidity effect on drying shrinkage and cracking of self-consolidating concrete. *Cement and Concrete Research*, 115:519–529, 2019. 95

A. Sellier, S. Multon, L. Buffo-Lacarrière, T. Vidal, X. Bourbon, and G. Camps. Concrete creep modelling for structural applications: non-linearity, multi-axiality, hydration, temperature and drying effects. *Cement and Concrete Research*, 79:301–315, 2016. 114

P. Suwanmaneechot, A. Aili, and I. Maruyama. Creep behavior of csh under different drying relative humidities: Interpretation of microindentation tests and sorption measurements by multi-scale analysis. *Cement and Concrete Research*, 132, 2020. 113

Z. Tomičević, F. Hild, and S. Roux. Mechanics-aided digital image correlation. *The Journal of Strain Analysis for Engineering Design*, 48(5):330–343, 2013. 97, 100

P. Turcry, A. Aït-Mokhtar, K. Namoulniara, and F. Gendron. Investigation expérimentale de l'influence de l'état hydrique sur la cinétique de carbonatation accélérée de pâtes de ciment. *S27-Couplage durabilité-Comportement mécanique dans les structures de génie civil*, 2017. Publisher: AFM, Association Française de Mécanique. 106

M. Vandamme and F.-J. Ulm. Nanoindentation investigation of creep properties of calcium silicate hydrates. *Cement and Concrete Research*, 52:38–52, 2013. 113

I. Vlahinić, J. J. Thomas, H. M. Jennings, and J. E. Andrade. Transient creep effects and the lubricating power of water in materials ranging from paper to concrete and kevlar. *Journal of the Mechanics and Physics of Solids*, 60(7):1350–1362, 2012. viii, 114, 115

F.H. Wittmann and P.E. Roelfstra. Total deformation of loaded drying concrete. *Cement and Concrete Research*, 10(5):601–610, 1980. 95

V.F. Wittmann. Einflufl des feuchtigkeitsgehahes auf das friechen des fementsteines. *Rheologica Acta*, page 6, 1970. 113

Q. Zhang, R. Le Roy, M. Vandamme, and B. Zuber. Long-term creep properties of cementitious materials: Comparing microindentation testing with macroscopic uniaxial compressive testing. *Cement and Concrete Research*, 58:89–98, 2014. 113

Chapter 5

Creep of cement paste at variable humidity: Pickett effect and size effect - numerical simulations

Introduction

A part of the concrete containment buildings (CBB) in French nuclear power plants operated by EDF are double-walled. Concrete of the post-tensioned inner containment building plays a major role as a barrier against radiological release during a hypothetical accident. The leak-tightness of the inner CCB vastly depends on the pre-stress level. If it becomes too low due to the delayed strains, some parts of the structure may experience tension during the integrated leak rate test (performed every ten years) or an accident, inducing cracking and increased leakage. Therefore, EDF studies drying, creep, and shrinkage of concrete both from a theoretical (Sanahuja, 2013; Adia, 2017; Guihard et al., 2020) and an experimental point of view (Reviron, 2009; Huang, 2018; Charpin et al., 2018b). Those experiments aim at building simulation tools dedicated to the prediction of strains in CCBs, which requires properly calibrated models (Charpin et al., 2017; Mathieu et al., 2018; Charpin et al., 2018a). Often, models are calibrated on laboratory tests on rather small samples, while CCBs are very large structures. These different concrete thicknesses induce vastly different drying kinetics. Thus, concrete constitutive laws should be able to correctly take into account the effect of drying rate on delayed strains (creep, shrinkage) of concrete. As an introduction to this subject, experimental data from the literature (Day et al., 1984) were simulated with the delayed strains law used at EDF R&D (Benboudjema, 2002; Foucault et al., 2012) and the microprestress-solidification law (Bažant et al., 1997; Bažant et al., 2004; Jirásek and Havlásek, 2014). It was shown that both those constitutive laws can reproduce the main features of the shrinkage and creep tests, but also that the experimental program lacked some information to be truly discriminant (Kinda et al., 2018). This observation has motivated further experimental developments.
The present study presents a numerical analysis of the experimental results presented in chapter. 4. The objectives of this numerical study are (i) to simulate the different experimental results obtained from new protocols developed in this thesis, (ii) investigate the drying rate effect on drying creep and drying shrinkage through numerical analysis of experiments, and (iii) to compare different modeling approaches for drying creep (Bažant et al., 2014). To meet these goals, the chapter is divided into four parts. First, the experiments to be tested with the constitutive laws are described briefly. Second, the description of the delayed strains law used at EDF R&D (Charpin et al., 2017) is given as well

as the microprestress-solidification law (Jirásek and Havlásek, 2014). Third, the numerical analysis of the experiments is presented. Last, the drying rate effect and the different modeling approaches of drying creep are discussed.

5.1 Description of experimental data

The experiments were performed on specimens of two sizes: ⌀36×180 mm cylinders and 10×10×2 mm thin slabs. Shrinkage and creep were monitored for each test. Different techniques for controlling humidity were tested, including ESEM, Climatic Chamber, and Saturated Salt Solution. The designation of each test includes specimen geometry and drying thickness, plus the relative humidity control system and the rate of drying. For the sake of clarity, the abbreviations used to describe the experiments are listed in tab.5.1.

BC	Basic Creep
DSC	Drying Shrinkage and Creep
TCR	Total Creep and Recovery
LCIs	Length Change Isotherm
P2mm	Prism of 2 mm thickness
C18mm	Cylinder of 18 mm radius
SD	Slow Drying
FD	Fast Drying
CC	Climatic Chamber
SS	Saturated Solution[1]
RH20	20% Relative humidity
RH58	58% Relative humidity
RH80	80% Relative humidity

Table 5.1: Abbreviations used to describe experiments

The different tests we will simulate are given in tab.5.2; and the drying humidity conditions of these tests are presented in Fig.5.1a, 5.1b, 5.1c. Chapter 4 gives detailed description of the experiments. These experimental results provide a basis for establishing the correct theoretical model, especially regarding the relative humidity effects on creep.

Test	curing conditions	Geometry (mm)	Creep	Shrinkage	Mass
P2mm-ESEM-FD	80%RH	10×10×2	✓	✓	-
P2mm-ESEM-SD	Endogenous	10×10×2	✓	✓	-
DS-P500µm-CC-LCIs	Endogenous	10×10×0.5	-	✓	-
P2mm-CC-1-SD	80%RH	10×10×2	✓	✓	✓
P2mm-CC-2-FD	80%RH	10×10×2	✓	✓	✓
BC-C15mm-SS-RH95 (Tsitova 2021)	Endogenous	⌀30×60	✓	✓	-
DSC-C18mm-SS-RH80	Endogenous	⌀36×180	✓	✓	✓
DSC-C18mm-SS-RH58	Endogenous	⌀36×180	✓	✓	✓
DSC-C18mm-SS-RH20	Endogenous	⌀36×180	✓	✓	✓
TCR-C18mm-SS-RH80	Endogenous	⌀36×180	✓	✓	✓
TCR-C18mm-SS-RH58	Endogenous	⌀36×180	✓	✓	✓
TCR-C18mm-SS-RH20	Endogenous	⌀36×180	✓	✓	✓

Table 5.2: Summary of experimental campaign undertaken on cement paste.

Let's bring to attention that the basic creep data comes from Tsitova's thesis, which

[1] Saturated salt solution

started in 2018 and currently in progress within the framework of a tripartite partnership (CEA, LMT, and EDF).

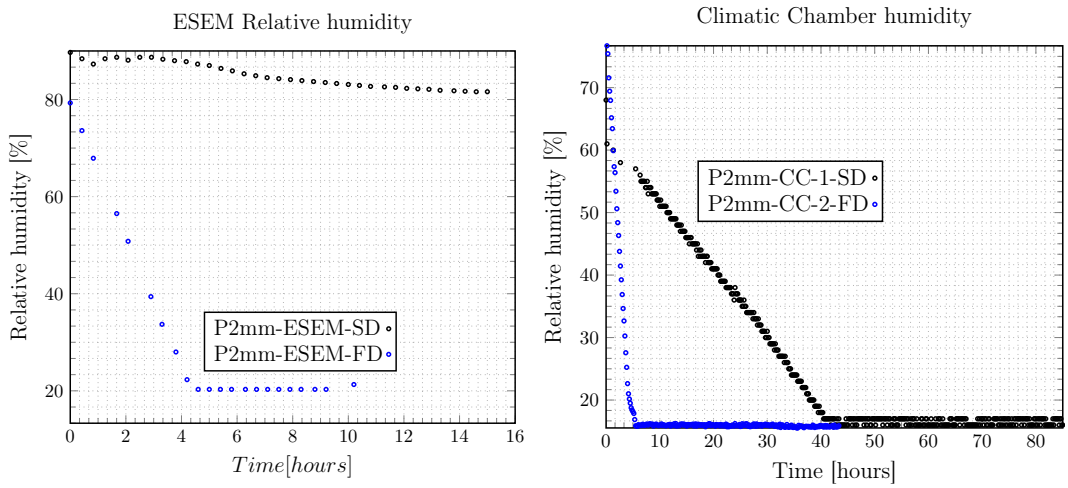

(a) ESEM

(b) Climatic chamber

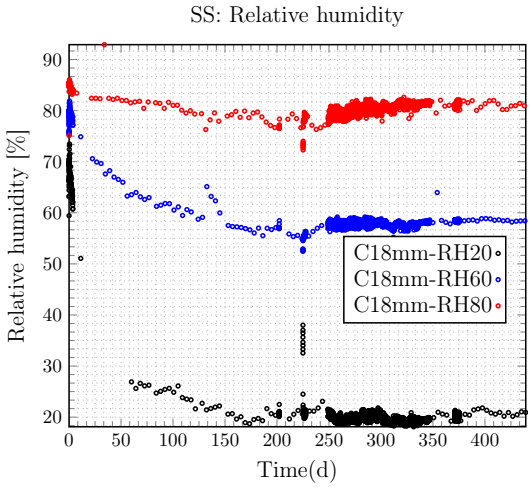

(c) Saturated Salt Solution

Figure 5.1: Drying conditions of different tests to be simulated

5.2 Description of the mechanical models

In this section, the models used for numerical analysis of the experiments are introduced. Two models are considered for this analysis: the first one is the so-called Burger model (Charpin et al., 2017), and the second is the Micro-prestress solidification (MPS) model (Jirásek and Havlásek, 2014).

5.2.1 Burger model

The Burger model (Charpin et al., 2017) was originally developed in the framework of linear viscoelasticity (Benboudjema et al., 2001). The basic creep part was later improved (Foucault et al., 2012) based on the work of (Sellier and Buffo-Lacarriere, 2009). The desiccation creep component is inspired by the work of (Bazant and Chern, 1985). The model

is built as a sum of four components

$$\dot{\boldsymbol{\epsilon}} = \dot{\boldsymbol{\epsilon}}^{el} + \dot{\boldsymbol{\epsilon}}^{bc} + \dot{\boldsymbol{\epsilon}}^{shr} + \dot{\boldsymbol{\epsilon}}^{dc} \tag{5.1}$$

with $\dot{\boldsymbol{\epsilon}}^{el}$ the elastic strain tensor , $\dot{\boldsymbol{\epsilon}}^{bc}$ the basic creep strain tensor, $\dot{\boldsymbol{\epsilon}}^{shr}$ the drying shrinkage strain tensor and $\dot{\boldsymbol{\epsilon}}^{dc}$ the desiccation creep strain tensor. The original model was implemented in Code−Aster, (R7.01.35, 2017). In the original version, the rate of variation of drying shrinkage was taken proportional to the variation of water content, $\dot{\boldsymbol{\epsilon}}^{shr} = k^{\mathrm{C}}\dot{\mathrm{C}}\mathbf{1}$, where k^{C} is a constant coefficient of proportionality. Based on experimental observations on cement paste, drying shrinkage at equilibrium as a function of relative humidity is quasi-linear for a wide range of relative humidity (100-20%) (Chapter 2). Then, the drying shrinkage equation of the model is modified to read: $\dot{\boldsymbol{\epsilon}}^{shr} = k^{h}\dot{h}\mathbf{1}$, where k^{h} is a constant coefficient of proportionality. Desiccation creep is modeled by the law proposed by Bazant and Chern (1985); Benboudjema et al. (2005), which relates the desiccation strain rate to the variation of internal relative humidity, expressed by

$$\dot{\boldsymbol{\epsilon}}^{dc} = |\dot{h}|\eta^{fd}\boldsymbol{\sigma} \tag{5.2}$$

A zero Poisson's ratio is associated with the desiccation creep, according to this model. This hypothesis was discussed elsewhere (Charpin et al., 2017). Further details on the model equations are given in appendix.5.6.

5.2.2 Micro-Prestress Solidification (MPS) model

The model was introduced by Jirásek and Havlásek (2014). It is built in the framework of aging viscoelasticity, and creep is completely described by a unique compliance function J depending on both the current time (t) and the loading time (t').

The total strain tensor reads Eq.5.16:

$$\boldsymbol{\varepsilon}(t) = \boldsymbol{\varepsilon}^{el} + \boldsymbol{\varepsilon}^{ve}(t) + \boldsymbol{\varepsilon}^{f}(t) + \boldsymbol{\varepsilon}^{shr}(t) \tag{5.3}$$

with $\boldsymbol{\varepsilon}^{el}$ the instantaneous strain, $\boldsymbol{\varepsilon}^{ve}$ the viscoelastic component of basic creep, $\boldsymbol{\varepsilon}^{f}$ the flow strain; an aging dashpot with viscosity dependent on microprestress S, for long term creep, $\boldsymbol{\varepsilon}^{shr}(t)$ the volumetric change due to drying. Desiccation creep in this model is coupled with the viscous flow term $\boldsymbol{\varepsilon}^{f}(t)$, by considering the viscosity as temperature-humidity dependent (Jirásek and Havlásek, 2014). Further details on the model equations are given in section.5.15, and on the implementation given in (Jirásek and Havlásek, 2014).

The model has been implemented in Code−Aster and validated by comparison to literature data (Adia et al., 2018).

5.3 Numerical analysis of experiments

For simulation of structure behavior, models are often calibrated on laboratory tests on rather small samples. However, structures like CCBs are very large. Thus, the concrete constitutive laws should be able to correctly take into account this size effect. In this study, two delayed strain models with two different modeling approaches of drying creep have been investigated. In the Burger model (sect.5.2.1), desiccation creep is modeled by stress-induced shrinkage theory, (Bazant and Chern, 1985), while in the MPS model, the microprestress relaxation theory (Bažant et al., 1997) is considered. One of the major objectives of these simulations is to establish an experimentally well-supported numerical

Table 5.3: Boundary conditions. u^0: uniform displacement, ND: Non Drying Surface, DSF: Drying Surface

Face	3D	2D
Top	F_z, u_z^0, ND	F_y, u_y^0, ND
Bottom	$u_z = 0$, ND	$u_y = 0$, ND
Left	$u_x = 0$, ND	$u_x = 0$, ND
Right	DSF, u	DSF, u
Front	F_y, u_y^0, ND	–
Back	DSF, u	–

model for drying creep. In the case of drying, a full water transport analysis is necessary. The drying model with the identification procedure has been detailed in chapter.3. The identified model is used to simulate drying in order to get the water content evolution. To obtain the optimal values of the model parameters, we use ADAO (a module for Data Assimilation and Optimization, http://www.salome-platform.org/). The finite element code is arranged as a subroutine for the optimization scheme.

5.3.1 Simulation of drying and creep: mesh and boundary conditions

An axisymmetric configuration for cylinders and 1/8 for prismatic samples is used. The discretization and the boundary conditions are presented in fig.5.2 and tab.5.3.

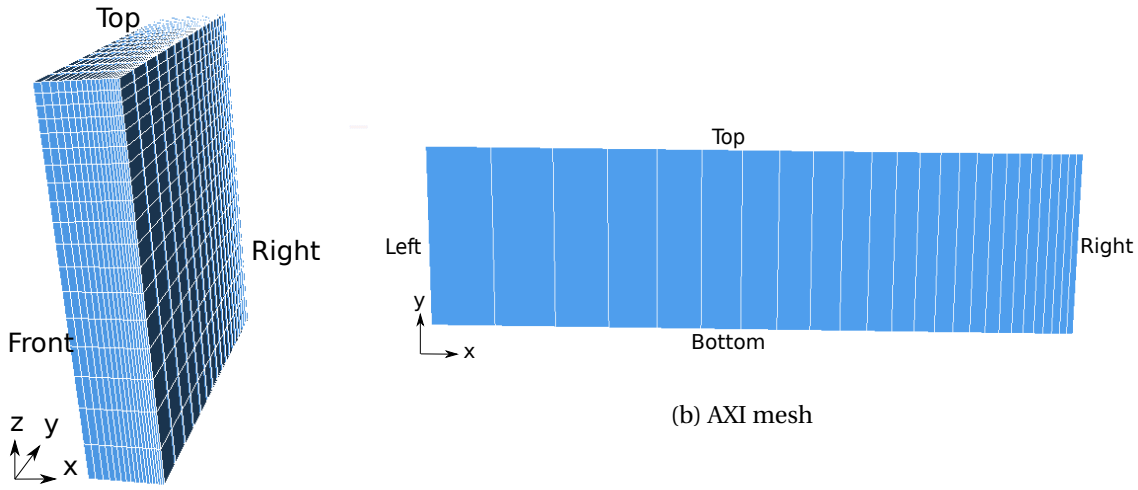

(a) 3D mesh

(b) AXI mesh

Figure 5.2: Mesh

Note that a fine mesh is considered at each drying face of the samples, where the hydric gradients are more pronounced.

5.3.2 Model identification

A staggered approach is adopted. The elastic modulus and the creep Poisson's ratio are respectively 14.5 GPa and 0.248 (Charpin et al., 2017).

Identification of drying shrinkage

We simply calculate the drying shrinkage capacity coefficient $k_{sh} = 8.6 \times 10^{-5}$[-] by linear regression from the experimental data (slope of the line). This parameter value of drying shrinkage is somewhat intrinsic to the material. In fact, the measurement was performed on an extremely thin specimen 500 µm in thickness, and the humidity was decreased gradually and so slowly that the pore humidity distribution is assumed to remain almost uniform at all times. The duration for equilibrium at different relative humidity steps are reported in tab.5.4. More details on the study of drying shrinkage can be found in the chapter 2 (experimental) and chapter 3 (numerical).

Table 5.4: Duration for equilibrium at different relative humidity steps

Relative humidity (%)	80	60	42	27	20
Duration (h)	24	24	30	60	165

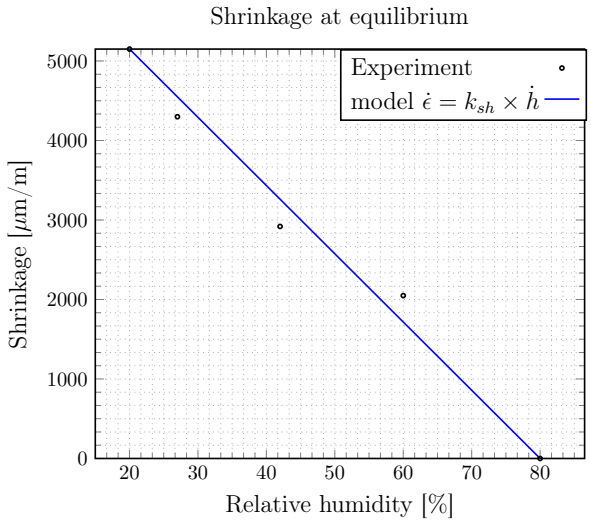

Figure 5.3: Determination of drying shrinkage coefficient $k_{sh} = 8.6 \times 10^{-3}$ [-] by sorption length change measurement on small prism ($10 \times 10 \times 0.5$ mm), performed in climatic chamber

Identification of basic creep

In a first attempt, we identified the creep parameters of the two models on the 7, 28, 90 days aging basic creep tests performed on cement paste by Huang (2018). However, let us emphasize that, unlike the material studied here, the author has added an admixture in the composition of the material. To verify the quality of the identified parameters, we predicted the basic creep tests BC-C15mm-SS-RH95, the result was not satisfactory (the results are not shown here for simplicity). Then using the identified models, we predict the basic creep tests C15mm-SS-RH95 (tab.5.2). But since the material used in the tests of C15mm-SS-RH95 (tab.5.2) is similar to the material of our study (same composition and exact manufacturing process); we found it more reliable to reidentify the basic creep parameters for both models on the this test exception made of the aging parameter m of the MPS model. The final parameters concerning basic creep of both models are presented in tabs.5.5-5.6. Note that the desiccation creep parameters of both models are not activated at this stage of identification. They are set to values such that they do not contribute to the output strain of simulation.

Table 5.5: Basic creep identified parameters of MPS model; μ_s[Pa.s^{-1}] is the parameter of desiccation creep, set to very low value, in order to shortcut its contribution.

Identified parameters	q_1 (Pa^{-1})	q_2 (Pa^{-1})	q_4 (Pa^{-1})	α (-)	n (-)	m (-)
Identified value	1.005×10^{-20}	5.997×10^{-10}	1.425×10^{-10}	0.17	0.15	1.09
Fixed parameters	α_s (-)	α_r(-)	α_e (-)	ν	μ_s (Pa.s)$^{-1}$	k_{sh} (-)
Value	0.1	0.1	10.	0.248	$1.\times10^{-24}$	8.6×10^{-3}

Table 5.6: Basic creep identified parameters of Burger-h model; η_{fd}[Pa.s^{-1}] is the parameter of desiccation creep, set to large value, in order to shortcut its contribution

Identified parameters	κ (-)	k_{rd} (Pa)	η_{rd} (Pa.s^{-1})	η_{id} (Pa.s^{-1})	-
Identified Value	0.0013	2.938×10^{10}	4.53×10^{15}	5.73×10^{16}	-
Fixed parameters	E_{el} (Pa)	ν_{el} (-)	ν_{flu} (-)	η_{fd} (Pa.s^{-1})	$k_{sh}(-)$
Value	1510^9	0.248	0.248	$1.\times10^{12}$	8.6×10^{-3}

The identification results are displayed in fig.5.4. The overall response is very well reproduced by both models. In particular, the recovery is well reproduced by Burger model during unloading demonstrating that the identification of the reversible part of the model went well. In fact, during unloading, the contribution of irreversible parts is vanishing. Meanwhile the MPS model shows an unrealistic response during unloading.

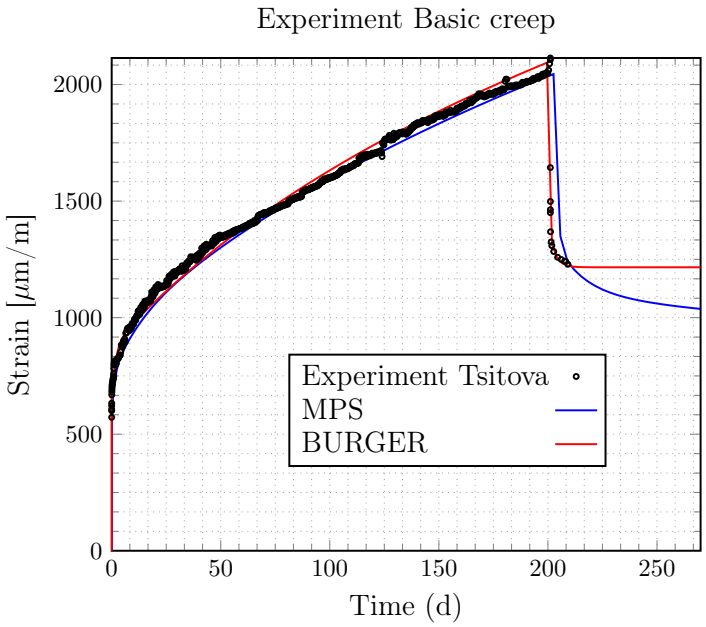

Figure 5.4: Identification of basic creep on test BC-C15mm-SS-RH95

Identification of drying creep

The desiccation creep parameter η_{fd} of the Burger model and μ_s of the MPS model are identified using the biaxial creep test P2mm-CC-2-FD. For a recall, the test was performed on 10×10×2 mm prism, with relative humidity decreasing from 80% to 20% in 4.5 h. The test is considered as fast. The best agreement was reached with the parameters are summarized in tab.5.7.

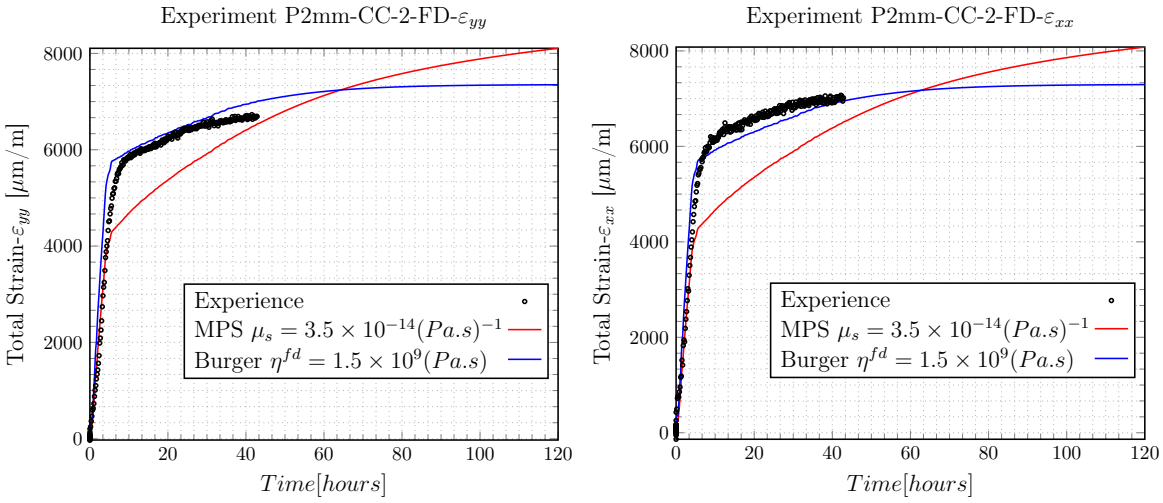

(a) Axial strain

(b) Lateral strain

Figure 5.5: Identification of drying creep parameters of both models using fast drying rate biaxial test in climatic chamber (P2mm-CC-2-FD) both axial (a) and lateral strain (b)are identified simultaneously assuming a constant creep Poisson's ratio.

Model	Burger	MPS
Desiccation creep parameter	η_{fd} (Pa.s^{-1})	μ_s (Pa.s)$^{-1}$
Value	1.5×10^{9}	3.5×10^{-14}

Table 5.7: Best fitting of desiccation creep parameters of Burger and MPS models

The identification results for both models are displayed in fig.5.5. The Burger model reproduces the experiment well, while the best fitting with the MPS model overestimates the strain in the long term.

5.3.3 Prediction of drying rate effect

In this section, the models are evaluated on their capability to predict the drying rate effect on creep. In the following, all simulations were run with the parameters of basic creep, drying creep, and drying shrinkage identified in the previous section. The tests are for different drying rates

Climatic chamber tests

The uniaxial test with slow drying (P2mm-CC-SD) is simulated with the identified models. This test is considered slow drying. In fig.5.6, the Burger model reproduces quite well the experiment data, both lateral and axial strains. For the MPS model, however, the prediction of axial strain is somehow acceptable, while the lateral response of the model tends to decrease at the end (fig.5.6). Since a constant Poisson's ratio $\nu = 0.248$ was imposed, this response of the model is quite unexpected.

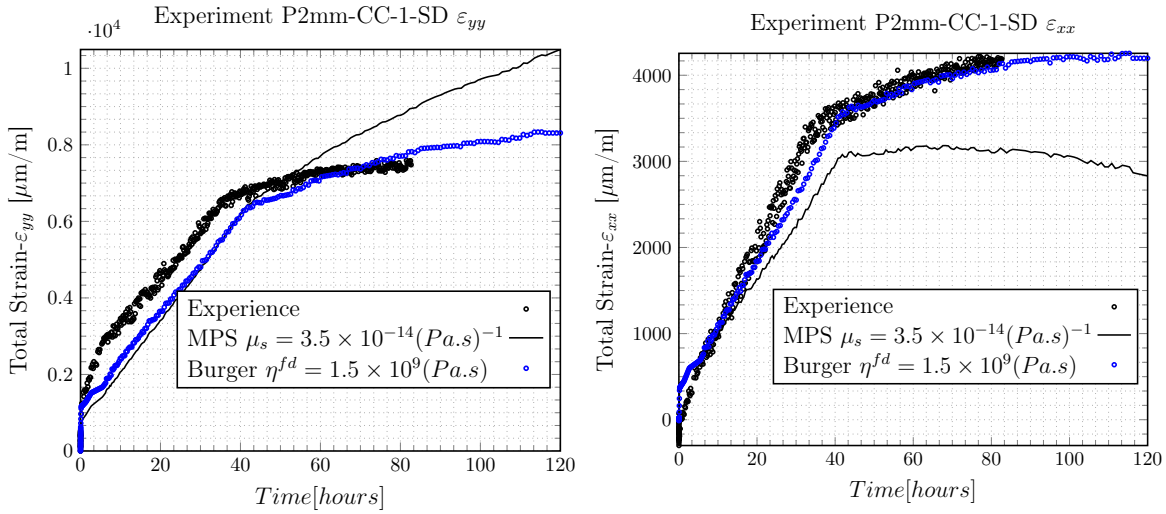

(a) Axial Strain

(b) Lateral Strain

Figure 5.6: Prediction of creep in Slow Drying (SD) rate test in climatic chamber (P2mm-CC-1-SD) axial strain (a) and axial strain (b)

ESEM tests

Fig.5.7 compares the microscopic in-situ creep tests in ESEM, including fast and slow drying rates with numerical simulations. In the case of fast-drying rate (fig.5.7.a), both models overestimate the creep rate when the relative humidity was decreased from 80 % to 20 %, but they capture well the asymptotic value. For slow drying rate (fig.5.7.b), however, the responses of the two models are similar and below the experimental data and diverge at the end: MPS underestimates, and Burger overestimates the creep rate.

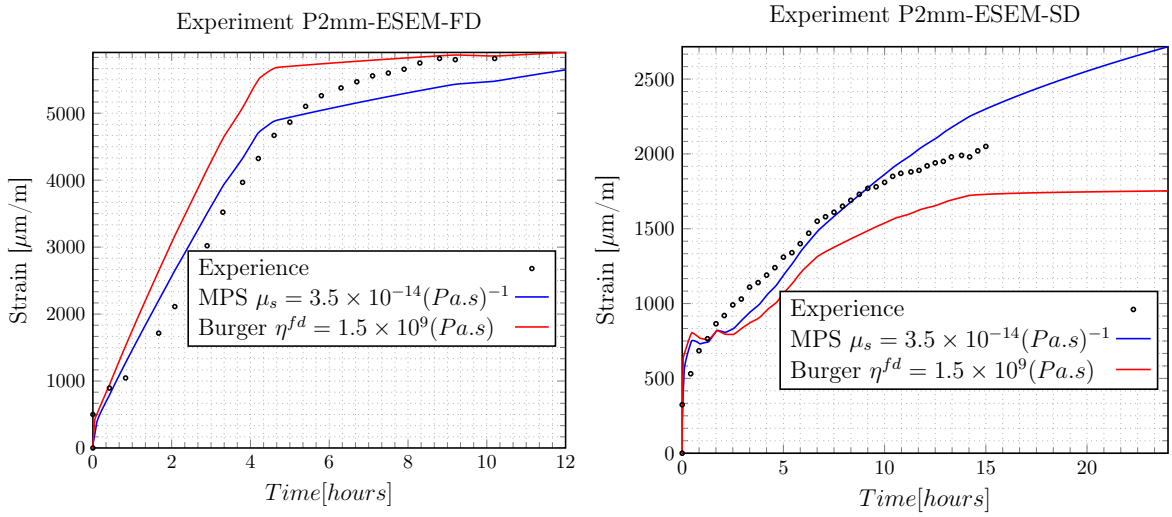

(a) Fast Drying

(b) Slow Drying

Figure 5.7: Prediction of creep tests in ESEM P2mm-ESEM-FD (a) and P2mm-ESEM-SD (b)

5.3.4 Evaluation of model scaling capability

In this section, the objective is to evaluate the two model capability to account for size effects on drying creep. For that purpose, predictions are probed on drying creep tests

carried out on ⌀36×180 mm cylinders at 60 % and 80 % relative humidity. The results are shown in fig.5.8. The prediction accuracy is quite satisfactory with the Burger model, while the MPS model drastically overestimates the experimental results.

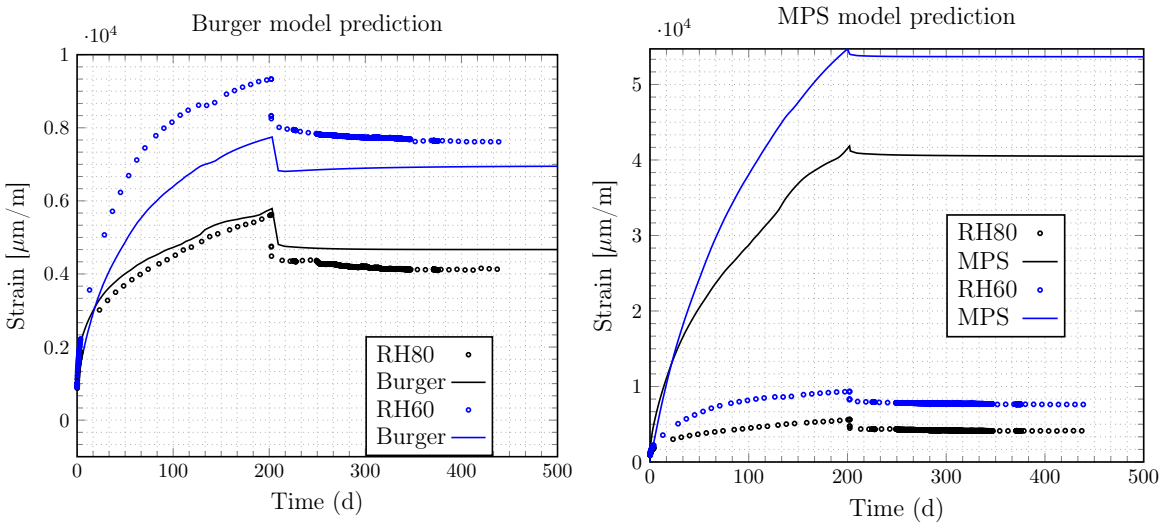

(a) Burger

(b) MPS

Figure 5.8: Scaling capability of the models with drying creep, prediction from 10×10×2 mm to ⌀36 × 180 mm size: Comparison with experimental results of total creep at 80% and 60% relative humidity

5.3.5 Prediction of basic creep at different relative humidities

In this section, the capability of both models to predict the long-term basic creep dependence on relative humidity is investigated. Three experiments at different relative humidities 20%, 60% and 80% are simulated (DSC-C18mm-SS-RH20, DSC-C18mm-SS-RH58, and DSC-C18mm-SS-RH80, tab.5.2). As already pointed out in chapter.4, in the first period of these tests (0-200 days), the specimens were only drying and free of external load; thus, drying shrinkage was measured. Then once moisture equilibrium was reached, the specimens were loaded, allowing to measure basic creep. The confrontation of numerical simulation results with experimental data is displayed in fig.5.9.

The Burger model better predicts the dependence of long-term basic creep on relative humidity than the MPS model. Let us point out that the prediction of the kinetics with the Burger model is much better for tests at 80% and 60% RH than at 20% RH. At 20% RH, the kinetics of creep of the model is significantly different from the experiment. Again, the MPS model drastically overestimates the kinetics of creep; the lower the relative humidity, the more the model overestimates this mechanism.

5.3.6 Analysis of microcracking: prediction of stress profile evolution

In this section, the stress distribution $\sigma_{\theta\theta}$ and σ_{zz} along the axial radius of ⌀36 × 180 mm cylinder in DSC-C18mm-SS-RH58 test (tab.5.2) is studied. The prediction concerns the prior loading period (the sample was not loaded during the first 220 days of testing while drying). The computation was performed with the identified Burger model, and the result is displayed in fig.5.10.

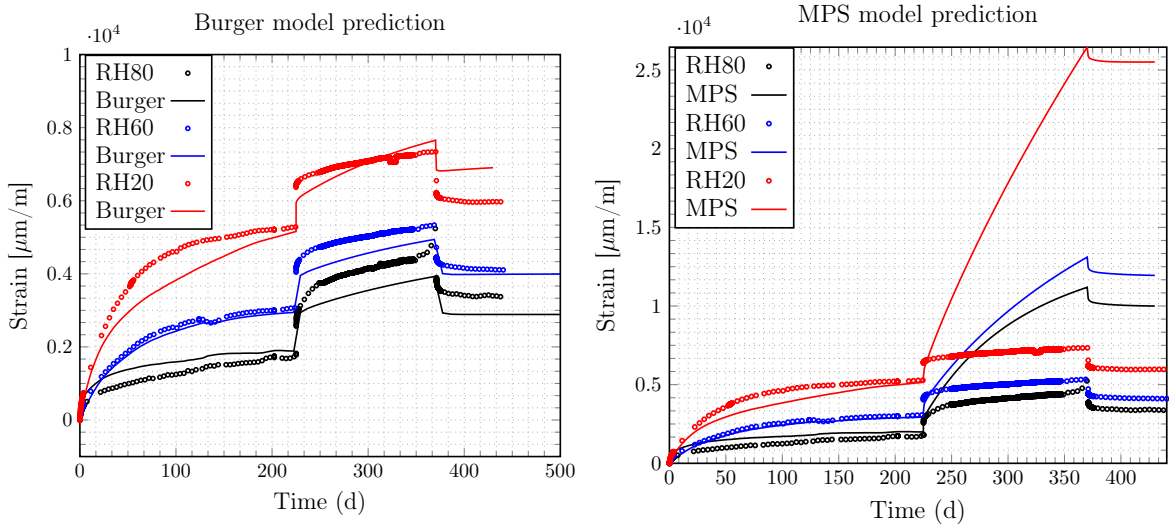

(a) Burger

(b) MPS

Figure 5.9: Dependence of long term basic creep on relative humidity. Prediction with Burger and MPS models vs. experimental measurements

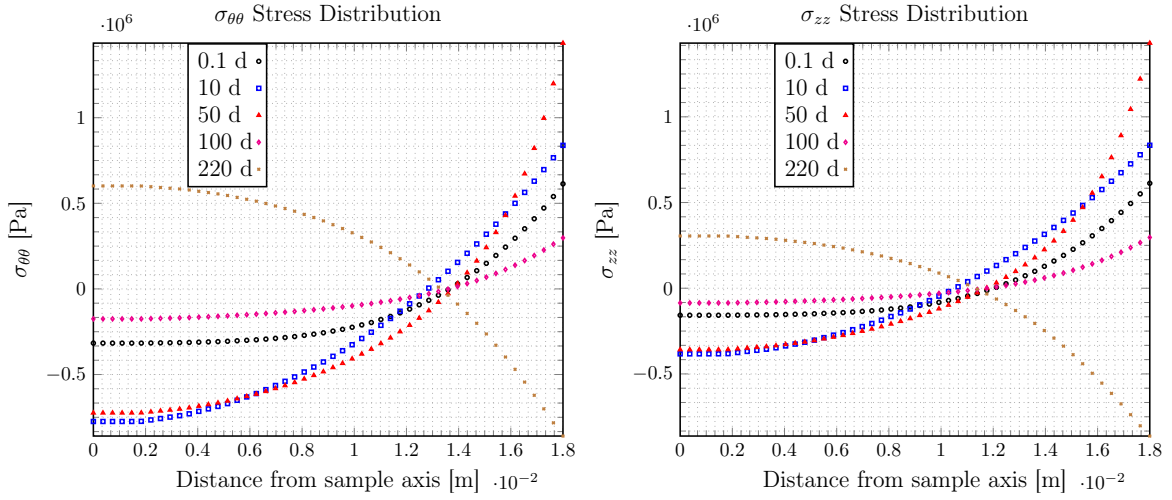

(a) $\sigma_{\theta\theta}$

(b) σ_{zz}

Figure 5.10: Stress Distribution along the central radius of cylindrical ⌀36 × 180 mm specimen submitted to environmental variable relative humidity (ref fig.5.1.c)-C18mm-RH60)

During the first stage of drying, the specimen surface experiences tensile stresses, while the core is under compressive stresses. The tensile stress grows to reach a maximum of 1.5 MPa after about 50 days of drying and then decreases. At the final drying stage, the stress profile is inversed, the core is under tension while the surface is under compression. It is noteworthy to highlight that during the entire drying process, the stress level in the entire section remains less than the tensile strength of the material ($f_t \approx 2.5-3$ MPa).

5.4 Discussion

The simulations using various drying conditions and different specimen sizes allow us to discuss some points of the model.

5.4.1 Basic creep dependence on relative humidity

Experimental observations of the present study showed that cement paste and concrete creep less at reduced water content, which corroborates literature results (Abiar, 1986; Bažant et al., 1976; Wittmann, 1970). However, the Burger model overestimates or underestimates the long-term kinetics of creep, depending on the relative humidity, as shown in fig.5.9. Meanwhile, Mathieu et al. (2018) calibrated the model on laboratory tests on concrete and were able to predict with good accuracy the delayed strains evolution at the structure level; the structure was submitted to an environment of average 50% RH. Thus the poor accuracy of the model at lower relative humidities has little impact in this case. For clarity of analysis, the modeling of long-term kinetics of the two models is recalled below. In the Burger model, the humidity effect on the long term kinetics of basic creep is accounted for by multiplying the local stress with the relative humidity value

$$\dot{\boldsymbol{\epsilon}}^{s,d} = \frac{h}{\eta^{is,id}}\boldsymbol{\sigma}^{s,d} \tag{5.4}$$

where subscript s, d denotes spherical and deviatoric parts respectively, h the relative humidity, $\boldsymbol{\sigma}$ the local stress at a material point, and η^i is the long term viscosity at the saturated state.

The MPS model overestimates the basic creep deformation when relative humidity is low. To investigate that non-intuitive response of the model, let us look closer to how the model considers the humidity effect on basic creep: On the one hand, a reduced time tr increment (Eq.5.5) replaces the load duration t for evaluating the viscoelastic compliance (see appendix.5.5, Eq.5.18). Mind that the humidity dependent factor (Eq.5.6) becomes very small at low relative humidities. For α_r= 0.1, and for 20%RH, this factor is 0.136, which means that the compliance evolution rate is 7.3× (1./0.136=7.3) faster than at full saturation.

$$\mathrm{d}t_r = \Psi_r(\mathrm{T}, h)\,dt \tag{5.5}$$

$$\Psi_r(\mathrm{T}, h) = \exp\left(\frac{\mathrm{Q}_r}{k_\mathrm{B}}\left(\frac{1}{\mathrm{T}_0} - \frac{1}{\mathrm{T}}\right)\right).(\alpha_r + (1-\alpha_r)h^2) \tag{5.6}$$

In the other hand, the relative humidity impacts the evolution of the viscous flow component of basic creep, Eq.5.28:

$$\dot{\boldsymbol{\epsilon}} = \frac{\Psi_s(h)}{q_4}\boldsymbol{\sigma} \tag{5.7}$$

Where $\boldsymbol{\sigma}$ is the local stress, and q_4 the parameter of the long term basic creep. The humidity-dependent factor Ψ_s (Eq.5.8) is similar to that of the viscoelastic strain.

$$\Psi_s(h) = (\alpha_s + (1-\alpha_s)h^2) \tag{5.8}$$

with $\alpha_s = 0.1$. The lower the relative humidity, the lower is the viscosity variation rate (ref. Eq.5.28), and the less the viscous flow part of basic creep develops. Hence, at low humidity, the viscoelastic component of basic creep of MPS model increases while the purely viscous component of the model decreases. The former contribution is by far more important according to the results obtained here. To summarize, the humidity-dependent factor is $\alpha_s+(1-\alpha_s)h^2$ for the MPS model and h for the Burger model. Such expressions are very practical since they do not require any identification, but they appear to show some limitations in the present study. One alternative consists of determining the dependence

of basic creep to relative humidity, based on micro-indentation or nano-indentation tests (Vandamme and Ulm, 2013; Zhang et al., 2014). Recently Frech-Baronet et al. (2017); Chen et al. (2020); Suwanmaneechot et al. (2020) have taken advantage of those advanced techniques to study the evolution of the basic creep modulus with relative humidity. Thus, from such experiments, a refinement of the expression of humidity reducing factors is possible and improves the model capability to predict the long-term creep behavior (Aili et al., 2020).

5.4.2 Identification of drying creep or Pickett effect

Because basic creep reduces when the relative humidity decreases make it difficult to investigate the mechanisms separately at play in basic creep and drying creep. Ignoring that fact may also cause an underestimation of the well-known Pickett effect (Bažant and Yunping, 1994). Then, using drying creep data of very thin specimens is an opportunity for investigation of the Pickett effect by allowing the separation of basic creep and drying creep. In the case of very thin specimens, they remain at a quasi-instantaneous equilibrium state with drying humidity, and thus, the contribution of basic creep may be neglected, at least during the transitional drying period. From a practical point of view, this statement could be checked by considering the basic creep on macroscopic tests. The creep rate factor, which is inspired but different from the one defined by (Vlahinić et al., 2012) C^F, is expressed in Eq.5.9.

$$C^F = \frac{\varepsilon^{total} - \varepsilon^{basic}}{\varepsilon^{basic}} \tag{5.9}$$

Where ε^{total} is the uniaxial total creep strain, while ε^{basic} is the uniaxial basic creep strain. The creep rate factor evaluates the drying strain contribution to the total stain of various materials, subjected to drying. The creep rate factor, computed using Eq.5.9, basically represents the ratio of drying creep over basic creep. Fig.5.11 shows the evolution of the creep rate factor computed for 10×10×2 mm samples submitted to different drying rates (P2mm-CC-1-FD (uniaxial) and P2mm-CC-3-SD (biaxial)). Drying creep grows rapidly and reaches amplitudes of about 8× that of basic creep. This shows that the creep rate factor evolves linearly with mass loss. It can be noted that the starting time $t = 0$ corresponds to the elastic response, and because the elastic strain in a biaxial test is lower than in a uniaxial test, the creep rate factor of P2mm-CC-3-SD (biaxial) is negative at the beginning.

5.4.3 Assessment of intrinsic drying shrinkage on macroscopic specimens

The evolution of self-equilibrated stresses across the specimen thickness during the drying process is illustrated in fig.5.10. Even though for the period between the onset of drying and the onset of loading, the sample is macroscopically unloaded, it is not internally stress-free. Self-equilibrated stresses develop for two main reasons: (i) macroscopic non-uniformity of the drying process, and (ii) if the local stress induced by hydric gradient exceeds the tensile strength of the material, micro-cracking will occur. The second origin of local stresses is due to the incompatibility of shrinking phases (mainly C-S-H) and non-shrinking phases (CH, for instance) of the material. Similarly, if the self-restraint stress exceeds the tensile strength, micro-cracking occurs. It is interesting to note that the local stresses will cause creep, which in turn will release the stresses partially. Fig.5.10 shows

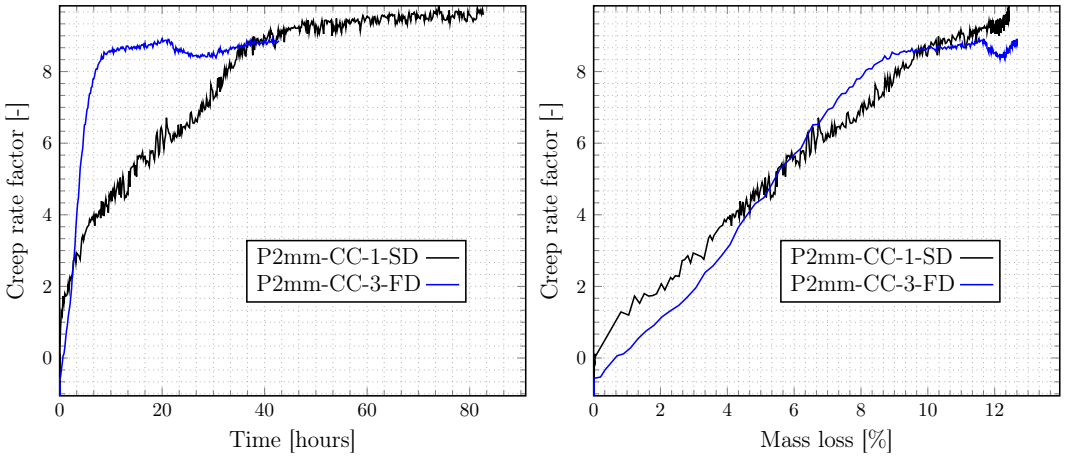

(a) C^F Vs. time (b) C^F Vs. mass loss

Figure 5.11: Evolution of the creep rate factor with time (a) and mass loss (b)

self-equilibrated stresses, resulting from the combination of these three phenomena. It is noteworthy to highlight that, despite the relatively large dimensions of ⌀36 × 180 mm cylinders (equivalent drying thickness of 18 mm), drying has not induced micro-cracking since the stress gradients reported in fig.5.10 remains under the tensile strength of the material ($f_t \approx 2.5-3$ MPa). This is also supported by the analysis of water profiles displayed in fig.5.12. This was possible because the prescribed drying humidity was slow enough to limit the rise of hydric gradient stress, likely to induce skin-micro-cracking. Therefore the measured shrinkage can be considered as uniform within the specimen at this investigation scale.

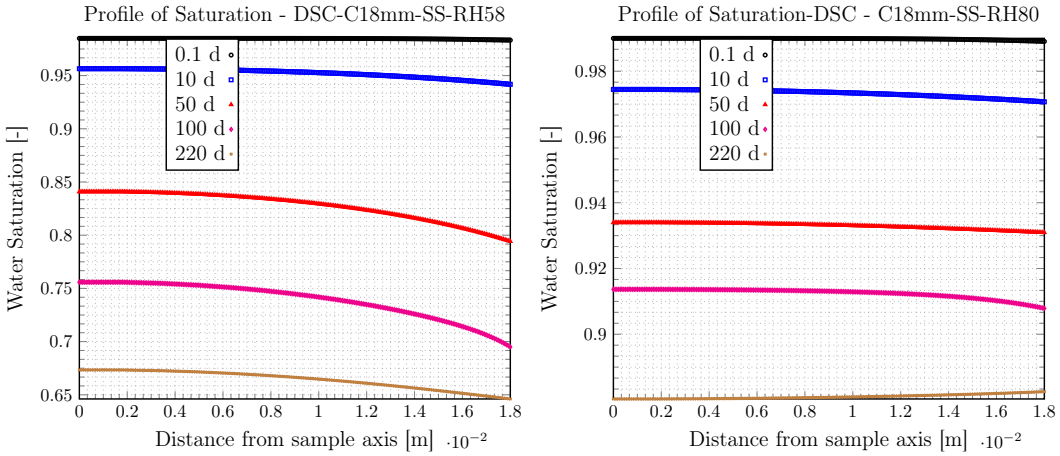

(a) (b)

Figure 5.12: Evolution of water saturation profile of cylindrical specimen, ⌀36 × 180 mm dimensions in tests (see tab.5.2) DSC-C18mm-SS-RH60 (a) and DSC-C18mm-SS-RH80 (b)

5.4.4 Pickett effect: separation between micro-cracking and the intrinsic mechanism

Drying creep, also known as the Pickett effect, corresponds to the additional deformation when concrete is stressed together with internal moisture change. One of the possible

origins is micro-cracking. When the specimen is subjected simultaneously to compression and drying, micro-cracking is less prominent than unloaded samples. Therefore, the measured strain is greater than the sum of basic creep and drying shrinkage measured separately. The larger is the specimen size, and the more likely cracking will occur unless the humidity is decreased very slowly, such that the specimen remains at quasi-instantaneous equilibrium with the drying environment. Earlier investigations of drying shrinkage using the DIC technique, both in ESEM and climatic chamber, have shown that using 10×10×2 mm specimens allows to assess the intrinsic drying shrinkage (Kinda et al., 2021) experimentally. Hence, skin-micro-cracking contributions to drying shrinkage and creep of small size samples in the present study could be neglected, fig.5.13. Many mechanisms have been proposed in the literature to explain the origin of drying creep, but no consensus has been reached yet. Among them, can be cited drying induced shrinkage (Bazant and Chern, 1985; Benboudjema et al., 2005) and micro-prestress relaxation theory (Bažant et al., 1997; Bažant et al., 2004; Jirásek and Havlásek, 2014; Rahimi-Aghdam et al., 2019). The most widely used mechanism is drying-induced shrinkage. According to this hypothesis, simultaneous loading and drying cause micro-diffusion of water between micro-pores and macro-pores. The linearity of drying creep vs. shrinkage relation in fig.5.13, during the biaxial creep test P3mm-CC-3-FD, suggests that the kinetics of drying shrinkage and drying creep are both driven by the same process, which is drying (Day et al., 1984; Hilaire, 2014).

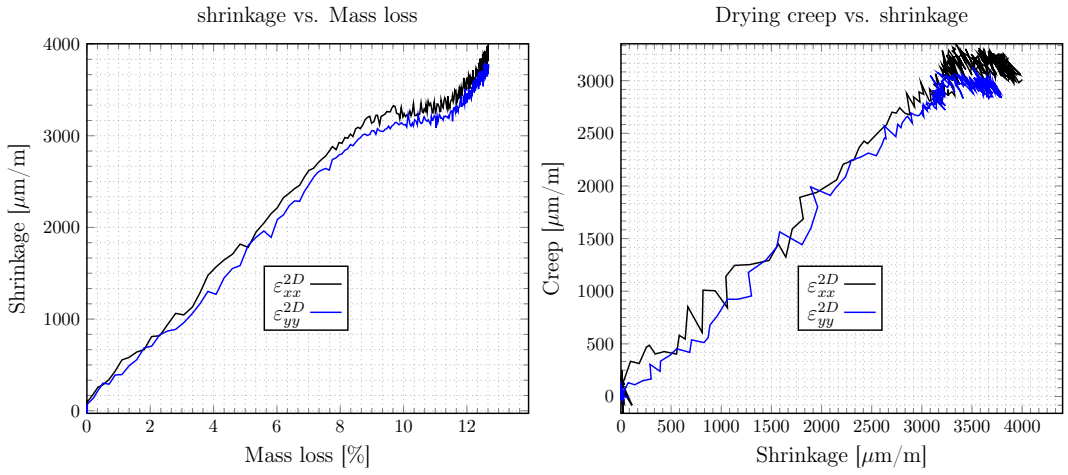

(a) Drying shrinkage vs. Mass loss

(b) Desiccation creep vs. Drying shrinkage

Figure 5.13: Relationship between drying shrinkage and mass loss (a); and Desiccation creep vs. Drying shrinkage during biaxial loading test in climatic chamber on prism of 10×10×2 mm

From recent findings (Vlahinić et al., 2012), drying of cement-based materials operates at two scales. At the macroscale, a macro-diffusion of water vapor occurs from large capillary pores toward the environment. However, at the micro-scale, micro-diffusion of water from nanopores of C-S-H gel to capillary pores happens. Let us assume, on the one hand, that drying shrinkage is driven by macro-diffusion, which is a quasi-instantaneous process, and then considered as elastic, $\dot{\boldsymbol{\varepsilon}}^{sh} = k_{sh}\dot{h}\mathbf{1}$. On the other hand, let's consider drying creep as a result of micro-diffusion promoting bond breakage in C-S-H gel which is a purely viscous process, $\dot{\boldsymbol{\varepsilon}}^{dc} = \mu|\dot{h}|\boldsymbol{\sigma}$ (Bazant and Chern, 1985). Then, the linear relationship between drying creep and drying shrinkage, in fig.5.13, also reported by (Day et al., 1984; Hilaire, 2014), suggests that micro-diffusion compensates macro-diffusion. More importantly, fig.5.13 demonstrate that drying creep is stress-induced shrinkage. In

the framework of stress-induced theory, (Bazant and Chern, 1985) proposed Eq.5.10.

$$\dot{\boldsymbol{\varepsilon}} = \mu|\dot{h}|\boldsymbol{\sigma} \tag{5.10}$$

where μ is a material parameter; $\dot{h}$ the local relative humidity variation rate; $\eta = (\mu(\dot{h}))^{-1}$ is the viscosity of drying creep; and the drying creep rate $\dot{\boldsymbol{\varepsilon}}$ is a viscous response completely controlled by the drying process. The viscosity dependence on the humidity change rate allows to retrieve the drying creep results for different drying rates and specimen thicknesses with one single material parameter η^{fd} of the Burger model (sect.5.2.1) as shown in the present study. This result tells us that drying creep and drying have the same kinetics; since drying has a limited potential, drying creep is therefore bounded. This means that for a given relative humidity variation, there is an amplitude for drying creep, which can be measured, if the specimen is very thin and drying very slowly enough to avoid cracking (Day et al., 1984; Bažant et al., 1976). Moreover, drying shrinkage and drying creep are very strongly related; this feature has to be taken into account in models (Bažant, Z. P., 2015; Wittmann and Roelfstra, 1980).

5.4.5 Modeling of drying creep: size effect

The results of fig.5.8 suggest that drying creep in the Burger model better accounts for size effects than the modeling approach adopted in the MPS model. For the sake of clarity, the two modeling approaches are recalled:

- Burger model (sect.5.2.1): a single viscosity parameter η^{fd} (Bazant and Chern, 1985) (Eq.5.10), is able to reproduce the drying creep response of cement paste, regardless of the drying rate and specimens size. That means that the drying process and drying creep have the same kinetics. Since drying has a limited potential, drying creep is also bounded (Dohnalová and Havlásek, 2018). In other words, for a given relative humidity, there might exist an ultimate value for drying creep, which is independent of the drying rate. It could be measured experimentally if the specimen is thin enough and drying low enough to avoid cracking. When cracking occurs, numerical simulations (Benboudjema et al., 2005) on concrete data (Granger, 1995) show that no suitable value of the material parameter η^{fd} can be identified in order to retrieve experimental drying creep results.

- MPS model (sect.5.2.2) overestimate the drying creep strain when the specimen size increases. This reversed size effect of the model has already been pointed out by (Bažant et al., 2014) who carried out a numerical study on experimental data (Bryant and Vadhanavikkit, 1987). The main reason explained by the authors is that the originally postulated equation for microprestress relaxation is too simple and does not cover a full spectrum of relaxation times. This leads to a delay between the humidity changes and the resulting increase of viscosity that contributes to drying creep. A modification that takes into account instantaneous effects on viscosity by an additional viscous dashpot has been proposed by adding a viscosity, term which is dependent on humidity variations, (Bažant et al., 2014). Recently, Rahimi-Aghdam et al. (2019) proposed the extended MPS theory (XMPS), inspired by molecular dynamics (MD) simulations of Vandamme et al. (2015). The viscosity relationship with the microprestress (sect.5.2.2), initially defined as a power function of micro-prestress (Bažant et al., 2004), is reformulated as

$$\frac{1}{\eta} = aS + b|\dot{S}| \tag{5.11}$$

where S is the microprestress, and η is the viscosity of the dashpot. The evolution of microprestress $\dot{S}$ (Eq.5.11) is mainly caused by the variation of capillary pore pressure and disjoining pressure. Numerical analysis by the authors demonstrates that this extended version predicts well the size effect on drying creep. It will be interesting to test this improved version of the MPS model on the current experimental data.

5.5 Conclusion

Creep and shrinkage have been monitored on 10×10×2 mm and ⌀36×180 mm samples. Simulations were carried out with two constitutive models. Based on the numerical analysis carried out, the following conclusions are drawn:

1. First, the models were challenged with basic creep results at three relative humidities (80%, 58% and 20%). The recovery part of the tests allows identifying the reversible components of the models. However, the identification of the irreversible component of creep was difficult. For both models, no suitable value of the viscosity of Maxwell dashpot was found. This may be due to the fact that long-term basic creep is strongly dependent on relative humidity, and none of the investigated models accounts well for this dependence. Therefore, the creep modulus relation with relative humidity needs to be improved, especially for the low relative humidity range (50-20% RH). Experimental studies with the nano-indentation technique will be of great help.

2. Second, the drying components of creep were studied. The experimental study on thin 10×10×2 mm specimens allows, on the one hand, to minimize the interaction between drying creep and basic creep, and on the other hand, to minimize cracking. Moreover, the drying shrinkage capacity coefficient was directly identified on the sorption length change isotherm, and the same parameter is used for both models in all simulations. Then simulations carried out on 10×10×2 mm samples focused on the characteristics of intrinsic drying creep. It was found that drying in the Burger model (sect.5.2.1) predicts well the drying rate and size effects, while the MPS model (sect.5.2.2) underestimated the drying creep component if the specimen size was reduced. More importantly, for cement paste, drying and drying creep have the same kinetics. In addition, the amplitude of drying creep is independent of the drying rate. Thus, it is possible for a given material to build a drying creep isotherm so that for a given environmental humidity, the drying creep amplitude can be determined in a straightforward manner.

References

G. Abiar. *cinétique de dessiccation et déformations différées du béton (analyse et modélisation)*. PhD thesis, Ecole Nationale des Ponts et Cjaussées, 1986. 136

J-L. Adia. *Modélisation multi échelle des phénomènes de retrait et de fluage dans les matériaux cimentaires : approches numériques couplant les éléments finis et la méthode de Lattice-Boltzmann*. PhD thesis, Université Paris-Est, 2017. 125

J-L. Adia, J. Kinda, L. Charpin, and J. Sanahuja. 6125-2104-2018-02716-FR-Projet CiWAP2 - Modèle de retrait et de fluage des bétons : implémentation sous le formalisme de MFront Code Aster et validation de la théorie de la microprécontrainte-solidification (MPS). Tech. rep., R&D MMC. Technical report, EDF R&D, 2018. 128

A. Aili, M. Vandamme, J-M. Torrenti, and B. Masson. A viscoelastic poromechanical model for shrinkage and creep of concrete. *Cement and Concrete Research*, 129, 2020. 137

Z. P. Bazant and J. C. Chern. Concrete creep at variable humidity: constitutive law and mechanism. *Materials and Structures*, 18(1), 1985. ISSN 1871-6873. 127, 128, 139, 140

Z.P. Bažant, A.B. Hauggaard, S. Baweja, and F-J Ulm. Microprestress-solidification theory for concrete creep. I: Aging and drying effects. *Journal of Engineering Mechanics*, 123 (11):1188–1194, 1997. 125, 128, 139

Z.P. Bažant, P. Havlásek, and M. Jirásek. Microprestress-solidification theory : Modeling of size effect on drying creep. In *EURO-C 2014 Conference*, pages 749–758, 2014. 125, 140

Z. P. Bažant, A. A. Asghari, and J. Schmidt. Experimental study of creep of hardened portland cement paste at variable water content. *Matériaux et Constructions*, 9(4):279–290, 1976. ISSN 0025-5432, 1871-6873. 136, 140

Z.P. Bažant and X. Yunping. Drying creep of concrete: constitutive model and new experiments separating its mechanisms. *Materials and Structures*, 27(1):3–14, 1994. 137

Z.P. Bažant, G. Cusatis, and L. Cedolin. Temperature effect on concrete creep modeled by microprestress-solidification theory. *Journal of engineering mechanics*, 130(6):691–699, 2004. 125, 139, 140

Bažant, Z. P. RILEM draft recommendation: TC-242-MDC multi-decade creep and shrinkage of concrete: material model and structural analysis*: Model b4 for creep, drying shrinkage and autogenous shrinkage of normal and high-strength concretes with multi-decade applicability. *Materials and Structures*, 48(4):753–770, 2015. ISSN 1359-5997, 1871-6873. 140

F. Benboudjema. *Modélisation des déformations différées du béton sous sollicitations biaxiales. Application aux enceintes de confinement des bâtiments des réacteurs nucléaires*. phdthesis, 2002. 125

F. Benboudjema, F. Meftah, A. Sellier, G. Heinfling, and JM. Torrenti. A basic creep model for concrete subjected to multiaxial loads. In *Fourth International Conference on Fracture Mechanics of Concrete and Concrete Structures*, pages 162–168, 2001. 127

F. Benboudjema, F. Meftah, and J.M. Torrenti. Interaction between drying, shrinkage, creep and cracking phenomena in concrete. *Engineering Structures*, 27(2):239–250, 2005. 128, 139, 140

A. H. Bryant and C. Vadhanavikkit. Creep, shrinkage- size and age at loading effects. *Materials Journal*, 84(2):117–123, 1987. 140

L. Charpin, TO. Sow, X d'Estève De Pradel, F. Hamon, and J-P Mathieu. Numerical simulation of 12 years long biaxial creep tests: Efficiency of assuming a constant poisson's ratio. In *Poromechanics VI*, pages 997–1004, 2017. 125, 127, 128, 129

L. Charpin, A. Courtois, F. Taillade, B Martin, B. Masson, and J. Haelewyn. Calibration of Mensi/Granger constitutive law: evidences of ill-posedness and practical application to VeRCoRs concrete. In *SMSS*, 2018a. 125

L. Charpin, Y. Le Pape, E. Coustabeau, E. Toppani, G. Heinfling, C. Le Bellego, B. Masson, J. Montalvo, A. Courtois, J. Sanahuja, and N. Reviron. A 12 year EDF study of concrete creep under uniaxial and biaxial loading. *Cement and Concrete Research*, 103:140–159, 2018b. ISSN 00088846. 125

Z. Chen, J. Frech-Baronet, and L. Sorelli. Microindentation two-fold creep model for characterizing short- and long-term creep behavior of cement pastes. *Mechanics of Materials*, 2020. ISSN 0167-6636. 137

RL Day, P Cuffaro, and JM Illston. The effect of rate of drying on the drying creep of hardened cement paste. *Cement and Concrete Research*, 14(3):329–338, 1984. 125, 139, 140

L. Dohnalová and P. Havlásek. COMPARISON OF DRYING SHRINKAGE AND DRYING CREEP KINETICS IN CONCRETE. *Acta Polytechnica CTU Proceedings*, 15:12–19, 2018. 140

A. Foucault, S. Michel-Ponnelle, and E. Galenne. A new creep model for npp containment behaviour prediction. In *International conference on Numerical modeling Strategies for sustainable concrete structures*, 2012. 125, 127

J. Frech-Baronet, L. Sorelli, and J. P. Charron. New evidences on the effect of the internal relative humidity on the creep and relaxation behaviour of a cement paste by micro-indentation techniques. *Cement and Concrete Research*, 91:39–51, 2017. 137

L. Granger. *Comportement différé du béton dans les enceintes de centrales nucléaires: analyse et modélisation.* PhD thesis, Ecole Nationale des ponts et Chaussées, 1995. 140

V. Guihard, J-L. Adia, F. Lavergne, J. Sanahuja, and J P. Balayssac. Assessing the permittivity of an usaturated sand by combining a lattice boltzmann method simulation, electromagnetic homogenization models and measurements. *Journal of Applied Geophysics*, 173, 2020. 125

A. Hilaire. *Etude des déformations différées des bétons en compression et en traction, du jeune au long terme : application aux enceintes de confinement.* Theses, École normale supérieure de Cachan - ENS Cachan, 2014. 139

S. Huang. *Ageing behaviour of concrete creep : application to the VeRCoRs concrete.* Thesis, Université Paris-Est, 2018. 125, 130

M. Jirásek and P. Havlásek. Microprestress–solidification theory of concrete creep: Reformulation and improvement. *Cement and Concrete Research*, 60:51–62, 2014. 125, 126, 127, 128, 139

J. Kinda, L. Charpin, J-L. Adia, F. Benboudjema, and S. Michel-Ponnelle. Impact of drying rate on delayed strains in cement-based materials. In *Interdisciplinary Approaches for Cement-based Materials and Structural Concrete: Synergizing Expertise and Bridging Scales of Space and Time*, pages 719–723, 2018. 125

J. Kinda, L. Charpin, F. Benboudjema, A. Bourdot, S. Michel-Ponnelle, and A. Bourtef. Investigation of drying shrinkage of cement based materials assisted by digital image correlation. *Journal of materials in civil engineering*, 2021. 139

J.P. Mathieu, L. Charpin, P. Sémété, C. Toulemonde, G.H.J. Boulant, and F. Taillade. Temperature and humidity-driven ageing of the VeRCoRs mock-up. In *Computational Modelling of Concrete and Concrete Structures*, 2018. 125, 136

R7.01.35. Relation de comportement BETON_burger pour le fluage, 2017. 128

S. Rahimi-Aghdam, Z. P. Bažant, and G. Cusatis. Extended microprestress-solidification theory (XMPS) for long-term creep and diffusion size effect in concrete at variable environment. *Journal of Engineering Mechanics*, 145(2), 2019. 139, 140

N. Reviron. *Etude du fluage des bétons en tractions. Application aux enceintes de confinement des centrales nucléaires à eau sous pression.* PhD thesis, Ecole Normale Supérieure de Cachan, 2009. 125

J. Sanahuja. Effective behavior of ageing linear viscoelastic composites; homogenization approach. *International Journal of Solids and Structures*, 50(19):2846–2856, 2013. 125

A. Sellier and L. Buffo-Lacarriere. Towards a simple and unified modelling of basic creep, shrinckage and drying creep of concrete. *European Journal of Environmental and Civil Engineering*, 13(10):1161–1182, 2009. 127

P. Suwanmaneechot, A. Aili, and I. Maruyama. Creep behavior of csh under different drying relative humidities: Interpretation of microindentation tests and sorption measurements by multi-scale analysis. *Cement and Concrete Research*, 132, 2020. 137

M. Vandamme and F.-J. Ulm. Nanoindentation investigation of creep properties of calcium silicate hydrates. *Cement and Concrete Research*, 52:38–52, 2013. 137

M. Vandamme, Z. P. Bažant, and S. Keten. Creep of lubricated layered nano-porous solids and application to cementitious materials. *Journal of Nanomechanics and Micromechanics*, 5(4), 2015. 140

I. Vlahinić, J. J. Thomas, H. M.Sh Jennings, and J. E. Andrade. Transient creep effects and the lubricating power of water in materials ranging from paper to concrete and kevlar. *Journal of the Mechanics and Physics of Solids*, 60(7):1350–1362, 2012. 137, 139

F.H. Wittmann and P.E. Roelfstra. Total deformation of loaded drying concrete. *Cement and Concrete Research*, 10(5):601–610, 1980. 140

V.F. Wittmann. Einflufl des feuchtigkeitsgehahes auf das kriechen des zementsteines. *Rheologica Acta*, page 6, 1970. 136

Q. Zhang, R. Le Roy, M. Vandamme, and B. Zuber. Long-term creep properties of cementitious materials: Comparing microindentation testing with macroscopic uniaxial compressive testing. *Cement and Concrete Research*, 58:89–98, 2014. 137

Conclusion and Perspectives

Conclusion

The prediction of the delayed strain behavior of concrete structures submitted to environmental drying conditions is crucial for the serviceability of concrete structures. Most of the time, models are calibrated on laboratory tests on rather small samples and used to predict the behavior of structures that are far larger. These different concrete thicknesses induce different drying kinetics. Thus, the constitutive laws should be able to correctly take into account the effect of the rate of drying on the delayed strains (creep, shrinkage) of concrete. In this thesis, the objective was to investigate, both from experimental and numerical viewpoints, the impact of the rate of drying on the delayed strain behavior of cement paste. For that purpose, experimental tests were carried out for shrinkage and creep at the cement paste scale for different sample sizes under various drying rates. The study was performed on small representative samples of cement paste to allow reasonable test duration on the one hand, and on the other hand, to avoid cracking due to hydric gradients. Cement paste is the source of the delayed deformations and, therefore, qualitatively presents the same shrinkage and creep behavior as concrete. The experiments enable us to understand better the impact of drying rate on drying shrinkage and drying creep and propose a model taking into account that influence.

Contributions

From experimental viewpoint

Tests were performed on hardened cement paste specimens. One cement paste was tested with different geometries: $\varnothing 36 \times 180$ mm cylinders and thin slabs ($10 \times 10 \times 0.5$, $10 \times 10 \times 1$, $10 \times 10 \times 2$ mm). The specimens were dried at various rates and with different steps of humidity, using different conditioning systems. The experimental study is summarized as follows:

1. axial creep and shrinkage measurements in Environmental Scanning Electron Microscopy (ESEM) on $10 \times 10 \times 2$ mm samples, for different drying rates.

2. drying desorption isotherm and mass loss assessed by DVS, using cement powder and $10 \times 10 \times 1$ mm specimen; drying length change isotherm investigated on $10 \times 10 \times 0.5$ mm, $10 \times 10 \times 2$ mm specimens using ESEM and climatic chamber.

3. axial and biaxial creep, shrinkage, and mass loss measurements in a climatic chamber, on $10 \times 10 \times 2$ mm specimens, for different drying rates.

4. axial creep (drying and pre-dried) with recovery, shrinkage, mass loss measurements for relative humidity 20%, 60%, and 80% controlled by saturated saline solutions using 36x180 mm cylinders.

This experimental campaign is very large and enable to study a lot of parameters. The creep tests in ESEM and climatic chamber under axial and biaxial mechanical loadings are particularly innovative and informative. These techniques allow the investigation of the relationship between drying, free drying shrinkage, and intrinsic drying creep, within a short amount of time, for a large range of relative humidity and different drying rates. Since the method made possible the assessment of drying shrinkage, free of skin cracking, the part of the Pickett effect attributed to cracking was avoided, allowing to investigate the intrinsic mechanism of drying creep. The drying creep test on small slabs allowed us to investigate the purely drying creep behavior of the material for two reasons (1) since the test durations were short, the development of basic creep was limited, (2) cracking was not present or diffuse. These experiments were assisted by Digital Image Correlation (DIC). Thanks to the uncertainty analysis, it is demonstrated that DIC is trustworthy for investigating delayed strains of cement-based materials under complex drying conditions. The cement paste's natural contrast allows reaching an uncertainty level below 100 μm/m for relative humidities ranging from 80 % to 9%. The use of DIC also allowed checking that the strains were uniform at the observation scale, which validated that crack was not present or diffuse. These experimental investigations allowed us to learn about the influence of relative humidity, drying rate, and size effects on creep. From the experimental results, some conclusions were drawn.

1. Drying shrinkage. The results show that the final drying shrinkage at the material level is independent of drying rate. Moreover, it was found that drying shrinkage bears a quasi-linear relationship with relative humidity for a broad range (100-20% RH). These findings are of first importance since they suggest that it is possible to build simple drying shrinkage models for concrete.

2. Creep study. The most important outcomes are: (1) the kinetics of basic creep in the long term decreases with decreasing humidity; (2) drying creep of thin specimens (2 mm) bears a linear relationship with their mass loss, regardless of the drying rate, which tells us that at the material level, drying creep and drying have same kinetics. In particular, drying creep seems to be driven mainly by the gradient between the flux water movement in macro-pores, which causes mass loss and flux of water flow in the nanoporosity, which induces drying creep.

From numerical viewpoint

The experimental database served for numerical investigations of drying, drying shrinkage, and creep models. The objective was to propose a delayed strain constitutive law for concrete structures, which could take into account the effect of the rate of drying. This is a critical point when such models are used at the structure level because the experiments used in the lab to calibrate models exhibit much faster drying than in structures. The main contributions regarding numerical aspects are as follow:

1. First, the proposed Richards-Fick drying model, which accounts for water permeation and vapor diffusion, is shown to account well for size effects, drying rate and works well for a range of relative humidity from 100% down to 20% RH at room temperature. This point is important since it demonstrates that the parameters of the model could be determined from laboratory tests and further used to predict drying at the structure level. A sensitivity analysis on the surface exchange coefficient was carried out, and the results showed that for the usual environmental conditions (20°C, 50% RH, normal airflow rate), the effect of the surface exchange coefficient

on drying could be neglected for specimens of large drying thicknesses (18 mm in this case). At the same time, it was essential for very thin specimens. However, when the airflow rate was quite low, the impact of surface exchange coefficient was important for any specimen size (in the range of sizes tested in this campaign, i.e., up to 18 mm).

2. Second, the drying shrinkage model adopted reads $\dot{\boldsymbol{\epsilon}}^{sh} = k_{sh}\dot{h}\mathbf{1}$, where $\dot{h}$ is the rate of variation of pore relative humidity. Let us stress that the proportionality factor k_{sh} was identified directly on experiment results of only 250 h duration, on a 0.5 mm thick sample. The results demonstrate that this kind of model could account well for drying rate and size effects on drying shrinkage at room temperature. In particular, the model was found to be trustworthy for a broad range of relative humidity (100-20%). Since this model is only based on the pore humidity variation rate, the quality of results was mainly due to the quality of drying results, which was strongly dependent on the water desorption isotherm. The linearity of drying shrinkage with relative humidity made it possible to fully calibrate the model for a large range of relative humidity based on one single drying shrinkage experiment.

3. Third, two constitutive laws for creep were studied (Burger and MPS models). The main concern was evaluating the capacity of those constitutive laws to account for size effects correctly. A staggered approach was used for simulations, cracking was not considered, and the temperature was set to 20°C. Particular attention was paid to the identification of model parameters by inverse analysis, and the identification was successful. In a first step, basic creep parameters were identified on the basic creep test with recovery, which allowed better identification of reversible parts of basic creep. In a second step, the drying shrinkage capacity coefficient was identified directly on sorption length change isotherm. The drying creep component was identified in a last step thanks to creep measurement (in climatic chamber) on thin 10×10×2 mm specimens since the interaction between drying creep and basic creep was limited and cracking was not present or diffuse. The identified parameters are used for predictions of tests at various drying rates and specimens size. It was found that the Burger model predicted well the drying rate and size effects, while the MPS model overestimated the drying creep component for increasing specimen size. The simulation results support that drying and drying creep has the same kinetics. Moreover, the amplitude of drying creep was independent of drying rate, which means that it is possible for a given material to build a drying creep isotherm so that for a given environmental humidity, the drying creep amplitude can be determined straightforwardly. The simulations also revealed that the dependence of long-term creep viscosity on relative humidity should be refined for both models.

Perspectives

Further improvements can be proposed to complete the work of this thesis both on experimental and numerical viewpoints:

1. The experimental database could serve for extensive comparisons of others creep models, including constitutive laws such as LMDC model Manzoni et al. (2020), Extended Microprestress Solidification (XMPS) model Rahimi-Aghdam et al. (2019), as well as prediction models like fib Model Code 2010, B4 model Dohnalová and

Havlásek (2018). The results could help testing or building delayed strain models for concrete structures, which are able to take into account the effect of drying rate. One possible way to tackle that goal is to predict drying shrinkage tests of large size specimens with the length change isotherm coefficient obtained using the method presented in this study. Moreover, by homogenization, drying shrinkage values at equilibrium for a given relative humidity can be upscaled from the cement paste to concrete if one assumes in first approach a perfect cohesion between the cement paste matrix and aggregates. This is an oversimplification of reality and could potentially lead to overestimated shrinkage. The present database, which includes axial and biaxial creep, drying shrinkage under various drying conditions for cement paste, could also be extended for different temperatures and loading conditions and different material formulations.

2. The quality of predictions of delayed strains vastly relies on drying input, which in turn depends on two factors: desorption isotherm and model parameters. Therefore, for improving the prediction of delayed strains of nuclear containment buildings (CCB), a good knowledge of the desorption isotherm of on-site concrete of each CCB is very important. For the last decade, innovative techniques to characterize the sorption-desorption isotherm of cement-based materials have emerged, such as the volumetric or Dynamic Vapor Sorption methods. The advantage of those techniques is that they are time-cost effective. The drying model could also be extended to variable temperature for sake of generality.

3. In this work, we focused on cement paste, and the variety of tests allowed us to propose an original method of calibration of the models: to complete this study, we propose to test the identification of the parameters of the models on concrete tests according to the following procedure.

   (a) Determination of the long-term viscosity of basic creep based on nano-indentation tests combined with homogenization techniques. Identification of the reversible component and the consolidation parts of basic creep on short-term tests, including recovery of few days.

   (b) The drying shrinkage parameter of the model could be identified by (1) inverse analysis on one single drying shrinkage experiment on concrete (long duration method) or by homogenization of the drying shrinkage isotherm of paste to obtain the drying shrinkage capacity coefficient of concrete.

   (c) Determination of the parameter of drying creep by inverse analysis of drying creep test on concrete with basic creep and drying shrinkage parameters set.

   And then, as a final step, to predict the evolution of deformations at the structural scale. By doing so, we will have a proven method to go from the laboratory scale to the structural scale, with a considerable saving in testing time, even more so if we study different concrete compositions.

4. The structural effects of drying creep or Pickett effect were not addressed in this study. From experimental results, we inferred that at room temperature, the final drying shrinkage at the material level is independent of the rate of drying. It would be interesting to verify if the same conclusion stands at mortar and concrete levels since aggregates could induce cracking at the mesoscopic level in these materials compared to cement paste. In massive structures, such as nuclear containment

buildings, large bridges, the depth of skin-cracks is negligible compared to the overall thickness of the structure. Moreover, most of the cracks would re-close upon the pre-stressing (in prestressed structures). So the drying rate will not affect that much the final drying shrinkage for the pre-stressed structures

5. Variation of temperature and RH, including drying and wetting, should be studied experimentally and numerically since structures are submitted to various climatic conditions. Besides, tensile stresses should be applied in order to build a robust model able to predict delayed strains in cement›based materials.

References

L. Dohnalová and P. Havlásek. Comparison of drying shrinkage and drying cree kinetics in concrete. *Acta Polytechnica CTU Proceedings*, 15:12–19, 2018. 149

Florent Manzoni, Thierry Vidal, Alain Sellier, Xavier Bourbon, and Guillaume Camps. On the origins of transient thermal deformation of concrete. *Cement and Concrete Composites*, 107:103508, 2020. 149

S. Rahimi-Aghdam, Z. P. Bazant, and G. Cusatis. Extended microprestress-solidification theory (XMPS) for long-term creep and diffusion size effect in concrete at variable environment. 145(2), 2019. 149

Appendix

5.6 Burger model

5.6.1 Elasticity and basic creep

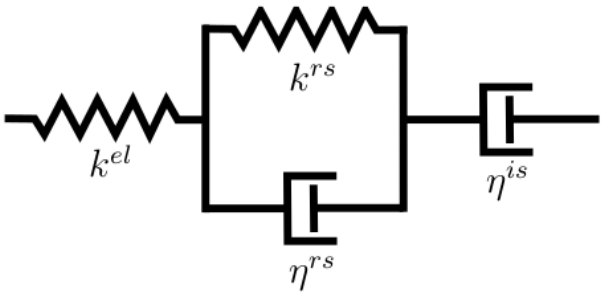

Figure 5.14: Basic creep and elasticity unit of Burger-h model (spherical chain)

The model is assumed to be isotropic. It is split into spherical and deviatoric parts (hereafter, subscript s will refer to spherical, and subscript d will denote deviatoric components). Creep Poisson's ratio relates the spherical and the deviatoric strains. Each part is modeled using a rheological chain model, fig.5.14. Each chain is composed of elastic strain ($\boldsymbol{\varepsilon}_s^{el}$ and $\boldsymbol{\varepsilon}_d^{el}$), reversible basic creep modeled by Kelvin-Voigt elements ($\boldsymbol{\varepsilon}_s^{rbc}$ and $\boldsymbol{\varepsilon}_d^{rbc}$) and irreversible basic creep modeled by Maxwell elements using a viscosity that is dependent on the current state of strain (Sellier and Buffo-Lacarriere, 2009; Sellier et al., 2016). The basic creep strains are assumed to be proportional to relative humidity. The model equations are now recalled for the spherical part (the equation for the deviatoric part is obtained by replacing s with d.

- The spherical part of the elastic deformation is represented by Eq.(5.12):

$$\epsilon_s^{el} = \frac{\sigma_s}{3k^{el}} \tag{5.12}$$

  with $\boldsymbol{\sigma}_s$ the spherical component of the stress tensor and k^{el} the elastic compressibility modulus.

- The spherical part of the reversible creep strain given by Eq.(5.13):

$$h\sigma_s = k^{rs}\boldsymbol{\varepsilon}_s^{rbc} + \eta^{rs}\dot{\boldsymbol{\varepsilon}}_s^{rbc} \tag{5.13}$$

  with h the relative humidity, k^{rs} and η^{rs} the Kelvin-Voigt chain variables.

- The spherical part of the irreversible creep strain given by Eq.(5.14):

$$h\boldsymbol{\sigma}_s = \eta^{is}\dot{\epsilon}_s^{is} \tag{5.14}$$

where the viscosity depends on the current state of irreversible strain through $\eta^{is} = \eta_0^{is}\exp(\| \boldsymbol{\varepsilon}^{ibc_m} \| /\kappa)$ where $\boldsymbol{\varepsilon}_m^{ibc} = \max(\boldsymbol{\varepsilon}_m^{ibc}, \sqrt{\boldsymbol{\varepsilon}^{ibc} : \boldsymbol{\varepsilon}^{ibc}})$. κ is a fitting parameter of order of 10^{-3} for ordinary concrete, and if it is too high, the viscosity becomes independent of the strain level.

Another hypothesis of the model is a constant Poisson's ratio assumption for basic creep. Hence, the relation between parameters of spherical and deviatoric strains reads $\frac{\eta^{is}}{\eta^{id}} = \frac{\eta^{rs}}{\eta^{rd}} = \frac{k^{rs}}{k^{rd}} = \frac{1+\nu^{el}}{1-\nu^{el}}$.

5.6.2 Drying shrinkage

The drying shrinkage variation rate is considered to be proportional to the humidity change rate following $\boldsymbol{\varepsilon}^{shr} = k^{shr}\dot{h}\mathbf{1}$ where $\mathbf{1}$ is the second-order identity tensor and k^{shr}, a proportional scalar factor.

5.6.3 Desiccation creep

Desiccation creep is modeled by the law proposed by Bazant and Chern (1985); Benboudjema et al. (2005), which relates the desiccation strain rate to the variation of internal relative humidity, expressed by

$$\dot{\boldsymbol{\varepsilon}}^{dc} = |\dot{h}|\eta^{fd}\boldsymbol{\sigma} \tag{5.15}$$

A zero Poisson's ratio is associated with the desiccation creep, according to this model. This hypothesis was discussed elsewhere (Charpin et al., 2017).

5.7 Detailed Description of Micro-prestress solidification (MPS) model

The model is developed in the framework of aging viscoelasticity (Bazant and Prasannan, 1989; Bažant et al., 1997, 2004) and later improved by Jirásek and Havlásek (2014). Hence, creep is completely described by a unique compliance function J depending on both the current time t and the loading time t'. The complete constitutive model is represented by the rheologic schematic of fig.5.15.

It consists of (i) a non-aging elastic spring for instantaneous strain, (ii) solidifying Kelvin chain series, representing short term creep, (iv) an aging dashpot with viscosity dependent on microprestress S for long term creep, (iv) a shrinkage unit for the volumetric changes due to drying, and (v) a unit representing the thermal expansion.

The number of units depends on the simulation duration and is fixed to 11 units by default.

Because all these units are connected in series, the total strain tensor is the sum of the individual contributions, while the stress across all units is the same. The total strain sensor of the model reads Eq.5.16.

$$\boldsymbol{\varepsilon} = \boldsymbol{\varepsilon}^{el} + \boldsymbol{\varepsilon}^{ve} + \boldsymbol{\varepsilon}^{f} \tag{5.16}$$

where each term is specified below:

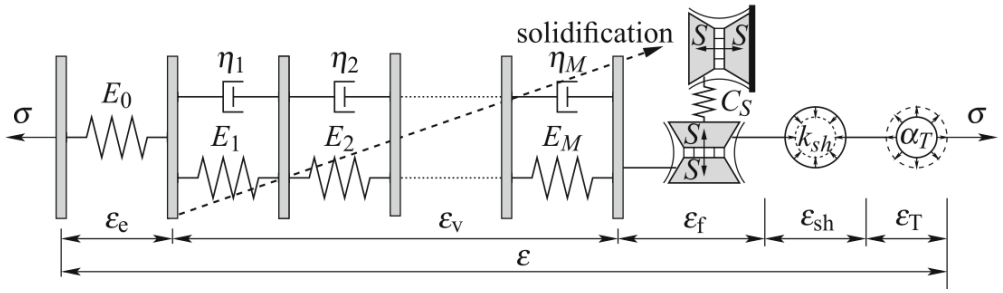

Figure 5.15: Rheological schematic of complete microprestress-solidification theory. Serial coupling of an elastic spring, solidifying Kelvin chain, flow element affected by microprestress relaxation, and units corresponding to free shrinkage and thermal expansion

- Elastic strain tensor:

$$\boldsymbol{\varepsilon}^{el} = q_1 : \boldsymbol{\sigma} \tag{5.17}$$

The instantaneous strain, modeled by a non-aging elastic spring, should not be confused with the material elastic modulus, which is time-dependent. It is a kind of asymptotic modulus corresponding to a very short time of loading, typically of 10^{-4} s.

- The viscoelastic strain tensor $\boldsymbol{\varepsilon}^{ve}$ originates from the solid gel of calcium silicate hydrates and is described by the solidification theory (Bazant and Prasannan, 1989). The aging property of creep is attributed to new solidified hydration products, mainly calcium-silicate-hydrates (C-S-H). C-S-H is considered a non-aging component with material properties invariable in time, and the dependence of compliance with loading age is attributed to the growth of volume fraction of hydration products. These considerations lead to Eq.5.18 linking the viscoelastic strain rate to the rate $\dot{\boldsymbol{\gamma}}$ of the non-aging viscoelastic function and to the function $\nu(t)$ of the specific volume of cement gel that has been solidified up to time t.

$$\boldsymbol{\varepsilon}^{ve} = \frac{\dot{\boldsymbol{\gamma}}}{\nu} \tag{5.18}$$

$$\boldsymbol{\gamma} = \int_0^t \phi(t-\tau)\dot{\boldsymbol{\sigma}}(\tau)d\tau \tag{5.19}$$

where $\phi(t-\tau) = q_2 ln(1+\psi^n)$; $\psi = \frac{t-t'}{\lambda_0}$; and $\nu(t)^{-1} = \alpha + (\frac{\lambda_0}{t})^n$.

The free parameters of the viscoelastic strain in the model are q_2 (MPa^{-1}) and α (-) while for usual concrete, the others take the following values: $n = 0.11$ (-), $\lambda_0 = 86400$ s and $m = 0.5$ (-). Those values have been determined based on a large set of experimental data on concrete Bažant et al. (1997) . Let us note that $\boldsymbol{\gamma}$, which is the viscoelastic strain of cement gel, is fully recoverable under unloading but $\boldsymbol{\varepsilon}^{v}$ is only partially because of the multiplicative aging function $\nu(t)$.

The viscoelastic strain should be adjusted to take into account the effect of humidity and temperature changes. The effect of humidity and temperature on microstructure aging and creep rate is modeled by introducing two transformed times, t_e and t_r (Bažant et al., 2004). t_e (Eq.5.20) is the equivalent hydration time, which

characterizes the degree of hydration impact on aging. t_r (5.22) is the reduced time representing the impact on the rate of bound breaking and restoration at creep sites

$$\mathrm{d}t_e = \Psi_e(\mathrm{T}, h)\,dt \tag{5.20}$$

$$\Psi_e(\mathrm{T}, h) = \exp(\frac{\mathrm{Q}_e}{k_\mathrm{B}}(\frac{1}{\mathrm{T}_0} - \frac{1}{\mathrm{T}})).\frac{1}{1 + [\alpha_e(1-h)]^4} \tag{5.21}$$

$$\mathrm{d}t_r = \Psi_r(\mathrm{T}, h)\,dt \tag{5.22}$$

$$\Psi_r(\mathrm{T}, h) = \exp(\frac{\mathrm{Q}_r}{k_\mathrm{B}}(\frac{1}{\mathrm{T}_0} - \frac{1}{\mathrm{T}})).(\alpha_r + (1-\alpha_r)h^2) \tag{5.23}$$

In Eqs.5.21-5.23, T (K) the absolute temperature, T_0(K) is the reference temperature and h(-) the pore relative humidity. Q_e and Q_r are the activation energies and k_B is Boltzmann's constant. By default, $\mathrm{Q}_e/k_\mathrm{B} = 2700\mathrm{K}$ and $\mathrm{Q}_r/k_\mathrm{B} = 5000\mathrm{K}$, $\alpha_e = 10$, and $\alpha_r = 0.1$. $\frac{1}{1+[\alpha_e(1-h)]^4}$ is the correction factor for the progress of the hydration rate as a function of the degree of saturation. For $\alpha_e = 10$, the value of this factor is 1/17 at 80% RH, which means that hydration is slowed down 17 times compared to that at saturation. A 60% relative humidity, the hydration rate is 257 times slower than at full saturation.

- $\boldsymbol{\epsilon}^f$ stands for the flow strain tensor occurring in long term. On the one hand, the viscous dashpot in fig.5.15 is the age dependent-viscosity,

$$\eta(t) = \frac{t}{q_4} \tag{5.24}$$

where q_4 is a fitting parameter. Let us emphasize that this creep is completely irrecoverable. Moreover, Bažant et al. (1997, 2004) pointed out that micro-prestress facilitates sliding of the C-S-H sheets at the micro-structure scale, which means that the flow strain increases as the micro-prestress decreases

$$\dot{\boldsymbol{\epsilon}}^f = \frac{\boldsymbol{\sigma}}{\eta(\mathrm{S})} \tag{5.25}$$

where η(S) is the dashpot viscosity for flow strain and is related to the so called microprestress S by power law function:

$$\frac{1}{\eta(\mathrm{S})} = cp\mathrm{S}^{p-1} \tag{5.26}$$

where c and p are positive constants.

The microprestress is considered to be much bigger than any stress acting at the macroscopic level. Hence it is not influenced by macroscopic stress. Its evolution is essentially driven by internal relative humidity and temperature changes and follows

$$\frac{d\mathrm{S}}{dt} + \Psi_s(\mathrm{T}, h)c_0\mathrm{S}^p = k_1.|\frac{d(\mathrm{T}ln(h))}{dt}| \tag{5.27}$$

where c_0 and k_1 are constant parameters, p an exponent set equal to 2 (Jirásek and Havlásek, 2014); Ψ_s the multiplying factor to account for the acceleration of micro-prestress relaxation at higher temperatures, and its deceleration at low humidities. The dependence of Ψ_s on humidity and temperature is assumed in a form similar to Eq.5.23, but with different parameters in general, $Q_s/k_B = 3000$ K and $\alpha_s = 0.1$. The governing differential equation of the viscosity reads

$$\dot{\eta} + \frac{\mu_S}{T_0}|\dot{T}ln(h) + T\frac{\dot{h}}{h}|\eta^2 = \frac{\Psi_s}{q_4} \tag{5.28}$$

where μ_s reads Eq.5.29 and has to be identified by numerical inverse analysis.

$$\mu_s = c_0 T_0 k_1 q_4 \tag{5.29}$$

with the initial condition for viscosity as

$$\eta(t_0) = \frac{t_0}{q_4} \tag{5.30}$$

where q_4 is the parameter for flow strain, which includes long term basic creep and drying creep.

References

Z. P. Bazant and J. C. Chern. Concrete creep at variable humidity: constitutive law and mechanism. 18(1), 1985. ISSN 1871-6873. 154

Z P Bažant, A B Hauggaard, S Baweja, and F-J Ulm. Microprestress-solidification theory for concrete creep. I: Aging and drying effects. *Journal of Engineering Mechanics*, 123 (11):1188–1194, 1997. 154, 155, 156

Z.P Bazant and S. Prasannan. Solidification theory for concrete creep. i: Formulation. *Journal of engineering mechanics*, 115(8):1691–1703, 1989. 154, 155

Z.P Bažant, G. Cusatis, and L. Cedolin. Temperature effect on concrete creep modeled by microprestress-solidification theory. *Journal of engineering mechanics*, 130(6):691–699, 2004. 154, 155, 156

F. Benboudjema, F. Meftah, and J.M. Torrenti. Interaction between drying, shrinkage, creep and cracking phenomena in concrete. *Engineering Structures*, 27(2):239–250, 2005. 154

L. Charpin, TO. Sow, X. De Pradel, F. Hamon, and J-P Mathieu. Numerical simulation of 12 years long biaxial creep tests: Efficiency of assuming a constant poisson's ratio. pages 997–1004, 2017. 154

M Jirásek and P Havlásek. Microprestress–solidification theory of concrete creep: Reformulation and improvement. 60:51–62, 2014. 154, 157

A. Sellier and L. Buffo-Lacarriere. Towards a simple and unified modelling of basic creep, shrinckage and drying creep of concrete. *European Journal of Environmental and Civil Engineering*, 13(10):1161–1182, 2009. 153

A. Sellier, S. Multon, L. Buffo-Lacarrière, T. Vidal, X. Bourbon, and G. Camps. Concrete creep modelling for structural applications: non-linearity, multi-axiality, hydration, temperature and drying effects. *Cement and Concrete Research*, 79:301–315, 2016. 153

ÉCOLE DOCTORALE
Sciences mécaniques et énergétiques, matériaux et géosciences (SMEMAG)

Titre: On the impact of drying rate on delayed strain behavior of cement-based materials: experimental and numerical study.

Mots clés: Effet de taille, vitesse de séchage, fluage, retrait, humidité relative, MEBE, Enceinte, climatique, Corrélation d'images.

Résumé: Le présent travail vise à apporter une contribution à la compréhension des mécanismes de séchage, de retrait et de fluage de la pâte de ciment et de pouvoir ensuite proposer un modèle prenant en compte l'effet de taille sur le comportement différé du béton. En premier lieu, le but de la campagne expérimentale est d'étudier l'effet de la vitesse de séchage sur le fluage et le retrait. Une difficulté lors de la caractérisation du retrait et du fluage séchant est la fissuration des échantillons en raison des gradients de séchage au sein de l'échantillon. Ainsi, afin d'isoler les effets purement «matériaux » à l'échelle de la pâte de ciment, nous avons décidé de réaliser des essais sur la pâte de ciment avec humidité contrôlée: au Microscope Electronique à Balayage Environnemental, en Enceinte Climatique à taux de CO2 maîtrisée et par Solutions Salines Saturées.
En deuxième lieu, ces essais nous ont permis de proposer des modèles simples de séchage, de retrait et de fluage qui intègrent l'impact de la vitesse de séchage sur le comportement des matériaux cimentaires sous solliccitations hydromécaniques.

Title: On the impact of drying rate on delayed strain behavior of cement-based materials: experimental and numerical study.

Keywords: Size effect, drying rate, Creep, Shrinkage, Relative humidity, ESEM, Climatic chamber, Digital Image Correlation.

Abstract: This work aims to contribute to the understanding of drying, shrinkage and creep mechanisms at the cement paste scale and in the light of that, to propose a model taking into account these hydric effects on the delayed behaviour of cement-based materials. Firstly, an experimental campaign is carried out to study the effect of drying rate on creep and shrinkage. A difficulty in characterizing shrinkage and drying creep is the cracking of the samples due to drying gradients within the sample. Thus, in order to isolate the purely "material" effects at the cement paste scale, it was decided to study cement paste samples at controlled humidity by mean of: Environmental Scanning Electron Microscope, Climatic Chamber with controlled CO2 concentration and Saturated Saline Solution.
Secondly, the analysis of experimental results allows us to propose drying, shrinkage and creep models that best integrate the impact of drying rate on the hydro-mechanical behavior of cement-based materials.

Université Paris-Saclay
Espace Technologique / Immeuble Discovery
Route de l'Orme aux Merisiers RD 128 / 91190 Saint-Aubin, France